UNIVERSITY OF LIVERPOOL

Synthesis of perylene diimide-based nanoparticles as NIR probes for in vivo imaging

Thesis submitted in accordance with the requirements of the University of Liverpool for the degree of Doctor of Philosophy

By

Yonghong Yang

October 2017

Contents

Abbreviations

ACN	Acetonitrile
AFM	Atomic Force Microscopy
BLI	Bioluminescence Imaging
CCD	Charged Coupled Device
CFSE	Carboxyfluorescein Succinimidyl Ester
CT	Computed Tomography
DAPI	4',6-Diamidino-2- Phenylindole
DBU	1,8-Diazobicyclo[5.4.0]Undec-7-Ene
DCM	Dichloromethane
DiR	3,3,3',3'-Tetramethylindotricarbocynaine Iodide
DLS	Dynamic Laser Scattering
DMEM	Dulbecco's Modified Eagle's Medium
DMSO	Dimethyl Sulfoxide
ECCs	Embryonic Carcinoma Cells
ECM	Extracellular Matrix
EDTA	Ethylenediaminetetraacetic Acid
EEA	Early Endosome Antigen
EM	Electron Microscopy
EPCs	Endothelial Progenitor Cells
EPR	Enhanced Permeation and Retention
ESCs	Embryonic Stem Cells
FBS	Foetal Bovine Serum
FGF	Fibroblast Growth Factors
FI	Fluorescence Imaging
GP	B-Glycerol Phosphate
Hb	Deoxyhemoglobin
HbO2	Oxyhemoglobin
HEC	Hydroxyethyl Cellulose
HSA	Human Serum Albumin
HSCs	Haematopoietic Stem Cells
iPSCs	Induced Pluripotent Stem Cells

IV	Intravenous
IVM	Intravital Microscopy
LCST	Low Critical Solution Temperature
LDH	Lactate Dehydrogenase
MPS	Mononuclear Phagocyte System
MRI	Magnetic Resonance Imaging
MSCs	Mesenchymal Stem/Stromal Cells
MSOT	Multispectral Optoacoustic Tomography
MTT	3-(4,5-Dimethylthiazol-2-Yl)-2,5-Diphenyltetrazolium Bromide
Mw	Molecular Weight
NaTPP	Sodium Triphosphate Pentabasic
NIR	Near Infra-Red
NMR	Nuclear Magnetic Resonance spectroscopy
O/W	Oil-in-Water
PAI	Photoacoustic Imaging
PAS	Photoacoustic Spectroscopy
PAT	Photoacoustic Therapy
PBS	Phosphate Buffer Solution
PCL	Poly (ε-Caprolactone)
PCS	Photon Correlation Spectroscopy
PDI	Perylene Diimide derivative
PET	Positron Emission Tomography
PFA	Paraformaldehyde
PLG/PLGA	Poly(Lactide-co-Glycolide)
PNIPAm	Poly(N-Isopropylacrylamide)
PTCDA	Perylenetetracarboxylic Dianhydride
PVA	Poly (Vinyl Alcohol)
QELS	Quasi-Elastic Light Scattering
RES	Reticuloendothelial System
RF	Radiofrequency
RMTs	Regenerative Medicine Therapies
ROS	Reactive Oxygen Species

SD	Standard Deviation
SDS	Sodium Dodecyl Sulfate
SEM	Scanning Electron Microscopy
SHH	Sonic Hedgehog
SPECT	Single-Photon Emission Computed Tomography
SPNs	Semi-Conducting Polymers Nanoparticles
SPR	Surface Plasmon Resonance
SSCs	Somatic Stem Cells
TGFβ	Transforming Growth Factor Beta
THF	Tetrahydrofuran
TPEG	Tocopherol Polyethylene Glycol Succinate
US	Ultrasound
UV-Vis	Ultraviolet-Visible
XCT	X-Ray Computed Tomography

Abstract

Cell-based regenerative medicine therapies (RMTs) have great potential to treat chronic diseases and the diseases that are currently difficult to be cured, via the use of stem cells, progenitor cells or stromal cells. However, before they can be translated into the clinic, the safety and efficacy of RMTs needs to be evaluated in animal models. An important part of this evaluation is to monitor the viability and biodistribution of the cells after they have been implanted. Non-invasive in vivo imaging techniques, mainly including optical imaging modalities and non-optical imaging modalities, are powerful tools for evaluating viability and biodistribution as they enable the cells to be monitored longitudinally in each individual animal. Among these modalities, an emerging technology known as multispectral optoacoustic tomography (MSOT) is well-suited for this purpose because it combines high spatial resolution and high temporal resolution with high sensitivity. Another advantage of MSOT is that its multispectral capabilities means that multiple photoabsorbers can be imaged simultaneously. A major aim of this project was to develop non-toxic, stable organic nanoparticles that can be taken up by cells with high efficiency, enabling the cells to be monitored in vivo using MSOT.

A perylene diimide (PDI) compound was synthesized, which showed strong light absorbance in the near infrared (NIR) region in organic solution. Due to its high hydrophobicity, in order to use it as a probe for cell imaging, aqueous PDI nanoparticle suspensions were developed by nanoprecipitation and emulsion freeze-drying, with poly (vinyl alcohol) (PVA), tocopherol polyethylene glycol succinate (TPEG), and an in-house synthesized block copolymer as stabilizer. The PDI nanoparticle suspensions showed maximum NIR absorbance at 700 nm. Both PVA and block copolymer-stabilized PDI nanoparticles showed low cytotoxicity under standard concentration ranges, as tested with mouse mesenchymal stem/stromal cells (MSCs). However, unlike PVA-stabilized PDI nanoparticles, block copolymer-PDI nanoparticles showed strong uptake by the MSCs and could produce strong signals as tested by UV-Vis and flow cytometry. The MSCs labelled with block copolymer-PDI nanoparticles were injected subcutaneously into mice to evaluate their effectiveness as fluorescence and MSOT imaging probes. The results showed that with fluorescence imaging, the signals generated by MSCs labelled with PDI particles were not much stronger than the

fluorescence signals generated from the background. In contrast, the MSCs labelled with PDI nanoparticles could be easily visualised with MSOT for at least 11 days (study end point).

Another problem with cell-based RMTs is that a large proportion of the injected population usually dies within 24-48 hours, which could possibly render the cells less effective. This problem could potentially be overcome by implanting the cells in a hydrogel, as previous studies have indicated that this tends to improve viability. A second main aim of this study was therefore to develop a hydrogel to encapsulate cells for implantation, and to functionalise the hydrogel so that its stability can be monitored in vivo with MSOT. The results showed that MSCs encapsulated in injectable thermosetting chitosan hydrogel survived, and the presence of PDI nanoparticles in the hydrogel enabled the gel system to be imaged using MSOT.

To summarise, this project has demonstrated the use of PDI nanoparticles as NIR probes for MSOT imaging. Because chemical synthesis methods are available to prepare a series of PDI compounds with tunable NIR absorption wavelength and hydrophilicity, this method can be a powerful route to synthesize desired PDI nanoparticles (and the mixture of them for multimodal imaging) as well as PDI-based hydrogels. In turn, this can offer effective in vivo live cell imaging longitudinally and help to better understand the safety and efficacy of RMTs.

Acknowledgement

First, I would like to thank both of my supervisors, Dr Haifei Zhang and Professor Patricia Murray, for the opportunity to work on this exciting and interdisciplinary project. Over the past four years, their advice, guidance, and encouragement helped me keep going through the highs and lows. I am truly grateful for their help and comments during the thesis-writing stage. Without them, I wound have not completed the project and produced this thesis.

Over the years, I have worked in the chemistry lab and the physiological lab of the stem cell group. There have been a lot of things to learn: the location of chemicals/reagents, characterization and imaging instruments, analysing software and many more. These have only been made possible from the help of many friends and colleagues in both labs: Jack, Arthur, Chris, Isabel, Ilaria, Jing, Joe, Aled, Mike, Dan, Ulrike, Alex, and many others including all the year 3 and year 4 students. Special thanks are given to Dr Jack Sharkey, who helped me patiently with animal work and MSOT imaging. I have good memories of discussion and laughs in labs and in offices.

It goes without saying that all these would not be possible without my family support. It has been a hard but exciting journey but this has been made easier with the love and support of my two wonderful kids and all my friends.

Chapter 1 Introduction and review on relevant research topics

1.1 Cell-based Regenerative Medicine Therapies (RMTs)

By definition, regenerative medicine is used to replace or regenerate human cells, tissue or organs, to restore or establish normal function [1]. RMTs have great potential for a variety of difficult-to-cure diseases, regenerating organ and tissue loss due to disease and injury, and reducing reliance on transplantation [2-4]. Stem cells are mainly involved in RMTs although stromal cells and macrophages are also used [2]. Stem cells have two distinct properties: the capacity to self-renew and the ability to differentiate into specialized cells [5]. They are typically defined in terms of their fate of differentiation, with unipotent stem cells giving rise to just one type of specialized cell; multipotent stem cells giving rise to a range of different specialized cells; and pluripotent stem cells generating all cell types within the mature organism. Progenitor cells, which are usually derived from stem cells, can also differentiate to generate different types of specialized cells but have a limited capacity to self-renew [5].

The stem cells that are used in RMTs mainly include embryonic stem cells (ESCs), induced pluripotent stem cells (iPSCs), and somatic stem cells (SSCs), also known as adult stem cells [6]. SSCs can be found and isolated from a range of different tissues, with examples including mesenchymal stem/stromal cells (MSCs), haematopoietic stem cells (HSCs) and endothelial progenitor cells (EPCs) [6]. **Figure 1-1** illustrates how stem cells can be used for RMTs and in drug discovery. ESCs and iPSCs are particularly advantageous because they can generate any cell type, and because they do not become senescent, they can easily be expanded. However, there

are ethical issues relating to the use of ESCs, and for both cell types there are some safety concerns because it is known that undifferentiated ESCs and iPSCs can generate tumours. The risk of tumourigenicity seems proportional to the length of time that the cells are cultured [6,7].

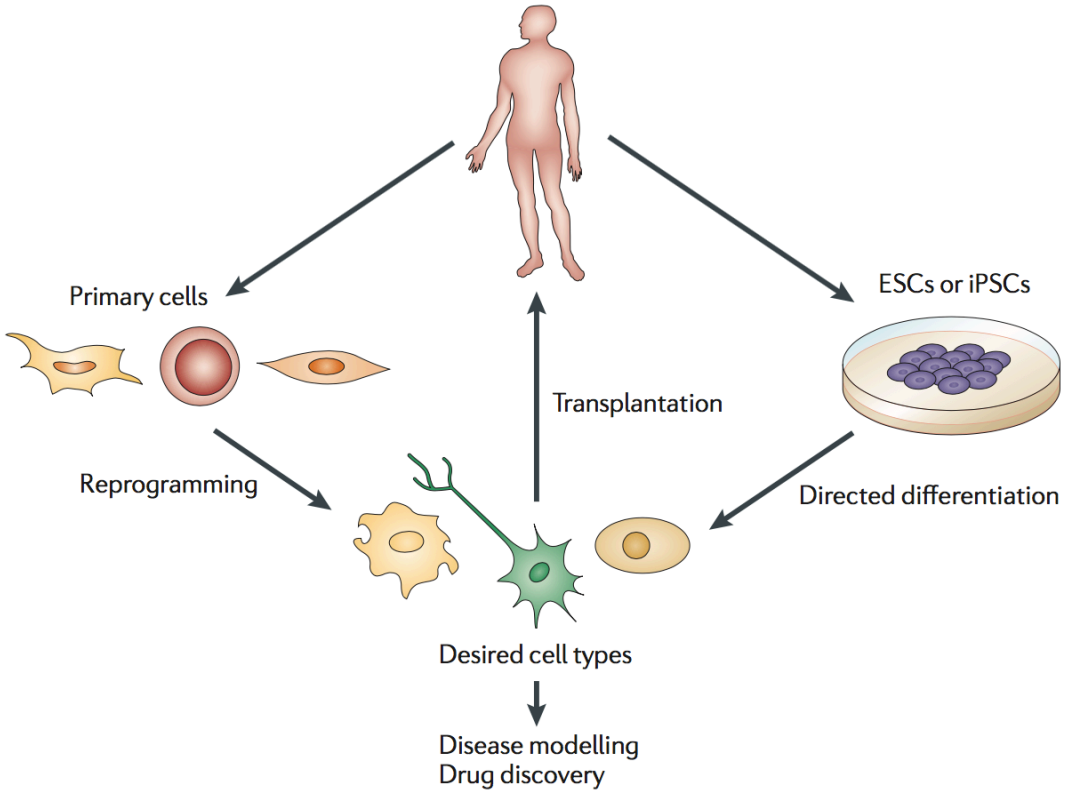

Figure 1-1. Diagram showing how stem cells can be used to generate patient-specific cells of a desired type for regenerative medicine or drug discovery. Reprinted from ref 4.

SSCs, on the other hand, are less tumourigenic, but have some disadvantages. For instance, they can be difficult to source, and because they tend to become senescent in culture, they can be difficult to expand. However, MSCs have quite a good scale-up potential as they can be cultured for a number of weeks before becoming senescent [7]. Furthermore, MSCs can be sourced from a number of tissues, including bone marrow,

adipose tissue and the umbilical cord. Indeed, MSCs have been the mostly used cell type in regenerative medicine [8-10], and for this reason, are the main focus of this project.

1.1.1 The differentiation and fate of stem cells

Before describing MSCs, the factors and pathways that regulate the differentiation and the fate of the stems are explained here. The same principles (or factors) may be applied for all types of stem cells although the specific details may be different for MSCs.

The differentiation of stem cells is regulated by soluble factors such as growth factors, cytokines, small molecules (chemical cues), cell-cell interactions and the extra-cellular matrix, which all together comprise the stem cell niches [4, 11, 12]. Families of protein signaling molecules include the TGFβ (transforming growth factor beta) superfamily (33 in mammals, including activators such as Activin A, BMP4, TGFβ3, TGFβ1 and inhibitors such as Noggin, LeftyA, Ceberus); the FGF (fibroblast growth factors) family (23, e.g., activators such as FGF2, FGF8); the WNT family (19, activators such as WNT3A, inhibitors such as DKK1, Frizzled 8); and the Hedgehog family (3, e.g., activators such as sonic hedgehog (SHH)) [11]. These protein factors can act either to promote or inhibit differentiation towards a specific cell type. Examples of small molecules that can promote cell differentiation include ascorbic acid, nicotinamide, retinoic acid, indolactam V, etc. [11]. The combination of protein factors and small molecules may be used to direct cell differentiation efficiently.

Niches are the 3D local tissue microenvironments that maintain and regulate the fate of stem cells. Identifying and characterizing niches are crucial to maintain healthy growth/renewal of stem cells and regulate their self-renewal and differentiations. There

are different ways in which stem cells can divide: asymmetric (generates one identical daughter stem cell and one committed progenitor cell) and symmetric (either generates two identical daughter stem cells, or two committed progenitor cells) [12,13]. The balance between asymmetric and symmetric divisions determines the size of the stem cell population, as illustrated in **Figure 1-2** [13]. Asymmetric division maintains the size of the stem cell population; symmetric division that generates two committed cells, leads to the size of the stem cell population becoming exhausted; symmetric division that generates two stem cells leads to expansion of the stem cell population. When stem cell populations are being expanded in vitro, culture conditions that facilitate symmetric division to generate two identical daughter stem cells are typically used.

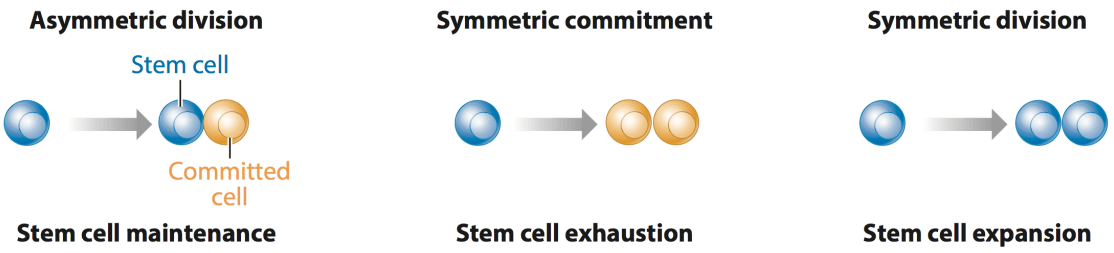

Figure 1-2. Schematic showing the division patterns of stem cells. Reprinted from ref 13.

1.1.2 MSCs

MSCs were first isolated from bone marrow. It was found that bone marrow contained a population of HSCs and a rare population of plastic-adherent stromal cells. These stromal cells displayed multipotency [14] and were named as MSCs because they were thought to reside in the stromal compartment of various tissues. There are no specific surface markers to unequivocally identify MSCs, but a set of criteria has been proposed: (i) adherence to plastic when cultured in vitro; (ii) expression of typical

surface markers, which may be different for different species (**Table 1-1**); (iii) capacity to differentiate to osteoblasts, adipocytes, and chondroblasts in vitro. These criteria are for human MSCs but may not be completely applicable to other species [9]. MSCs can now be isolated from various tissues including umbilical cord, adipose tissue, placenta, lung, liver, skin, and synovial tissue [9,15]. These MSCs are heterogeneous with different growth potential but exhibit similar surface markers and mesodermal differentiation potential [9].

Table 1-1. Surface markers used to characterise MSCs. (Adapted from refs 9 and 18).

Positive Markers		**Negative Markers**	
Mouse	Human	Mouse	Human
Sca-1	Sca-1	CD45	CD45
CD44	CD44	CD34	CD34
CD105	CD105	CD19	CD19
MHC I^{low}	MHC I^{low}	CD11b	CD11b
CD140a	CD71	CD11c	CD11c
	CD73	MHC II	MHC II
	CD90	CD31	CD79a

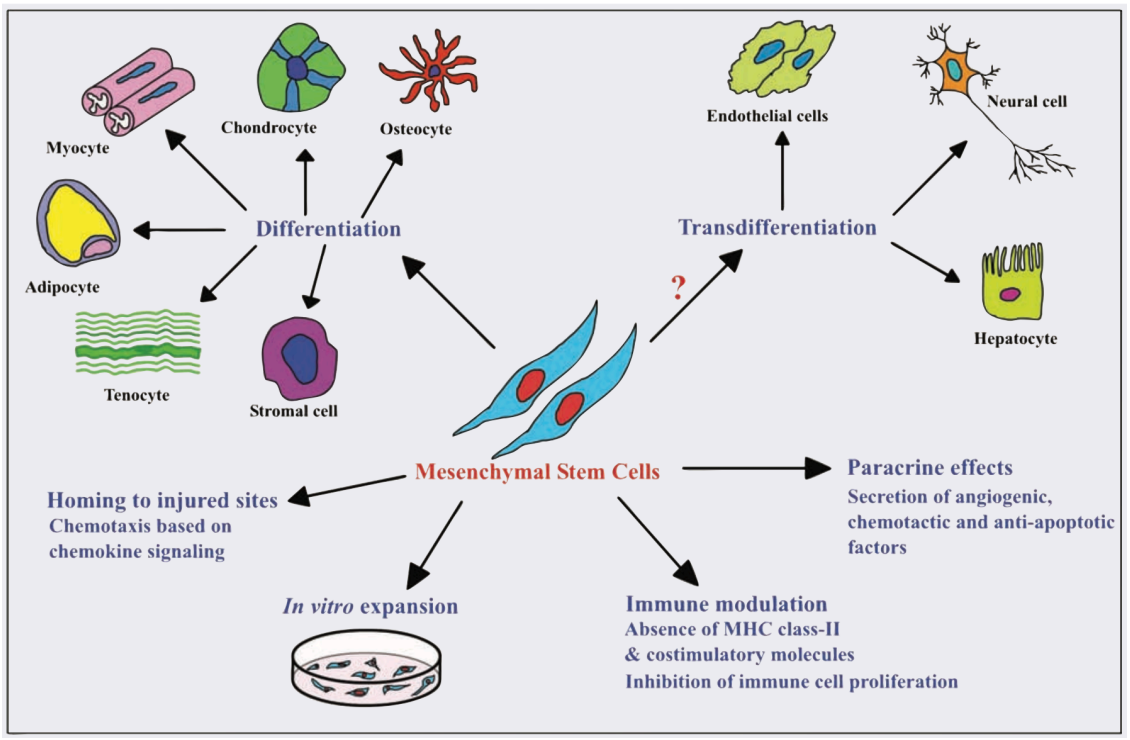

Figure 1-3. The types of specialized cells that MSCs can differentiate into and the significant therapeutic properties that MSCs exhibit. Reprinted from ref 8.

Figure 1-3 shows that MSCs can be differentiated into different types of specialized cells [8]. However, despite some reports suggesting that MSCs can transdifferentiate into non-skeletal cells such as endothelial cells, neural cells, and hepatocytes, it is now thought that MSCs are not able to do this, and previous reports suggesting this did not use appropriate evaluation methods [8]. The differentiation of MSCs is mainly regulated by the WNT canonical pathway and the TGFβ superfamily pathway, plus the influence of small molecules [9,15]. For example, MSCs can differentiate into osteogenic cells in the presence of dexamethasone, β-glycerol phosphate, and ascorbic acid. When the medium contains dexamethasone and TGFβ-3, MSCs can differentiate to chondrocytes. To differentiate into an adipogenic lineage,

MSCs can be cultured in the presence of dexamethasone, insulin, indomethacin, and 1-methyl-3-isobutylxanthine [9].

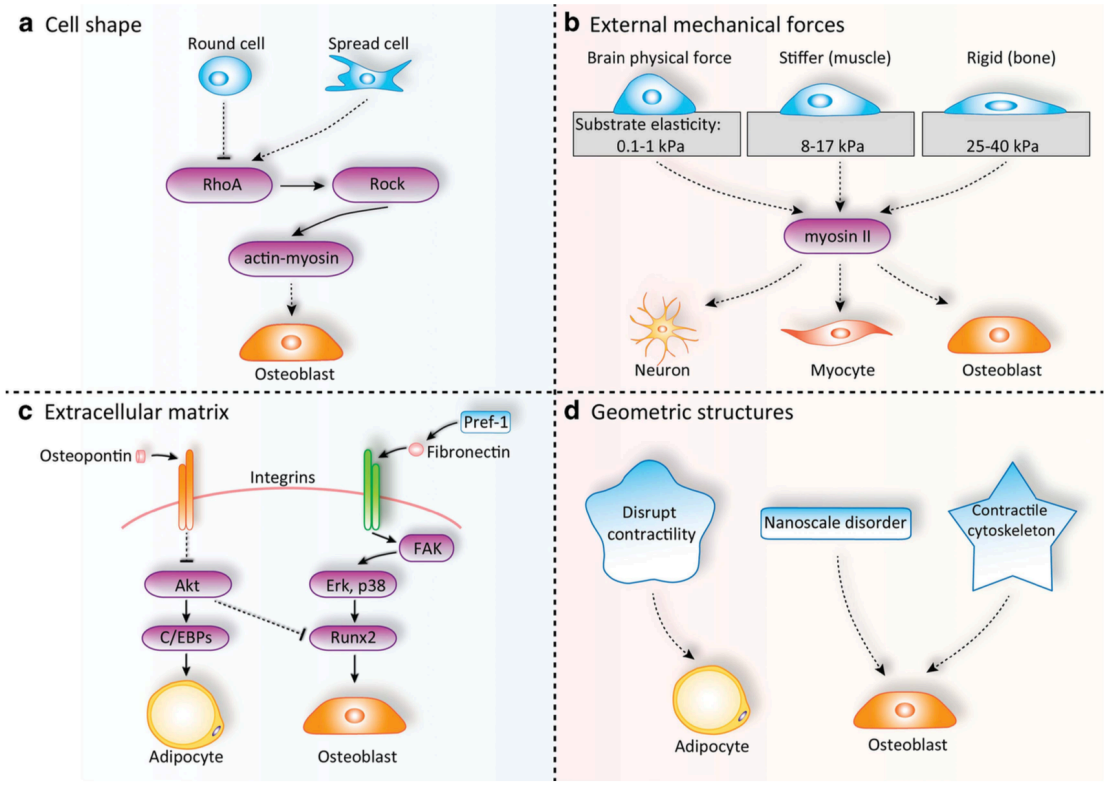

Figure 1-4. The diagram shows the physical factors regulating MSC differentiation. Reprinted from ref 15.

In addition to the chemical cues, the differentiation of MSCs can be significantly influenced by physical factors including cell shape, elasticity of substrates, types of matrix, and nanoscale geometric features (Figure 1-4) [15]. These physical factors are investigated by constructing substrate mimicking the extracellular matrix (ECM) in order to regulate the fate of stem cells. Parameters of the ECM, including adhesion to stem cells, stiffness and topography, all play a role in influencing the growth and differentiation of the stem cells [16]. When culturing stem cells with the substrates, the mechanical forces and geometry can considerably influence stem cell

behavior [17]. For the MSCs, stiffer hydrogels enhance the differentiation to the neuronal direction with increased proliferation rates. Stiffer gels also favour osteogenic differentiation over an adipogenic course. Soft substrates with addition of a growth factor (VEGF) promote the differentiation into endothelial cells. [17]. Using polyacrylamide gels of tunable stiffness, it was found that substrate stiffness and the presence of neighboring cells could regulate osteogenesis in MSCs [18]. Tensile forces have been shown to improve osteogenic differentiation of MSCs or towards smooth muscle cells upon application of growth factors [17].

Patterned substrates can also regulate MSC differentiation. It was found that small islands promoted osteogenic differentiation while large islands enhanced adipogenic differentiation [19]. The substrates with different patterns of 100 nm-deep nanopits had a high impact on MSC differentiation into osteogenic cells [20]. For the substrates with patterned nanopillars (diameters 10/30 nm, interpillar distances 50 – 120 nm and heights 20-35 nm), the MSC differentiation to osteogenic cells was enhanced with the higher nanopillars preferred [21. The surface modification of the substrates can also guide MSC differentiation. For example, -NH_2 and –SH-modified surfaces promoted and maintained osteogenesis while –OH and –COOH-modified surfaces promoted and maintained chondrogenesis [22].

MSCs can secrete soluble paracrine factors that contribute to endogenous cardiomyogenesis and angiogenesis, including a variety of cytokines and growth factors that can suppress the immune system, inhibit fibrosis/apoptosis, and improve angiogenesis [9] (Figure 1-3). In spite of promising results obtained from stem cell transplantation, it has been noticed in vivo that the engraftment and differentiation of the MSCs is very low. Consequently, the encouraging results have been attributed to the secretion of paracrine factors by the MSCs in the tissue microenvironment [9, 23].

In a study by our group, intravenous (IV) administration of human kidney-derived cells in mice were found to promote renal regeneration [24]. However, the kidney cells were exclusively located in the lungs (instead of homing to the kidney) and disappeared by 24 hours. The renal repair was believed to be mediated by the secreted paracrine factors [24]. An earlier report suggested that MSCs act in a similar way; *i.e.,* after IV administration, MSCs were entrapped in the lungs and did not migrate to injured kidneys, but were still able to promote repair [25].

Apart from their ability to promote the repair of injured tissues, MSCs are immunosuppressive, and can suppress both the adaptive immune system (e.g*.,* T-cells) [26] and also the innate immune system (e.g*.,* macrophages). This makes MSCs highly appealing for allogeneic (donated from someone else) transplantation.

1.1.3 Safety and translation of RMTs

A big barrier to the clinical translation of RMTs is safety. The main safety problems are tumourigenicity and immunogenicity [2,7,27].

It is not surprising that stem cell tumourigenicity has been recorded because stem cells share many of similar traits with tumour cells, e.g., long-term self-renewal, expression of similar markers [7]. Indeed, teratocarcinoma and its benign counterpart teratoma are tumours with high populations of pluripotent cells and differentiated tissues. The research on embryonic carcinoma cells (ECs) laid the foundation for isolating and propagating ESCs. ECs and ESCs both exhibit pluripotency and robust tumourigenicity [7]. One of the most common assays to demonstrate pluripotency is the teratoma assay. Also, a key assay of "stemness" is a tumour assay. iPSCs are obtained by re-programming with proto-oncogenes such as c-Myc and KLF4 , both strongly linked to tumourigenesis. With the advance of iPSC technology, it is now

possible to generate iPSCs without c-Myc. However, the absence of c-Myc has reduced the efficiency of generating iPSCs and yet these iPSCs can still produce tumours in the form of teratomas [7]. To address the tumourigenicity issue, it is suggested stem cells should be differentiated into progenitor cells or specialized cell types [28], and any remaining undifferentiated stem cells should be sorted out or killed before transplantation [7]. Another exciting route is to avoid the pluripotent stage, *i.e.,* reprogramming somatic cells directly to the specialized cells or progenitor cells, for RMTs [4, 29].

The main administration routes of RMTs are systemic injection (e.g., intravenous) and direct implantation (others including intranasal, endoscopic, surface application) [27]. Following systemic injection, the cells tend not to survive for a long time, which can be attributed to the attack on the injected cells by the immune system. Another challenge is that the stem cells can end up located in organs such as the lungs or liver rather than being enriched in the target tissues/organs. Implanting the cells directly at the injury/diseased sites could help to improve efficacy and also prevent off-target effects. The immunogenicity issue could be addressed via cell encapsulation with hydrogels before implantation, as this can help to isolate the cells from the immune system. Furthermore, encapsulation with carefully designed hydrogel capsules can improve cell viability and prevent cells from migrating to non-target sites [3,8,11]. Cell encapsulation is discussed in details in section 1.4.

Understanding the biodistribution and fate of cells following implantation is very important for assessing safety and efficacy and also for understanding the mode of action [2]. It is expected that a proportion of cells will die shortly following implantation, which can be due to various factors, such as lack of oxygen, attack by the

immune system, and in diseased tissues, inflammatory cytokines and reactive oxygen species could also have a negative effect on the cells [30].

Being able to assess the viability and biodistribution of implanted cells over time is therefore very important. For this purpose, non-invasive in vivo imaging techniques are required.

1.2 Cell tracking by non-invasive imaging techniques

1.2.1 Non-invasive imaging techniques

There are many imaging techniques/modalities available for preclinical and clinical applications. The techniques may be generally divided into two categories: optical microscopy, where non-ionizing radiation, particularly visible and infrared light, is used to obtain images of cells, tissues and other objects (including fluorescence imaging (FI), bioluminescence imaging (BLI), and intravital microscopy (IVM)) and non-optical techniques (including magnetic resonance imaging (MRI), positron emission tomography (PET), single-photon emission computed tomography (SPECT), computed tomography (CT), ultrasound, and photoacoustic imaging (PAI)) (**Figure 1-5**) [31, 32]. The key features of the imaging modalities are given in **Table 1-2**. It should be noted that the data quoted in Table 1-2 for resolutions and sensitivity are approximate and they may vary between different reports or reviews [2, 32, 33]. Among the imaging techniques mentioned here, optical imaging modalities are mostly only used in pre-clinical applications while the rest are employed in both preclinical and clinical applications.

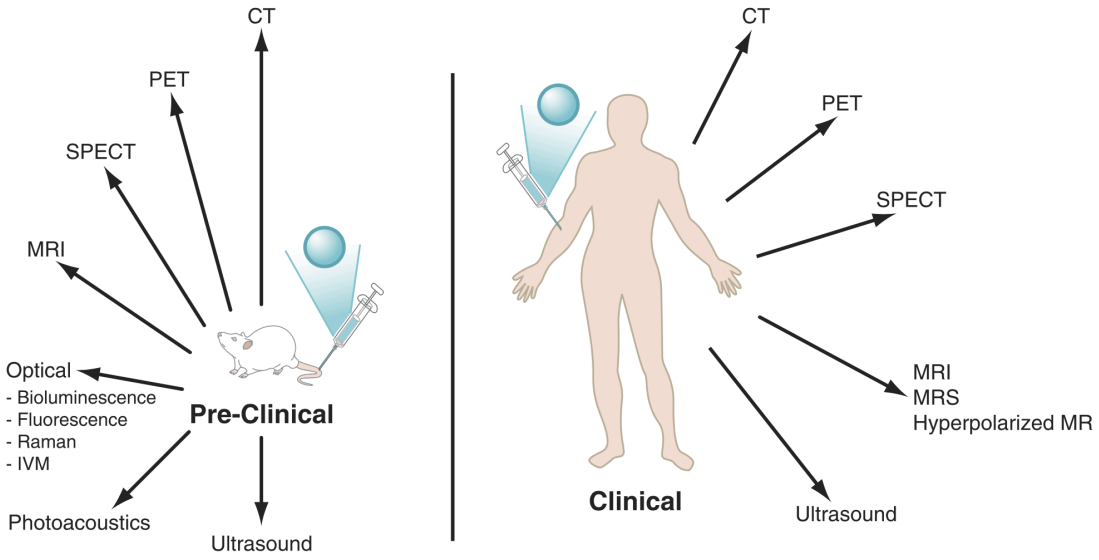

Figure 1-5. Key imaging modalities for preclinical and clinical applications. Reprinted from ref 32.

Table 1-2. Characteristics of different imaging modalities (adapted from ref 32)

Modality	Temporal resolution	Spatial resolution*	Penetration depth	Sensitivity
MRI	Minutes - hours	25 – 100 µm [0.5 – 1mm]	limitless	10^{-3} – 10^{-5} M
PET	Seconds-minutes	1 -2 mm [5 – 7 mm]	limitless	10^{-11} – 10^{-12} M
SPECT	minutes	1 -2 mm [8 - 10 mm]	limitless	10^{-10} – 10^{-11} M
CT	minutes	50 – 200 µm [0.5 – 1mm]	limitless	Not determined
Ultrasound	Seconds - minutes	0.01 – 2 mm	mm-cm	Excellent with microbubbles
FI	Seconds - minutes	2-3 mm	< 1 cm	10^{-9} – 10^{-12} M
BLI	Seconds - minutes	3-5 mm	1-2 cm	10^{-15} – 10^{-17} M
IVM	Seconds - days	1 – 10 µm	~ 700 µm	10^{-15} – 10^{-17} M
PAI	Seconds - minutes	10 µm – 1 mm	6 mm – 5 cm	Not determined

* The data without bracket indicate spatial resolution for preclinical imaging modalities while the data in brackets are spatial resolution for clinical imaging modalities.

1.2.1.1 Non-optical imaging modalities

Magnetic resonance imaging (MRI): MRI uses magnets to polarize and align the hydrogen nuclei (protons) in water molecules in the tissue. When a radiofrequency (RF) is applied, the nuclei are excited to a higher energy level. When the RF is turned off, the nuclei go back to the ground state, releasing energy which is detected by radiofrequency coils [34]. MRI has unlimited penetration depth as well as high spatial resolution and thus provides excellent anatomical information. However, the sensitivity of MRI is relatively low and temporal resolution is poor, making it difficult to assess the biodistribution of administered cells across the whole body. (Table 1-2). Furthermore, due to the presence of air or endogenous contrast (e.g., ferritin), it can be difficult to detect labelled cells in organs such as the lungs and spleen, respectively [2].

Positron emission tomography (PET): PET is a nuclear imaging technique that requires radioactive probes comprising positron (positive electron) emitting radionuclides [35]. PET probes have different half-lives, with the most commonly used probes for cell tracking being based on ^{18}F (half-life, 110 minutes) or ^{89}Zr (half-life, 78.4h). For PET imaging, the sensitivity for tracking cells is very high, with unlimited penetration depth. The temporal resolution is good but the spatial resolution is limited. The use of this imaging technique is also limited by the short-lived radioisotopes and the potential negative impacts on cell health due to the use of ionising radiation [2, 35].

Single-photon emission computed tomography (SPECT): SPECT is another nuclear imaging technique using radionuclide probes. Like PET, SPECT has a limitless depth of penetration and high sensitivity (slightly lower than that of PET clinically). SPECT employs nuclides such as ^{99m}Tc (half-life, 6 hours), ^{123}I (half-life, 13.3 hours), and ^{111}In (half-life, 2.8 days). These nuclides decay via the emission of single γ-ray with differing energies. The similar limitations as for PET apply to SPECT [2, 32].

Computed tomography (CT): CT employs X-rays to scan the whole sample by sections and can produce 3D anatomical images. The X-ray source is linked to the detector array and both can be rotated together around the subject. In the images produced, the parts (e.g., tissue, medium) that absorb X-rays strongly appear white while those poorly absorbing X-rays appear black. An iodinated contrast agent is often added to improve spatial resolution and contrast [32]. CT produces images with high spatial resolution, good temporal resolution, and has been widely used in clinics. However, the sensitivity is low and it is difficult to image soft tissue, and also uses radiation [32].

Ultrasound (US): US detects and utilizes ultrasound waves (frequencies 1 – 20 MHz) as they travel through tissues and media. It can be used for diagnostic imaging and as a therapeutic device. A transducer can detect the waves and convert the information into electrical signals, which are then processed to generate an image. US is relatively inexpensive, has good temporal resolution, and generates no ionizing radiation. However, it is limited to imaging soft tissues only and has a limited depth of penetration [32].

1.2.1.2 Optical imaging modalities

Optical imaging is based on the detection and quantification of light from the subject. The instruments are relatively cheap and there is no need for radioactive agents. A cooled charged coupled device (CCD) camera is usually used which facilitates the detection of weak light signals [36]. For optical imaging, the imaging quality can be improved by increasing the contrast between what is required (signal) and what is not required (background).

Bioluminescence imaging (BLI): BLI detects the bioluminescence emitted from cells labelled with light-generating enzymes (luciferase). Bioluminescence is generated by converting chemical energy to visible light via luciferase and their substrates in tissues. The wavelength of emitted light varies with the use of different luciferase. There are four types of luciferases that are widely used: Firefly luciferase (emission maximum wavelength, 562 nm; substrate, D-Luciferin), Renilla luciferase (emission maximum wavelength, 482 nm; substrate, Coelenterazine), Gaussia luciferase (emission maximum wavelength, 480 - 600 nm; substrate, Coelenterazine), Bacterial luciferase (emission maximum wavelength, ~ 490 nm; substrate, not necessary) [37]. Among them, the firefly luciferase-encoded gene obtained from *Photinus pyralis* is the most commonly used. The substrate, D-luciferin, is a small molecule that can freely diffuse across the cell membrane. To generate bioluminescence, the presence of D-luciferin and cofactors ATP, Mg^{2+}, and oxygen are required [37]. BLI can be used to image cells and track stem cells/immune cells with high sensitivity. However, the depth of penetration is limited and the spatial resolution is low (Table 1-2). Furthermore, the signals cannot be quantified with great accuracy due to loss of light and scattered light in the body [37].

Fluorescence imaging (FI): With FI, a light source (higher energy, shorter wavelength, known as the excitation light) excites a fluorophore to an excited state. When the fluorophore returns to the ground state, light with greater wavelength is emitted, which is then detected. Fluorophores can be proteins, chemical dyes, or nanoparticles [36]. Because the emitted light travels through the medium and tissues, it is critical to design, fabricate, and employ suitable fluorophores with high photostability and minimal attenuation, absorption and scattering by the tissue and medium [32]. As with bioluminescence, FI is convenient to use (not so expensive), has

good temporal resolution and high sensitivity. But the depth of penetration and spatial resolution are limited (Table 1-2).

Intravital Microscopy (IVM): IVM works essentially in the same way as traditional fluorescence microscopy. However, for IVM, the data are collected with a digital camera set-up and an image acquisition network and then analyzed using a computer equipped with relevant algorithms and mathematical models [32]. Compared to FI, the depth of penetration and spatial resolution are improved although still rather limited (Table 1-2). IVM can be performed with various light microscopy techniques, such as wide-field fluorescence microscopy and confocal laser scanning microscopy [38]. However, the combination of IVM with two-photon (multiphoton) microscopy can further improve imaging depth. Compared to traditional one-photon FI, the fluorophores are excited by two or more photons simultaneously. Nearly no out-of-focus emission is detectable and more detectors can be equipped to collect the emission efficiently, providing new insights into physiology and pathophysiology [39].

1.2.1.3 Photoacoustic Imaging (PAI) and MSOT

PAI is a relatively new imaging modality [2, 32]. PAI detects the ultrasound wave generated by strong light (near infra-red (NIR) light) absorption using endogenous or exogenous molecules or probes, exhibiting both high sensitivity and high spatial resolution [40]. Multispectral optoacoustic tomography (MSOT) is a particular type of photoacoustic imaging (PAI) technique that utilizes multiple excitation wavelengths and allows multiple photo-absorbers to be identified simultaneously [41].

The basic principle of PAI is that the absorption of laser energy, either by endogenous photoabsorbers or exogenous photoacoustic probes, results in thermo-

elastic expansion and the generation of a sound wave that can be picked up by an ultrasound detector [40, 42]. **Figure 1-6** schematically describes how ultrasound is generated and detected.

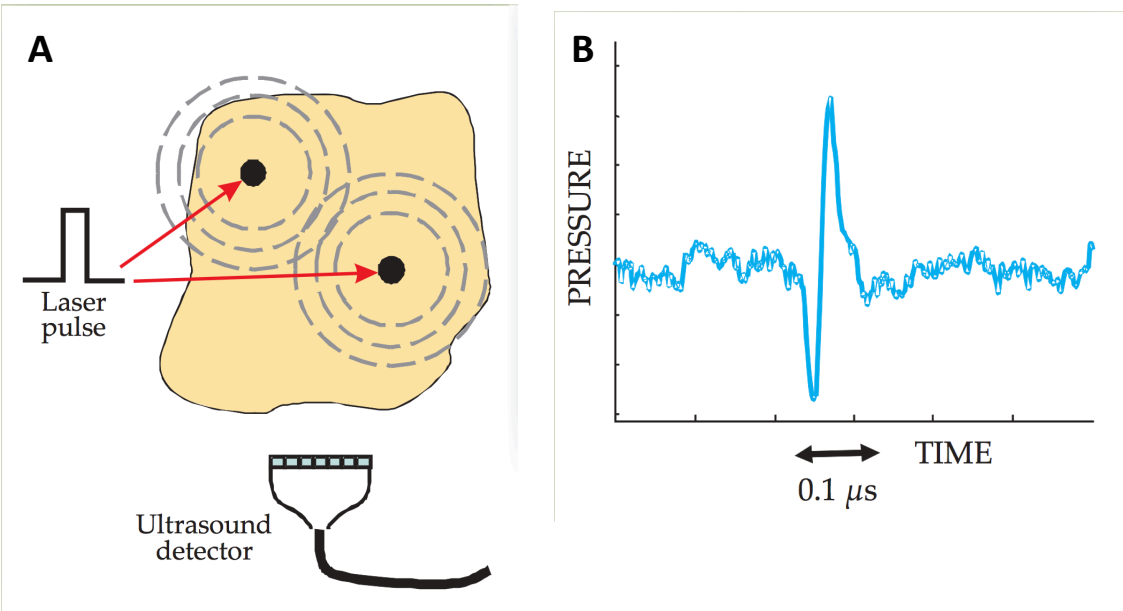

Figure 1-6. Photoacoustic generation and detection. Black dots in the left panel represent regions of high optical absorption. When heated by a laser pulse, they give rise to acoustic waves, which are picked up by an ultrasound detector. The ultrasound waveform shown in the right panel is approximately proportional to the time derivative of the optical pulse. Reprinted from Ref 42.

For PAI, spatial resolution is determined by the acoustic frequency. Penetration depth is considerably impacted by the wavelength of laser illumination. Greater depth is achieved with NIR light because of less optical absorption and diffraction. When travelling in tissue, the ultrasonic attenuation coefficient is nearly linear with operating frequency. Therefore, a trade-off between penetration depth and spatial resolution exists. Generally, penetration depth of 15 cm is associated with a sub-millimetre spatial resolution. A higher resolution of 100 μm may be achieved but with a reduced depth of several centimetres [42]. Mallidi et al compared ultrasound and PAI in terms of

resolution and penetration depth (**Table 1-3**). The PAI techniques are grouped into macroscopic PAI, microscopic PAI, and optical PAI based on the transducer frequency and the size of objects to be imaged [33, 43]. Macroscopic PAI is used with lower frequency and higher imaging depth. However, both axial resolution and lateral resolution are low. Higher frequency can be used for microscopic and optical PAI, resulting in much higher resolution but lower imaging depth [43].

Table 1-3. Comparison of ultrasound and PAI imaging parameters (adapted from ref 43)

Parameter	Transducer frequency (MHz)	Axial resolution (μm)	Lateral resolution (μm)	Imaging depth (mm)
Ultrasound	5	150	300	70
	20	75	165	30
Macroscopic PAI	5	150	300	40
Microscopic PAI	50	15	50	3
Optical resolution PAI	75	15	5	0.7

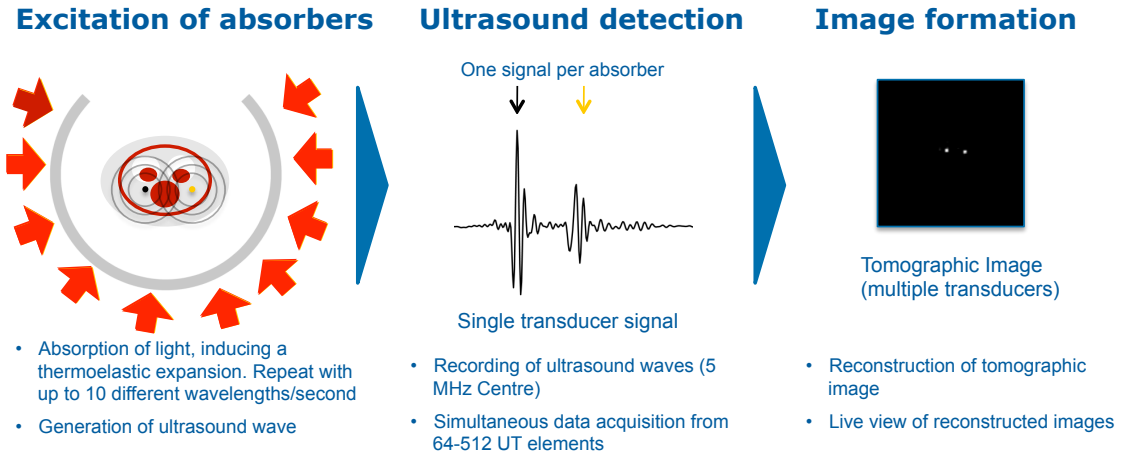

Figure 1-7. Scheme showing MSOT image generation (courtesy of iTheraMedical).

MSOT is a PAI technique which uses multispectral light beams to illuminate a sample or small animal such as a mouse. **Figure 1-7** shows the diagram of how MSOT works. Compared to conventional PAI, MSOT is capable of imaging at multiple wavelengths and the information obtained from multiple wavelengths improves image accuracy as a function of penetration depth [31, 44]. Furthermore, multiple absorbers may be employed and the signals generated from multiple wavelengths can be spectrally unmixed. This allows the identification of these absorbers and provides detailed information about the imaged subject [45]. Due to the combined high spatial resolution and high depth of penetration, MSOT can be used in real time to monitor pharmacokinetics and biodistribution of cells in particular organs [46], enabling both cell tracking and efficacy studies [2].

1.2.1.4 Multimodal Imaging

Each of the imaging modalities have their own intrinsic strength and weak points (Table 1-2). No single imaging modality can be used alone to sufficiently evaluate the safety and efficacy of the RMTs. Thus, multimodal imaging is always preferred in order to get a full picture of the RMTs at different stages, combining imaging modalities that can complement each other. For example, in the multimodality imaging of PET/CT, CT provides the anatomic context to interpret the functional PET study [47]. In general, the use of both imaging probes and genetic reporter is crucial for long-term *in situ* multimodal imaging. This may be a simple mixture of different probes/reporters and/or purposely designed multimodal probes.

1.2.2 Imaging probes and reporters

Cells can be labelled directly with probes or can be genetically modified to express reporter genes [28]. There are various imaging probes which can be either taken up by the cells or attached to the cells via antigen-antibody interaction for antibody-modified probes before imaging. **Figure 1-8** lists the main advantages and disadvantages of both labelling methods [2]. Imaging probes can generate very strong signals at the initial stage and are therefore good for short-term imaging. Compared with reporters, probes also tend to have a very rapid and efficient uptake, enabling a whole cell population to be labelled in a short time period. However, with the growth and proliferation of the cells, the concentration of the imaging probes is diluted, so that after several cell divisions, the cells can no longer be detected. There are also other potential problems, such as leaking of imaging probes, cell toxicity, and difficulties in distinguishing dead cells from live cells. For the reporter genes, the detection sensitivity and specificity can be very high, although this depends on the specific reporter gene used. Because reporter gene labelling is achieved via genetic modification of cells, they are transferred to daughter cells during cell proliferation and are thus suitable for long-term cell tracking without dilution of signal intensity. In principle, imaging signals from reporter genes are only generated from live cells. This property can be used to differentiate live and dead cells during imaging [2]. However, this biological alteration can permanently alter the phenotype of the cells and could adversely affect safety and/or efficacy for RMTs [2, 28, 48].

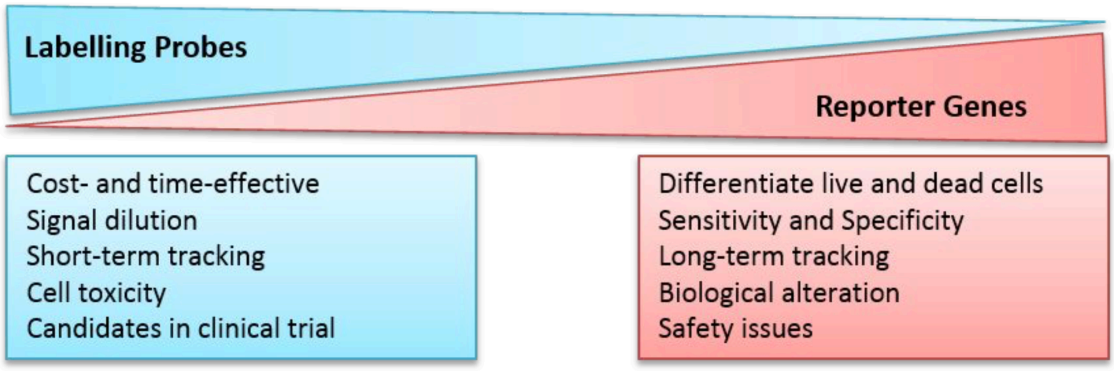

Figure 1-8. Characteristics of direct cell labelling with probes and indirect cell labelling with reporter genes. Reprinted from ref 2.

For bioluminescence imaging, luciferase reporters are most commonly used (described in detail in section 1.2.1.2). For fluorescence imaging, both imaging probes and genetic reporters are frequently used. Because this project aims to develop imaging probes for MSOT and also fluorescence imaging, the main focus here is on imaging probes.

Fluorescent probes for cell labelling mainly includes the following 4 approaches [48]: (i) Amine-reactive probes which diffuse into cells and react with cytosolic amine-containing residues; (ii) Lipophilic dyes which are incorporated into lipid membranes; (iii) Nanoparticle probes which are taken up by endocytosis and/or pinocytosis; (iv) Antibodies that bind to the extracellular domains of membrane proteins.

Fluorescence imaging microscopy detects the emitted light while MSOT uses light to generate ultrasound. In both cases, light wavelength is a critical factor for high quality imaging. Near infra-red (NIR) light enables imaging by both fluorescence and MSOT.

1.2.2.1 Importance of NIR light in imaging

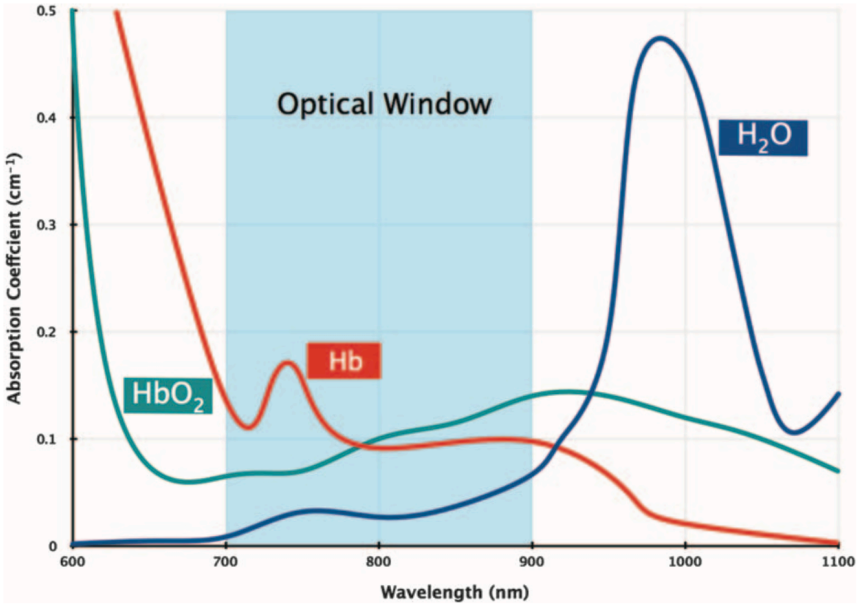

Figure 1-9. Light absorption by water and endogenous chromophores as a function of light wavelength. The wavelength range of 600 – 1100 nm (reprinted from ref 49).

When light travels through tissues and medium, the absorption of light by water and endogenous chromophores, including melanin, oxyhemoglobin (HbO_2) and deoxyhemoglobin (Hb), varies as a function of wavelength. The absorption by chromophores generally decreases with increasing wavelength whilst the absorption by water increases with increasing wavelengths. However, it should be pointed out that this trend is not linear. For NIR wavelengths of 2000 – 3000 nm, the penetration depth is limited to 0.1-1 mm because water is the major light absorber. In the UV region, the low absorption depth is caused by cellular macromolecules [42]. There is an 'optical window' between the wavelengths of 650 nm and 1300 nm where the penetration depth can reach several centimetres and the contrast is still high [33, 42-43], with the optimal optical window being in the wavelength range of 650 – 900 nm (**Figure 1-9**), as above

900 nm, water within the tissues starts to absorb more light [49]. Therefore, imaging probes that absorb and emit light in this range are required both for fluorescence imaging and MSOT.

NIR imaging probes are advantageous for both fluorescence imaging and PAI. They have different requirements but the requirement for reducing light absorption and scattering is the same. For fluorescence imaging, light emitted by the NIR probes is detected [49, 50]. For MSOT, it is the absorbed light that is detected.

1.2.2.2 Imaging probes for fluorescence imaging

Various imaging probes have been employed, including amine-reactive dyes (e.g., carboxyfluorescein succinimidyl ester (CFSE)), lipophilic dyes (e.g., PKH26, 3,3,3',3'-tetramethylindotricarbocynaine iodide (DiR), DiD, DiI) [48], fluorescent quantum dots [50], upconversion nanoparticles [51], nanodiamonds [52, 53], silicon nanoparticles [53], and other nanostructured fluorophores [54]. Different fluorescent proteins based on spectral class (far-red, red, orange, yellow-green, green, cyan, and UV-excitable green) may be selected to image live cells [55, 56].

1.2.2.3 Imaging probes for PAI/MSOT

These agents can be small molecular dyes, quantum dots, carbon nanotubes, nanodiamonds, metal nanoparticles such as Au nanorods [57 - 59]. A range of the NIR agents for PAI have been recently summarized by Wu et al. [57]. **Table 1-4** shows the commonly used small molecular dyes for PAI. In solutions, these dyes have sizes of < 2 nm.

Table 1-4. Common small molecular NIR fluorescent dyes (adapted from ref 5)

NIR dyes	Absorption peak (nm)	Application*
Indocyanine-green	810	PAT, in tissue phantoms and in vivo
Methylene blue	650 - 700	PAT, , in tissue phantoms
Alexa Fluor 750	750	MSOT, in vivo
IRDye800CW	750 - 800	PAS, in vivo
IRDye800-c(KRGDf)	750 - 790	PAS, in vivo
Evans Blue	550	PAT, in vivo
PPCy-C8	754 - 789	Dual-modality, PAI-FI, in vivo
Cypate-C18	754 - 790	Dual-modality, PAI-FI, in vivo
Caspase-9 Probe	640	PAI, in vivo
NMPSence^{TM} 680	620, 680	PAI, in tissue phantoms

* Abbreviations: PAT, photoacoustic therapy; PAS, photoacoustic spectroscopy; PAI-FI, photoacoustic imaging-fluorescence imaging.

However, with some probes, particularly lipophilic dyes (e.g., DiI [red], PKH26 [red], DiD[far red], DiR [NIR]), there is a risk of false positive staining due to the dyes being transferred to host cells. Dyes may be released by diffusion, or by transferring to neighbouring host cells via trogocytosis (exchange of membrane microdomains) and/or by extracellular vesicles [48]. Regarding nanoparticles that are uptaken by endocytosis, these have a lower tendency to transfer to host cells because they are located within the endosomes and/or lysosomes, and tend not to be readily transferred unless they are exocytosed. However, if the cells die, then the nanoprobes can be taken up by macrophages, generating misleading results. For this reason, for preclinical imaging, it can be useful to combine genetic reporters with nanoprobes to enable viability and biodistribution to be monitored simultaneously.

Nanoparticles as PAI contrast agents have been designed, synthesized, and investigated extensively in recent years [60, 61]. The use of these nanoparticles are based on surface plasmon resonance or dye-containing nanoparticles. The former type is mainly for metal or inorganic nanoparticles. The latter type accounts for the dye-modified nanoparticles and organic dye nanoparticles [62, 63]. For a NIR contrast

agent, the important characteristics include intensity (absorbance coefficient) and stability. Compared to small molecular dyes, nanoparticle probes usually exhibit high stability. Due to the concerns in cytotoxicity of heavy metals, which are always present in quantum dots and inorganic nanoparticles, the development and use of organic nanoparticle probes for PAI would be highly beneficial.

1.3 Semiconducting polymer and perylene diimide (PDI) nanoparticles for PAI

A key aim of this project is to develop new NIR probes for MSOT to facilitate cell tracking in vivo. Polymeric or organic dyes with NIR absorbance are potentially good candidates. For example, organic dyes and semi-conducting polymers are widely used for dye-sensitized solar cells (and other photo-electronic devices) where the absorbance of light is critical to achieve high efficiency of transformation from solar energy to electricity. These materials may be used as potential NIR agents for PAI/MSOT. However, these molecules are usually highly hydrophobic and bulky. To use them for in vivo imaging, aqueous nanoparticle suspensions are required.

There are different methods that can be used to fabricate organic nanoparticles, either for drug nanoparticles or imaging probes [64-66]. The commonly used methods are nanoprecipitation and emulsion evaporation. For the nanoprecipitation method (**Figure 1-10A**), an organic compound or polymer is dissolved in a water-miscible organic solvent (e.g., acetone, methanol, tetrahydrofuran). The organic solution is then mixed (usually by dropwise addition) with an aqueous solution containing a surfactant or polymer (to stabilize the nanoparticles). After evaporating the volatile organic solvent, aqueous organic nanoparticle suspensions are formed. However, if the organic compound can only be dissolved in a non-polar organic solvent, an emulsion instead of

a mixing solution is formed. An aqueous nanoparticle suspension is formed after the evaporation of the volatile organic solvent from the emulsion (**Figure 1-10B**). This method is termed as emulsion evaporation.

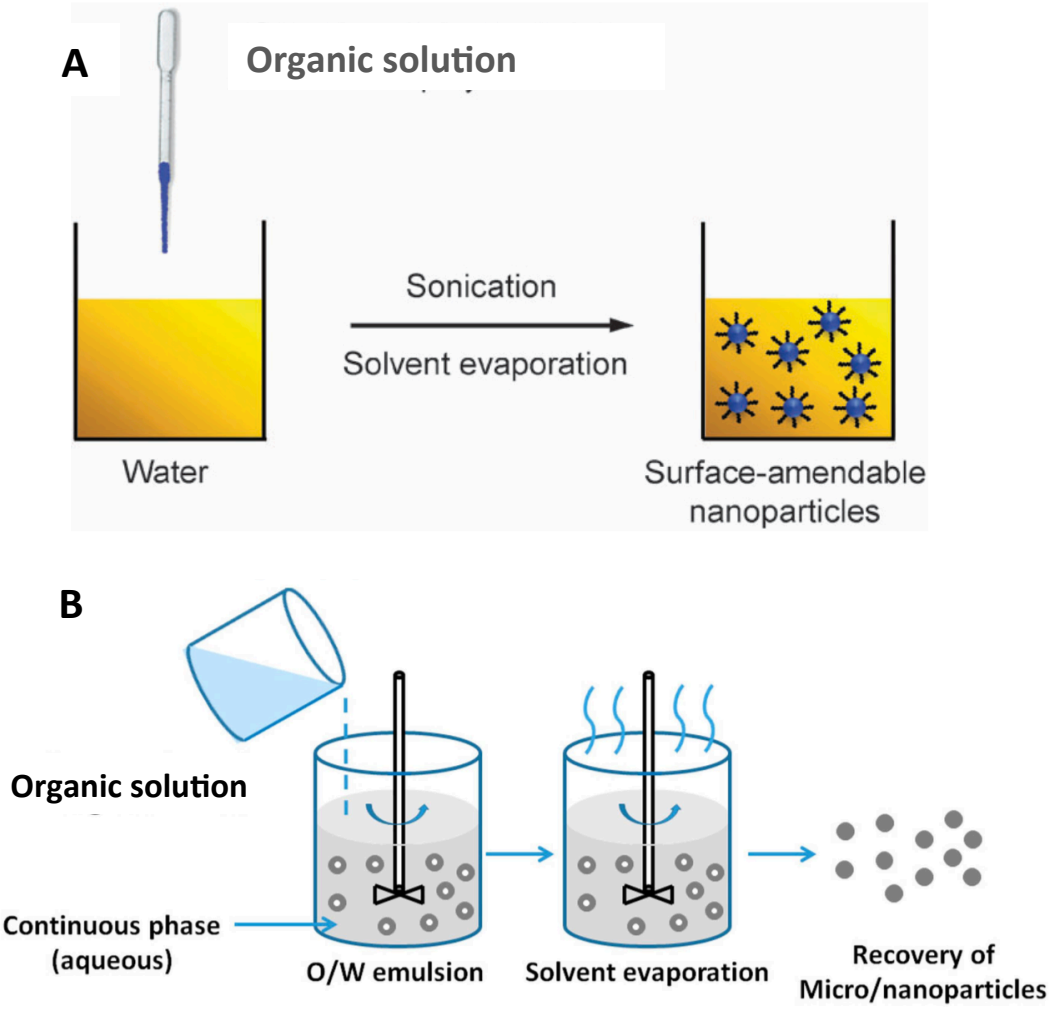

Figure 1-10. Schematic representations for the preparation of aqueous organic nanoparticle suspensions. Depending on the solubility of the stabilizers, they can be initially dissolved in water or in organic solvent. (A) Nanoprecipitation (reprinted from ref 66); (B) Emulsion evaporation (reprinted from ref 65).

For the emulsion evaporation method, the difficult part is the stability of the emulsion. If the emulsion is stable during solvent evaporation, the droplets can fuse or coalesce, leading to larger microparticles or aggregated particles. This issue has been

addressed by an emulsion freeze-drying approach. The emulsion is immediately frozen after formation, followed by a freeze-drying process so that the emulsion stability is not a problem anymore [66]. The process is schematically described in **Figure 1-11**. The organic compound is dissolved in a non-polar (or water-immiscible) organic solvent. The resulting solution is emulsified into aqueous solution containing polymer and surfactant. When freezing the emulsion, the organic solute in the droplet phase is concentrated. The subsequent freeze-drying process removes both water and organic solvent, which ensures the formation of organic nanoparticles within a porous polymer. The organic nanoparticles with the dry porous polymer are highly stable and easy to store and transport. When required, the organic nanocomposites can be readily dissolved in water to instantly produce aqueous organic nanoparticle suspensions [67].

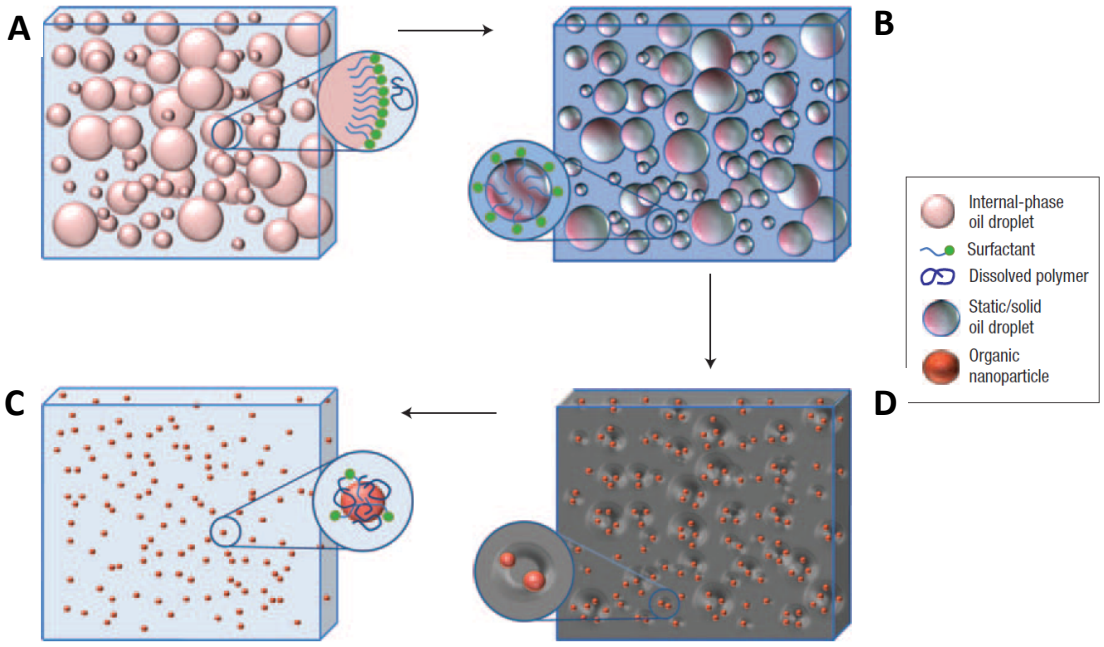

Figure 1-11. The schematic representation of preparing organic nanoparticles by emulsion freeze-drying. (A) An oil-in-water emulsion is formed; (B) During freezing of the emulsion, the organic solute is concentrated in the droplets; (C) After freeze-drying, organic nanoparticles are formed in situ within the porous polymer; (D) The

porous structure is dissolved in water to produce an aqueous nanoparticle suspension. Reprinted from Ref 67.

Organic nanoparticles with NIR absorbance (either from the nanoparticle itself or by attaching an NIR dye to the nanoparticle) have been used for PAI. Some of the examples include cyanine dyes [57, 68], methylene blue [57], Prussian blue [69], polypyrrole [70], conjugated polymer [71], MTT formazan [72], PEGylated black phosphorous nanoparticles [73], dye-based nanoparticles (porphyrin-based, melanin-based, squaraine dye-based [63].

1.3.1 Semiconducting polymer nanoparticles (SPNs)

SPNs have been investigated intensively as PAI probes, where the NIR absorbance results from the polymer (i.e., no further NIR dyes attached) [74]. Semi-conductive polymers are optically and electronically active and are used in many applications such as sensors, solar cells, and electronic devices. These polymers may be commercially available or synthesized. Since these polymers are hydrophobic, a nanoprecipitation approach is usually employed to prepare SPNs [75]. The intraparticle molecular orbital engineering between the SPNs and ultra-small fullerene dots were found to simultaneously enhance photoacoustic brightness and photothermal therapy efficacy [76]. Other agents may be incorporated into the SPNs for imaging changes in pH, temperature, reactive oxygen species (ROS), and protein sulfenic acid in diseased tissues [63]. For example, a cyanine dye derivative (IR775S) was incorporated into the SPNs for ROS imaging; and a pH-responsive NIR croconine dye could induce the self-assembly of human serum albumin (HSA). The resulting nanoparticles were used for real-time photoacoustic pH imaging and pH-responsive photothermal therapy [77].

1.3.2 Perylene/Naphthalene-based nanoparticles for PAI

Very recently, naphthalene and perylene-based dyes have been used for PAI [78-82]. These dyes are highly hydrophobic and can exhibit both fluorescence and NIR absorption, with high quantum yield and high stability [83-86]. Naphthalocyanine derivative could self-assemble into nanoparticles of ~ 20 nm in the presence of the biocompatible polymeric surfactant Pluronic F127. There was no nanoparticle aggregation observed when the temperature was reduced to 4ºC [77]; this was attributed to the formation of frozen micelles. After oral administration, these nanoparticles could pass safely through the gastrointestinal tract of mice where the PAI technique could be used to visualize intestinal distribution with low background and high resolution [78]. These nanoparticles were further used for dual-colour photoacoustic lymph node imaging in both small animals and human breast cancer patients [79]. A hydrophobic perylene diimide (PDI) derivative was prepared and aqueous PDI nanoparticle dispersions were then formed by a solvent evaporation (or nanoprecipitation) method, with strong absorbance at around 700 nm and high extinction coefficient of 2 x 10^8 M^{-1} cm^{-1} [81]. The PDI nanoparticles were demonstrated to be highly effective photoacoustic agents for deep brain tumour imaging in living mice [80]. ^{64}Cu-labeled PDI nanoparticles were prepared and employed as dual PET and PAI probes in lymph node mapping and cancer imaging while the photothermal therapeutic efficacy was also demonstrated [81]. Terrylenediimide (TDI) was modified with poly (acrylic acid), which produced a star-like compound with hydrophobic TDI core and hydrophilic corona [82]. The spontaneously self-assembled nanoparticles were used as theranostic agents for efficient PAI-guided tumour photothermal therapy [82].

As discussed above, perylene diimide derivatives (PDIs) have been used as chromophores for imaging. However, the use of PDIs is quite new for PAI. Furthermore, the synthesis of PDIs has been extensively investigated for advanced dyes, photo-related devices, and semi-conducting materials for microelectronics [84, 85]. These methods may be adopted or developed further to produce PDI compounds with tuneable NIR absorbance. In addition, the nanoparticle fabrication methods can be used to fabricate aqueous PDI nanoparticle suspension, which will provide a novel and highly efficient platform for MSOT imaging. As such, the preparation of PDI nanoparticles as NIR probes for MSOT is the focus of this project.

The molecular structures of naphthalene, perylene, and PDIs are shown in **Figure 1-12**. Perylene is a chemically inert compound. The synthesis of PDIs usually starts with perylene-3,4,9,10-tetracarboxylic dianhydride (PTCDA), which is commercially available. Different functional groups may be introduced to the different positions on perylene. The hydrophilicity of the PDIs is achieved by adding hydrophilic groups to the amide position (or peri position for perylene in general). Similarly, hydrophobic PDIs can be formed if linear or cyclic alkyl chains are added to the amide position.

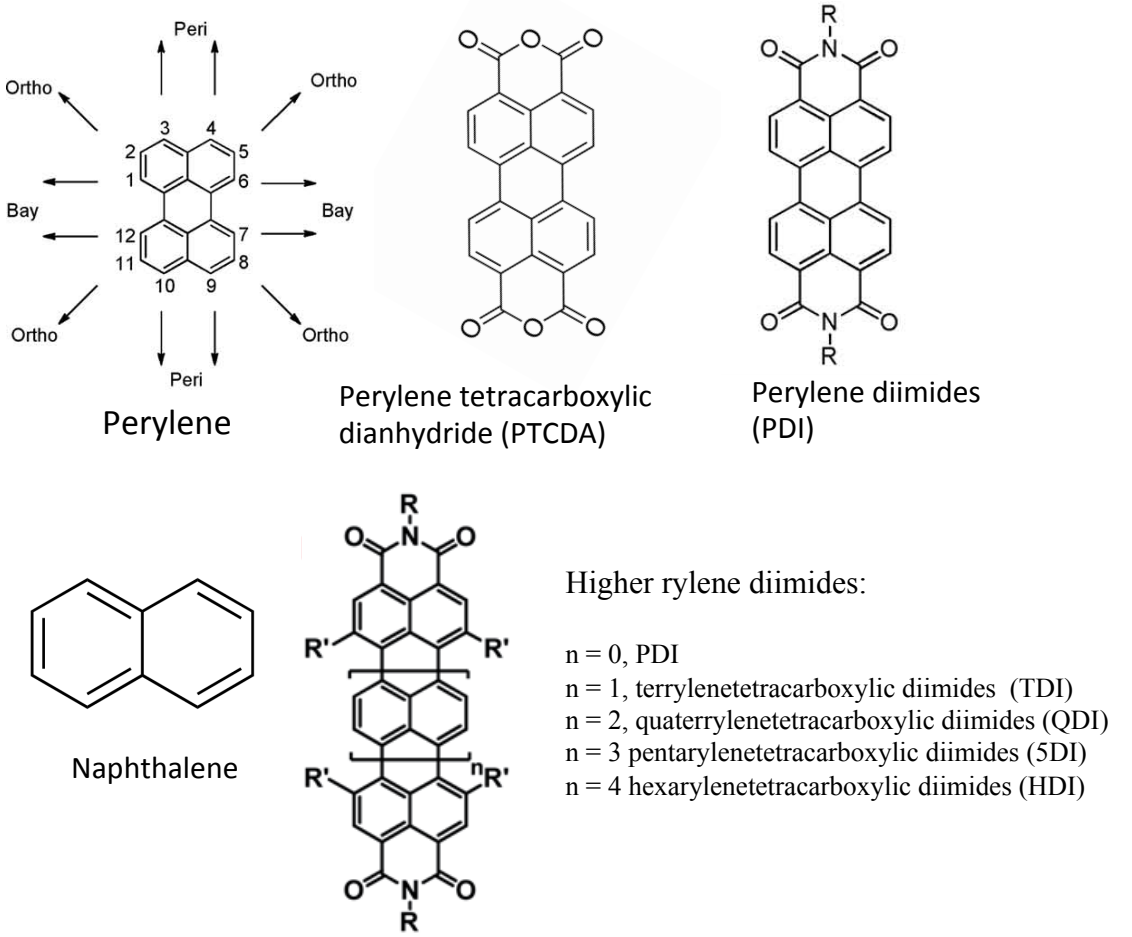

Figure 1-12. Molecular structures of naphthalene and perylene-based compounds.

However, the change of light absorption properties is usually caused by adding functional groups (usually bulky) at the bay positions [84] or more effectively by enlarging the core of the PDIs via synthetic chemistry [86]. Higher rylene diimides can be synthesized by introducing naphthalene units (Figure 1-12), which can significantly move the absorption wavelength towards the NIR region. **Figure 1-13** shows how the absorption wavelength and extinction coefficient change with the higher rylene diimides [87]. The maximal absorption wavelengths are shifted bathochromically by about 100 nm per naphthalene unit, exhibiting strong NIR absorbance. And the extinction coefficient increases linearly with the increasing number of naphthalene

units in rylene diimides [85, 86]. As such, the synthesis and use of higher rylene diimides may be a highly effective route to highly efficient PAI agents.

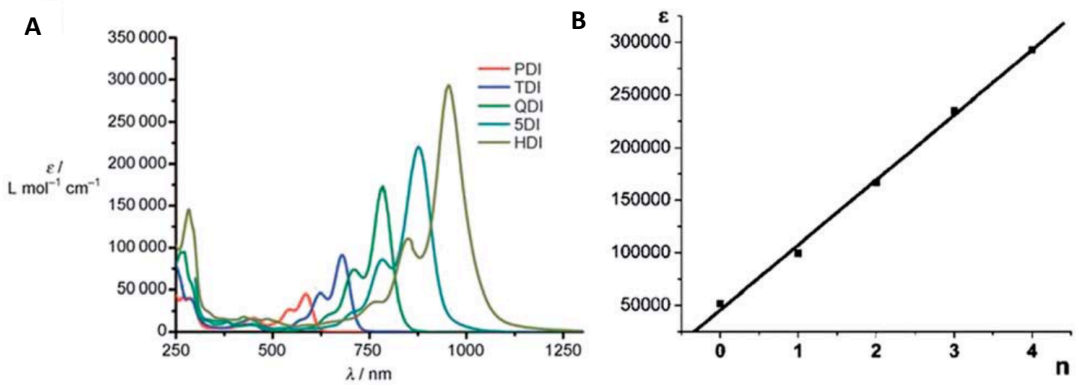

Figure 1-13. A) Absorption spectra of rylene diimides. B) The relationship between the extinction coefficient and the number of naphthalene units. Reprinted from Ref 87.

1.3.3 Physicochemical characterization of organic nanoparticles

The size, shape, and surface charge are important characteristics for nanoparticles. The size can be hydrodynamic size which is obtained by light scattering of nanoparticle suspensions [88], or the size of dry nanoparticles which can be obtained by electron microscopy (EM) or Atomic Force Microscopy (AFM). While the light scattering techniques provide the hydrodynamic diameters of spheres or equivalent spheres for non-spherical particles or irregular-shaped particles, the shape of the nanoparticles can be seen from EM or AFM images. UV-Vis spectroscopy may be used to determine the size of Au nanoparticles based on plasma effect. This, however, is not a universal technique for sizing nanoparticles. The surface charge of a nanoparticle can be measured by zeta potential. EM and AFM measure/image dry nanoparticles. The shape and surface morphology of the nanoparticles can be obtained. During the dry state, the stabilizer molecules on the nanoparticles are collapsed and the nanoparticles may aggregate. For biomedical applications, nanoparticles suspended in aqueous media

are always used. Due to the hydrated shell of the stabilizer, the size of nanoparticles is considerably different between dry states and hydrated cells. To better understand the effect of particles in biomedical applications, the size of hydrated nanoparticles in aqueous suspensions is more relevant. Dynamic light scattering (DLS) measures the size of hydrated nanoparticles in suspension, assuming the particles are spherical. Information on the shape and aspect ratio of nanoparticles cannot be obtained from the DLS technique. This can be a significant disadvantage for non-spherical nanoparticles. In this project, DLS and Scanning Electron Microscopy (SEM) have been mainly used to characterize the samples.

DLS is sometimes mentioned as Photon Correlation Spectroscopy (PCS) or Quasi-Elastic Light Scattering (QELS). DLS measures the distance travelled by the particles during a certain period (the velocity) due to the random Brownian motion [88]. The larger the particles, the slower the motion. Due to the random movement of the particles, the scattering intensity fluctuates with time. The size of the particle is obtained from the correlation function by using various algorithms. The size distribution can be plotted as the intensity versus sizes. A smooth and sharp peak of the plot indicates the particles of uniform sizes. However, when multiple peaks are present, this suggests the particles of different sizes in the medium. As the intensity contributed from small particles is very small. Therefore, the intensity size distribution profile may not represent the true picture of the particles. With the input of other parameters, the Mie theory can be used to convert the intensity distribution to a volume or number distribution. Generally, the size of the particles follows the order of d(intensity) > d(volume) > d(number) [89]. This can be simply illustrated in **Figure 1-14** when measuring a sample with equal populations of 5 nm and 50 nm particles.

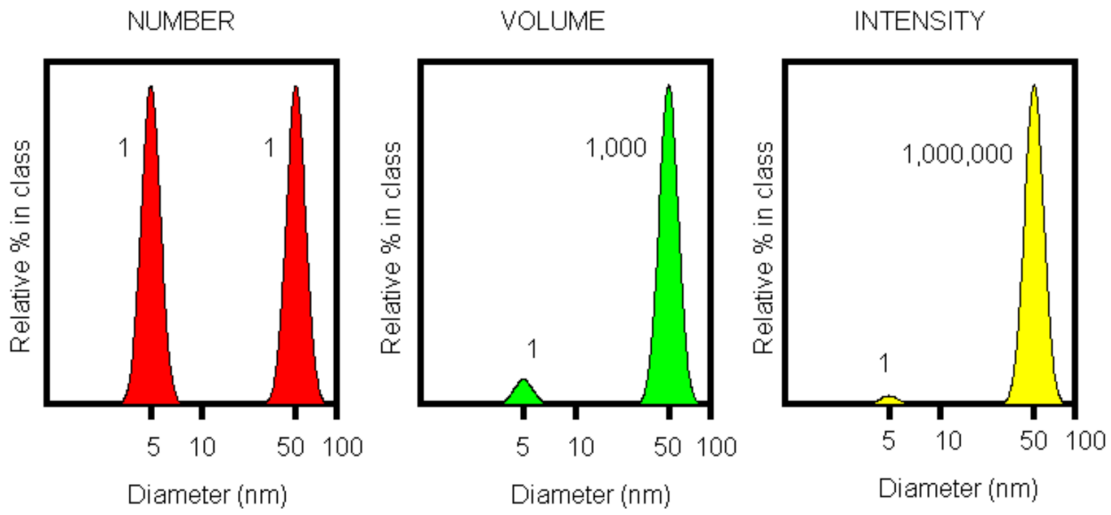

Figure 1-14. Different size distribution profiles for a sample containing equal number of 5 and 50 nm particles. Reprinted from ref 89.

The DLS equipped with a zeta analyzer can also measure the charges (zeta potential) carried by the particles. These data can indicate the stability of the particles in the dispersing medium. The zeta potential value is independent of nanoparticle concentration in the stable region (10^{-2} – 10^{-4} wt% for the nanoparticles investigated, Ludox silica, gold, carbon nanotubes). However, below this concentration range, the zeta potential values shifted to become less negative, accompanied by an increase in particle size. This was attributed to the artifact signals from extraneous particles for zeta potential and the homodyne optical configuration of the instrument for particle size [90].

1.3.4 Cellular uptake of nanoparticles: mechanism and toxicity

When nanoparticles are used as probes for bioimaging, their biological evaluation when exposed to cells or injected into a body is of paramount importance. The stabilizer (and ligands)-coated nanoparticles firstly bind onto cell membrane, initiating

a signaling cascade and leading to cellular uptake or internalization of the nanoparticles [91]. The mechanisms for cellular uptake of nanoparticles include [92]:

- Phagocytosis. This process is completed by phagocytic cells of the mononuclear phagocyte system (MPS) and reticuloendothelial system (RES). It is usually initiated by opsonization and highly effective for larger nanoparticles.
- Clathrin-mediated endocytosis. It is the main mechanism to obtain nutrients and plasma membrane components. This process can be achieved by receptor-specific uptake or non-specific adsorptive uptake. During the process, vesicle with diameter of 100 – 150 nm are formed, engulfing a volume of extracellular fluid which may contain foreign nanoparticles. The nanoparticles from this process are localized in degradative lysosomes.
- Caveolae-dependant endocytosis. This mechanism is used in many biological processes such as cell signaling, transcytosis, etc.
- Clathrin/caveolae independent endocytosis.
- Macropinocytosis. This process does not involve the use of pit-forming proteins. In this process, large membrane extensions are formed as a result of cytoskeleton rearrangement, generating a large vesicle with diameter of 0.2 – 5 μm that traps a large volume of extracellular fluid. The nanoparticles in this volume of fluid are taken up by the cell.
- Enhanced permeation and retention (EPR) effect [91]. Relatively larger nanoparticles (usually in the range of 30 – 200 nm but can be larger) are taken up by tumor cells via the EPR effect. This is due to the large fenestrations generated between endothelial cells and blood vessels by angiogenesis.

The physical properties of the nanoparticles, such as size, shape, and surface charge, have significant impacts on cellular uptake of the nanoparticles. As discussed above of

the uptake mechanism, different size of nanoparticles can be taken up by different cells and via different mechanism. When cultured with cells, there are no definite trends of particle size on cellular uptake. Size dependent uptake is related to membrane-wrapping processes. Small nanoparticles have less ligand-to-receptor interaction than larger particles, which reduces the tendency of cellular uptake. However, for much larger particles, the uptake is limited by the redistribution of the surface charges. It has been observed that 50 nm spherical nanoparticles are optimal for the uptake by certain mammalian cells [91, 93, 94]. Aggregated nanoparticles can have lower uptake but this effect is different from single large nanoparticles, as demonstrated by the aggregated gold nanoparticles (15 nm) [95].

The effect of particle shape influences the cellular uptake considerably [91]. For nanospheres and nanorods with similar diameters, the uptake of nanorods is less, as demonstrated with gold [96] and silver [97] nanoparticles. However, if the volume of the nanoparticles is kept the same, for example, by stretching 200 nm polystyrene nanospheres in one direction (394 nm nanorod) or in two directions (forming disc with diameter of 293 nm), the uptake of both nanorods and discs by Caco-2 cells was found to be twice quickly as nanospheres [98].

Surface charge and surface functionality of the nanoparticles are also important parameters. In general, positive surface charge facilitates fast uptake by cells. This is because cell membranes possess a slightly negative charge [91]. The adsorption of proteins onto the nanoparticles can modulate cellular uptake, as found with gold nanoparticles (40 nm, 80 nm, both with negative, positive, and neutral charges) and hepatocyte cells [99]. Compared to human plasma protein (HPP), the adsorption of human serum albumin (HAS) showed reduced uptake and toxicity [99]. For sub-10 nm gold nanoparticles (2 nm, 4 nm, 6 nm) with neutral, anionic, and cationic stabilizers, it

was found that the uptake by HeLa cells decreased with increasing particle size for particles with neutral and negative surface charges whilst the cellular uptake increased with increasing size of positively charged gold nanoparticles [100]. This was attributed to the energy-dependent cellular uptake pathways for sub-10 nm particles [100].

The toxicity of nanoparticles is complicated and under investigated. It is associated with the properties exhibited by nanoparticles including small size, high surface energy, and surface composition [101]. Nanoparticles can be taken up by a body via different routes such as gastrointestinal tract, skin, lung, and systemic administration. The nanoparticles can interact with cells, body fluid, and proteins. Accelerated protein denaturation on nanoparticles leads to biological functional and structure change. The nanoparticles in the body may be excreted or deposit in organs, penetrate cell membranes, and lodge into mitochondria [101].

In order to utilize the excellent properties shown by nanoparticles, their toxicity must assessed first. This can be achieved by in vivo assessment and in vitro cytotoxicity assay [102]. In vivo assessment is the ultimate target by evaluating the effect of the injected or absorbed nanoparticles on the whole organs. This is realized by investigating the pharmacokinetic behavior of the nanoparticles, i.e., the absorption, biodistribution, metabolism, and elimination. However, before moving to the stage of in vivo assessment, the in vitro evaluation should be completed first. The in vitro cytotoxicity evaluation employs different assays to look at the response of the cells when the nanoparticles are cultured with or exposed to cells [102]. It should be pointed out that the cytotoxicity may be different for different cells, even for the same nanoparticles. Common assays to assess cytotoxicity include [102]:

- Lactate dehydrogenase (LDH) assay: a colorimetric assay measuring the release of LDH into the culture medium as an indicator of cellular membrane disruption.
- MTT (3-(4,5-dimethylthiazol-2-yl)-2,5-diphenyltetrazolium bromide): a metabolic and colorimetric assay measuring the enzymatic activity of cellular mitochondria. MTT is added into the culturing medium usually at a concentration of 0.2-0.5 mg/mL. Viable cells convert MTT into a purple formazan with an absorbance peak around 570 nm. The dead cells cannot convert MTT to formazan.
- Reactive oxygen species (ROS) assay: used to monitor oxidative stress by measuring the ROS level.

Cytotoxicity data are obtained by exposing different nanoparticles to the cells [103]. It is often related to the uptake level by the cells. Higher uptake by the cells usually indicates higher toxicity. Therefore, the factors (size, shape, surface property) that influence cellular uptake have significant impact on cytotoxicity [95, 97, 99]. For example, size dependent toxicity was observed for citrate stabilized gold nanoparticles (5 nm and 15 nm) when exposed to mouse fibroblasts [104]. Cytotoxicity was only observed for the cells treated with 5 nm nanoparticles at > 50 μM for 72 hours. Disruption of the actin cytoskeleton was greater for the cells exposed to 5 nm nanoparticles [104].

1.4 Cell encapsulation and cell delivery

1.4.1 The need for cell encapsulation and hydrogels

Cell encapsulation has been frequently carried out when transplanting therapeutic cells. This is because the encapsulation can provide several benefits. These

mainly include: (i) Improving viability by reducing or preventing immunogenicity, especially when transplanting allogeneic cells; in this case, the encapsulation can provide an immune-isolating layer to prevent the immune cells from attacking the implanted cells; (ii) Providing a scaffold with suitable mechanical and chemical cues to support the growth and differentiation of stem cells; (iii) To serve as a barrier to avoid or reduce the leaking of therapeutic cells from the transplantation site.

Hydrogels are mostly used to encapsulate cells (other materials may include semi-permeable membranes, etc.). Hydrogels are hydrated polymer networks, formed either by chemical crosslinking or physical crosslinking, which can retain a large amount of water [105]. The use of hydrogels gained popularity in the 1960s, and from hydrogels formed by simply polymerizing water-soluble monomers and polymers, we now have smart hydrogels where gelation can be controlled using various triggers, and stereocomplexed hydrogels that can be synthesized from the self-assembly of peptides/polypeptides [105]. When selecting hydrogels for cell culture, mechanical, structural, and compositional cues are often considered because they can regulate cell behaviour, either alone or in synergy [106]. These cues are reflected by the hydrogel properties such as type of polymer, stiffness, porosity, and biodegradability [107]. In general, hydrogels are formed from natural polymers (e.g., fibrin, collagen, gelatin, polysaccharides) and synthetic polymers (e.g., polyacrylamides, poly (acrylic acid), poly (ethylene glycol), polyoxazolines, poly(vinyl alcohol), poly(lactide-co-glycolide), polycaprolactone) [107]. There are commercial hydrogels which can be purchased from providers and used for cell culture directly. The commonly used ones are from collagen, fibrin, alginate, polyacrylamide, poly (ethylene glycol), hyaluronic acid, and polypeptides [108].

1.4.2 The basics of cell encapsulation

Cell encapsulation may be classified into two categories. The first category is to encapsulate cells in biodegradable hydrogels for tissue engineering [109]. This is in contrast to seeding cells in prefabricated porous scaffolds or hydrogels. To achieve cell encapsulation, cells are suspended in a liquid precursor solution and the solution is injected to the site of interest. In situ gelation of the solution ensures the encapsulation. Because the presence of the cells in the solution, the components in the solution should be non-toxic and the gelation condition should be mild so that the cells can survive and are not negatively impacted upon [109]. For the hydrogels used in cell encapsulation, small molecular monomers are usually not used due to cytotoxicity issues. Macromers with molecular weight of 3 kDa or higher and natural polymers are generally used instead. The biodegradation rate of these hydrogels may be adjusted by choosing suitable precursors or incorporating hydrolytically or enzymatically labile segments during gelation [109].

The second category of cell encapsulation, probably the more often referred to meaning, is to encapsulate cells for cell transplant, aiming for cell delivery and/or drug delivery [110, 111]. Encapsulation helps to prevent the implanted cells from being attached by the host's immune cells, which include macrophages, granulocytes, lymphocytes, fibroblasts, etc. A key objective of cell encapsulation is to suppress the attack by the immune system whilst enabling factors secreted by the cells to be able to diffuse out of the hydrogel [112].

In this work, the focus is on the second category of cell encapsulation although many of the properties might also be useful for the first category of cell encapsulation.

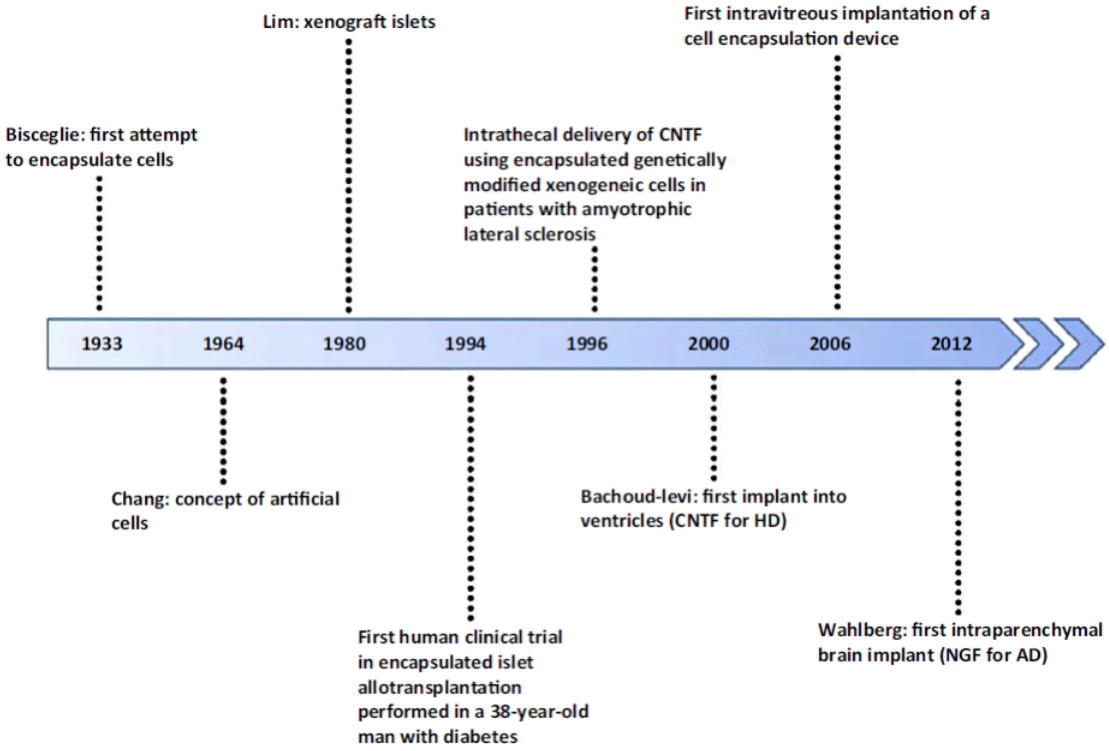

Figure 1-15. Timeline showing key milestones in cell encapsulation technology. Reprinted from Ref 113.

While the first concept of cell encapsulation was mentioned in 1933, it is generally regarded that the attempt to generate 'artificial cell' by Chang in 1964 intensified the studies on cell encapsulation (**Figure 1-15**) [113, 114]. In Chang's work, carbonic anhydrase was encapsulated in semipermeable microcapsules, which showed efficient catalytic hydration of CO_2 as was obtained by the enzyme in free solution, and the activity remained after weeks of storage [114].

For the encapsulated cells to survive, nutrients and oxygen should be able to sufficiently move across the hydrogel membrane while antibodies and immune cells are kept out. Therapeutic agents excreted by the cells diffuse out of the hydrogel membrane to achieve the objectives of cell therapy [115]. This process is schematically illustrated in **Figure 1-16A**. A sufficient supply of oxygen is critical for the survival

and healthy growth of the cells. This can be enhanced by the use of pre-vascularized support system (Figure 1-16B).

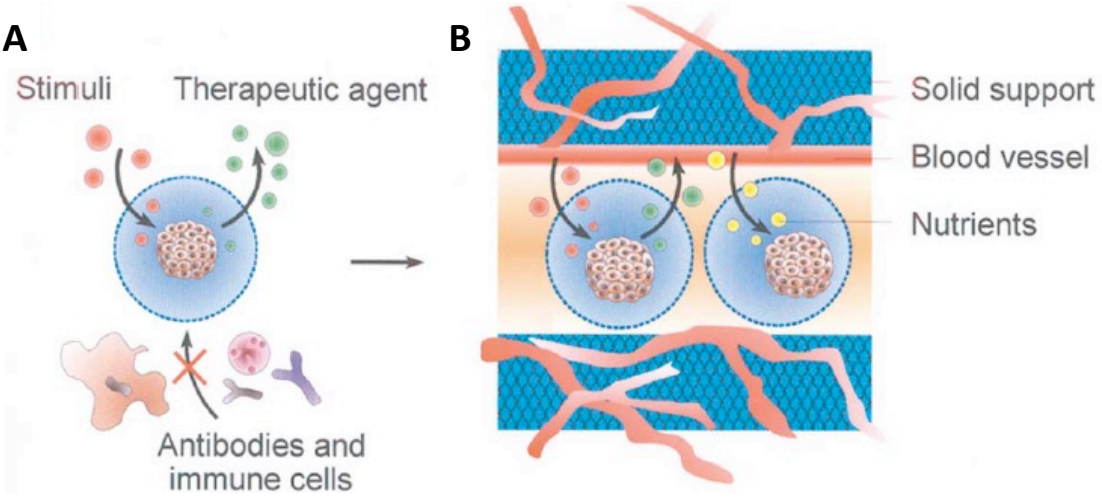

Figure 1-16. Schematic representation of cell microencapsulation. (A) Nutrients and stimuli diffuse across the membrane while antibodies and immune cells are kept out. (B) Pre-vascularized support promotes the transfer of oxygen and nutrients. Reprinted from Ref 115.

1.4.3 Important parameters of cell encapsulation

1.4.3.1 Encapsulation materials

The criteria used in finding or selecting an encapsulation material include biocompatibility, immune-isolation ability, and ability to maintain viability and phenotype [116]. Different types of synthetic and natural polymers have been used to encapsulate cells [117]. Natural polymers are more often used due to their intrinsic biocompatibility and biodegradability. These may include DNA-based hydrogels, protein-based hydrogels (also peptide hydrogels), polysaccharide-based hydrogels (alginate, chitosan, chondroitin sulfate, hyaluronic acid, agarose) [109, 117]. The hydrogels are formed by physical crosslinking (via hydrophobic interactions and ionic interactions), free radical polymerization, or chemical crosslinking using novel

chemistry [109, 117, 118]. Some of the crosslinking methods that are particularly effective for injectable hydrogels are Michael addition (e.g., between thiols/amines and double bond next to the carbonyl bond), click reaction (Cu(I)-catalyzed reaction between azide and terminal acetylene groups), Schiff based reaction (between an amine group and an aldehyde group), and photocrosslinked hydrogels (acrylate monomers or macromers by UV radiation) [118].

In terms of preparing encapsulated cells for pre-clinical and clinical applications, simple physical crosslinking methods via hydrophobic interaction (e.g., chitosan thermosetting gels) or ionic crosslinking (e.g., alginate crosslinked by Ca^{2+}) can be used. For example, in a study to find the encapsulation system for pancreatic islets, a thousand combinations of polyanions and polycations were tested to form capsules simply by dropping each polyanion solution into each polycation solution [119].

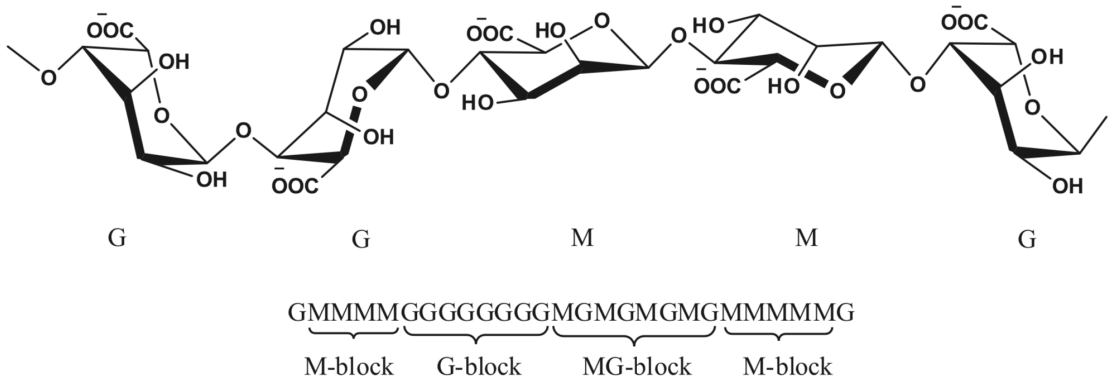

Figure 1-17. The molecular structure of alginate and description of M and G blocks. Reprinted from Ref 117.

Alginate is the most commonly used polymer for cell encapsulation. The majority of the encapsulating gels are formed from sodium alginate (Alg) as polyanion and poly-L-lysine (PLL) as polycation [112]. Alginate is a natural anionic polymer

composed of 1,4'-linked β-D-mannuronic acid (M) and α-L-gluoronic acid (G) residues in different sequences (**Figure 1-17**) [117]. The ratio of G and M blocks is an important parameter, which varies depending on its natural sources (e.g., algae). It is generally believed that high G content contributes a more rigid structure whilst high M content in alginate is preference for pliable gels [117]. There are contradictory findings about the G content of alginate for cell encapsulation, with some researchers believing that high G alginates are more suitable for cell encapsulation based on their results [113].

Mechanical stability of the microscapsules is an important parameter. Stable microscapsules can protect the cells and are easy to handle. In general, mechanical stability may be improved by using a high concentration of precursors and a high crosslinking density. This, however, may not be easily applicable for a selected encapsulation system. In the case of alginate, this has been achieved by the use of different polycations, e.g., the use of poly-L-ornithine, Ba^{2+}, layer-by-layer coating [112].

1.4.3.2 Fabrication methods

Cells can be encapsulated in bulky hydrogels, hydrogel beads, microcapsules and other micronized systems. For encapsulation in bulky hydrogels, cells are suspended in a liquid precursor solution, followed by gelation. The cell-encapsulated hydrogels are also formed in hollow fibers to suit the need of different applications [89]. To form hydrogel beads, as often seen with alginate beads, alginate solution containing cells can be injected into aqueous $CaCl_2$ solution and the gel beads are formed in the solution. When a polycation solution is used, capsules instead of beads may be

produced [119], due to the limited mass transfer of polycation molecules. The size of the beads may be reduced by using a pressurized nozzle or vibration nozzle [120].

However, bulky hydrogels and thick capsules can be a significant barrier for the diffusion of nutrients and oxygen, which can negatively impact on cell viability. When cells are encapsulated in microcapsules, the large ratio of surface-to-volume facilitates transport of nutrients. For example, one study showed that cell viability and metabolic activity was optimal when the cells were encapsulated in microcapsules in the order of 100 μm [121]. Cell encapsulation in microcapsules or microspheres can be prepared via an emulsion-based approach, where the droplets are turned into microspheres or microcapsules [120, 122]. There may be limitations for the emulsion method because of the use of organic solvent or oil phase. Cell encapsulation can be effectively fabricated by microtechnologies, including microfluidics and micromolding methods [110].

1.4.3.3 Nutrient and oxygen transport

While the pores in the microcapsules are small enough to keep out immune cells, and to prevent the cells from exiting, they should be large enough to allow sufficient transport of nutrients, oxygen, and therapeutic agents. In addition to shortening the diffusion path, increasing the porosity is a route to promoting transport.

One of the big challenges is to supply sufficient oxygen to maintain the viability and function of the encapsulated cells [123]. The oxygen transport may be enhanced by (i) Using a smaller device or microcapsules to reduce diffusion distance; (ii) Using organic compounds with high oxygen solubility (such as perfluorocarbons, silicone oils, soybean oils) with the microcapsules or in the device, thus increasing the permeability of oxygen; (iii) Induction of neovascularization adjacent to the

microcapsules or use of a pre-vascularized support (Figure 1-16B) to bring blood flow close to the tissue; (iv) Provision of exogenous oxygen (gaseous oxygen supply, in situ oxygen generation) to increase partial pressure of oxygen adjacent to the tissue [123].

1.4.4 Applications of cell encapsulation

Cell encapsulation has been used for cell delivery, which can also be combined with drug delivery [111,124]. There have been enormous research activities in encapsulating pancreatic islet cells to treat diabetes [116, 120, 122] and also other diseases such as cancer [111, 115], brain [125], kidney [126]. More examples are given in Table 1-5. It is clear that different cell types are encapsulated for a wide range of biomedical applications, with alginate being the mostly used polymer. More details can be obtained from Ref 112 and the references therein.

Table 1-5. Different cell sources used for cell encapsulation (adapted from ref 112).

Cell type	Application	Material
Fibroblasts	Metabolic deficiencies, epilepsy	Alginate, HEMA-MMA
Myoblasts	Metabolic deficiencies, cancer	Alginate, HEMA-MMA
Pancreatic islets	Diabetes	AN69, Cellulose sulfate
Ovary cells	Fabry disease	Alginate, HEMA-MMA
Parathyroid cells	Artificial organs	Alginate
Hepatocytes	Liver transplantation	Alginate, HEMA-MMA
Chondrocytes	Bone and cartilage regeneration	Alginate
Leydig cells	Hormone replacement	Alginate
Adrenal chromaffin cells	Parkinson's disease, chronic pain	Alginate
Stem cells	Bone regeneration	Alginate
Myeloma cells	Hepatic growth factor	Alginate
Hybridoma cells	Antibody production	Alginate, acetate, alginate-agarose
Tumor cells	Cancer vaccine, interleukins	Alginate, chitosan
Virus producer cells	Cancer	Cellulose sulfate
Bacteria	Elimination of urea	Alginate

The use of cell encapsulation for delivery of therapeutic agents has two advantages: (i) the immunoisolating microcapsules make it unnecessary to take immunosuppressant drugs and (ii) long-term delivery depending on the types of cells used (**Figure 1-18**) [124].

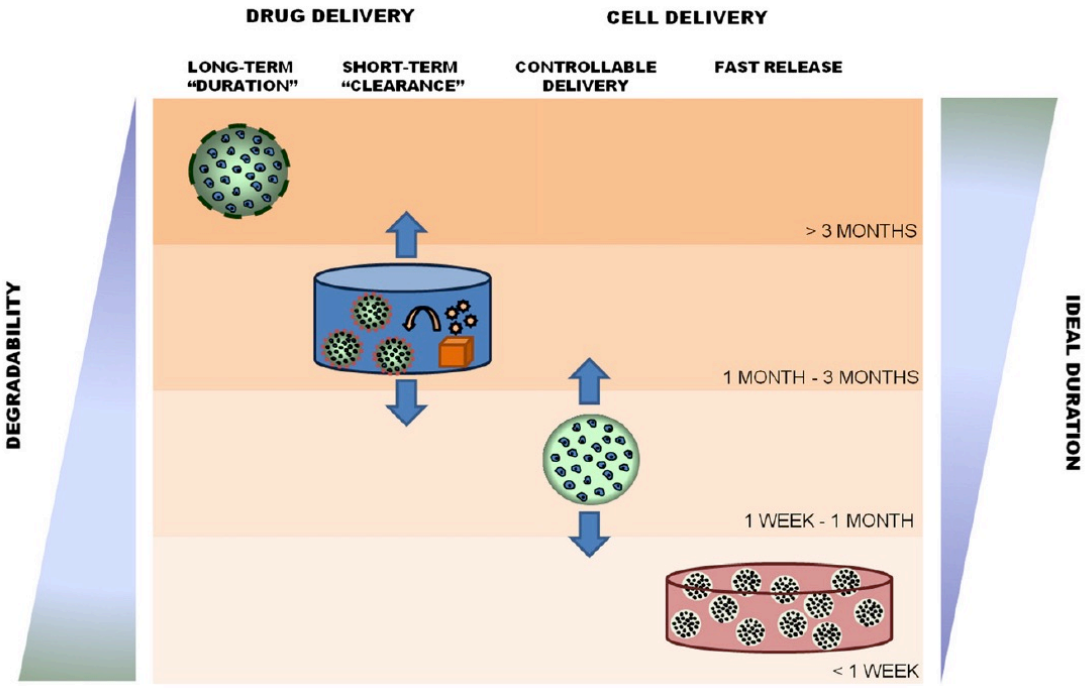

Figure 1-18. Represented timescale of drug delivery and cell delivery via cell encapsulation. Reprinted from Ref 124.

The selection of suitable cells for encapsulation is essential for biomedical applications. Many cell types have been used, some of which are given in **Table 1-5**. The proliferation behaviour of the cells should be considered, as with continued proliferation, the cells may eventually fill the capsular space, which may hinder diffusion of the therapeutic agents. For cells that do not proliferate, it can be an advantage for long-term delivery [112].

MSCs have been mostly used for encapsulation approaches in in regenerative medicine applications [111, 116, 127]. Examples include implanting encapsulated MSCs to accelerate bone regeneration or induce vascularization [124].

As such, the degradation of the capsule hydrogel with a suitable rate is a critical factor. The rate of degradation is determined by polymer type, molecular weight, pH, temperature, ionic strength, and presence of other molecules in aqueous medium. For some applications, where the therapeutic effects are mediated by paracrine factors, it would be desirable for the hydrogel to remain intact until after the implanted cells have died, as this would prevent the cells migrating to off-target sites. For other applications, where the aim is for the implanted cells to integrate into the diseased tissue, then it would be desirable for the hydrogel to degrade while the cells are still viable. Thus, monitoring the integrity of the hydrogels in vivo using non-invasive imaging approaches can provide key information on their effectiveness for specific applications. For PAI/MSOT imaging, this can be achieved by functionalizing the hydrogels with fluorescent groups [126], encapsulating NIR dye particles [72] and/or more advanced PDI nanoparticles that are to be developed in this project.

The understanding of the fate of the cells and the change of the capsules/hydrogels and the surrounding microenvironment in vivo after implanting with robust data is crucial for developing enhanced therapeutic methods based on cell encapsulation.

1.5 Chitosan hydrogels

As mentioned in section 1.4, there are many types of polymers or composites that are used to form hydrogels. For biomedical applications, the basic requirements include biocompatibility, biodegradability, mild processing conditions, and the ease for

further modification. Chitosan hydrogels can meet all these requirements and uniquely exhibit positive charges, which may facilitate strong interactions with cells and/or high uptake by cells. Chitosan is the only cationic natural polymer and has been extensively used as scaffolds for tissue engineering [129, 130], cell culturing [131], and drug delivery [132, 133]. Chitosan is the deacetylation product of chitin (**Figure 1-19**). Chitin is a natural polysaccharide, poly (β-(1→4)-N-acetyl-D-glucosamine) and is the second most abundant polymer after cellulose [134]. The common source of chitin has been crab and shrimp shells. There are two forms of chitin, α-chitin and β-chitin. α-chitin is the most common one. It is difficult to dissolve chitin in conventional solvents, which limits its applications. Chitin can be deacetylated under heating in concentrated NaOH to produce chitosan [135]. Chitosan is usually present as a copolymer, defined by the degree of acetylation or degree of deacetylation. When the degree of deacetylation is greater than 50 %, it is called 'chitosan' and can be soluble in acidic water. The structure of chitosan (considering it is 100 % deacetylated) is very similar to cellulose, with $–NH_2$ group replacing one of the –OH groups on cellulose. The presence of the $–NH_2$ groups on chitosan is significant. It can be protonated to be soluble in water, provide positive charges, and offer facile chemical modifications [134]. One of the most common ways to modify chitosan is by carboxylation at the –O or –N position [134]. Carboxymethyl chitosan is soluble in neutral water and has found unique applications in drug delivery and tissue engineering [136]. There are also other chemical modifications [134], for example, amino acid-modified chitosan for biomedical applications [137]. Chitosan can also be blended with other polymers for hybrid hydrogels, e.g., chitosan-alginate hydrogel for tumour treatment [138], collagen-chitosan for endothelial differentiation and angiogenesis [139].

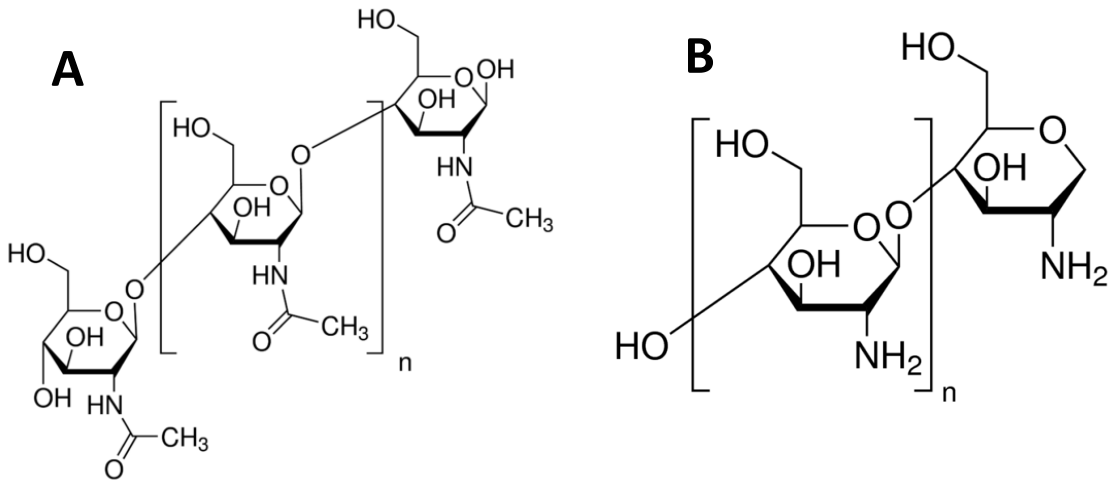

Figure 1-19. Molecular structures of (A) chitin and (B) chitosan.

Chitosan hydrogels can be formed by chemical crosslinking, physical crosslinking, or electrostatic interaction [140]. Due to the positive charge of chitosan in solution, multivalent cations or negatively charged polymers (e.g., certain proteins, nucleic acids) are employed to form hydrogels via ionic interaction. Another way to produce physically crosslinked hydrogels is by adding base into the chitosan solution. The increase of pH leads to deprotonation of chitosan chains, reduced solubility, and assembled gels by H bonding, hydrophobic interaction, and Van der Waals forces. This can be simply achieved by adding NaOH or Na_2CO_3. These hydrogels are more heterogeneous due to the dramatic local pH change. The hydrogels for cell culturing are usually produced by crosslinking chitosan with calcium phosphate [131], triphosphate [141], and β-glycerol phosphate [142-144]. Chitosan is often chemically crosslinked with glutaraldehyde [134, 145]. However, due to its toxicity, glutaraldehyde is usually replaced with biocompatible crosslinkers such as heparin [146] and genipin [147]. Chitosan hydrogels may be prepared as bulky gels (by simple gelation of chitosan solution), injectable gels [142-144], microparticles [148], nanoparticles [135, 148-149], and nanofibers [150]. Chitosan hydrogels are not often

used for cell encapsulation as alginate hydrogels [112]. This may be partly due to the relatively harsh conditions used for forming chitosan hydrogels. However, with the recent development in forming thermosensitive chitosan gels at body temperature [141-144], there is a good opportunity to use chitosan hydrogels for cell encapsulation, as will be investigated in this project.

Because of the biocompatibility, biodegradability, the unique positive charge, and various mild fabrication methods available, this project will aim to develop or optimize procedures to prepare chitosan hydrogels, particularly injectable thermosetting chitosan hydrogels to encapsulate cells and the PDI nanoparticles.

1.6 Project Aims

The main aim of this PhD study is to develop novel NIR probes for cell labelling and for hydrogel functionalization that will enable the biodistribution of administered cells and the integrity of cell-encapsulating hydrogels to be monitored non-invasively in vivo using MSOT.

In **Chapter 2**, a hydrophobic PDI compound with NIR absorption (wavelength > 650 nm) will be synthesized and characterized by NMR and UV-vis spectroscopy. Because of very poor solubility of PDI in water, aqueous PDI nanoparticle suspensions will be prepared for potential biomedical applications. PDI nanoparticles with polymer stabilizers of low cytotoxicity will be fabricated by nanoprecipitation or emulsion freeze-drying. In order to investigate the potential for MSOT, the NIR absorbance of aqueous PDI nanoparticles will be confirmed by UV-Vis spectroscopy. The PDI nanoparticles will be characterized by DLS and SEM.

In **Chapter 3**, the PDI nanoparticles will be used to label MSCs for fluorescence imaging and MSOT. In order to achieve these targets, cytotoxicity and NIR signals for imaging will be initially evaluated by flow cytometry, UV-Vis, and confocal laser scanning microscopy. Furthermore, the PDI-labelled mouse MSCs will be injected into mice for in vivo imaging. Fluorescence imaging will be used to confirm the injection of PDI-labelled MSCs while bioluminescence imaging will be used to confirm cell viability. Most importantly, in vivo imaging of the PDI-labelled MSCs in mice will be performed by MSOT longitudinally (e.g., over 1 – 2 weeks), thus to confirm PDI nanoparticles as efficient NIR probes for MSOT imaging. Finally, any effect of the PDI nanoparticles on MSC differentiation will be investigated by assessing their ability to differentiate to bone and cartilage cells following in vivo transplantation.

In **Chapter 4**, in order to monitor the status of hydrogel scaffolds by MSOT, the potential of using PDI nanoparticles to functionalize cell-encapsulating hydrogels will be investigated. To this end, an injectable thermosetting chitosan hydrogel system will first be developed. PDI nanoparticles will then be used to functionalize the hydrogels by suspending them in the chitosan solution at room temperature. The behaviour of mouse MSCs in the functionalized hydrogels will be monitored using live cell imaging, and the imaging properties of the hydrogel will be assessed using UV-Vis and MSOT.

In **Chapter 5**, a summary of conclusions for the whole project is included, with perspective for the future development of this project.

In addition to the main results chapters, I have also included one manuscript in appendix. This manuscript is not directly linked to the main project aims of in vivo cell

imaging, but nevertheless, describe some interesting materials chemistry and some of associated applications.

1.7 References

[1] Mason, C.; Dunnill, P. A brief definition of regenerative medicine. *Regen. Med.,* **2008**, 3, 1-5.

[2] Scarfe, L. et al. Preclinical imaging methods for assessing the safety and efficacy of regenerative medicine therapies. *NPJ Reg. Med.,* **2017**, 2:28.

[3] Mao, A.S.; Mooney, D.J. Regenerative medicine: current therapies and future directions. *PNAS*, **2015**, 112, 14452-14459.

[4] Cohen, D.E.; Melton, D. Turning straw into gold: directing cell fate for regenerative medicine. *Nat. Rev. Genetics*, **2011**, 12, 243 – 252.

[5] Santeramo, I.; Wilm, B.; Murray, P. Nephron progenitors (Chapter 76) in the book 'Kidney transplantation, bioengineering, and regeneration', Orlando, G.; Remuzzi, G.; Williams, D.F. (eds), Elsevier 2017, Academic Press, pp 1053 – 1065.

[6] Herberts, C.A.; Kwa, M.S.G.; Hermsen, H.P.H. Risk factors in the development of stem cell therapy. *J. Translational Med.*, **2011**, 9:29.

[7] Knoepfler, P. Deconstructing stem cell tumorigenicity: a roadmap to safe regenerative medicine. *Stem Cells*, **2009**, 27, 1050 – 1056.

[8] Satija, N.K.; Singh, V.K.; Verma, Y.K.; Gupta, P.; Sharma, S.; Afrin, F.; Sharma, M.; Sharma, P.; Tripathi, R.P.; Gurudutta, G.U. Mesenchymal stem cell-based therapy: a new paradigm in regenerative medicine. *J. Cell. Mol. Med.,* **2009**, 13, 4358 – 4402.

[9] Williams, A.R.; Hare, J.M. Mesenchymal stem cells: biology, pathophysiology, translational findings, and therapeutic implications for cardiac disease. *Circ. Res.,* **2011**, 109, 923-940.

[10] Bianco, P.; Cao, X.; Frenette, P.S.; Mao, J.J.; Robey, P.G.; Simmons, P.J.; Wang, C.-Y. The meaning, the sense and the significance: translating the science of mesenchymal stem cells into medicine. *Nat. Med.,* **2013**, 19, 35 – 42.

[11] Tabar, V.; Studer, L. Pluripotent stem cells in regenerative medicine: challenges and recent progress. *Nat. Rev. Genetics*, **2014**, 15, 82 – 92.

[12] Morrison, S.; Spradling, A.C. Stem cells and niches: mechanisms that promote stem cell maintenance throughout life. *Cell*, **2008**, 132, 598-611.

[13] Ito, K.; Ito, K. Metabolism and the control of cell fate decisions and stem cell renewal. *Annu. Cell Dev. Biol.,* **2016**, 32, 399-409.

[14] Friedenstein, A.J.; Chailakhijan, R.K.; Lalykina, K.S. The development of fibroblast colonies in monolayer cultures of guinea-pig bone marrow and spleen cells. *Cell Tissue Kinet*. **1970**, 3, 393 – 403.

[15] Chen, Q.; Shou, P.; Zheng, C.; Jiang, M.; Cao, G.; Yang, Q.; Cao, J.; Xie, N.; Velletri, T.; Zhang, X.; Xu, C.; Zhang, L.; Yang, H.; Hou, J.; Wang, Y.; Shi, Y. Fate decision of mesenchymal stem cells: adipocytes or osteoblasts? *Cell Death Differ.,* **2016**, 23, 1128-1139.

[16] Watt, F.M.; Huck, W.T.S. Role of the extracellular matrix in regulating stem cell fate. *Nat. Rev. Mol. Cell Biol*., **2013**, 14, 467-473.

[17] Rosenfeld, D.; Levenberg, S. Chapter 15: Effect of matrix mechanical forces and geometry on stem cell behavior. In "Biology and Engineering of Stem Cell Niches", 2017, Elsevier.

[18] Mao, A.S.; Shin, J.-W.; Mooney, D.J. Effects of substrate stiffness and cell-cell contact on mesenchymal stem cell differentiation. *Biomaterials*, **2016**, 98, 184-191.

[19] Kilian, K.A.; Bugarija, B.; Lahn, B.T.; Mrksich, M. Geometric cues for directing the differentiation of mesenchymal stem cells. *Proc. Natl. Acad. Sci.,* **2010**, 107, 4872-4877.

[20] Dalby, M.J.; Gadegaard, N.; Tare, R. et al. The control of human mesenchymal cell differentiation using nanoscale symmetry and disorder. *Nat. Mater.,* **2007**, 6, 997-1003.

[21] Fiedler, J.; Özdemir, B.; Bartholomä, J.; Plettl, A.; Brenner, R.E.; Ziemann, P. The effect of substrate surface nanotopography on the behaviour of multipotnent mesenchymal stromal cells and osteoblasts. *Biomaterials*, **2013**, 34, 8851-8859.

[22] Curran, J.M.; Chen, R.; Hunt, J.A. The guidance of human mesenchymal stem cell differentiation in vitro by controlled modifications to the cell substrate. *Biomaterials*, **2006**, 27, 4783-4793.

[23] Phinney, D.G.; Prockop, D.J. Concise review: mesenchymal stem/multipotent stromal cells: the state of transdifferentiation and modes of tissue repair – current views. *Stem Cells*, **2007**, 25, 2896-2902.

[24] Santeramo, I.; Perez, Z.H.; Illera, A.; Taylor, A.; Kenny, S.; Murray, P.; Wilm, B.; Gretz, N. Human kidney-derived cells ameliorate acute kidney injury without engrafting into renal tissue. *Stem Cells Transl. Med*., **2017**, 6, 1373-1384.

[25] Geng, Y.; Zhang, L.; Fu, B.; Zhang, J.; Hong, Q.; Hu, J.; Li, D.; Luo, C.; Cui, S.; Zhu, F.; Chen, X. Mesenchymal stem cells ameliorate rhabdomyolysis-induced acute kidney injury via the activation of M2 macrophages. *Stem Cell Res. Ther.,* **2014**, 5, 80.

[26] Caplan, A.I. Adult mesenchymal stem cells for tissue engineering versus regenerative medicine. *J. Cell. Physiol*., **2007**, 213, 341-347.

[27] Naumova, A.V.; Modo, M.; Moore, A.; Murry, C.E.; Frank, J.A. Clinical imaging in regenerative medicine. *Nat. Biotechnol.,* **2014**, 32, 804 – 818.

[28] Thompson, L.H.; Parish, C.L. Transplantation of fetal midbrain dopamine progenitors into a rodent model of Parkinson's disease. *Methods Mol. Biol.,* **2013**, 1059, 169-80.

[29] Srivastava, D.; DeWitt, N. In vivo cellular reprogramming: the next generation. *Cell*, **2016**, 166, 1386 – 1396.

[30] Dimmeler, S.; Ding, S.; Rando, T.A.; Trounson, A. Translational strategies and challenges in regenerative medicine. *Nat. Med*., **2014**, 20, 814 – 821.

[31] Ntziachristos, V. Going deeper than microscopy: the optical imaging frontier in biology. *Nature Methods*, **2010**, 7, 603-614.

[32] James, M.L.; Gambhir, S.S. A molecular imaging primer: modalities, imaging agents, and applications. *Physiol. Rev.,* **2012**, 92, 897 – 965.

[33] Mallidi, S.; Luke, G.P.; Emelianov, S. Photoacoustic imaging in cancer detection, diagnosis, and treatment guidance. Tr*ends Biotechnol.,* **2011**, 29, 213 – 221.

[34] Srivastava, A.K.; Kadayakkara, D.K.; Bar-Shir, A.; Gilad, A.A.; McMahon, M.T.; Bulte, J.W. Advances in using MRI probes and sensors for in vivo cell tracking as applied to regenerative medicine. *Dis. Model. Mech.,* **2015**, 8, 323 – 336.

[35] Ametamey, S.M.; Honer, M.; Schubiger, P.A. Molecular imaging with PET. *Chem. Rev.,* **2008**, 108, 1501 – 1516.

[36] Tangney, M.; Francis, K.P. In vivo optical imaging in gene & cell therapy. *Curr. Gene Ther.*, **2012**, 12, 2-11.

[37] Kim, J.E.; Kalimuthu, S.; Ahn, B.-C. In vivo cell tracking with bioluminescence imaging. *Nucl. Med. Mol. Imaging*, **2015**, 49, 3-10.

[38] Masedunskas, A.; Milberg, O.; Porat-Shliom, N.; Sramkova, M.; Wigand, T.; Amornphimoltham, P.; Weigert, R. A practical guide on imaging intracellular structures in live animals. *BioArchitecture*, **2012**, 2:5, 143-157.

[39] Schieβl, I.M.; Castrop, H. Deep insights: intravital imaging with two-photon microscopy. *Eur. J. Physiol.,* **2016**, 468, 1505-1516.

[40] Wang, L.V.; Hu, S. Photoacoustic tomography: in vivo imaging from organelles to organs. *Science,* **2012**, 335, 1458-1462.

[41] Comenge, J.; Fragueiro, O.; Sharkey, J.; Taylor, A.; Held, M.; Burton, N.C.; Park, B.K.; Wilm, B.; Murray, P.; Brust, M.; Lévy, R. Preventing plasmon coupling between gold nanorods improves the sensitivity of photoacoustic detection of labelled stem cells in vivo. *ACS Nano*, **2016**, 10, 7106-7116.

[42] Emeliano, S.Y.; Li, P.-C.; O'Donnell, M. Photoacoustics for molecular imaging and therapy. *Phys. Today*, **2009**, 62, 34-39.

[43] Weissleder, R.; Pettet, M.J. Imaging in the era of molecular oncology. *Nature*, **2008**, 452, 580-589.

[44] Helmchen, F.; Denk, W. Deep tissue two-photon microscopy. *Nat. Methods*, **2005**, 2, 932-940.

[45] Razansky, D.; Distel, M.; Vinegoni, C.; Ma, R.; Perrimon, N.; Köster, R.W.; Ntziachristos, V. Multispectral opto-acoustic tomography of deep-seated fluorescent proteins in vivo. *Nat. Photonics*, **2009**, 3, 412 – 417.

[46] Taruttis, A.; Morscher, S.; Burton, N.C.; Razansky, D.; Ntziachristos, V. Fast multispectral optoacoustic tomography (msot) for dynamic imaging of pharmacokinetics and biodistribution in multiple organs. *Plos One*, **2012**, 7, e30491.

[47] Cherry, S.R. Multimodality imaging: beyond PET/CT and SPECT/CT. *Semin. Nucl. Med.*, **2009**, 39, 348-353.

[48] Lassailly, F.; Griessinger, E.; Bonnet, D. "Microenvironmental contaminations" induced by fluorescent lipophilic dyes used for noninvasive in vitro and in vivo cell tracking. *Blood*, **2010**, 115, 5347 – 5354.

[49] Phan, T.G.; Bullen, A. Practical intravital two-photon microscopy for ummunological research: faster, brighter, deeper. *Immunol. Cell Biol*., **2014**, 88, 438 – 444.

[50] Hong, G.; Antaris, A.L.; Dai, H. Near-infrared fluorophores for biomedical imaging. *Nat. Biomed. Eng.*, **2017**, 1, 0010.

[51] Yu, M.; Li, F.; Chen, Z.; Hu, H.; Zhan, C.; Yang, H.; Huang, C. Laser Scanning Up-Conversion Luminescence Microscopy for Imaging Cells Labeled with Rare-Earth Nanophosphors. *Anal. Chem*., **2009**, 81, 930-935.

[52] Merchant, K.; Sarkar, S.K. Fluorescent nanodiamonds for molecular and cellular bioimaging. *IEEE J. Sel. Topics Quantum Electron.,* **2016**, 22, 6802311.

[53] Montalti, M.; Cantelli, A.; Battistelli, G. Nanodiamonds and silicon quantum dots: ulstrastable and biocompatible luminescent nanoprobes for long-term bioimaging. *Chem. Soc. Rev.*, **2015**, 44, 4853-4921.

[54] Chen, M.; Yin, M. Design and development of fluorescent nanostructures for bioimaging. *Prog. Polym. Sci.,* **2014**, 39, 365-395.

[55] Stephens, D.J.; Allan, V.J. Light microscopy techniques for live cell imaging. *Science*, **2003**, 300, 82 – 87.

[56] Shaner, N.C.; Steinbach, P.A.; Tsien, R.Y. A guide to choosing fluorescent proteins. *Nat. Methods*, **2005**, 2, 905-910.

[57] Wu, D.; Huang, L.; Jiang, M.S.; Jiang, H. Contrast agents for photoacoustic and thermoacoustic imaging: a review. *Int. J. Mol. Sci.,* **2014**, 15, 23616-23639.

[58] Li, W.; Chen, X. Gold nanoparticles for photoacoustic imaging. *Nanomed*., **2015**, 10, 299-320.

[59] Zhang, T.; Cui, H.; Fang, C.Y.; Su, L.J.; Ren, S.; Chang, H.C.; Yang, X.; Forrest, M.L.; Photoacoustic contrast imaging of biological tissues with nanodiamonds fabricated for high near-infrared absorbance. *J. Biomed. Opt*., **2013**, 18, 020018.

[60] Ricles, L.M.; Nam, S.Y.; Trevino, E.A.; Emelianov, S.Y.; Suggs, L.J. A dual gold nanoparticle system for mesenchymal stem cell tracking. *J. Mater. Chem. B*, **2014**, 2, 8220 – 8230.

[61] Yang, X.; Stein, E.W.; Ashkenazi, S.; Wang, L.V. Nanoparticles for photoacoustic imaging. *WIREs Nanomed. Nanobiotechnol.,* **2009**, 1, 360 – 368.

[62] Lemaster, J.E.; Jokerst, J.V. What is new in nanoparticle-based photoacoustic imaging? WIREs Nanomed Nanobiotechnol., 2017, 9:e1404.

[63] Jiang, Y.; Pu, K. Advanced photoacoustic imaging applications of near-infrared absorbing organic nanoparticles. *Small*, **2017**, 13, 1700710.

[64] Wais, U.; Jackson, A.W.; He, T.; Zhang, H. Nanoformulation and encapsulation approaches for poorly water-soluble drug nanoparticles. *Nanoscale*, **2016**, 8, 1746-1749.

[65] Wang, Y.; Li, P.; Tran, T.T.-D.; Zhang, J.; Kong, L. Manufacturing techniques and surface engineering of polymer based nanoparticles for targeted drug delivery to cancer. *Nanomaterials*, **2016**, 6, 26.

[66] Li, K.; Liu, B. Polymer-encapsulated organic nanoparticles for fluorescent and photoacoustic imaging. *Chem. Soc. Rev.,* **2014**, 43, 6570 – 6597.

[67] Zhang, H.; Wang, D.; Butler, R.; Campbell, N.L.; Long, J.; Tan, B.; Duncalf, D.J.; Foster, A.J.; Hopkinson, A.; Taylor, D.; Angus, D.; Cooper, A.I.; Rannard, S.P. Formation and enhanced biocidal activity of water-dispersable organic nanoparticles. *Nature Nanotechnol.,* **2008**, *3*, 506-511.

[68] Wang, G.; Zhang, F.; Tian, R.; Zhang, L.; Fu, G.; Yang, L.; Zhu, L. Nanotubes-Embedded Indocyanine Green−Hyaluronic Acid Nanoparticles for Photoacoustic-Imaging-Guided Phototherapy. *ACS Appl. Mater. Interfaces*, **2016**, 8, 5608-5617.

[69] Liang, X.; Deng, Z.; Jing, L.; Li, X.; Dai, Z.; Li, C.; Huang, M. Prussian blue nanoparticles operate as a contrast agent for enhanced photoacoustic imaging. *Chem. Commun.*, **2013**, 49, 11029-11031.

[70] Pu, K.; Mei, J.; Jokerst, J.V.; Hong, G.; Antaris, A.L.; Chattopadhyay, N.; Shuhendler, A.J.; Kurosawa, T.; Zhou, Y.; Gambhir, S.S.; Bao, Z.; Rao, J. Diketopyrrolopyrrole-based semiconducting polymer nanoparticles for in vivo photoacoustic imaging. *Adv. Mater.,* **2015**, 27, 5184-5190.

[71] Liu, J.; Geng, J.; Liao, L.; Thakor, N.; Gao, X.; Liu, B. Conjugated polymer nanoparticles for photoacoustic vascular imaging. *Polym. Chem*., **2014**, 5, 2854 – 2862.

[72] Zhang, Y.S.; Cai, X.; Yao, J.; Xing, W.; Wang, L.V.; Xia, Y. Non-invasive and in situ characterization of the degradation of biomaterial scaffolds by volumetric photoacoustic microscopy. *Angew. Chem. Int. Ed.,* **2014**, 53, 184-188.

[73] Sun, C.; Wen, L.; Zeng, J.; Wang, Y.; Sun, Q.; Deng, L.; Zhao, C.; Li, Z. One-pot solventless preparation of PEGylated black phosphorus nanoparticles for photoacoustic imaging and photothermal therapy of cancer. *Biomaterials*, **2016**, 91, 81-89.

[74] Cui, D.; Xie, C.; Pu, K. Development of semiconducting polymer nanoparticles for photoacoustic imaging. *Macromol. Rapid Commun.,* **2017**, 38, 1700125.

[75] Pu, K.; Shuhendler, A.J.; Jokerst, J.V.; Mei, J.; Gambhir, S.S.; Bao, Z.; Rao, J. Semiconducting polymer nanoparticles as photoacoustic molecular imaging probes in living mice. *Nature Nanotechnol.,* **2014**, 9, 233-239.

[76] Lyu, Y.; Fang, Y.; Miao, Q.; Zhen, X.; Ding, D.; Pu, K. Intraparticle molecular orbital engineering of semiconducting polymer nanoparticles as amplified theranostics for in vivo photoacoustic imaging and photothermal therapy. *ACS Nano*, **2016**, 10, 4472-4481.

[77] Chen, Q.; Liu, X.; Zeng, J.; Cheng, Z.; Liu, Z. Albumin-NIR dye self-assembled nanoparticles for photoacoustic pH imaging and pH-responsive photothermal therapy effective for large tumors. *Biomaterials*, **2016**, 98, 23-30.

[78] Zhang, Y.; Jeon, M.; Rich, L.J.; Hong, H.; Geng, J.; Zhang, Y.; Shi, S.; Barnhart, T.E.; Alexandridis, P.; Huizinga, J.D.; Seshadri, M.; Cai. W.; Kim, C.; Lovell, J.F. Non-invasive multimodal functional imaging of the intestine with frozen micellar naphthalocyanines. *Nature Nanotechnol.,* **2014**, 9, 631-638.

[79] Lee, C.; Kim, J.; Zhang, Y.; Jeon, M.; Liu, C.; Song, L.; Lovell, J.F.; Kim, C. Dual-color photoacoustic lymph node imaging using nanoformulated naphthalocyanines. *Biomaterials*, **2015**, 73, 142-148.

[80] Fan, Q.; Cheng, K.; Yang, Z.; Zhang, R.; Yang, M.; Hu, X.; Ma, X.; Bu, L.; Lu, X.; Xiong, X.; Huang, W.; Zhao, H.; Cheng, Z. Perylene-diimide-based nanoparticles as highly efficient photoacoustic agents for deep brain tumor imaging in living mice. *Adv. Mater.,* **2015**, 27, 843-847.

[81] Yang, Z.; Tian, R.; Wu, J.; Fan, Q.; Yung, B.C.; Niu, G.; Jacobson, O.; Wang, Z.; Liu, G.; Yu, G.; Huang, W.; Song, J.; Chen, X. Impact of semiconducting perylene diimide nanoparticle size on lymph node mapping and cancer imaging. *ACS Nano*, **2017**, 11, 4247-4255.

[82] Zhang, S.; Guo, W.; Wei, J.; Li, C.; Liang, X.; Yin, M. Terrylenediimide-based intrinsic theranostic nanomedicines with high photothermal conversion efficiency for photoacoustic imaging-guided cancer therapy. *ACS Nano*, **2017**, 11, 3797 – 3805.

[83] Bhosale, S.V.; Jani, C.H.; Langford, S.J. Chemistry of napththalene diimides. *Chem. Soc. Rev.,* **2008**, 37, 331-342.

[84] Würthner, F.; Saha-Möller, C.R.; Fimmel, B.; Oqi, S.; Leowanawat, P.; Schmidt, D. Perylene Bisimide Dye Assemblies as Archetype Functional Supramolecular Materials. *Chem. Rev*., **2016**, 116, 962-1052.

[85] Chen, S.; Slattum, P.; Wang, C.; Zang, L. Self-assembly perylene imide molecules into 1D nanostructures. *Chem. Rev.,* **2015**, 115, 11967-11998.

[86] Avlasevich, Y.; Li, C.; Müllen, K. Synthesis and applications of core-enlarged perylene dyes. *J. Mater. Chem*., **2010**, 20, 3814-3826.

[87] Chen, L.; Li, C.; Müllen, K. Beyond perylene diimides: synthesis, assembly and function of higher rylene chromophores. *J. Mater. Chem. C.,* **2014**, 2, 1938-1956.

[88] Brar, S.K.; Verma, B.M. Measurement of nanoparticles by light-scattering techniques. *Trends Anal Chem*., **2011**, 30, 4-17.

[89] Dynamic laser scattering: An introduction in 30 minutes. Technical note, by Malvern Instruments.

[90] Tantra, R.; Schulze, P.; Quincey, P. Effect of nanoparticle concentration on zeta-potential measurement results and reproducibility. *Particuology*, **2010**, 8, 279-285.

[91] Albanese, A.; Tang, P.S.; Chan, W.C.W. The effect of nanoparticle size, shape, and surface chemistry on biological systems. *Annu. Rev. Biomed. Eng.,* **2012**, 14, 1-16.

[92] Behzadi, S.; Serpooshan, V.; Tao, W.; Hamaly, M.A.; Alkawareek, M.Y.; Dreaden, E.C.; Brown, D.; Alkilany, A.M.; Farokhzad, O.C.; Mahmoudi, M. Cellular uptake of nanoparticles: journey inside the cell. *Chem. Soc. Rev.,* **2017**, 46, 4218 – 4244.

[93] Chithrani, B.D.; Chan, W.C. Elucidating the mechanism of cellular uptake and removal of proteincoated gold nanoparticles of different sizes and shapes. *Nano Lett.,* **2007**, 7, 1542-1550.

[94] Lu, F.; Wu, S.H.; Huang, Y.; Mou, C.Y. Size effect on cell uptake in well-suspended, uniform mesoporous silica nanoparticles. *Small*, **2009**, 5, 1408-1413.

[95] Albanese, A.; Chan, W.C. Effect of gold nanoparticle aggregation on cell uptake and toxicity. *ACS Nano*, **2011**, 5, 5478 – 5489.

[96] Chithrani, B.D.; Ghazani, A.A.; Chan, W.C. Determining the size and shape dependence of gold nanoparticle uptake into mammalian cells. *Nano Lett.,* **2006**, 6, 662-668.

[97] Favi, P.M.; Valencia, M.M.; Elliott, P.R.; Restrepo, A.; Gao, M.; Huang, H.; Pavon, J.J.; Webster, T.J. Shape and surface chemistry effects on the cytotoxicity and cellular uptake of metallic nanorods and nanospheres. *J. Biomed. Mater. Res. A*, **2015**, 103A, 3940-3955.

[98] Banerjee, A.; Qi, J.; Gogoi, R.; Wong, J.; Mitragotri, S. Role of nanoparticle size, shape and surface chemistry in oral drug delivery. *J. Control. Release*, **2016**, 238, 176-185.

[99] Choi, K.; Riviere, J.E.; Monteiro-Riviere, N.A. Protein corona modulation of hepatocyte uptake and molecular mechanisms of gold nanoparticle toxicity. *Nanotoxicology*, **2017**, 11, 64-75.

[100] Jiang, Y.; Huo, S.; Mizuhara, T.; Das, R.; Lee, Y.; Hou, S.; Moyano, D.F.; Duncan, B.; Liang, X.; Rotello, V.M. The Interplay of Size and Surface Functionality on the Cellular Uptake of Sub-10 nm Gold Nanoparticles. *ACS Nano*, **2015**, 9, 9986-9993.

[101] Nel, A.; Xia, T.; Madler, L.; Li, N. Toxic potential of materials at the nanolevel. *Science,* **2006**, 311, 622-627.

[102] Alkilany, A.M.; Murphy, C.J. Toxicity and cellular uptake of gold nanoparticles: what we have learned so far? *J. Nanopart. Res.,* **2010**, 12, 2313-2333.

[103] Yang, H.; Liu, C.; Yang, D.; Zhang, H.; Xi, Z. Comparative study of cytotoxicity, oxidative stress and genotoxicity induced by four typical nanomaterials: the role of particle size, shape and composition. *J. Appl. Toxicol*., **2009**, 29, 69-78.

[104] Coradeghini, R.; Gioria, S.; Garcia, C.P.; Nativo, P.; Franchini, F.; Gilliland, D.; Ponti, J.; Rossi, F. Size-dependent toxicity and cell interaction mechanisms of gold nanoparticles on mouse fibroblasts. *Toxicol. Lett.,* **2013**, 217, 205-216.

[105] Buwalda, S.J.; Boere, K.W.M.; Dijkstra, P.J.; Feijen, J.; Vermonden, T.; Hennink, W.E. Hydrogels in a historical perspective: From simple networks to smart materials. *J. Control. Release*, **2014**, 1901, 254 – 273.

[106] Baker, B.M.; Chen, C.S. Deconstructing the third dimension – how 3D culture microenvironments alter cellular cues. *J. Cell. Sci.,* **2012**, 125, 3075-3083.

[107] Thiele, J.; Ma, Y.; Bruekers, S.M.C.; Ma, S.; Huck, W.T.S. Designer hydrogels for cell cultures: a materials selection guide. *Adv. Mater*., **2014**, 26, 125-148.

[108] Caliari, S.R.; Burdick, J.A. A practical guide to hydrogel for cell culture. *Nat. Methods*, **2016**, 13, 405 – 414.

[109] Nicodemus, G.D.; Bryant, S.J. Cell encapsulation in biodegradable hydrogels for tissue engineering applications. *Tissue Eng. B*, **2008**, 14, 149-165.

[110] Kang, A.; Park, J.; Ju, J.; Jeong, G.S.; Lee, S.-H. Cell encapsulation via microtechnologies. *Biomaterials*, **2014**, 35, 2651 – 2663.

[111] Fliervoet, L.A.L.; Mastrobattista, E. Drug delivery with living cells. *Adv. Drug Del. Rev.,* 2016, 106, 63-72.

[112] Orive, G.; Hernández, R.M.; Gascón, A.R.; Calafiore, R.; Chang, T.M.S.; de Vos, P.; Hortelano, G.; Hunkeler, D.; Lacík, I.; Pedraz, J.L. History, challenges and perspectives of cell microencapsulation. *Trends Biotechnol.,* **2004**, 22, 87-92.

[113] Orive, G.; Santos, E.; Poncelet, D.; Hernández, R.M.; Pedraz, J.L.; Wahlberg, L.U;. de Vos, P.; Emerich, D. Cell encapsulation: technical and clinical advances. *Trends Pharmacol. Sci.,* **2015**, 36, 537 – 546.

[114] Chang, T.M.S. Semipermeable microcapsules. *Science*, **1964**, 146, 524-525.

[115] Orive, G.; Hernández, R.M.; Gascón, A.R.; Calafiore, R.; Chang, T.M.S.; de Vos, P.; Hortelano, G.; Hunkeler, D.; Lacík, I.; Shapiro, A.M.J.; Pedraz, J.L. Cell encapsulation: promise and progress. *Nat. Med.,* **2003**, 9, 104 – 107.

[116] Desai, T.; Shea, L.D. Advances in islet encapsulation technologies. *Nat. Rev. Drug Disc.,* **2017**, 16, 338-350.

[117] De Vos, P.; Lazarjani, H.A.; Poncelet, D.; Faas, M.M. Polymers in cell encapsulation from an enveloped perspective. *Adv. Drug Del. Rev.,* **2014**, 67-68, 15-34.

[118] Yang, J.-A.; Yeom, J.; Hwang, B.W.; Hoffman, A.S.; Hahn, S.K. In situ-forming injectable hydrogels for regenerative medicine. *Prog. Polym. Sci*., **2014**, 39, 1973-1986.

[119] Wang, T.; Lacik, I.; Brissová, M.; Anilkumar, A.V.; Prokop, A.; Hunkeler, D.; Green, R.; Shahrokhi, K.; Powers, A.C. An encapsulation system for the immunoisolation of pancreatic islets. *Nat. Biotechnol.,* **1997**, 15, 358 – 362.

[120] Steele, J.A.M.; Hallé, J.-P.; Poncelet, D.; Neufeld, R.J. Therapeutic cell encapsulation techniques and applications in diabetes. *Adv. Drug Del. Rev.,* **2014**, 67-68, 74-83.

[121] Canaple, L.; Rehor, A.; Hunkeler, D. Improving cell encapsulation through size control. *J. Biomater. Sci. Polym. Ed.*, **2002**, 13, 783-796.

[122] Luca, G.; Basta, G.; Calafiore, R.; Rossi, C.; Giovagnoli, S.; Esposito, E.; Nastruzzi, C. Multifunctional microcapsules for pancreatic islet cell entrapment: design, preparation and in vitro characterization. *Biomaterials*, **2003**, 24, 3101-3114.

[123] Colton, C.K. Oxygen supply to encapsulated therapeutic cells. *Adv. Drug Del. Rev.,* **2014**, 67-68, 93 – 110.

[124] Orive, G.; Santos, E.; Pedraz, J.L.; Hernández, R.M.. Application of cell encapsulation for controlled delivery of biological therapeutics. *Adv. Drug Del. Rev.,* **2014**, 67-68, 3-14.

[125] Shoichet, M.S.; Winn, S.R. Cell delivery to the central nervous system. *Adv. Drug Del. Rev.*, **2000**, 42, 81-102.

[126] Feng, G.; Zhang, J.; Li, Y.; Nie, Y.; Zhu, D.; Wang, R.; Liu, J.; Gao, J.; Liu, N.; He, N.; Du, W.; Tao, H.; Che, Y.; Xu, Y.; Kong, D.; Zhao, Q.; Li, Z. IGF-1 C Domain–Modified Hydrogel Enhances Cell Therapy for AKI. *J. Am. Soc. Nephrol.*, **2016**, 27 (doi: 10.1681/ASN.2015050578).

[127] Cantu, D.A.; Hematti, P.; Kao, W.J. Cell Encapsulating Biomaterial Regulates Mesenchymal Stromal/Stem Cell Differentiation and Macrophage Immunophenotype. *Stem Cells Transl. Med.*, **2012**, 1, 740-749.

[128] Artzi, N.; Oliva, N.; Puron, C.; Shitreet, S.; Artzi, S.; bon Ramos, A.; Groothuis, A.; Sahagian, G.; Edelman, E.R. In vivo and in vitro tracking of erosion in biodegradable materials using non-invasive fluorescent imaging. *Nat. Mater.,* **2011**, 10, 704 – 709.

[129] Martins, A.M.; Alves, C.M.; Kasper, F.K.; Mikos, A.G.; Reis, R.L. Responsive and in situ-forming chitosan scaffolds for bone tissue engineering applications: an overview of the last decade. *J. Mater. Chem*., **2010**, 20, 1638-1645.

[130] Custódio, C.A.; Cerqueira, M.T.; Marques, A.P.; Reis, R.L.; Mano, J.F. Cell selective chitosan microparticles as injectable cell carriers for tissue regeneration. *Biomaterials*, **2015**, 43, 23-31.

[131] Moreau, J.L.; Xu, H.H.K. Mesenchymal stem cell proliferation and differentiation on an injectable calcium phosphate – chitosan composite scaffold. *Biomaterials*, **2009**, 30, 2675-2682.

[132] Bernkop-Schnürch, A.; Dünnhaupt, S. Chitosan-based drug delivery systems. *Eur. J. Pharm. Biopharm.*, **2012**, 81, 463-469.

[133] Naahidi, S.; Jafari, M.; Edalat, F.; Raymond, K.; Khademhosseini, A.; Chen, P. Biocompatibility of engineering nanoparticles for drug delivery. *J. Control. Release,* **2013**, 166, 182-194.

[134] Rinaudo, M. Chitin and chitosan: properties and applications. *Prog. Polym. Sci.,* **2006**, 31, 603-632.

[135] Shukla, S.; Mishra, A.K.; Arotiba, O.A.; Mamba, B.B. Chitosan-based nanomaterials: a state-of-the-art review. *Int. J. Biol. Macromol.,* **2013**, 59, 46-58.

[136] Upadhyaya, L.; Singh, J.; Agarwal, V.; Tewari, R.P. The implications of recent advances in carboxymethyl chitosan based targeted drug delivery and tissue engineering applications. *J. Control. Release*, **2014**, 186, 54-87.

[137] Casettari, L.; Vllasaliu, D.; Lam, J.K.W.; Soliman, M.; Illum, L. Biomedical applications of amino acid-modified chitosans: A review. *Biomaterials*, **2012**, 33, 7565-7583.

[138] Kievit, F.M.; Florczyk, S.J.; Leung, M.C.; Veiseh, O.; Park, J.O.; Disis, M.L.; Zhang, M. Chitosanealginate 3D scaffolds as a mimic of the glioma tumor microenvironment. *Biomaterials*, **2010**, 31, 5903-5910.

[139] Deng, C.; Zhang, P.; Vulesevic, B.; Kuraitis, D.; Li, F.; Yang, A.F.; Griffith, M.; Ruel, M.; Suuronen, E.J. A collagen–chitosan hydrogel for endothelial differentiation and angiogenesis. *Tissue Eng. A*, **2010**, 16, 3099-3109.

[140] Bhattarai, N.; Gunn, J.; Zhang, M. Chitosan-based hydrogels for controlled, localized drug delivery. *Adv. Drug Del. Rev.,* **2010**, 62, 83-99.

[141] Jonassen, H.; Kjøniksen, A.-L.; Hiorth, M. Effects of ionic strength on the size and compactness of chitosan nanoparticles. *Colloid Polym. Sci.,* **2012**, 290, 919-929.

[142] Chenite, A.; Chaput, C.; Wang, D.; Combes, C.; Buschmann, M.D.; Hoemann, C.D.; Leroux, J.C.; Atkinson, B.L.; Binette, F.; Selmani, A. Novel injectable neutral solutions of chitosan form biodegradable gels in situ. *Biomaterials*, **2000**, 21, 2155-2161.

[143] Ahmadi, R.; de Bruijn, J.D. Biocompatibility and gelation of chitosan-glycerol phosphate hydrogel. *J. Biomed. Mater. Res.,* **2008**, 86A, 824-832.

[144] Naderi-Meshkin, H.; andreas, K.; Matin, M.M.; Sittinger, M.; Bidkhori, H.R.; Ahmadiankia, N.; Bahrami, A.R.; Ringe, J. Chitosan-based injectable hydrogel as a promising in situ forming scaffold for cartilage tissue engineering. *Cell Biol. Int*., **2014**, 38, 72-84.

[145] Ji, C.; Khademhosseini, A.; Dehghani, F. Enhancing cell penetration and proliferation in chitosan hydrogels for tissue engineering applications. *Biomaterials*, **2011**, 32, 9719-9729.

[146] Skop, N.B.; Calderon, F.; Levison, S.W.; Gandhi, C.D.; Cho, C.H. Heparin crosslinked chitosan microspheres for the delivery of neural stem cells and growth factors for central nervous system repair. *Acta Biomater.,* **2013**, 9, 6834-6843.

[147] Bi, L.; Cao, Z.; Hu, Y.; Song, Y.; Yu, L.; Yang, B.; Mu, J.; Huang, Z.; Han, Y. Effects of different cross-linking conditions on the properties of genipin-cross-linked chitosan/collagen scaffolds for cartilage tissue engineering. *J. Mater. Sci. Mater. Med.,* **2011**, 22, 51-62.

[148] Agnihotri, S.A.; Mallikarjuna, N.N.; Aminabhavi, T.M. Recent advances on chitosan-based micro- and nanoparticles in drug delivery. *J. Control. Release*, **2004**, 100, 5-28.

[149] Grenha, A. Chitosan nanoparticles: a survey of preparation methods. *J. Drug Targeting*, **2012**, 20, 291-300.

[150] Jayakumar, R.; Prabaharan, M. Nair, S. V.; Tamura, H. Novel chitin and chitosan nanofibers in biomedical applications. *Biotechnol. Adv*., **2010**, 28, 142-150.

Chapter 2 Synthesis of perylene diimide derivative with NIR absorption and its aqueous nanoparticle suspensions

2.1 Introduction

Perylene-based dyes are widely used in the dye industry [1]. Perylene is poorly soluble in most common solvents and therefore, modified perylene-based compounds are required for processing and formulation. One of the most widely used types are perylene diimide (PDI) compounds (see **Figure 1-12** in chapter 1). The modification of PDIs usually starts with the halogenated compound, which typically utilize perylenetetracarboxylic dianhydride (PTCDA) as the starting material. Conventionally, PTCDA is treated in concentrated sulphuric acid or chlorosulfonic acid in the presence of I_2 or Br_2 [2]. Not only is the reaction condition harsh and demanding, a mixture of halogenated isomers is formed without purification. The synthesis of brominated PTCDA is improved without the use of concentrated acid and the isomers are separated by extraction and running through a silica column [3].

Halogenated PDIs can be used to synthesize various diimides with functional groups at the bay position. While the groups at the imide positions can significantly change the solubility in water or organic solvent, the modification at the bay positions can considerably vary the UV-vis absorption [1,4]. For example, by adding pyrrolidine to the bay position, the maximum absorption wavelength is changed from 531 nm to 704 nm in dichloromethane [2].

The core of PDI is a planar π-conjugated system, prone to forming crystal aggregates or nanofibers via π-π interaction and hydrophobic interaction. When introducing naphthalene units into the perylene core, higher perylene diimmides are

formed with significant shift of light absorption in the NIR region. Approximately, a shift of 100 nm towards the higher NIR wavelength region can be achieved [5]. These dyes cover the light-absorbing region of visible 400 – 760 nm and NIR 760 – 1300 nm. Quite importantly, these dyes usually exhibit fluorescence with high quantum yields. They also show excellent thermal, chemical, and photochemical stabilities [5]. Therefore, PDIs could be useful for in vivo bioimaging applications involving both NIR fluorescence and photoacoustics if their maximum absorbance was above 650nm,

Because of the conjugated aromatic core of the PDIs, they usually dissolve in organic solvent although it is possible to modify the PDIs at the immide position to make them water-soluble. However, even in the latter case, the PDIs are only soluble in basic water instead of neutral water [6]. Therefore, it is essential to fabricate aqueous nanoparticle suspensions for biomedical applications, *e.g.*, as probes for NIR imaging.

In general, organic nanoparticles can be fabricated by top-down or bottom-up approaches [7]. The top-down approaches mainly include milling and high-pressure homogenization. However, these methods always produce sub-micron particles (or larger nanoparticles, *e.g.*, > 500 nm) that have a tendency to aggregate. This is not suitable for biomedical applications such as bioimaging where the nanoparticles are usually required to be < 200 nm [7,8]. Among various bottom-up approaches, where the organic compound is dissolved in an organic solvent and then processed, the nanoprecipitation is most widely used because it is simple and versatile [7]. Another bottom-up method developed by Zhang et al [9], emulsion freeze-drying, can produce dry porous nanocomposites with hydrophilic polymer, which offers high nanoparticle stability and facile storage and transport. The aqueous nanoparticle suspensions can be instantly formed by simply dissolving the porous nanocomposite in water.

In this chapter, surfactants and polymers to stabilize PDI nanoparticles and that are not cytotoxic will be identified for subsequent cell imaging applications. In addition to commercially available surfactants/polymers, a new type of block copolymer $DEAMA_{50}DEGDMA_2OEGMA_{80}$ developed by the Zhang group will also be examined. This block copolymer has been shown to stabilize emulsions and hydrophobic drug nanoparticles [10].

Objectives

1. Synthesize PDI nanoparticles in organic solvents with NIR absorbance wavelength > 650 nm
2. Prepare aqueous PDI nanoparticle suspensions using a nanoprecipitation and emulsion freeze-drying approach that maintains the NIR absorbance > 650 nm

2.2 Experimental Details

2.2.1 Chemicals and reagents

Perylenetetracarboxylic dianhydride (PTCDA, 97%) was purchased from Alfa Aesar. Bromobutane, bromine, acetonitrile (ACN), and p-toluenesulfonic acid monohydrate (p-TsOH.H_2O) were obtained from Acros Organics. Butanol and magnesium sulfate were bought from BDH laboratory supplies. 1,8-Diazobicyclo[5.4.0]undec-7-ene (DBU), potassium carbonate, hexane, sodium bisulfate, cyclohexamine, acetic acid, N-methyl-2-pyrrolidinone, poly(vinyl alcohol) (Mw 9-10K, 80% hydrolysed), cyclohexane, D-α-Tocopherol polyethylene glycol 1000 succinate (TPEG) were purchased from Sigma Aldrich. Dichloromethane (DCM), methanol, sodium bisulfate, toluene and pyrrolidine were purchased from Fisher. All chemicals were used as received. A hyperbranched block copolymer

$DEAMA_{50}DEGDMA_2OEGMA_{80}$ was synthesized and provided by Miss Ulrike Wais (H. Zhang laboratory, Dept of Chemistry, University of Liverpool).

2.2.2 Synthesis of brominated PTCDA (compound 4 in Scheme 2-1)

The synthesis followed a previously reported method with modifications [3]. PTCDA (4.0 g), bromobutane (20.0 g), butanol (13.0 g), DBU (15.0 g) and ACN (160 ml) were placed in a 500 ml round bottomed flask. The content in the flask was refluxed at 100ºC (heated in an oil bath) and left overnight (~ 18 hours). The red suspension turned orange during the reaction. After cooling down the reaction to room temperature, methanol (200ml) was added. The resulting precipitate was filtered and dried in a vacuum oven. The crude was purified from boiling butanol to produce compound 2 (4.42 g).

Compound 2 (perylene tetrabutyl ester, 4.0 g) and potassium carbonate (2.0 g) in dichloromethane (50 ml) was added to a 100 ml round bottomed flask to give an orange-red solution. Bromine (4 ml) was added slowly dropwise to the reaction mixture, turning the solution a dark purple colour. After stirring for 24 h, a saturated aqueous solution of sodium bisulfate was added dropwise with continued stirring until no more gas was released. The mixture separated into two layers: the organic layer at the top and the aqueous layer at the bottom. The aqueous layer was decanted and the final solution was washed three times using distilled water, and dried over magnesium sulfate. The aqueous layer was washed with dichloromethane, in order to obtain more product. The solvent was removed by rotary evaporation under reduced pressure. This crude product was recrystallised using dichloromethane (48 ml) and acetonitrile (400ml) and left for 3 days. The orange crystals (3.004 g) obtained by filtration were

compound 3. A small amount of additional product was obtained from the filtrates, which was believed to be compound 3a but not used in the following procedures.

Compound 3 (3.0 g), p-toluene sulfonic acid monohydrate (3.6 g), and toluene (105 ml) were added into a 250 mL round bottom flask. The contents were heated to 100ºC while stirring for 30 h. The reaction was stopped by cooling to room temperature. The precipitate was filtered and washed with methanol and water. The dried dark red solid was refluxed in chloroform (150ml) at 77ºC for 3 h and then collected by filtration as a dry product that was compound 4 (1.35g).

2.2.3 Synthesis of perylene diimide derivative (PDI) with NIR absorbance (compound 6 in Scheme 2-2).

The preparation followed a method reported before with modifications [2]. Typically, the compound **4** (brominated PTCDA, 0.95 g), cyclohexamine (0.58ml), acetic acid (0.477ml), and N-methyl-2-pyrrolidinone (20ml) were added into a 50 mL round bottom flask. The contents were stirred at 85ºC under N_2 atmosphere for 6 h in an oil bath. After cooling the reaction to room temperature, the precipitate was filtered and washed with methanol. The dark purple precipitate turned light red when washed. Compound 5 was obtained after drying using a vacuum oven (0.60 g).

Compound **5** (0.1 g) was dissolved into pyrrolidine (4.5g) and stirred under Argon for 48 h at 70ºC. The reaction mixture was then poured into 25ml diluted 10% HCl solution with stirring. A liquid extraction process was then performed 3 times with dichloromethane. The hydrophobic compound in dichloromethane was dried over $MgSO_4$ and then filtered. The dry dark green solid (0.045 g) was obtained after evaporating dichloromethane. This product was the PDI compound with NIR absorbance, compound 6.

2.2.4 Preparation of aqueous PDI nanoparticle dispersions by solvent evaporation

A PDI solution in acetone was prepared by dissolving 10mg PDI in 10 ml acetone. Aqueous PVA solution was formed by dissolving 100mg PVA in 10 ml water. 2 mL PDI solution was added into the PVA solution (8 ml) dropwise while stirring with a magnetic bar at the speed of 800 rpm. The resulting solution was kept stirring overnight in a fume cupboard to allow the full evaporation of acetone. This produced a clear and dark green nanoparticle suspension, with a concentration of 0.25mg/ml.

In the above preparation, PVA was used as a stabilizer to form stable nanoparticle dispersions. TPEG/PVA (0.1 wt%/1 wt% aqueous solution) and PVA-DEAE-Dextran (both are 1 wt% aqueous solution) were also employed to prepare PDI nanoparticle suspensions, following the same procedures as described above.

A slightly different method was used to prepare a PDI nanoparticle suspension when the block copolymer $DEAMA_{50}DEGDMA_2OEGMA_{80}$ was used as stabiliser. A PDI solution in acetone was prepared by dissolving 10mg PDI in 10 ml acetone. The block copolymer $DEAMA_{50}DEGDMA_2OEGMA_{80}$ solution in acetone was prepared by dissolving 20 mg block copolymer $DEAMA_{50}DEGDMA_2OEGMA_{80}$ in 10 ml acetone. These two stock solutions were used to prepare the mixing solutions with the ratios of PDI: $DEAMA_{50}DEGDMA_2OEGMA_{80}$ being 1:1, 1:2, and 2:1. The detailed preparation procedures are described here. *(I) for the ratio of 1:1:* 2 ml PDI solution, 1 ml $DEAMA_{50}DEGDMA_2OEGMA_{80}$ solution and 1 ml acetone were mixed to obtain a solution with the concentrations of PDI and $DEAMA_{50}DEGDMA_2OEGMA_{80}$ both at 0.5 mg/ml. *(II) for the ratio of 1:2:* 2 ml PDI solution and 2 ml $DEAMA_{50}DEGDMA_2OEGMA_{80}$ solution to make 0.5mg/ml for PDI and 1mg/ml for $DEAMA_{50}DEGDMA_2OEGMA_{80}$ mixture solution. *(III) for the ratio of 2:1:* 2 ml PDI

solution, 0.5 ml $DEAMA_{50}DEGDMA_2OEGMA_{80}$ solution and 1.5 ml acetone to make 0.5mg/ml for PDI and 0.25mg/ml for $DEAMA_{50}DEGDMA_2OEGMA_{80}$ mixture solution. In order to prepare the PDI nanoparticles, each of the solutions (2 ml) were slowly added dropwise into water (8 ml) while stirring with a magnetic bar at a speed of 800 rpm. The resulting solution was kept stirring overnight in a fume cupboard to allow the acetone to evaporate. This produced a clear dark green nanoparticle suspension.

2.2.5 Preparation of aqueous PDI nanoparticle dispersions by emulsion-freeze-drying

The emulsion-freeze-drying approach is highly effective for the preparation of aqueous organic nanoparticle suspensions, firstly reported by Zhang et al. [9]. A saturated PDI solution in cyclohexane (0.5mg/mL) was first prepared at room temperature. The PDI-cyclohexane solution (6 mL) was then emulsified into 2 mL of aqueous solution containing 1 wt% PVA (or 1 wt% TPEG or 1 wt% PVA and 1 wt% TPEG), by dropwise addition with mechanical stirring. After stirring for 5 minutes, the raw emulsion was homogenized for 2 minutes at the scale of 5 using a Fisher brand homogenizer (FB Gen 1200). The finer emulsion was immediately frozen by immersing in liquid nitrogen. The frozen emulsion was then placed in a freeze dryer (Cool Safe, 100-9 Pro, Labogene) for 48 hours to remove both water and cyclohexane by sublimation. The freeze-dried samples were stored in a desiccator before use. To form aqueous PDI nanoparticle dispersions with the desired concentrations, the controlled amount of freeze-dried sample could be readily dissolved in water within one minute.

2.2.6 Characterizations

The synthesized compounds were analysed using the Bruker Fourier 300HD for ^{1}H NMR and ^{13}C NMR. The elemental analysis was conducted using the Thermo flash EA 112 series. The NMR analysis and elemental analysis were used to assess the purity of the synthesized compounds. The UV-Vis profiles for aqueous suspensions were obtained using the μ-Quant Microplate Reader. The suspensions were filtered using a 0.22 μm syringe filter before the UV-vis analysis. For the PDI organic solutions, a conventional quartz cuvette was used for analysis on the UV instrument in the central teaching lab (CTL) of the University of Liverpool.

The size of the PDI nanoparticles in aqueous suspensions was measured by the Dynamic Laser Scattering (DLS) method at 25ºC using a Malvern ZetaSizer equipped with a zeta potential detector. The scattering intensity signal for the detector was passed through a correlator where the data was analysed by the software to give a size distribution of the hydrated nanoparticles. An attempt was also made to observe the PDI nanoparticles using a Hitachi S-4800 field emission scanning electron microscope (SEM) at 3.0 kV. A drop of the aqueous suspension was deposited on a SEM stud or carbon film grid and the water was evaporated overnight in a fume cupboard before imaging.

2.3 Results and discussion

2.3.1 Synthesis of PDI nanoparticles with NIR absorbance

The synthesis started from PTCDA, which is an industrial dye. PTCDA is highly hydrophobic and shows low solubility in most of the common solvents. It is also a highly inert compound. In order to increase the absorbance wavelength into the NIR region, halogenated PTCDA was modified at the bay position [2,4,5]. Halogenation at

the bay positions (usually with Br_2 or Cl_2) is usually performed in concentrated sulphuric acid at elevated temperatures [2]. Despite the harsh reaction conditions, the reactions produce a mixture of 1, 7-dihalogenated and 1, 6-dihalogenated perylene-based compounds, as confirmed by NMR analysis. The procedures for the separation of these isomers are time-consuming and not suitable for large-scale synthesis. Therefore, a method recently developed by Jager and co-authors with mild conditions and regioisomerically pure brominated PTCDA was used, as detailed in **Scheme 2-1** [3].

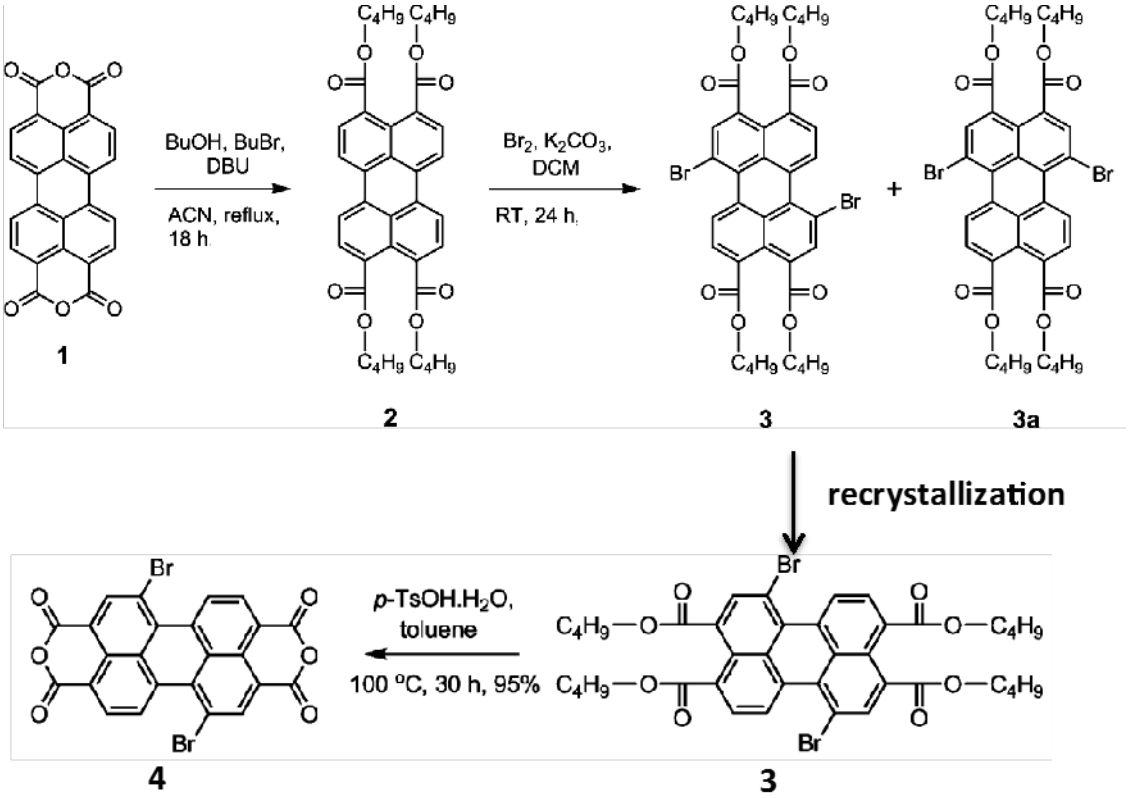

Scheme 2-1. Synthesis of brominated perylene-3,4,9,10-tetracarboxylic dianhydride (PTCDA). This synthesis method was adopted from ref 3.

Compound 2, tetrabutyl perylene-3,4,9,10-tetracarboxylate, was formed by an esterification reaction with DBU as catalyst. The crude product was purified from

boiling butanol. **Figure 2-1** shows the ^{1}H NMR spectrum of compound **2**. The clean spectrum indicates the compound has high purity. The doublets at 8.25ppm and 8.05 ppm are for the hydrogens directly bonded to the perylene core. The spectrum suggests two aromatic hydrogen environments: the hydrogens at the bay positions and at the other positions. The peak at 7.26 ppm is ascribed to the residual solvent peak of $CDCl_3$. The peak at 1.55 ppm is due to the presence of trace amounts of water in $CDCl_3$ when it is used and stored for a long time. The triplet at 4.35 ppm is due to the O-CH_2- being coupled to the neighbouring CH_2 group, and it has an integration of 8H. The multiplets at 1.80 ppm and 1.60 ppm are the CH_2 groups in the middle of the butyl chain. This is supported by the integration of 8H. The multiple peaks at 1.80 ppm are for the CH_2 group closer to the oxygen. This is because of the oxygen drawing electron density away via an inductive effect, causing the chemical shift to be further downfield chemical shift as shown. The triplet peaks around 1.0 ppm are for the terminal methyl group, coupling to the neighbouring –CH_2 group, with integration of 12H. The element analysis of compound 2 gave 73.34 % C and 6.72 % H, very close to the theoretically calculated values (73.6% C and 6.8% H). Compounds **1** and **2** can be distinguished by the presence of the chemical shifts from the butyl chains.

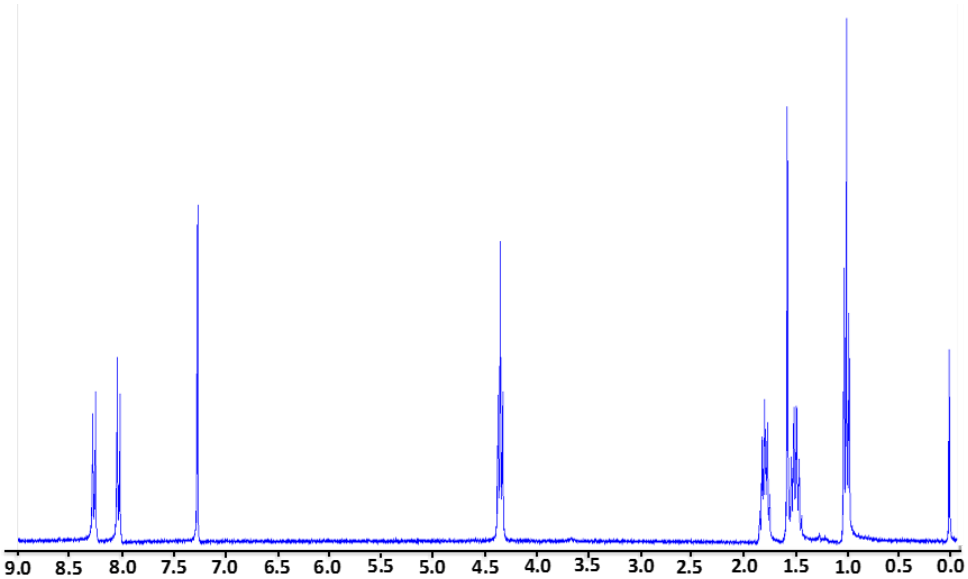

Figure 2-1. The ^{1}H NMR spectrum of compound 2 as described in Scheme 2-1.

In the synthesis of compound 3, a high yield was observed, including both isomers. After recrystallization to separate the isomers (see experimental details), a high percentage of compound 3 was obtained (~ 75 wt%, with the rest being compound 3a). The ^{1}H NMR for compound **3** is given in **Figure 2-2**. Again, the clean spectrum indicates a highly pure compound. Due to the bromination, three aromatic hydrogen environments are observed. The singlet peak at 8.30 ppm is assigned to the hydrogen between -Br and the ester group because it is not coupled to any other hydrogens. The integration of 2H for this peak is obtained because there are two such hydrogens in the molecule. The doublets at 8.98 ppm and 8.10 ppm are for the other aromatic hydrogens with the peaks at 8.10 ppm being the hydrogens in bay positions. As expected, the peaks for the butyl chains are still observed.

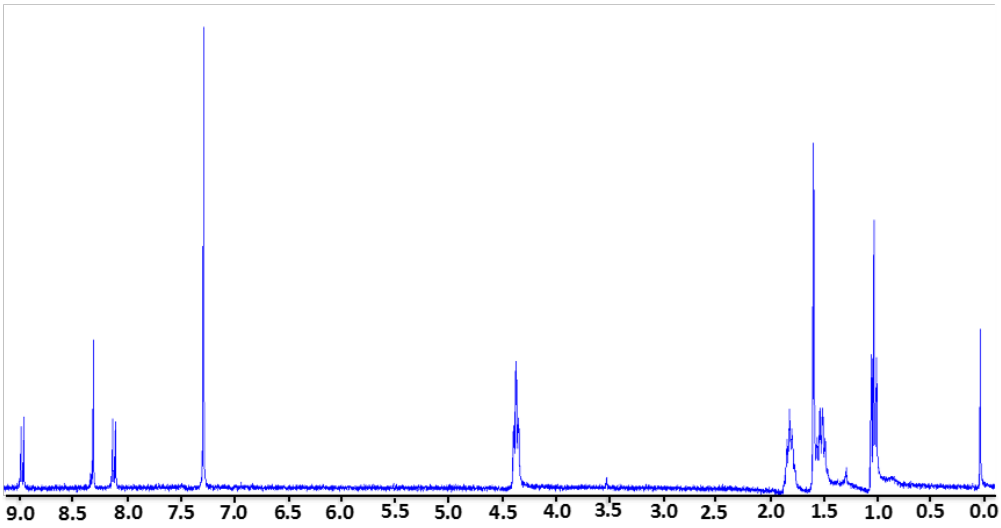

Figure 2-2. The ^{1}H NMR spectrum of compound 3 as described in Scheme 2-1.

Compound **4** was prepared from compound 3 at a temperature of 100ºC in a good solvent of toluene containing p-TsOH.H_2O. This was to prevent the precipitation of monoanhydride product from the solution. The reaction occurs via the initial insertion of the p-TsOH into the carbonyl, resulting in the release of butanol. The neighbouring ester adds into the carbonyl, which causes TsO^- to eliminate, facilitating the removal of the butyl group on the linking oxygen atom. The elemental analysis of compound 4 showed 52.17% C and 1.96% H, close to the calculated values of 52.3 % C but higher than the calculated H content of 1.1 %. **Figure 2-3** shows the ^{1}H NMR spectrum of compound 4 in DMSO. The peak intensities are relatively weak. This is due to the poor solubility of compound 4 in $CDCl_3$. Even with the use of DMSO, the solution was prepared by warming the contents in a NMR tube with hot water. Some of the compound 4 precipitated during the NMR analysis. Deuterated sulfuric acid was used previously as the solvent for NMR analysis [3], but was not used in this project due to safety concerns in handling concentrated acids.

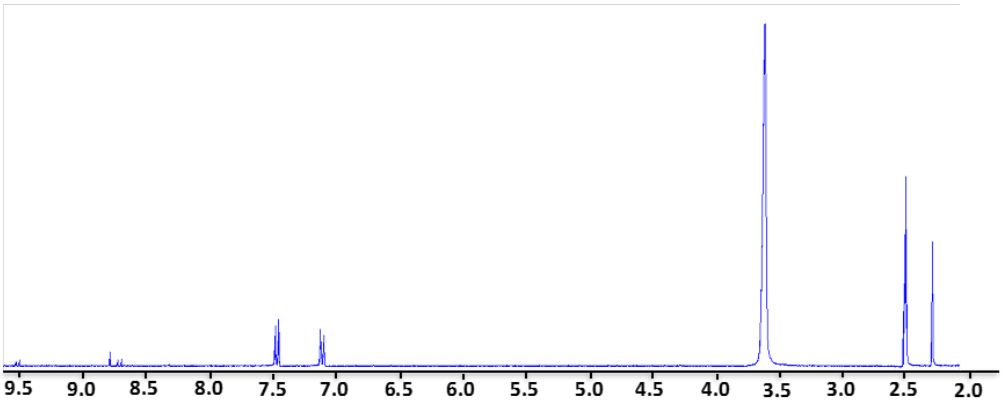

Figure 2-3. The ^{1}H NMR spectrum of compound 4 as described in Scheme 2-1.

From the NMR spectrum in Figure 2-3, the chemical shifts from the aromatic hydrogens on the perylene core are shifted further downfield than in compound **3** due

to the larger electron withdrawing nature of the anhydride groups. The multiplets at 7.5 ppm and 7.1 ppm, and the singlet at 2.3 ppm are likely caused by the presence of toluene which was not removed entirely in the drying process [11]. The singlet at 3.6 ppm and multiplet at 2.5 ppm are unknown impurities, which could be other residual solvent or reactants.

Brominated PTCDA can be used as the starting reagent for the synthesis of a range of perylene diimide derivatives. We adopted a procedure in ref 2 for the synthesis of PDI with NIR absorbance. As shown in **Scheme 2-2**, cyclohexamine was used as the nucleophile to form the amide bonds, catalysed by acetic acid. This step is necessary to protect the anhydride group in the next-step synthesis.

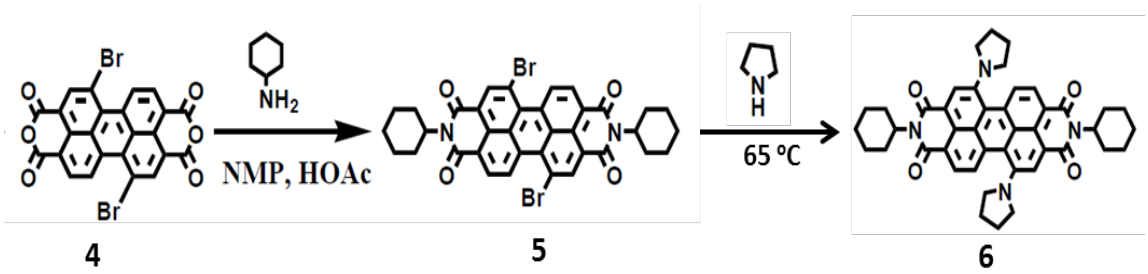

Scheme 2-2. Synthesis of perylene diimide derivatives with NIR absorbance from brominated PTCDA. This synthesis method was adapted from ref 2.

The ^{1}H NMR for compound **5** is given in **Figure 2-4**. As expected, there is no change of proton peaks in the aromatic region, because of the reaction occurring at the end groups (or the peri position). The peaks that demonstrate the formation of compound 5 are the multiplet at around 5.0 ppm from the cyclohexamine ring. The peak at 2.6 ppm is the downward facing axial hydrogens, which is supported by the integration of 4H. The remaining alkyl hydrogens on the cylcohexamine rings occur between 1.25 ppm and 2.0 ppm. The solvent used for this analysis was $CDCl_3$.

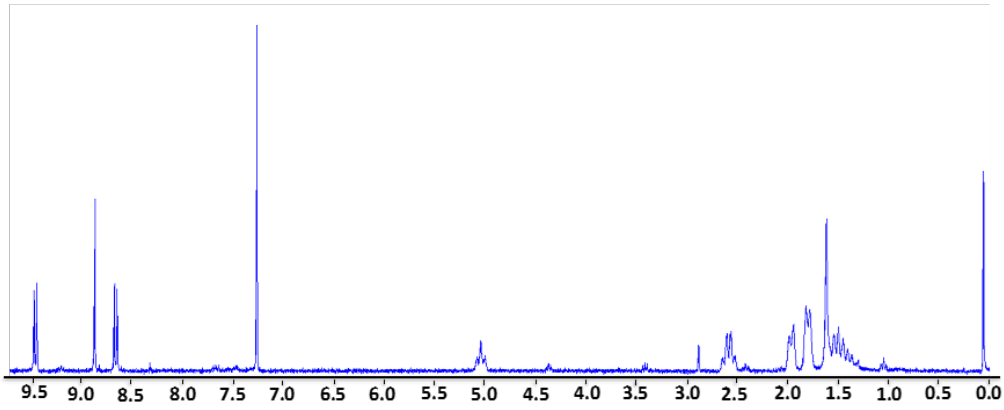

Figure 2-4. The ^{1}H NMR spectrum of compound 5 as described in Scheme 2-2.

The final step of the synthesis is the nucleophilic substitution of the bromines in the bay positions with pyrrolidine (Scheme 2.2). **Figure 2-5** shows the ^{1}H NMR of compound 6. Compared to the previous compounds, the broad peaks at 3.8 ppm and 2.8 ppm are caused by the two differing hydrogen environments on the pyrrolidine rings, showing the formation of compounds. However, there are some small peaks on the spectrum. Together with the discrepancy of the elemental analysis data between the measured and calculated values, it can be confirmed that there are some impurities, even after the recrystallization procedure.

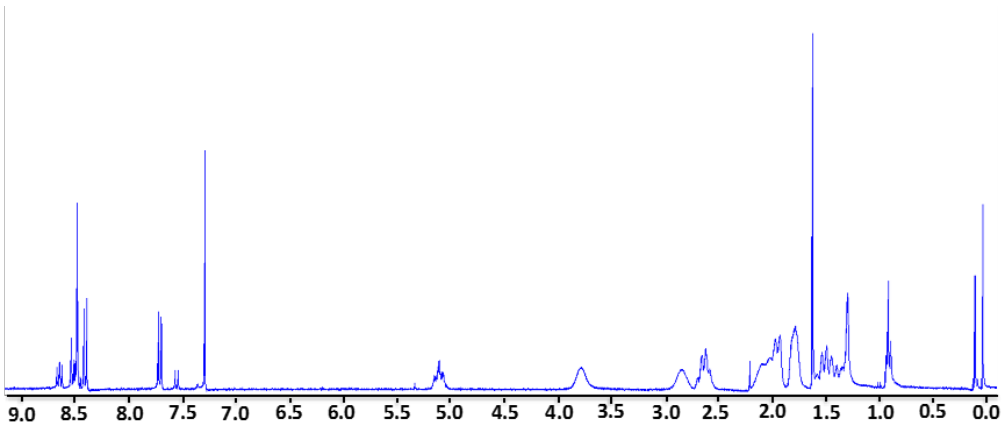

Figure 2-5. The ^{1}H NMR spectrum of compound 6 as described in Scheme 2-2.

Because the objective was to synthesize a PDI compound with NIR absorbance, it was therefore critical to examine the PDI solutions by UV-vis spectroscopy. The as-synthesized compound was dried in a vacuum oven at 60°C overnight. It was then dissolved in different organic solvents. **Figure 2-6** shows the UV-vis profiles of the PDI solution in cyclohexane, acetone, and dichloromethane. The shapes of the profiles were similar for all solvents, but peak shifts were observed for different solvents. This can be attributed to the different interaction between the solvent and PDI. This also results in different absorbance coefficients, indicating different absorbance intensity with the same concentration. The strongest absorbance peaks of these solutions fall in the NIR region, with the wavelength being 670 nm for cyclohexane, 696 nm for acetone, and 715 nm for dichloromethane (DCM). This shows the PDI compound synthesized has the potential for NIR imaging.

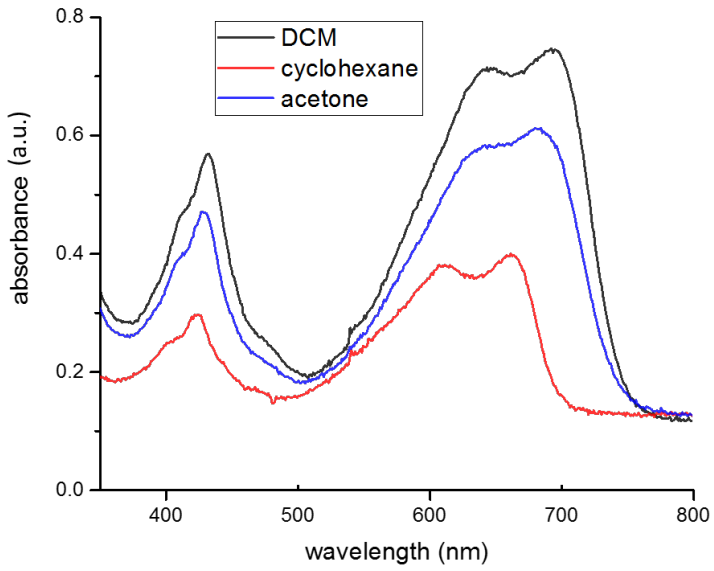

Figure 2-6. The UV-vis profiles of PDI solution in different solvents (acetone, cyclohexane, and dichloromethane (DCM)). The concentration is 0.05 mg/ml for all solutions.

2.3.2 Aqueous PDI nanoparticle suspensions

Aqueous PDI nanoparticles via nanoprecipitation

The PDI compound (always referring to compound 6 in this chapter) was hydrophobic and hence insoluble in water. Thus, despite its NIR absorbance, the PDI compound could not be used directly for bioimaging. Although some commercial dye particles have been directly used for photoacoustic imaging [12], due to the poor control of particle size, aqueous organic nanoparticles have often been used. The organic nanoparticles in water are either formed by self-assembly [13] or nanoprecipitation via solvent evaporation [14]. In this study, both the nanoprecipitation and the emulsion-freeze-drying method were used to produce PDI nanoparticles suspended in water. The latter method was developed in our group and has since been used for the preparation of poorly water-soluble drug nanoparticles [10].

For the nanoprecipitation preparation, 1 mg/ml PDI solution in acetone was added dropwise into aqueous PVA solution with a concentration of 1 wt % while stirring. These concentrations were selected based on previous studies [9, 14] with an aim to form stable nanoparticle suspensions with the higher ratio of PDI:stabilizer. After addition, the mixing solution was kept stirring at 500 rpm overnight to remove acetone. For the method to work, the organic solution must be miscible with the aqueous solution. Organic solutions from acetone, methanol, and tetrahydrofuran (THF) are usually employed. This study chose to use acetone because of the good solubility of PDI in acetone. During stirring and gradual evaporation of acetone, more PDI molecules are exposed to water and tend to aggregate. PVA then acts to stabilize the PDI nanoparticles and prevents aggregation. After the solvent evaporation process,

a clear dark green nanoparticle suspension was formed. A typical UV-Vis profile of the nanosuspension prepared by solvent evaporation is given in **Figure 2-7**. The absorbance peaks are clearly in the NIR region with a high wavelength peak around 700 nm, similar to the profile obtained from the PDI-acetone solution. Indeed, there is strong absorbance in the range of 640 – 700 nm.

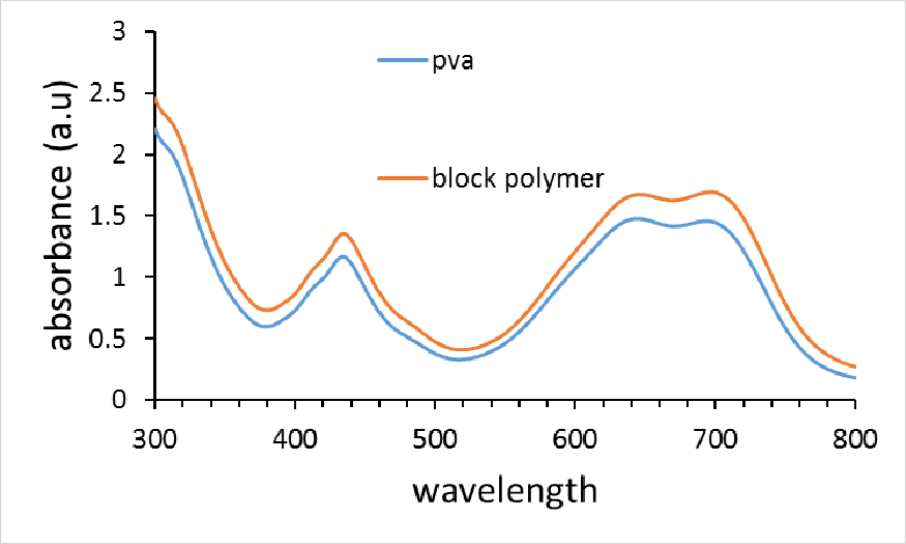

Figure 2-7. The UV-Vis profiles of aqueous PDI nanoparticle suspensions prepared by solvent evaporation using PVA and $DEAMA_{50}DEGDMA_2OEGMA_{80}$ as stabilizers. The concentration of the PDI was 0.17 mg/mL for all the suspensions.

The size of the PDI nanoparticles in the suspension with PVA stabilizer was determined by DLS analysis. **Figure 2-8a** shows the DLS graphs of the suspensions. A peak is seen around 100 nm with the particle sizes in the range of 50 – 200 nm. The zeta potential, depicting the charges on the surface of the nanoparticles, was measured to be 0 mV, as indicated by the peak position in **Figure 2-8b**.

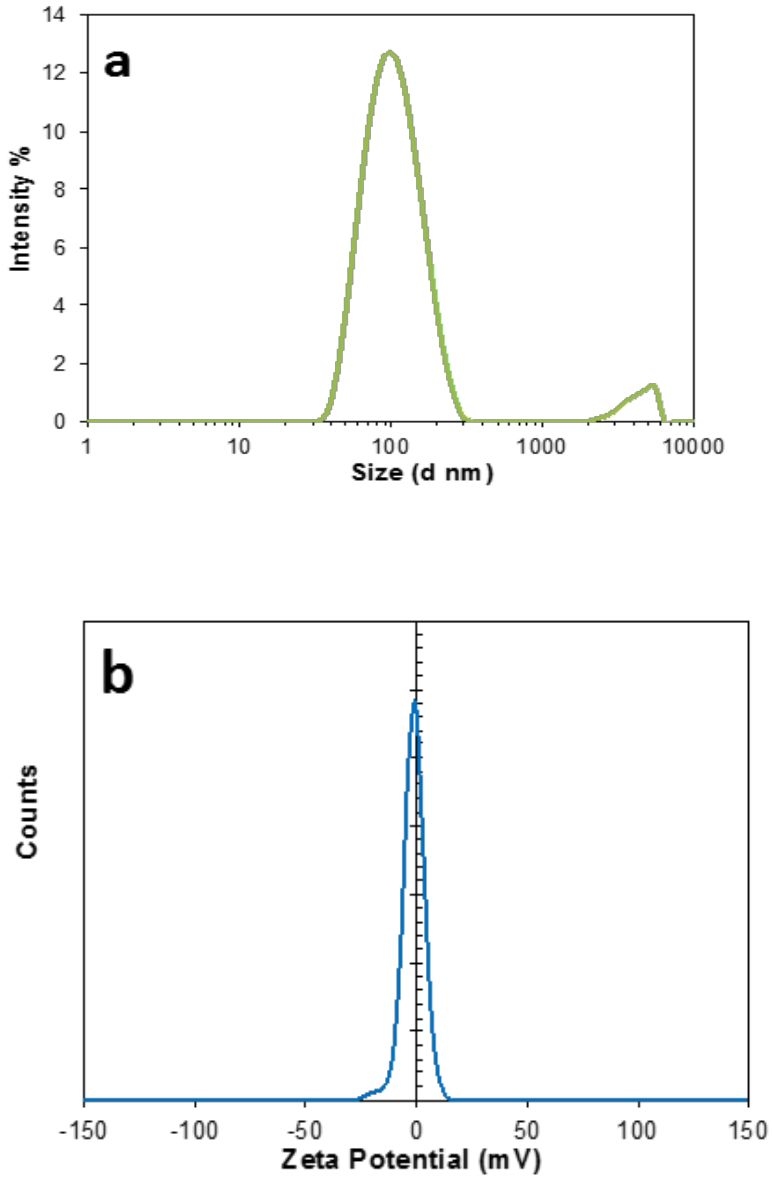

Figure 2-8. (a) The DLS graph of aqueous PDI nanosuspensions prepared by solvent evaporation with PVA as stabilizer; (b) the relevant zeta potential graph.

To compare the difference between PDI nanoparticles prepared using the nanoprecipitation and emulsion-freeze-drying methods, the nanoprecipitation experiments were also carried out by dropwise addition of PDI solution into aqueous TPEG (0.1 wt%) solution. Clear nanoparticle suspensions were produced. However,

the nanoparticles prepared in the presence of TPEG were found to be toxic to the MSCs. For this reason, a hyperbranched block copolymer

$DEAMA_{50}DEGDMA_2OEGMA_{80}$ was tried. This type of block copolymer has been used to stabilize hydrophobic drug nanoparticles and has not been found to be cytotoxic to cells [10]. **Figure 2-9** gives the structure of $DEAMA_{50}DEGDMA_2OEGMA_{80}$. The hydrophobic DEAMA core is surrounded by hydrophilic OEGMA arms. The block copolymer is pH-sensitive due to the protonation/deprotonation at the amine groups under different pHs. However, in this study, we only utilized its amphiphilic nature as stabilizer to form PDI nanoparticles. **Figure 2-7** gives the UV-vis profile of the PDI prepared with $DEAMA_{50}DEGDMA_2OEGMA_{80}$ as stabilizer at the mass ratio of 1:1. It has the same absorbance peaks as the PDI nanosuspension prepared with PVA as stabilizer.

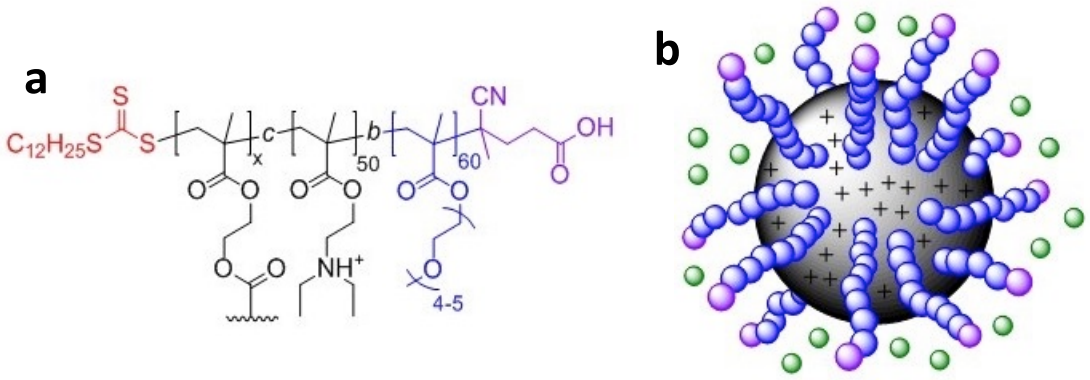

Figure 2-9. (a) The molecular structure of $DEAMA_{50}DEGDMA_2OEGMA_{80}$. (b) The schematic representation of the core-shell nanoparticle formed by the block copolymer $DEAMA_{50}DEGDMA_2OEGMA_{80}$.

The PDI particle sizes in the nanosuspensions were measured using DLS. As shown in **Figure 2-10a**, the particle sizes are very similar for the suspensions with

PDI:block copolymer ratios of 1:1 and 1:2, with the peak sizes at around 100 nm. The particle sizes are slightly smaller with the PDI:block copolymer ratio of 2:1. The size of $DEAMA_{50}DEGDMA_2OEGMA_{80}$ nanoparticles is around 50 – 60 nm. At lower pH (e.g., pH = 5), the nanoparticles are protonated and more hydrophilic. At neutral pH and high pH, the surface of the nanoparticles is deprotonated and the nanoparticle may become smaller. However, the hydrophobicity change may lead to particle aggregation so that the measured particle sizes are not small. **Figure 2-10b** shows there are no charges at the nanoparticle surface. This is because the nanosuspensions were prepared from neutral water.

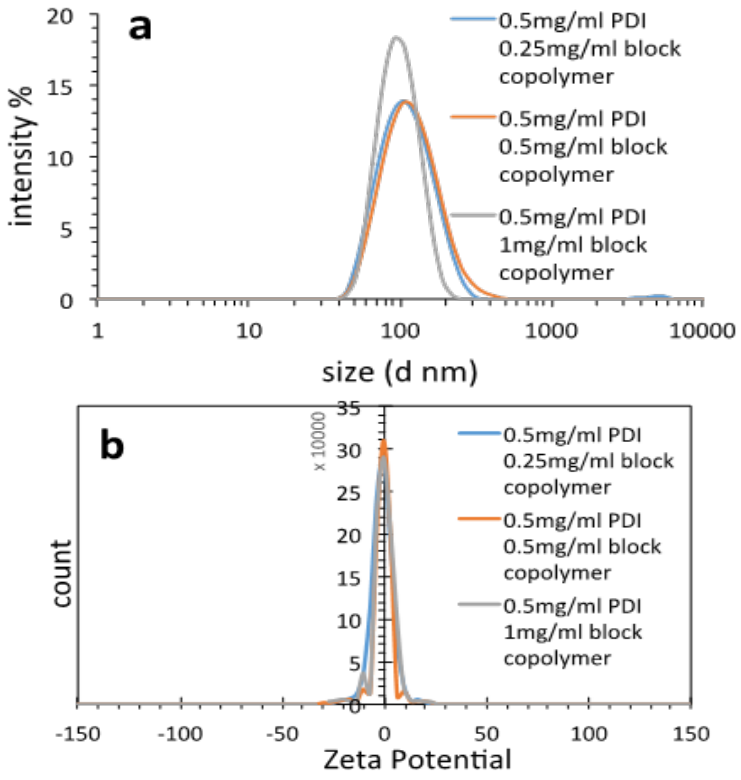

Figure 2-10. Characterization of aqueous PDI nanoparticle suspension prepared with different concentrations of block copolymer $DEAMA_{50}DEGDMA_2OEGMA_{80}$. (a) The

DLS graph shows the particle size distribution. (b) The zeta potential data measured for aqueous PDI nanosuspensions.

Aqueous PDI nanoparticles via emulsion-freeze-drying

The main advantage of the emulsion-freezing-drying is that a dry porous nanocomposite is prepared [9]. The organic nanoparticles are formed in situ within a porous material, presumably on the pore surface. Due to the highly interconnected porous structure, the porous nanocomposite can be dissolved in water and produce aqueous nanoparticle suspensions on demand [9]. An oil-in-water (O/W) emulsion, i.e., droplets of organic solution/solvent dispersed in the continuous aqueous water phase, is usually employed for this approach. Due to its miscibility with water, PDI-acetone solutions cannot be used for this preparation. A cyclohexane solution was therefore used to form the O/W emulsion. This is because cyclohexane is highly volatile and has a high melting point (~ 4°C), which facilitates the freeze-drying process. Cyclohexane is also known to have low residual toxicity [7]. However, cyclohexane is not an effective solvent to dissolve highly hydrophobic compounds. A saturated PDI solution (estimated to be 0.62 mg/mL from my experiment) was thus used to form the emulsion. PVA has been widely used as a surfactant or co-surfactant to stabilize emulsions or colloids, but PVA alone is usually difficult to form a stable emulsion. A conventional surfactant, for example, the anionic sodium dodecyl sulfate (SDS), is usually used together with PVA [9]. Because the intended application of the PDI nanoparticles is for in vitro and in vivo bio-imaging, it is essential to use a biocompatible and low toxic surfactant. TPEG has been selected as the surfactant in this study because it is a widely used surfactant for drug delivery [15].

As described in the Experimental section, the emulsion was frozen in liquid nitrogen and then freeze-dried to produce a dry blue monolith. **Figure 2-11A** shows a photo of a blue freeze-dried monolith in a glass vial. The pore structure of the monolith and the in-situ formed PDI nanoparticles were examined by SEM, as shown in **Figure 2-11 B-D** at different magnifications. The layered structure is formed from ice-templating whilst the cellular (near spherical) pores are templated from the emulsion droplets [16]. The uniform blue colour indicates the presence of PDI nanoparticles in the monolith. And the PDI nanoparticles can also be clearly observed within the monolith by SEM.

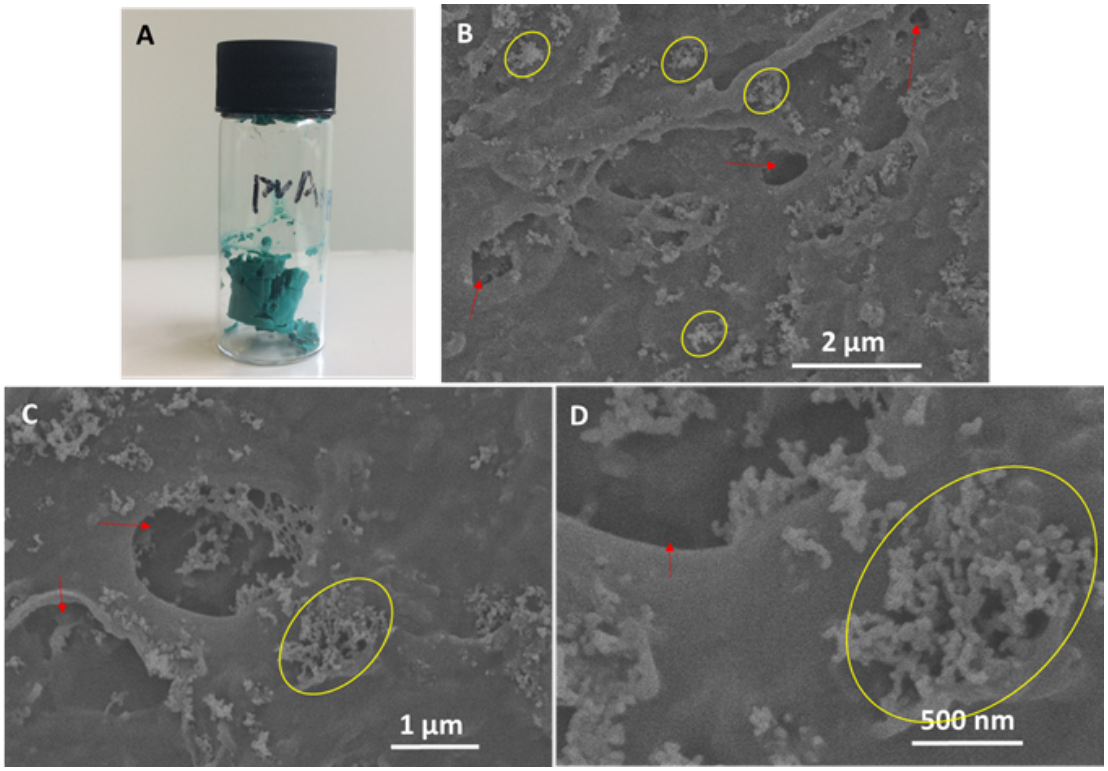

Figure 2-11 Photo (A) of freeze-dried PDI monolith and SEM images (B-D) of PDI nanoparticles with different magnification. Yellow circles indicate a lot of PDI nanoparticles together. Red arrows indicate the pore structures.

The dry porous PDI nanocomposites were stored in a desiccator before use. Upon dissolution in water, aqueous nanoparticle dispersions are instantly formed. Furthermore, the concentration of the PDI nanoparticles can be readily controlled by dissolving suitable amount of PDI nanocomposites in a certain amount of water while the ratio of PDI:stabilizer is unchanged.

The UV-vis profiles in **Figure 2-12** show the same absorbance peaks among the PDI nanosuspensions with different surfactants. It was noticed that the absorbance intensity of the PDI suspension with PVA as surfactant was much smaller than those containing TPEG as surfactant. PVA has been widely used as stabilizer but is not an efficient surfactant to form stable emulsions. The less stable emulsions can result in large droplets, translating into large PDI nanoparticles or aggregates. When filtered before the UV-vis analysis, larger PDI nanoparticles are filtered out, leading to lower concentrations and hence lower absorbance. The absorbance peaks of aqueous PDI nanosuspensions are similar to those of PDI solution in acetone. However, when comparing Figure 2-12, Figure 2-6, and Figure 2-7, the relative intensities of the absorbance peaks at 640 nm and 700 nm are changed – peak at 700 nm > peak at 640 nm for PDI-acetone solution, peak at 700 nm ≈ peak at 640 nm for aqueous PDI suspension from solvent evaporation, peak at 700 nm < peak at 640 nm for aqueous PDI suspension prepared by emulsion freeze-drying. Although the exact reason is not clear, this may be attributed to the difference of PDI status (molecules vs nanoparticles), the morphology/phase of PDI nanoparticles, and the types of stabilizer and surfactant.

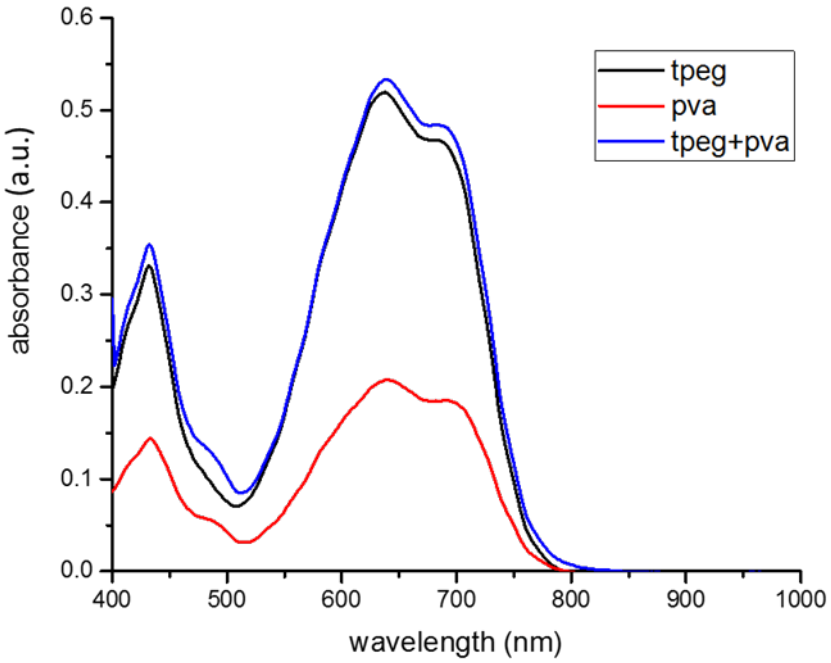

Figure 2-12. The UV-vis profiles of aqueous PDI nanoparticle by dissolving the freeze-dried materials in water, giving a raw concentration of 0.36 mg/mL PDI in the suspension. The suspensions were filtered before analysis using a 0.22 μm syringe filter.

The sizes of the PDI nanoparticles were measured by the DLS method. **Figure 2-13** shows the size distribution of the PDI nanoparticles based on scattering intensity. The PDI nanoparticles were in the region of 30 nm (based on peak size) when TPEG was used as the surfactant. Larger particles were produced when PVA was used as the only surfactant or used together with TPEG.

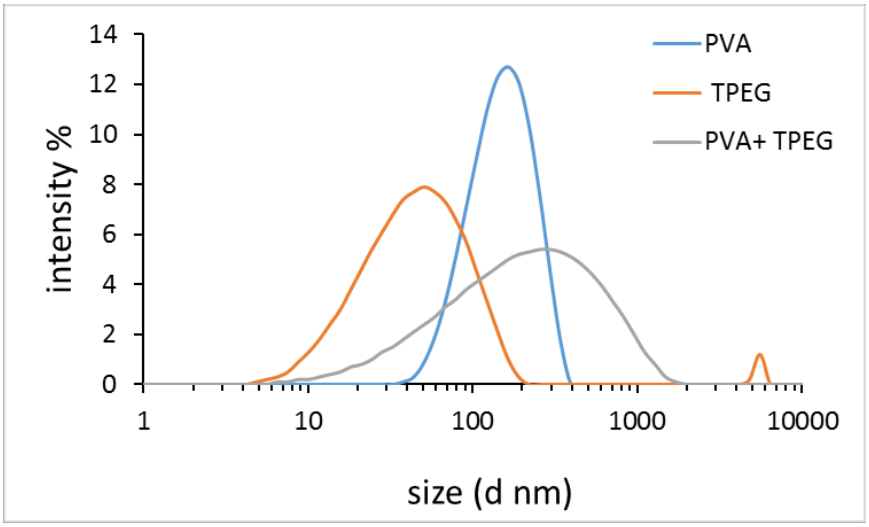

Figure 2-13. The DLS profiles of aqueous PDI nanoparticle by dissolving the freeze-dried materials in water, after filtering with a 0.22 μm syringe filter.

2.4. Conclusions

Starting from a commercially available and inexpensive perylene tetracarboxylic dianhydride, via a multiple-step synthesis, a perylene diimmide derivative (PDI) has been successfully synthesized. The PDI has been characterized by NMR and mainly evaluated by UV-vis to confirm the NIR absorbance. This PDI is hydrophobic and only soluble in organic solvents. In order to use PDI as probes for bioimaging, aqueous PDI nanoparticle suspensions have been produced by both nanoprecipitation and emulsion freeze-drying methods. PVA, TPEG, and the custom-synthesized block copolymer $DEAMA_{50}DEGDMA_{2}OEGMA_{80}$ have been used as stabilizers. Stable aqueous PDI nanoparticle suspensions were formed in all cases, with the NIR absorbance at 700 nm. This paves the way for using PDI nanoparticles as NIR probes for cell imaging.

2.5 References

[1] Würthner, F.; Saha-Möller, C.R.; Fimmel, B.; Oqi, S.; Leowanawat, P.; Schmidt, D. Perylene bisimide dye assemblies as archetype functional supramolecular materials. *Chem. Rev*. **2016**, 116, 962-1052.

[2] Sukul, P.K.; Datta, A.; Malik, S. Light harvesting and amplification of emission of donor perylene–acceptor perylene aggregates in aqueous medium. *Chem. Eur. J*. **2014**, 20, 3019-3022.

[3] Sengupta, S.; Dubey, R.K.; Hoek, R.W.M.; van Eeden, S.P.P.; Gunbas, D.D.; Grozema, F.C.; Sudhölter, E.J.R.; Jager, W.F. Synthesis of regioisomerically pure 1,7-dibromoperylene-3,4,9,10-tetracarboxylic acid derivatives. *J. Org. Chem*. **2014**, 79, 6655-6662.

[4] Chen, S.; Slattum, P.; Wang, C.; Zang, L. Self-assembly perylene imide molecules into 1D nanostructures. *Chem. Rev.* **2015**, 115, 11967-11998.

[5] Avlasevich, Y.; Li, C.; Müllen, K. Synthesis and applications of core-enlarged perylene dyes. J. *Mater. Chem*. **2010**, 20, 3814-3826.

[6] Liu, X.; Roberts, A.; Ahmed, A.; Wang, Z.; Zhang, H. Carbon nanofibers by pyrolysis of self-assembled perylene diimide derivative gels as supercapacitor electrode materials. *J. Mater. Chem. A* **2015**, 3, 15513-15522.

[7] Wais, U.; Jackson, A.W.; He, T.; Zhang, H. Nanoformulation and encapsulation approaches for poorly water-soluble drug nanoparticles. *Nanoscale* **2016**, 8, 1746-1749.

[8] Accomasso, L.; Gallina, C.; Turinetto, V.; Giachino, C. Stem cell tracking with nanoparticle for regenerative medicine purposes: an overview. *Stem Cells Int*. **2016**, article ID 7920358.

[9] Zhang, H.; Wang, D.; Butler, R.; Campbell, N.L.; Long, J.; Tan, B.; Duncalf, D.J.; Foster, A.J.; Hopkinson, A.; Taylor, D.; Angus, D.; Cooper, A.I.; Rannard, S.P.

Formation and enhanced biocidal activity of water-dispersable organic nanoparticles. *Nat. Nanotechnol.* **2008**, *3*, 506-511.

[10] Wais, U.; Jackson, A.W.; Zuo, Y.; Xiang, Y.; He, T.; Zhang, H. Drug nanoparticles by emulsion-freeze-drying via the employment of branched block copolymer nanoparticles. *J. Control. Release* **2016**, 222, 141 – 150.

[11] Fulmer, G.R.; Miller, A.J.M.; Sherden, N.H.; Gottlieb, H.E.; Nudelman, A.; Stoltz, B.M.; Bercaw, J.E.; Goldberg, K.I. NMR chemical shifts of trace impurities: common laboratory solvents, organics, and gases in deuterated solvents relevant to the organometallic chemist. *Organometallics* **2010**, 29, 2176–2179.

[12] Zhang, Y.S.; Cai, X.; Yao, J.; Xing, W.; Wang, L.V.; Xia, Y. Non-invasive and in situ characterization of the degradation of biomaterial scaffolds by volumetric photoacoustic microscopy. *Angew. Chem. Int. Ed*. **2014**, 53, 184-188.

[13] Zhang, Y.; Jeon, M.; Rich, L.J.; Hong, H.; Geng, J.; Zhang, Y.; Shi, S.; Barnhart, T.E.; Alexandridis, P.; Huizinga, J.D.; Seshadri, M.; Cai. W.; Kim, C.; Lovell, J.F. Non-invasive multimodal functional imaging of the intestine with frozen micellar naphthalocyanines. *Nat. Nanotechnol*. **2014**, 9, 631-638.

[14] Fan, Q.; Cheng, K.; Yang, Z.; Zhang, R.; Yang, M.; Hu, X.; Ma, X.; Bu, L.; Lu, X.; Xiong, X.; Huang, W.; Zhao, H.; Cheng, Z. Perylene-diimide-based nanoparticles as highly efficient photoacoustic agents for deep brain tumor imaging in living mice. *Adv. Mater*. **2015**, 27, 843-847.

[15] Guo, Y.; Luo, J.; Tan, S.; Otieno, B.O.; Zhang, Z. The applications of Vitamin E TPGS in drug delivery. *Eur. J. Pharm. Sci*, **2013**, 49, 175-186.

[16] Ahmed, A.; Clowes, R.; Myers, P.; Zhang, H. Hierarchically porous silica monoliths with tuneable morphology, porosity, and mechanical stability. *J. Mater. Chem*. **2011**, 21, 5753-5763.

Chapter 3 Perylene diimide derivative nanoparticles for MSOT imaging

3.1 Introduction

Bio-imaging in vivo may be divided into two categories: optical imaging methods and non-optical imaging methods [1]. A limitation of optical techniques is that light scattering and absorption by tissues means that there is signal attenuation with increasing depth, and spatial resolution is poor [1, 3]. However, there is an 'optical window' between the wavelengths of 650 nm and 1300 nm where the penetration depth can reach several centimetres [2, 3].

Photoacoustic imaging (PAI) is a non-invasive technique developed recently with high penetration depth and high spatial resolution achieved by ultrasound imaging [3, 4]. The basic principle of PAI is that the absorption of laser energy, either by endogenous photo-absorbers or exogenous photoacoustic probes and contrast agents, results in thermo-elastic expansion and the generation of a sound wave that can be picked up by an ultrasound detector [3, 4].

Multispectral optoacoustic tomography (MSOT) is a type of PAI that has the advantage of being multispectral, which means that information can be obtained at multiple wavelengths, thus improving the accuracy of the reconstructed images as a function of depth. Furthermore, due to the spectral differences of the photoacoustic probes (molecules or nanoparticles) from the background tissue, it is not always necessary to obtain baseline measurements [1]. However, in practice, a baseline measurement of the tissue or organ is usually performed before administering cell therapies.

PAI and MSOT have been intensively used for non-invasive biomedical imaging. However, in order to fully achieve imaging with high resolution and high penetration depth, the use of effective photoacoustic probes is essential. Various photoacoustic probes/contrast agents have been employed, which can be categorized into two main types: particles based on surface plasmon resonance (SPR) and dye-containing nanoparticles [5]. The SPR particles include noble metal nanoparticles and transition metal dichalcogenides [6]. Gold nanoparticles with different morphology are the most widely investigated metal nanoparticles [7], with some examples including Au nanovesicles [8] and Au nanoparticles [9, 10]. The NIR dye-containing nanoparticles including cyanine dyes [7]/MTT formazan [11] and light-sensitive semi-conducting polymers nanoparticles (SPNs) have been used [12]. Despite the use of such a variety of photoacoustic imaging both in vitro and in vivo [5-12], there have been uncertainty in toxicity (particularly for probes containing heavy metals), disadvantage of photobleaching and low emission intensity (e.g., currently used dyes), and difficulty in tuning absorption/emission wavelengths. There are continuously high demanding in developing less-toxic, photostable, high quantum yield, wavelength tuneable, and cost-effective probes for PAI.

The development and use of aromatic conjugated compounds may have the potential as photoacoustic probes, that can meet all the requirements in principle. Multiple aromatic conjugated organic compounds synthesized from naphthalene and more often perylene usually exhibit high hydrophobicity, fluorescence, high quantum yield and NIR absorbance [13-17]. The absorbance wavelengths can be tuned by the modification on the bay and peri-positions of the perylene-based compounds. The maximal absorption wavelengths are shifted bathochromically by about 100 nm per napththalene unit, exhibiting strong NIR absorbance [14]. Perylene diimide derivatives

can be synthesized with hydrophilic groups, which are soluble in basic solution. The basic solutions can form nanofibrous hydrogels, triggered by low pH [18-20]. Our group has prepared nanofibrous monoliths and microspheres from perylene diimide derivatives modified with 5-aminoisophthalic acid with the gelation triggered by the hydrolysis of glucone-δ-lactone, which ensured the formation of uniform hydrogels. These structures were then carbonized to produce porous carbon nanofiber structures [21,22]. For these hydrogels, the modifications were performed at the anhydride groups of perylene-based compounds. The absorbance of these compounds is not in the NIR region. However, by modifying the perylene compounds at the bay positions and peri positions with bulky group and/or alkane chains, not only could 1D nanostructures and organogels be formed from organic solutions, but also the light absorbance could be shifted into the NIR region [17,23,24].

Naphthalene- and perylene-based nanoparticles have been used for PAI [25-27]. A hydrophobic perylene diimide (PDI) derivative was prepared and aqueous PDI nanoparticle dispersions were then formed by a solvent evaporation (or nanoprecipitation) method, with strong absorbance at around 700 nm and high extinction coefficient of 2×10^8 M^{-1} cm^{-1} [27]. The PDI nanoparticles were demonstrated to be highly effective photoacoustic agents for deep brain tumour imaging in living mice [27].

As discussed above, PDIs have the potential to be a good candidate as effective probes for PAI and particularly MSOT. Drawing from our strong background in chemical synthesis and development of nanomaterials, the long-term target of the research is to develop PDI nanoprobes and hydrogels with wavelength-tuneable NIR absorbance. Such materials will then be evaluated for in vitro cytotoxicity and in vivo PAI/MSOT. The novelty lies in the development of NIR-active PDI materials but they have to show equivalent or improved imaging performance compared to currently

available PAI probes. Specifically in this work, we designed and synthesized a hydrophobic PDI which showed strong absorbance in the NIR region. Subsequently, the PDI nanoparticles in aqueous media were prepared by solvent evaporation or an emulsion-freeze-drying approach. The absorbance profiles of the PDI nanoparticles were confirmed (detailed in chapter 2). The focus of this chapter is to assess the effectiveness of these PDI nanoparticles for labelling mouse MSCs and enabling them to be tracked in vivo with MSOT.

Objectives:

1. Investigate the cytotoxicity effects of PDI nanoparticles on MSCs.
2. Optimise PDI nanoparticles for cell labelling, based on nanoparticle size, stabilizer type and nanoparticle concentrations.
3. Investigate the performance (fluorescence/NIR absorbance) of PDI nanoparticles and their localization after being up-taken by MSCs
4. Evaluate the effectiveness of PDI nanoparticles as MSOT imaging probes in vivo, based on long-term imaging intensity and quality.

3.2 Experimental Details

3.2.1 Chemicals and reagents

High glucose Dulbecco's Modified Eagle's Medium (DMEM) (containing pyruvate), L-glutamine, non-essential amino acid, mercapethanol, phosphate-buffered saline (PBS), trypsin/EDTA, cell freezing medium, Alizarin red-s, alcian blue solution (1% in 3% actic acid), penicillin-streptomycin, mitomycin-c, saponin were purchased from Sigma Aldrich. D-Luciferin and Cell Titer Glo ATP assay kit were purchased from Promega. Foetal bovine serum (FBS), secondary antibody chicken anti-rabbit Alexa 488

were purchased from Life Technologies. Lysosome associated membrane protein 2 (Lamp-2) rabbit anti-mouse antibody and early endosome antigen 1 (EEA 1) antibody (rabbit anti-mouse) were obtained from Abcam.

Note: The experimental details described below were used to complete the experimental work and produce the data that are discussed in the Results and Discussion section. Prior to this, a lot of screening work had been carried out in order to find out the suitable experimental conditions. The details of the screening work are not included in the chapter.

3.2.2 Cell line

The murine mesenchymal stem/stromal cell line MSC D1 (CRL-12424) was obtained from ATCC and transduced with lentiviral particles encoding firefly luciferase and ZsGreen or just ZsGreen under control of the constitutive promoter EF1a, by Dr Arthur Taylor (Murray and Poptani group, Centre for Preclinical Imaging, University of Liverpool) as previously described [28].

3.2.3 Cytotoxic evaluation of aqueous PDI nanoparticle suspensions

Mesenchymal stromal cells (MSCs) were seeded at a density of 200,000 cells/ml in the culture medium comprised of high glucose DMEM (Sigma, D6546), 10% FBS (Gibco, 10270), 2mM L-glutamine, 1% non-essential amino acids, 0.1mM 2-mercaptoethanol and 1% pen-strep. The cells were incubated at 37ºC in a humidified incubator with 5% CO_2. This standard MSCs culture method was used for all experiments. After 24 hours, the PDI nanoparticle suspension was added to the medium to achieve a PDI concentration range from 5 μg to 36 μg/ml. The MSCs were cultured

for a further 24 hours in the presence of the nanoparticle suspension, and were imaged live with phase contrast optical microscope using Leica DM IL inverted microscope coupled to a DFC420C camera. To assess cytotoxicity, an ATP assay (Cell Titer Glo kit, Promega) was used as follows.

MSCs were seeded at a density of 2 X 10^4 cells/well (96-well plate) in 200 µl MSC medium. 24 hours later, the medium was replaced with fresh medium containing PDI nanoparticles at the following concentrations: 0 µg/ml, 3 µg/ml, 6 µg/ml, 9 µg/ml, 12 µg/ml, 15 µg/ml, 20 µg/ml, 25 µg/ml, 30 µg/ml, 40 µg/ml. Controls consisted of wells that contained medium or medium with 40µg/ml PDI nanoparticles in the absence of cells. Samples were prepared in triplicate. Following 24h incubation, the medium was aspirated and after gentle washing with PBS, 100 µl complete medium and 20 µl ATP solution were added to each well. The plate was shaken at 600- 700 RPM for 1 minute, incubated at room temperature for 5 minutes, and then transferred to a plate reader (Fluostar Omega, BMG Labtech) to record the luminescence. The results are expressed as a fraction relative to the 0 µg/ml PDI containing medium samples which is expressed as 100 %.

To assess the effect of the PDI nanoparticles on MSC proliferation, cells were seeded at a density of 2 X 10^5 cells/well (6-well plate) in 1mL MSC culture medium. After the cells had attached, PDI nanoparticle suspension (prepared with hyper-branched block copolymer as stabiliser) was added at the concentration range 0-25 µg/ml. At the following time points, cells were removed from the wells and counted using an automated cell counter (TC10, Biorad): 24 h, 48 h and 72 h.

3.2.4 Intercellular location and fate of PDI nanoparticles

MSCs (expressing ZsGreen) were seeded in 8-well chamber slides (Ibidi) at a density of 2000 cells/well in a volume of 300µl MSC medium. PDI nanoparticle suspension (prepared with freeze drying method) were then added at a concentration of 360 µg/ml in a volume of 30µl and the MSCs were incubated for a further 24 h. Cells were imaged with a confocal microscope (3i spinning disc confocal microscope, CXU-X1, Intelligent-imaging). 405 nm, 488 nm, 640nm wavelength diode lasers were used and cells were images using a 63 x oil objective. Cells were either imaged live, or for immunostaining experiments, were first fixed for 5 min in 4% paraformaldehyde at room temperature. The data were acquired with Slidebook 6 software and analysed with Image J.

3.2.5 Mitomycin-C treatment

ZsGreen-expressing mouse MSCs were plated in Ibidi chamber slides at a density of 5000 cells/well and cultured in MSC medium supplemented with 15 µg/ml PDI nanoparticles (sample prepared with hyperbranched block copolymer as stabiliser). After 24 hours, the medium was replaced with mitomycin-c (Sigma, M4287) -containing medium at a concentration of 20µg/ml. Following 4 hours incubation, the cells were washed X3 with PBS, and were then incubated in MSC medium. Cells were analysed using a confocal microscope (details above).

3.2.6 Flow cytometry

ZsGreen-expressing MSCs were labelled with PDI nanoparticles by adding the nanoparticles at a concentration of 15ug/ml to the culture medium. After 24 h, the culture medium was replaced with fresh MSC medium. Cells were then analysed with flow cytometry.

A single cell suspension in 1×PBS (1×10^6 cells/mL) was prepared by dissociation with 1×trypsin/EDTA. Then the cells were washed with PBS X3 and fixed with 4% PFA followed by washing with PBS X2. Prior to the analysis, the cell suspension was filtered using a 40 μm strainer (BD Falcon, 352340) and cells were examined using a BD FACSCalibur (BD Biosciences) flow cytometer according to manufacturer's instructions. A 635 nm red diode laser was used for excitation and 670 nm long pass (LP) filter to detect the PDI signal. Data were acquired by the BD CellQuest (BD Biosciences) software based on 10^4 events and analysed using the Cyflogic (CyFlo Ltd) software.

3.2.7 Preparation of phantoms

4% agar phantoms were prepared by dissolving 4 g agar in 100 ml water and heating in a microwave. The molten agar was then poured into 30 ml tubes and two straws were placed in the agar, secured by inserting them into the lid tightly. The gel was refrigerated overnight to allow it to set. To prepare phantoms containing PDI nanoparticles, a suspension of the PDI nanoparticles at different concentrations was injected into the channels (created by the straws). PBS was injected into one channel to serve as a control and the phantom was imaged using MSOT (see below).

To prepare phantoms containing PDI nanoparticle-labelled MSCs, 10^5 cells expressing ZsGreen and luciferase were suspended in 150 μl PBS and injected into one of the channels. As a control, a suspension of unlabelled MSCs was injected in a channel and then imaged with MSOT (see below).

3.2.8 Experimental animals

All the working involving animals was performed by Dr Jack Sharkey. The immune-compromised nude CD1 mouse strain (purchased from Charles River, UK) was used to facilitate imaging. 6-8 week-old female mice were used. The mice had free access to water and food with 12 hours light/12 hours dark. The mice were habituated for 1 week prior to being prepared for imaging. All animal experiments were performed under a licence granted under the Animals (Scientific Procedures) Act 1986 and were approved by the University of Liverpool ethics committee. Mice were culled when their overall tumour burden exceeded 2 cm diameter.

MSCs expressing ZsGreen and luciferase were labelled with 15 μg/ml PDI nanoparticles for 24 hours. 1 X 10^6 cells were then suspended in 150 μl PBS. The mice was anaesthetised with isoflurane (flow rate 1 litre/min) and the cells were then injected subcutaneously into the back of the mouse at discrete locations. Then the mouse was imaged with MSOT under anaesthesia for about 30 minutes, followed by imaging using the IVIS Spectrum (for bioluminescence and fluorescence measurements) for about 5 minutes under the same anaesthetic session. The mouse was imaged three times (day 1, day 7, day 11) by MSOT and IVIS Spectrum and each time, imaging with both instruments was performed under the same anaesthetic session. On day 11 after the final imaging session, the mice was culled according to home office guidelines (schedule 1).

3.2.9 MSOT Imaging

The photoacoustic instrument used was an MSOT inVision 256-TF small animal imaging system (iThera Medical GmbH, Munich, Germany). For imaging PDI nanoparticle suspensions and cell suspensions, the scans were performed with phantoms wrapped in film and submerged in the MSOT water tank. 9 wavelengths ranging from 660 nm to 900 nm were chosen for PDI nanoparticle suspension scans. For cell

suspension scans, 26 wavelengths were chosen and 12 positions with 2 mm steps were performed. While under anaesthesia with isoflurane, mice were wrapped in film and submerged in the MSOT water tank. The water temperature was maintained at 34ºC. Whole body scans were performed with 0.5-1 mm steps. 26 wavelengths were used for acquisition: range from 660 nm to 900nm. All the data were acquired with viewMSOT. Linear-mode-based reconstruction and linear regression multispectral processing were applied using viewMSOT software (iThera Medical GmbH).

3.2.10 Fluorescence and bioluminescence imaging

Fluorescence and bioluminescence were acquired using an IVIS Spectrum system (Perkin Elmer, Seer Green, UK). While under anaesthesia (isoflurane) the mouse was placed in the IVIS imaging chamber. For fluorescence, mice were exposed to 710 nm wavelength laser light (760 nm emission) and the acquired data analysed with IVIS live imaging software. For bioluminescence, 150 µl D-Luciferin solution was injected into the peritoneal cavity, and after about 13 minutes, IVIS bioluminescence imaging was undertaken to detect the Luciferase+ cells. All data were analysed with Living Image (Perkin Elmer) and displayed in radiance for bioluminescence and radiance efficiency for fluorescence.

3.2.11 Histology

Following animal sacrifice (day 11), the MSC masses which were visible with the naked eye, were surgically removed from the animals and fixed in 4% paraformaldehyde (PFA) for 24 hours at 4°C, then washed with PBS twice, and soaked overnight in 30% sucrose at 4°C. Then the tissues were cryo-embedded in OCT (Thermo Fisher Scientific, 6769006) with dry ice and isopropanol, and stored at -80°C. Frozen

sections were prepared by cutting at 7 um thickness using a cryostat. Sections were stored at -20 °C.

Alcian blue staining: Frozen sections were soaked in PBS for 3 minutes, then stained with alcian blue solution (1% in 3% acetic acid) for 5 minutes, then washed with PBS. The cells were imaged under bright field using Leica DM IL inverted microscope coupled to a DFC420C camera.

Alizarin red staining: After soaking in PBS for 3 minutes, frozen sections were stained with alizarin red-s solution (prepared fresh by dissolving 2g Alizarin red in 100 ml distilled water, and adjusting the pH to 4.1-4.3 with 10% ammonium hydroxide). Cells were imaged under bright field (details above).

3.3 Results and discussion

3.3.1 Cytotoxicity evaluation of the PDI nanoparticles

The cytotoxicity of the PDI nanoparticles was evaluated by assessing their effect on MSC viability. This was carried out by adding PDI nanoparticles into the culture medium at a range of concentrations (5 – 36 μg/mL). **Figure 3-1** shows the representative optical images of MSCs after culturing for 24 h. For the PDI nanosuspensions containing TPEG as stabilizer (**Figure 3-1a and c**), the cells rounded up and detached from the substrate, suggesting that this nanosuspension had a toxic effect. However, for the PDI nanoparticle suspension containing only PVA as stabilizer, the cells remained attached to the substrate and appeared healthy, similarly to controls (**Figure 3-1d**). This was observed for the whole range of PDI concentrations tested in this study. This experiment shows that the presence of TPEG in the PDI suspensions is toxic, while PVA does not appear to be toxic at the concentration range used. The PDI nanosuspensions containing TPEG were thus not evaluated further.

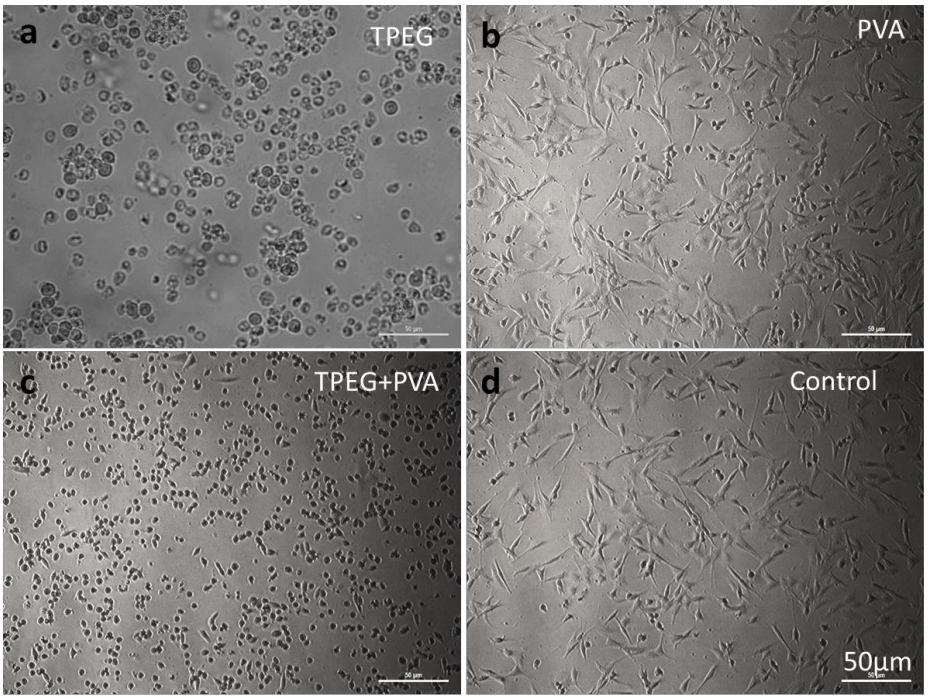

Figure 3-1. Representative optical images of MSCs cultured with medium containing PDI nanoparticles for 24 hours. The PDI nanoparticles were prepared by emulsion freeze-drying with different surfactants (a) TPEG, (b) PVA, and (c) TPEG + PVA. (d) Shows the result with PDI-free medium. All the images have the same magnification.

To further confirm that PDI nanoparticles prepared with PVA as stabilizer were not toxic, an ATP assay was performed to determine cell viability over a concentration range. As shown in **Figure 3-2**, the cell viability for PDI concentrations up to 50 μg/mL was not significant different from control cells where no PDI nanoparticles were added.

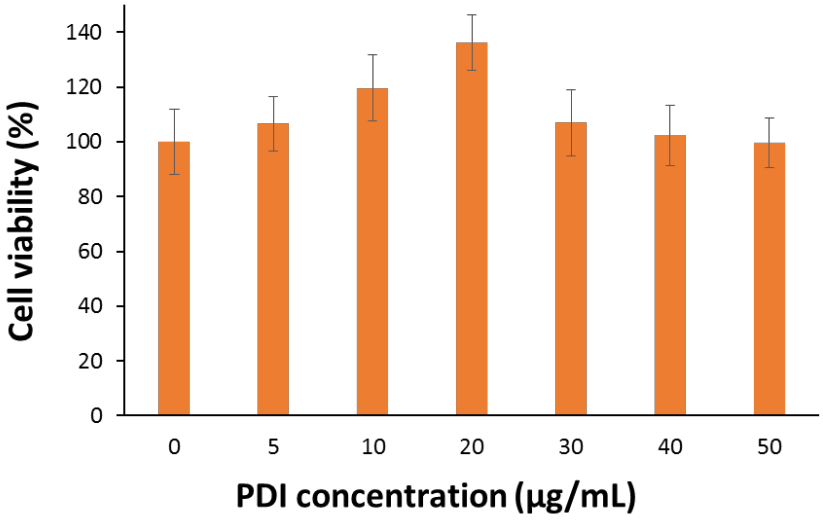

Figure 3-2. The effect of PDI nanoparticles prepared using PVA as stabilizer on MSC viability. Cells were cultured with PDI-containing medium for 24 h and analysed using an ATP assay. Error bars show standard division (SD) of three technical replicates.

However, although the PDI nanoparticles stabilized by PVA were not toxic, the signal intensity of labelled MSCs suspension by UV-vis analysis was too weak (see detail below). Therefore, the block copolymer $DEAMA_{50}DEGDMA_2OEGMA_{80}$ was used as stabiliser. **Figure 3-3** shows the effect of PDI concentrations (PDI: $DEAMA_{50}DEGDMA_2OEGMA_{80}$ = 1:1 w/w) on MSC viability. 100% cell viability was shown for PDI concentration up to 25 µg/mL. When the PDI concentration was higher, the cell viability deteriorated rapidly. Because higher PDI concentrations with PVA as stabilizer were not found to be cytotoxic, the low cell viability of PDI nanosuspensions with concentrations > 25 µg/mL is attributed to the presence of $DEAMA_{50}DEGDMA_2OEGMA_{80}$. Therefore, concentrations below 25 µg/mL were used in further studies as this was the highest concentration that could be used without any cytotoxic effects.

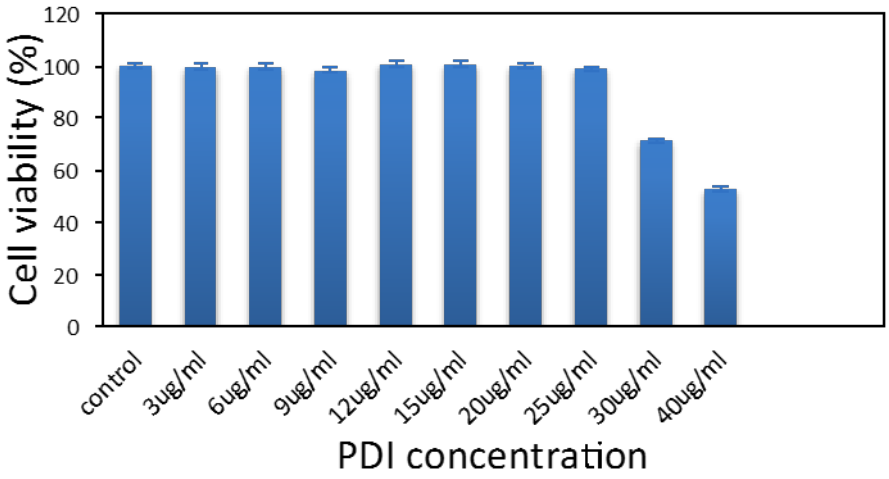

Figure 3-3. The effect of PDI nanoparticles prepared using block copolymer $DEAMA_{50}DEGDMA_2OEGMA_{80}$ as stabilizer on MSC viability. Cells were cultured in PDI-containing medium for 24 h and analysed using an ATP assay. Error bars show SD of three technical replicates.

To determine if the PDI nanoparticles (withblock copolymer as stabiliser) affected the proliferation rate of the MSCs, MSCs were cultured in the presence of PDI nanoparticles in the concentration range 3-25 µg /mL for 72 h, with cell numbers being counted at 24 h, 48 h and 72 h. Even at the highest concentration used, the degree of proliferation was not significantly different than the controls (**Figure 3-4**).

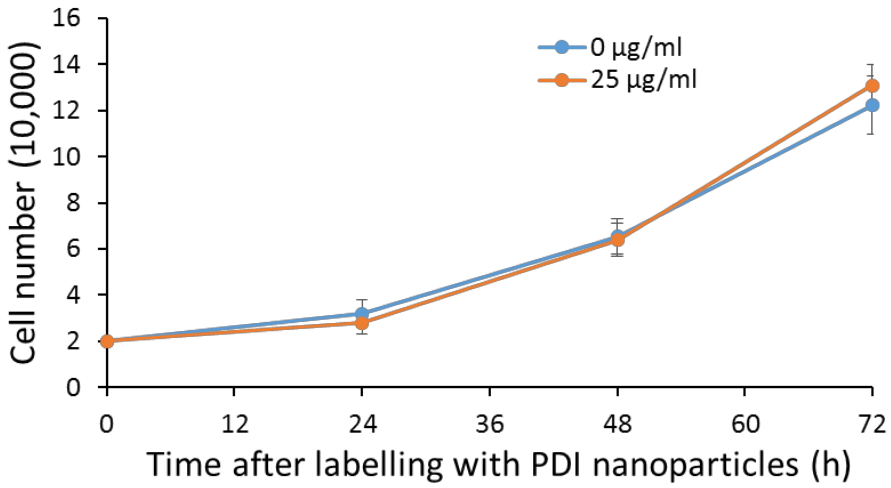

Figure 3-4. Proliferation of MSCs cultured in the presence of 25 µg/mL PDI nanoparticles with the ratio of PDI: block copolymer at 1:1 w/w. Error bars are standard deviation (SD) of three technical replicates.

3.3.2 Optimising PDI nanoparticles for cell labelling

After obtaining evidence that the PDI nanoparticles were not toxic to the MSCs, the study then moved on to investigate and optimise the use of PDI-labelled cells for MSOT imaging. MSCs were labelled with PDI nanoparticles for 24 hours and the labelled cell suspensions were analysed with UV-Vis. **Figure 3-5a** shows when PVA was used as a stabiliser, no signals by UV-vis could be detected even at the highest concentration of PDI particles used, despite the fact that with the naked eye, it was observed that the centrifuged cell pellets were pale green. This may be attributed to the low uptake of PDI nanoparticles by the MSCs. When using the PDI nanoparticles with the block copolymer as stabilizer, high intensity signals could be readily detected in the cells by the UV-vis spectroscopy after 24 hours labelling (**Figure 3-5b).** Based on this finding, PDI nanoparticles prepared with the block copolymer as stabiliser were used for further in vivo experiments.

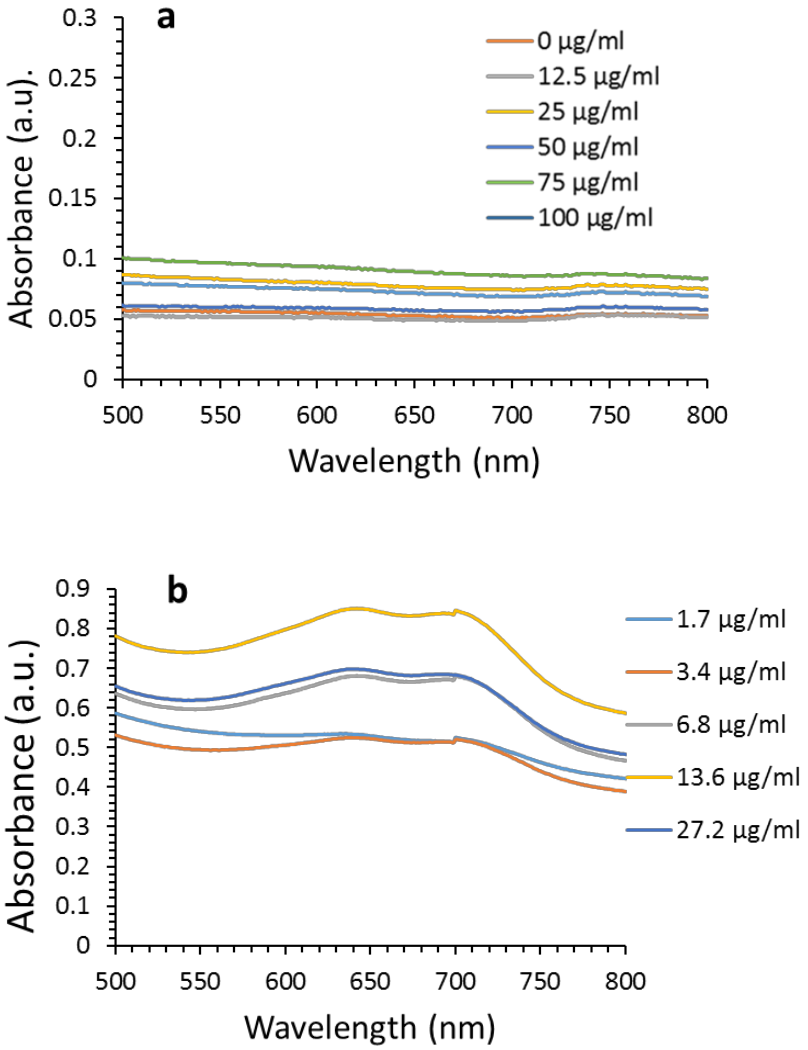

Figure 3-5. The UV-vis profiles of the MSC cell suspensions in PBS after culturing with PDI nanoparticles 24 hours at different concentrations with different stabilisers: **a**) PVA as stabiliser, **b**) the block copolymer as stabilizer.

Before carrying out the in vivo MSOT imaging, a study to find out the optimal PDI concentration (low toxicity high signal intensity) was performed by flow cytometry. The PDI concentrations in the range of 1.7 – 27.2 µg/ml were investigated. **Figure 3-6** shows that intensity increases with increasing PDI nanoparticle concentration up to 13.6 µg/ml. Further increases in PDI concentration (up to 27.2 µg/ml) did not lead to further

increases in intensity, suggesting that the PDI concentration was saturated beyond this point. This suggests that the uptake of PDI nanoparticles is optimal at 13.6 µg/ml, i.e., the highest uptake per unit cell. This concentration should result in higher MSOT signals as well because of the high uptake in the MSCs. For convenience, the medium with PDI nanoparticles at a concentration of 15 µg/ml was used for all MSOT imaging below.

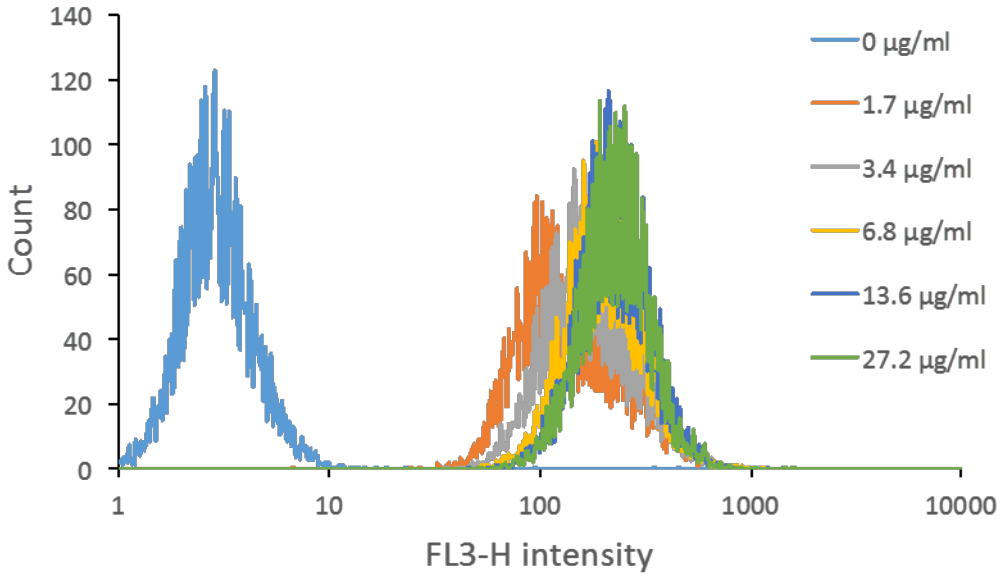

Figure 3-6. The effect of PDI concentrations on the intensity of the PDI-labelled MSCs as measured by flow cytometry. MSCs were cultured in medium containing PDI nanoparticles (with the block copolymer as stabilizer) at the defined conditions.

3.3.3 The fate of PDI nanoparticles after uptake by MSCs

What happens to the PDI nanoparticle after being taken up by the MSCs is an interesting and important question. Do the PDI nanoparticles remain inside the MSCs or are they exocytosed into the medium? In the latter case, the result would be decreasing signal intensity in the cells due to there being fewer PDI nanoparticles. This would mean that the particles would not be useful for cell tracking in vivo, because in addition to the

reduced signal intensity, there could be problems with false positive results if the particles were taken up by host cells.

To investigate if there was any evidence of exocytosis, MSCs labelled with PDI nanoparticles were co-cultured with unlabelled MSCs to see if any of the PDI particles were taken up by the unlabelled cells. To prevent the load of PDI nanoparticles per cell from being diluted due to cell division, the labelled cells were treated with mitomycin-c. The results show that PDI nanoparticles are not transport out of the MSCs and instead, remain inside the MSCs after uptake (**Figure 3-7**).

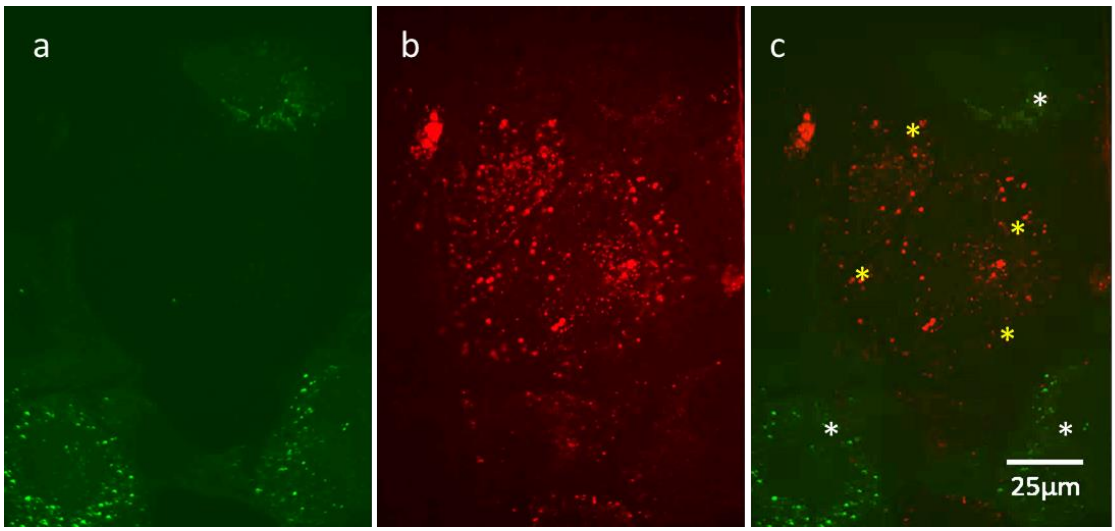

Figure 3-7. Confocal images showing MSCs after co-culturing PDI-containing MSCs (mitomycin-c treated) and ZsGreen+ MSCs in PDI-free medium for 5 days. The PDI nanoparticles were prepared with block copolymer as stabilizer. (**a**: ZsGreen, **b**: PDI, **c**: compsite of **a** and **b**), the yellow stars are PDI labelled cells, the white stars are ZsGreen+ cells.

After culturing the MSCs with PDI-containing medium for 24 h and then treating with Mitomycin-c, the non-proliferating MSCs were cultured in PDI-free medium for up

to 14 days. The fluorescence of the PDI nanoparticles inside the MSCs was monitored and measured by flow cytometry with the excitation wavelength of 635 nm. If the PDI nanoparticles were exocytosed this would result in a decrease in fluorescence intensity. **Figure 3-8** shows no change of intensity after culturing for 14 days. This further confirms that the PDI nanoparticles are retained inside the MSCs after uptake.

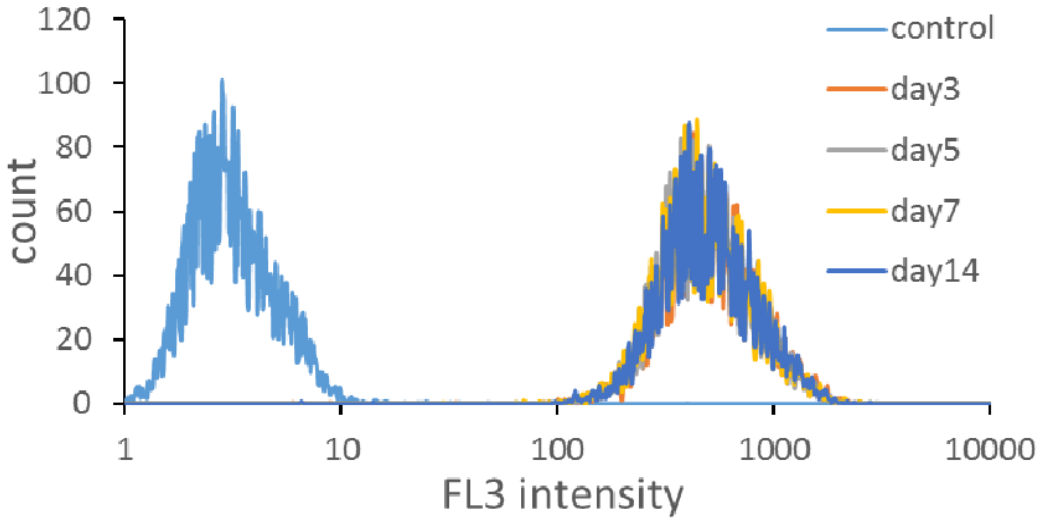

Figure 3-8. Flow cytometry analysis shows the intensity change of mitomycin C-treated non-proliferating PDI-containing MSCs cultured in PDI-free medium for 14 days with the control being non-labelled MSCs. The PDI nanoparticles were prepared with block copolymer as stabilizer

Instead of treating the labelled MSCs with mitomycin-C to stop them from proliferating, following a 24 h labelling period, MSCs were then cultured in fresh medium without PDI nanoparticles for 1 day and 3 days. The fluorescent intensity of the MSCs was measured by flow cytometry and the data are shown in **Figure 3-9**. The mean intensities of MSCs are 208 immediately after labelling, compared with 159 and 23 on the 1st and 3rd day following growth in nanoparticle-free medium. It is clear that

following culture in PDI-free medium, due to the proliferation of the MSCs, the density of PDI nanoparticles per cell decreases. This is evidenced by the decreasing intensity after culturing the PDI-containing MSCs in fresh medium for 1 day and 3 days. As expected, a very low intensity is observed for the non-labelled control sample. By comparing the results in in Figure 3-9 and Figure 3-8, it can be confirmed that the decrease of intensity in Figure 3-9 is because of the cell proliferation rather than the loss of PDI nanoparticles from the cells into the culture medium.

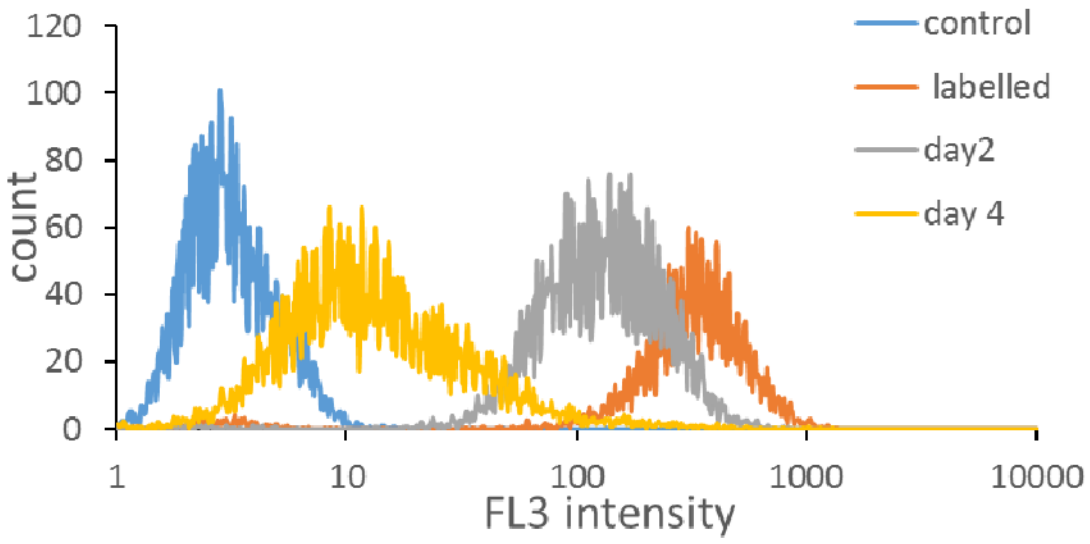

Figure 3-9. Flow cytometry analysis shows the signal intensity of the MSCs cultured in PDI-containing medium for 1 day (the 'labelled' sample), then in a fresh PDI-free medium for a further 24 h (sample 'day 2') or 72 h (sample 'day 4'), with the control being non-labelled MSCs. The PDI nanoparticles were prepared with block copolymer as stabilizer.

3.3.4. Evaluation of PDI nanoparticles as MSOT imaging probes in vivo

MSOT imaging of MSCs labelled with PDI nanoparticles

Before evaluating the potential of PDI nanoparticles as MSOT imaging probes for in vivo cell tracking, PDI-labelled MSCs were first imaged in a phantom with MSOT to compare with unlabelled MSCs.

MSC suspensions were injected into channels within an agar phantom for MSOT imaging. **Figure 3-10** show the multispectral processed images comparing the difference between PDI-labelled MSCs and non-labelled MSCs (1 X 10^5 cells in 150 µl PBS each sample). While the red image shows clearly the PDI-labelled MSCs, the non-labelled cells cannot be detected.

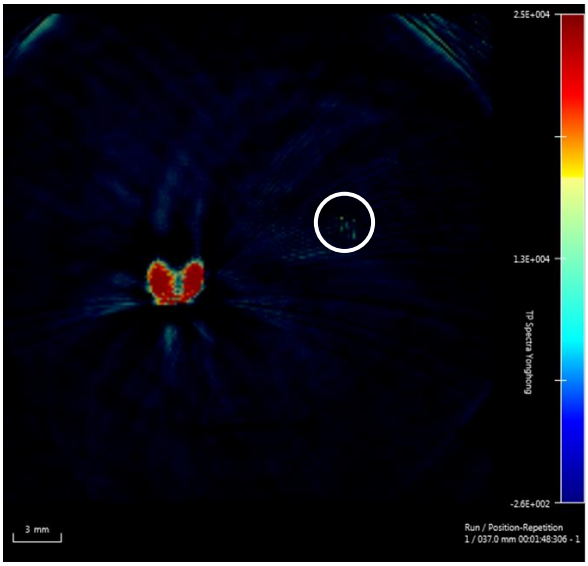

Figure 3-10. MSOT imaging of the MSCs in the phantom: PDI-labelled MSCs (left, red spot) and non-labelled MSCs (right, white circle).

In vivo imaging of PDI-labelled cells injected into mice

PDI-labelled MSCs expressing luciferase and ZsGreen were injected subcutaneously into a mouse with the unlabelled MSCs (expressing the same genetic reporters) serving as reference. Either 1 x 10^6 unlabelled MSCs, or 1 x 10^6, 0.5 x 10^6 or 0.25 x 10^6 labelled MSCs were injected at one of four locations on the dorsal aspect (back) of the mouse. Two mice were used for duplicate experiments and the data from one representative mouse is shown in this chapter.

After injecting with the MSCs, the mouse was imaged by MSOT. An initial quick preview scan was performed to locate the approximate position of the injected MSC spots. The mouse was then scanned slice by slice from shoulder to bottom. The data were acquired and analysed with MSOTview software, and images were obtained after multispectral processing accordingly and are shown in **Figure 3-11**. The series of images are arranged from left to right, then continue on to the 2nd row, and then from left to right again. Each of the images may be located by the coordinate of row number and column number. From Figure 3-11, when the scan is moved from top to bottom, the MSC spots are not seen first, but at location (1, 3), a bright spot starts to appear, which is represents the 1 x 10^6 PDI-labelled MSCs injected at the top right position of the mouse. With the scans moving down, the PDI-labelled MSC spot become brighter (indicated by the red circles in the image of (1, 4) to (1, 9). As expected, the un-labelled MSCs cannot be detected (the position indicated by the white arrow).

With the scanner moving further down past the top right MSC spot, no bright spots are observed (images of (2, 5) to (4, 1)). At the location (4, 2), the bright spots for the bottom positions of injected PDI-labelled MSCs start to appear. In the image of (4, 3) to (4, 7) the two bright spots (indicated by the yellow circles for 0.5 x 10^6 cells and green circles for 0.25 x 10^6 cells) are for the bottom left and bottom right positions of

injected PDI-labelled MSCs. Because the two bottom spots are not on the same level, the bright spot for the bottom left position is fading with the scan moving down, whilst the spot for the bottom right position gradually comes into view. When the scanner moves past the injected PDI-labelled MSCs, no bright spots can be seen any more. The higher number of PDI-labelled MSCs results in a more intense spot. However, the lowest number of PDI-labelled MSCs (0.25×10^6) can also be detected. **Figure 3-12** are three enlarged images from Figure 3-11 showing the three different injected cell spots at their brightest slice respectively. The same scans were performed after 7 days and 11 days of injecting the labelled MSCs. A similar quality of MSOT images were obtained and day 11 images are shown in **Figure 3-13** for the whole scan, and **Figure 3-14** shows three larger images for the three different injected cells spots at their brightest positions respectively. 3D images (**Figure 3-15)** were created with the software and three cross-sections are shown for each imaging time points: day 1, day 7 and day 11. The three injected PDI labelled- cell masses in the 3D views were found at the expected locations in the mouse, with the highest number of injected cells giving the most intense signal with MSOT throughout the imaging period from day 1 to day 11. All of the MSOT images were analysed with the same colour scale bars. These results show the potential of the PDI nanoparticles as photoacoustic probes for long-term cell tracking.

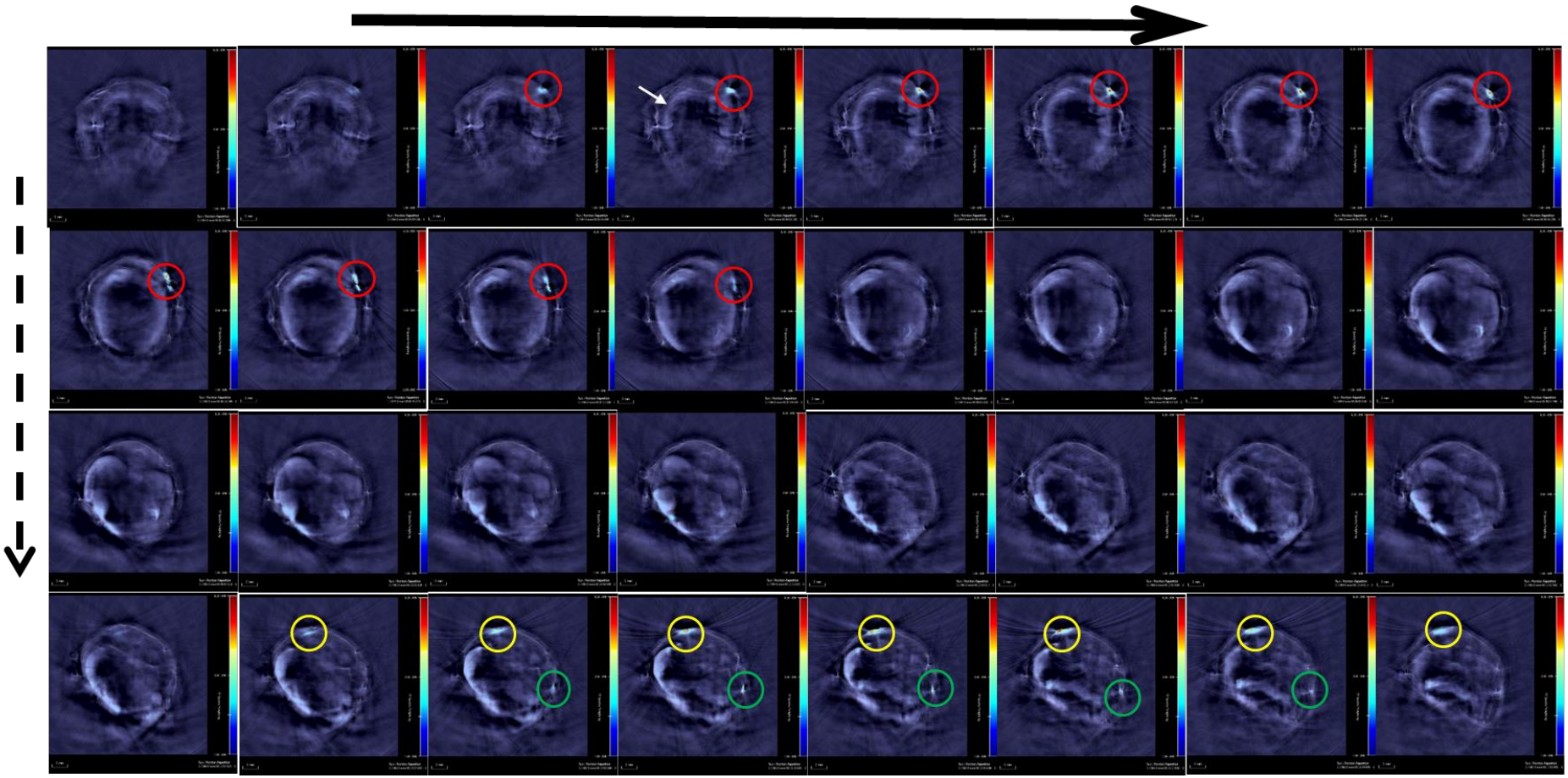

Figure 3-11. Day 1 MSOT imaging of the mouse just after injection with non-labelled MSCs and PDI-labelled MSCs. The white arrow indicates the position where 1 x 10^6 non-labelled MSCs were injected while the circles for the PDI-labelled MSCs are as follows: red: 1 x 10^6 cells, yellow: 0.5 x 10^6 cells, green: 0.25 x 10^6 cells.

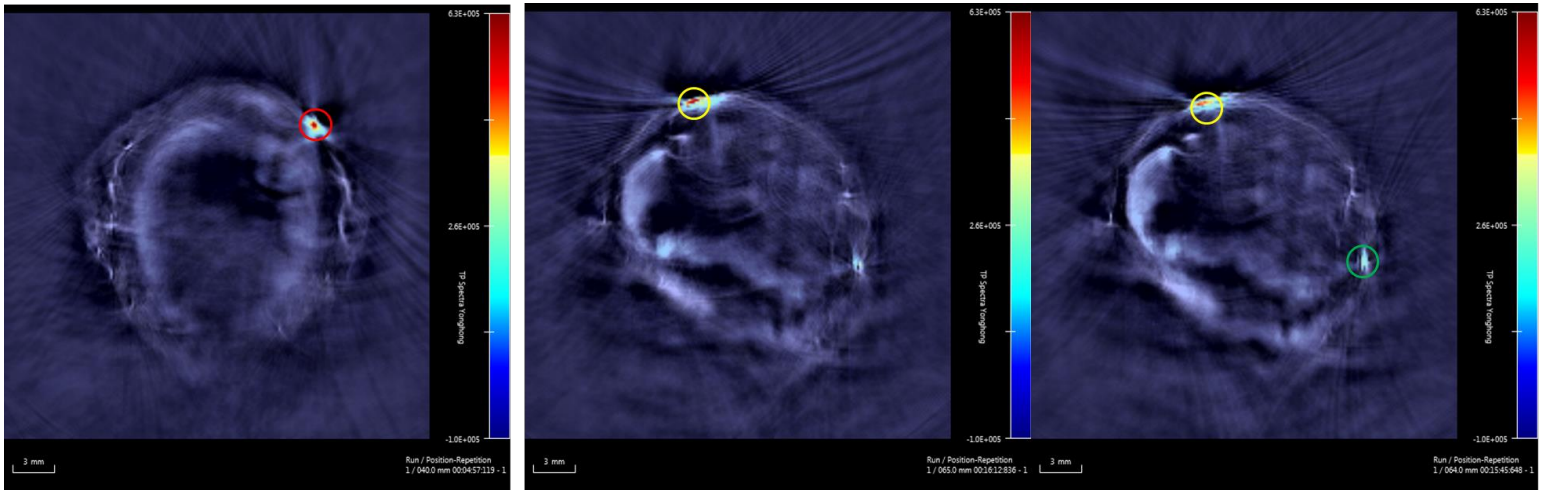

Figure 3-12. Enlarged MSOT images for day 1, red circle, indicate 1 x 10^6 PDI labelled cells, yellow circle indicates 0.5 x 10^6 PDI labelled cells and green circle indicates 0.25 x 10^6 PDI labelled cells.

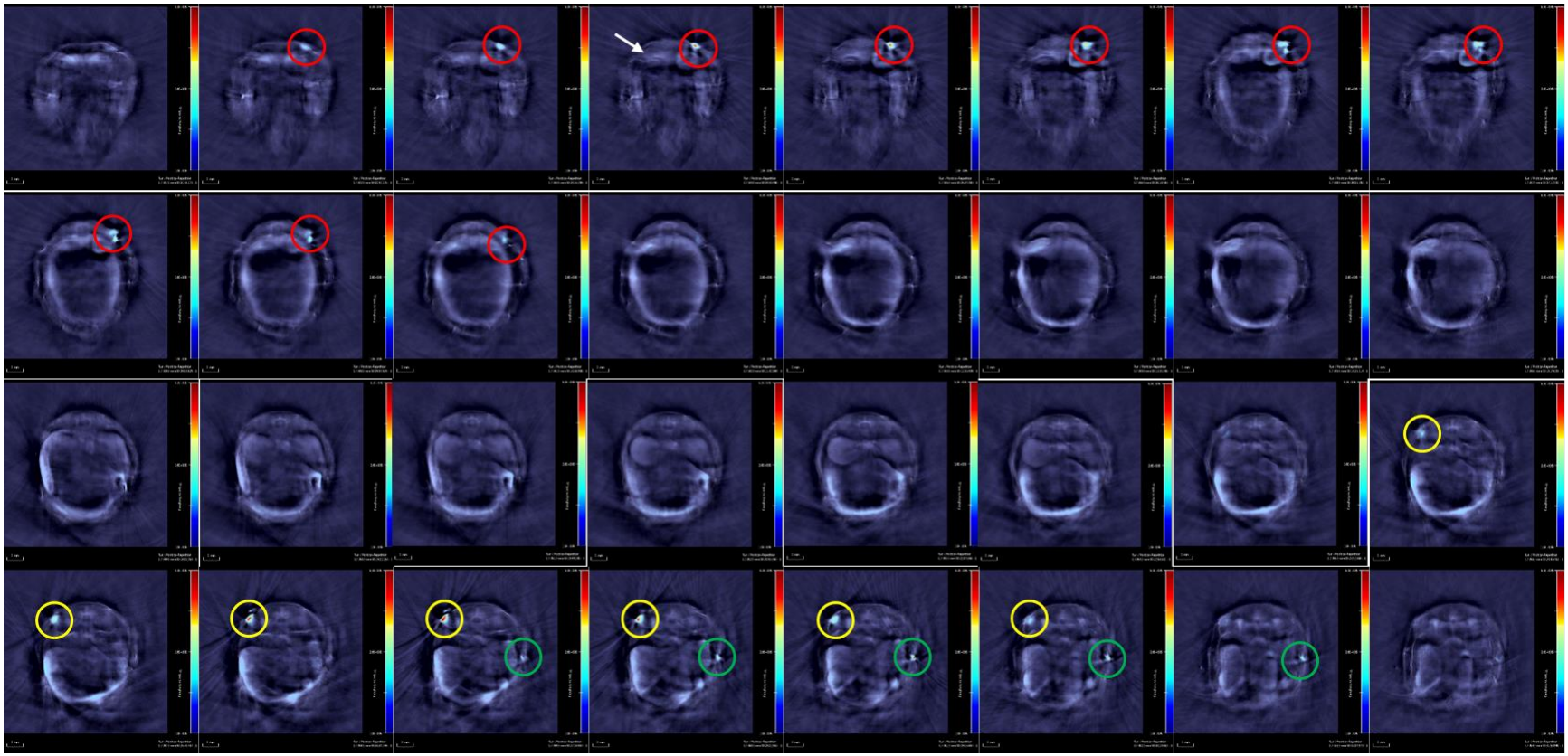

Figure 3-13. Day 11 MSOT imaging of mouse after injection with non-labelled MSCs and PDI-labelled MSCs. The white arrow indicates the position where 1 x 10^6 non-labelled MSCs were injected while the circles for the PDI-labelled MSCs are as follows: red, 1 x 10^6 MSCs; yellow, 0.5 x 10^6 MSCs; green, 0.25 x 10^6 MSCs.

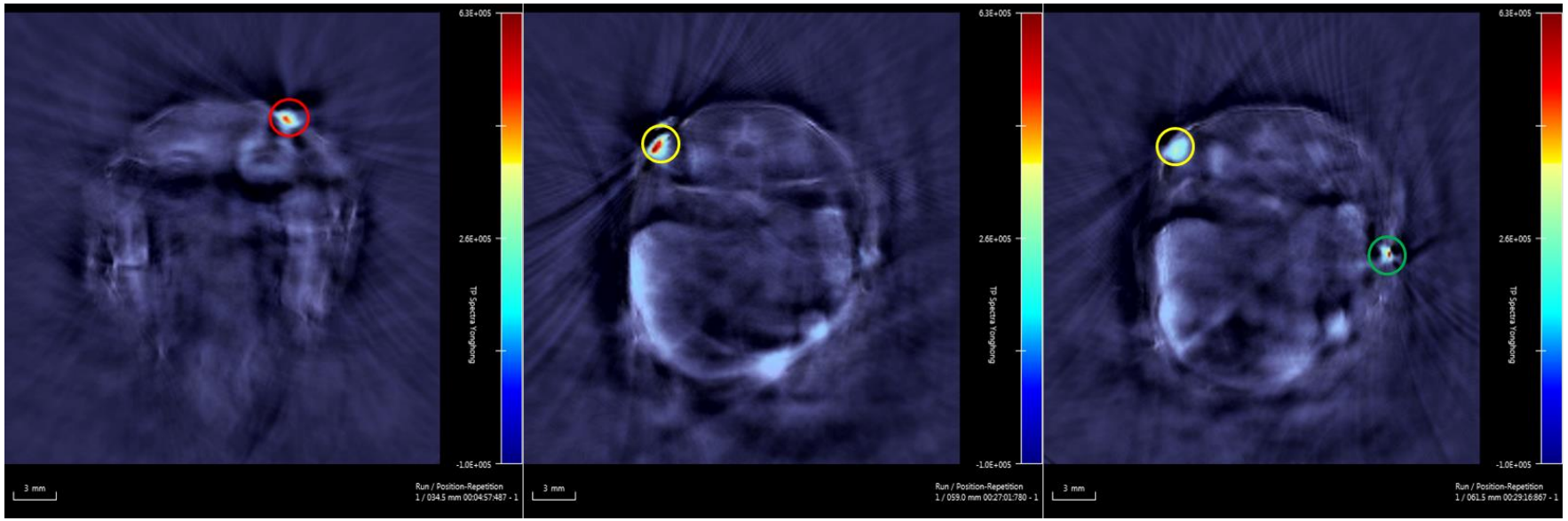

Figure 3-14. Enlarged MSOT images for day 11, red circle, indicate 1 x 10^6 PDI labelled cells; yellow circle indicates 0.5 x 10^6 PDI labelled cells; and green circle indicate 0.25 x 10^6 PDI labelled cells.

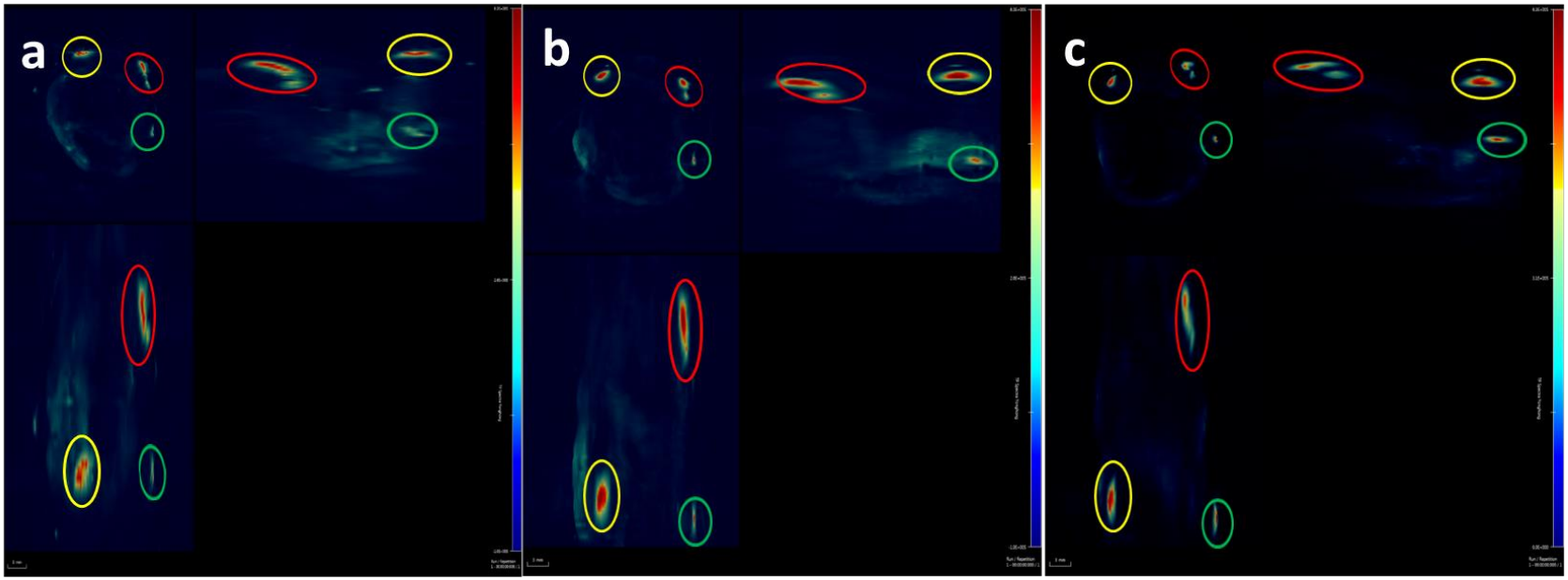

Figure 3-15. MSOT 3D view of mouse after injection with MSCs on: a) day 1, b) day 7 and c) day 11. Each panel shows the three cross-section views, transverse plane/ top left, sagittal plane/top right and coronal plane/bottom left. Red circles indicate 1 x 10^6 PDI labelled cells, yellow circles indicate 0.5 x 10^6 PDI labelled cells; and green circles indicate 0.25 x 10^6 PDI labelled cells.

Following MSOT imaging, bioluminescence imaging was used to confirm whether the cells were still alive and proliferating. **Figure 3-16a-c** shows the cells were still alive and proliferated 11 days after injection in the mouse, indicated by strong and increasing signals over time by the luminescent radiance. It should be noted that in contrast to the MSOT images, the bioluminescence image is only a planar image and has poor spatial resolution.

Subsequently, fluorescence imaging was employed to determine if the PDI-labelled MSCs generated sufficient signal to be detected with NIR fluorescence imaging. As can be seen from **Figure 3-16d-f**, fluorescent spots were clearly visible for the two areas that were implanted with the highest numbers of PDI-labelled MSCs, with the area injected with 10^6 PDI-labelled MSCs generating a more intense signal than the area injected with 0.5 x 10^6 PDI-labelled MSCs. For the area injected with the lowest number of cells, the signal could not be distinguished from background, indicating that in vivo fluorescence imaging of the PDI-labelled cells is not as sensitive as MSOT. As expected, no fluorescence signal was detected for the non-labelled MSCs. It was observed that at day 7 and day 11, the overall degree of fluorescence signal increased, but this was not restricted to the areas where the cells had been injected. Given that bioluminescence and MSOT imaging showed signals that were restricted to the areas where the cells were injected, it can be concluded that the increase in fluorescence in other parts of the mouse's back must have been due to an increase in the background signal over time. It is not clear what the explanation is for this.

These observations indicate that MSOT is superior to fluorescence imaging for indicating the precise position of PDI-labelled cells, and is also a more sensitive technique, as it enabled fewer numbers of cells to be detected than with MSOT. Ideally, for in vivo cell tracking, it is best to combine bioluminescence (firefly luciferase) with

MSOT (PDI nanoparticles), because this allows the viability and proliferation of the cells to be monitored with bioluminescence, while at the same time allowing then to be precisely located with MSOT.

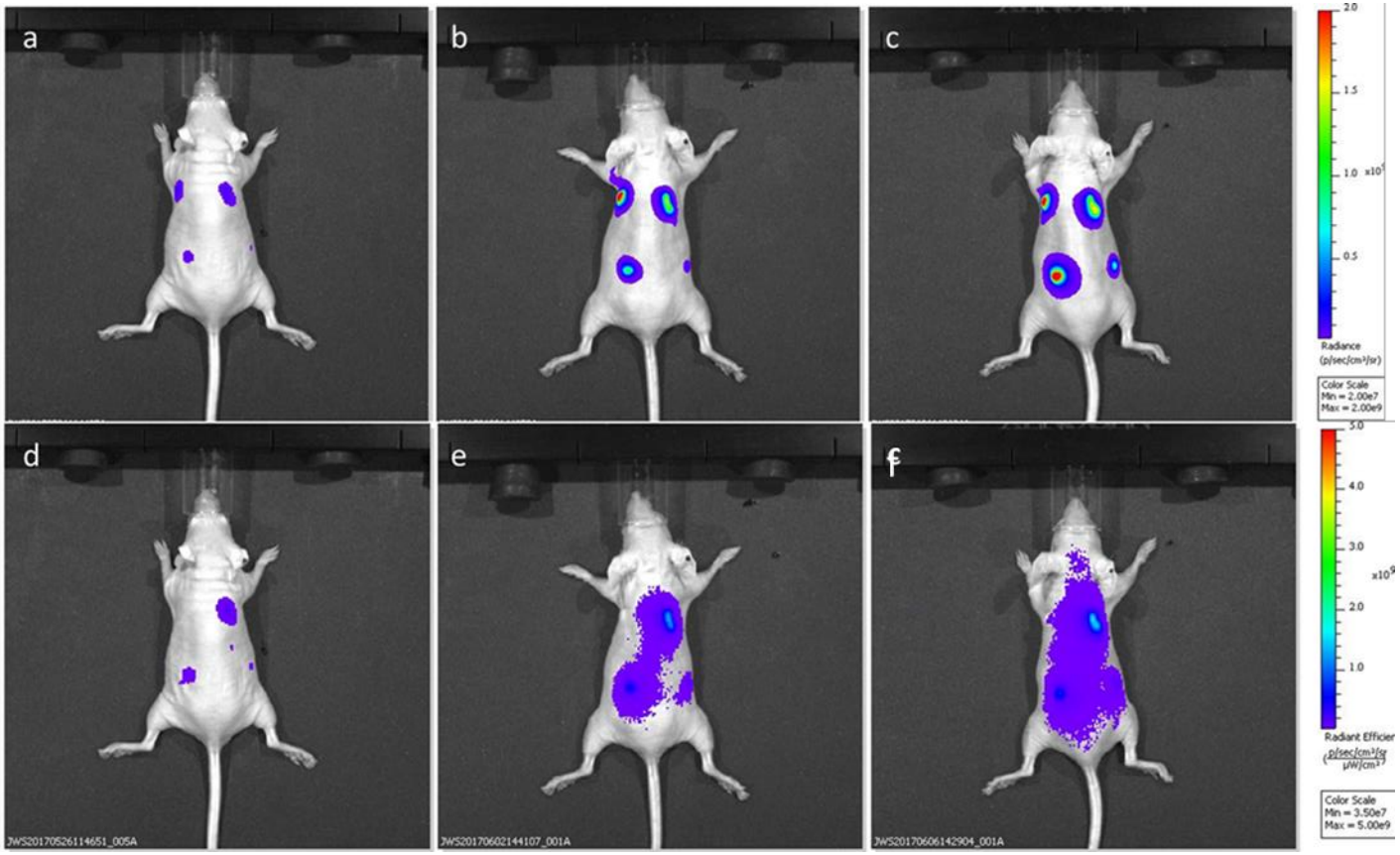

Figure 3-16. Bioluminescence imaging (a-c) and fluorescence imaging (d-f) of the mouse subcutaneously injected with MSCs; day 1 (a,d), day 7 (b,e), and day 11 (c,f). Top left: unlabelled MSCs, Top right: PDI-labelled MSCs, 1 x 10^6 cells/150 µl; Bottom left, PDI-labelled MSCs, 0.5 x 10^6 cells /75 µl; Bottom right, PDI-labelled MSCs, 0.25 x 10^6 cells /37.5 µl. The three bioluminescence images share same colour scale bar while the three fluorescence images share same colour scale bar.

After imaging on day 11, the mouse was sacrificed and the four MSC masses were surgically removed from the mouse. **Figure 3-17** shows images of the MSC masses. Compared to the non-labelled MSC masses, a dark blue core (due to the presence of PDI nanoparticles) can be seen in all three PDI-labelled MSC masses while the peripheral regions are clear. This may be attributed to the fact that it is probably the cells at the periphery that are more likely to proliferate, due to the inner cells being contact inhibited. The more the cells proliferate, the more the load of PDI particles per cells will be diluted.

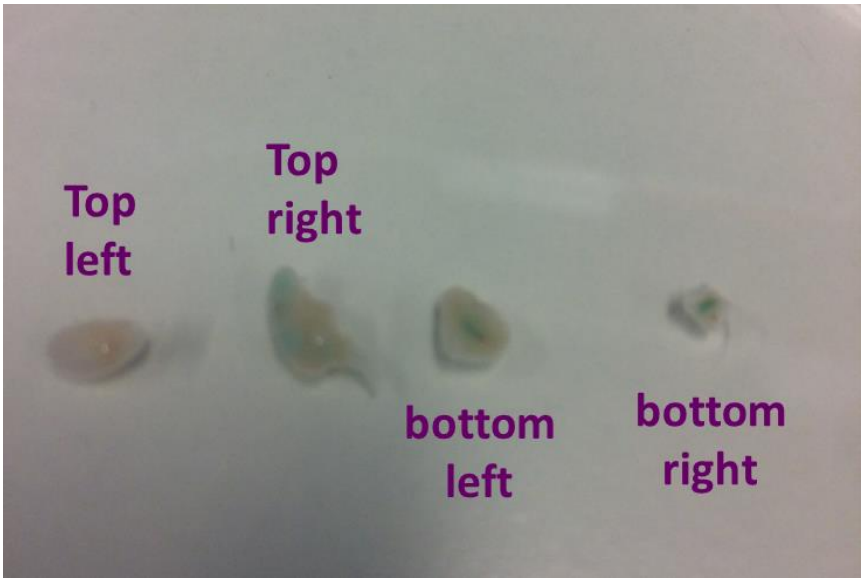

Figure 3-17. Images of the four dissected MSC masses at day 11, following culling. The original positions of the MSC masses in the mice are described in the image.

Frozen sections (7 μm in thickness) of the MSC masses were imaged by confocal microscopy (**Figure 3-18**). The implanted MSCs can be identified due to their expression of ZsGreen, which confirms that most of the cells within the masses are derived from the MSCs. As expected, the MSC mass derived from unlabelled MSCs did not display any red fluorescence. In contrast, the MSC masses derived from PDI-labelled MSCs

displayed a central area of red fluorescence, which faded towards the periphery (**Figure 3-18**). This agrees with the visual observation in **Figure 3-17**.

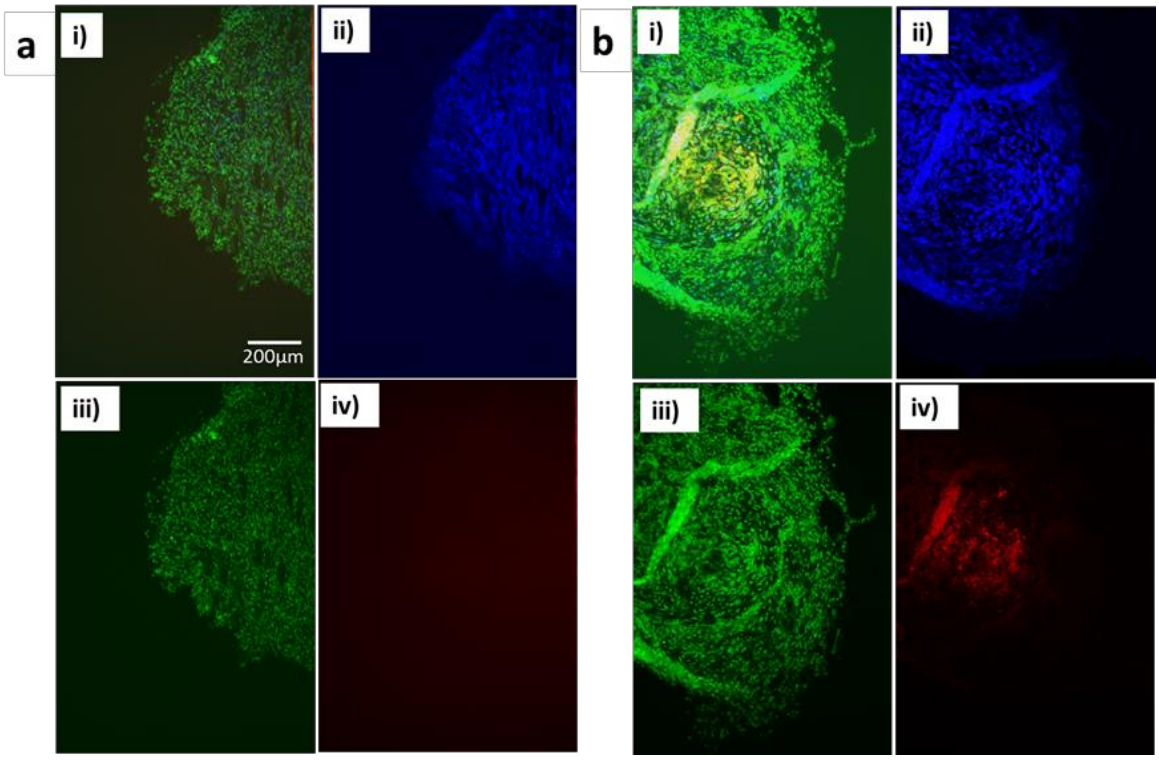

Figure 3-18. Confocal microscope images of frozen sections of dissected MSC masses co-stained with the nuclear stain, DAPI (blue). Green indicates ZsGreen-expressing MSCs and red indicates PDI-labelled MSCs. (a) top left MSC mass comprising unlabelled ZsGreen-expressing MSCs; (b) top right MSC mass comprising PDI-labelled ZsGreen-expressing cells. In each panel, image (i) is the composite images of (ii – iv); image (ii), DAPi staining; image (iii), ZsGreen fluorescence; image (iv), PDI fluorescence.

It has been reported previously that MSCs can differentiate into bone and cartilage when subcutaneously injected in mice [29]. The potential effects of PDI nanoparticles on MSC differentiation were investigated by staining the MSC masses for

the detection of bone and cartilage. **Figure 3-19** shows the images after staining sections of the MSC masses using alizarin red. The red colour in the image shows the presence of calcium, which is indicative of bone cell differentiation [28]. No obvious difference was found between non-labelled MSCs and PDI-labelled MSCs. **Figure 3-20** shows the image of the MSC sections stained with alcian blue. The light blue colour in the images indicates cartilage differentiation. Both **Figure 3-19** and **Figure 3-20** suggest that the uptake of PDI nanoparticles did not inhibit the ability of MSCs to differentiate into bone and cartilage in vivo.

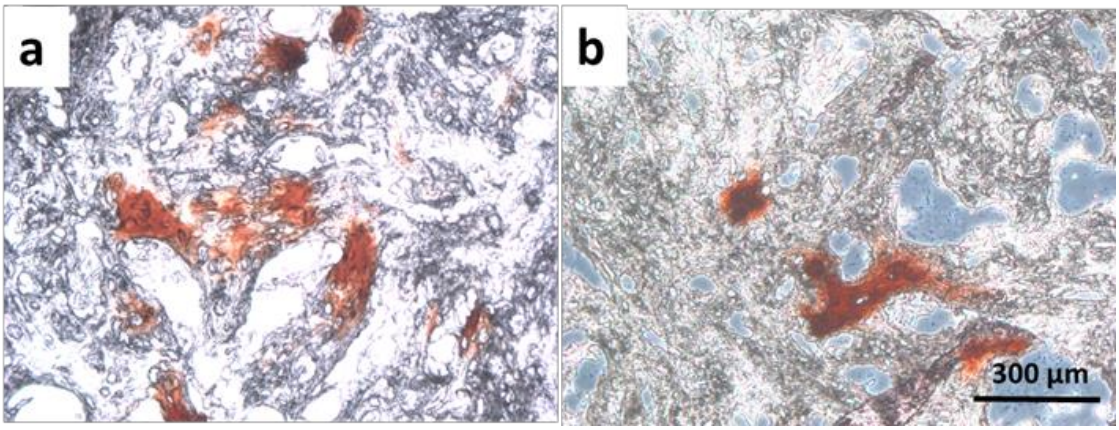

Figure 3-19 Histology of the MSC masses stained with alizarin red for the detection of calcium. (a) non-labelled MSCs (top left MSC mass); (b) PDI-labelled MSCs (top right MSC mass).

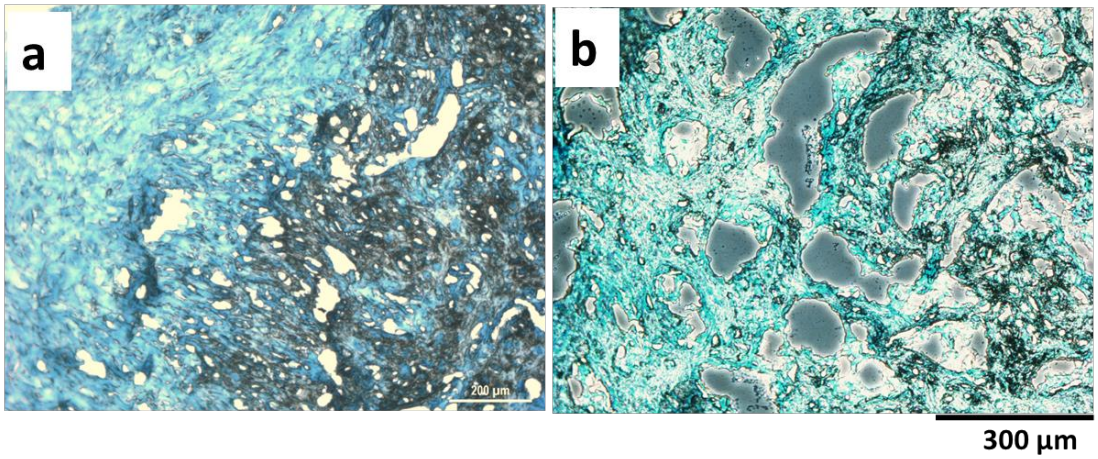

Figure 3-20 Histology of the MSC masses stained with alcian blue for the detection of cartilage. (a) non-labelled MSCs (top left MSC mass); (b) PDI-labelled MSCs in the position of top right.

3.4 Conclusions

Cytotoxic effects of aqueous PDI nanoparticle suspensions were evaluated by adding increasing concentrations to MSC culture medium. This showed that TPEG was toxic while aqueous PDI nanoparticle suspensions with PVA as stabilizer allowed the growth and proliferation of MSCs at high concentrations (up to 50 µg/ml where the cell viability was very close to the MSCs cultured in PDI-free medium). However, MSCs labelled with these particles showed very low or no absorbance as measured by UV-vis spectroscopy. This is probably due to low uptake of these PDI nanoparticles by the MSCs, which would render them unsuitable for cell tracking in vivo.

The low intensity problem from the PVA-stabilized PDI nanoparticles was addressed by using a hyperbranched block copolymer $DEAMA_{50}DEGDMA_2OEGMA_{80}$ which was developed in our group. This block copolymer was used as the stabilizer to prepare aqueous PDI nanoparticle suspensions by the solvent evaporation approach. High uptake of these PDI nanoparticles by the MSCs was noticed by visual observation

and confirmed by UV-vis analysis and flow cytometry of PDI-labelled MSC suspensions.

The PDI nanoparticles fabricated with the block copolymer as stabilizer had no effect on MSC viability when used at concentrations up to 25 μg/ml, based on the ratio of PDI: $DEAMA_{50}DEGDMA_2OEGMA_{80}$ = 1:1 w/w. The flow cytometry study showed a concentration of 15 μg/ml gave good labelling efficiency, and indicated a high uptake of the PDI nanoparticles. The PDI nanoparticles with the block copolymer as stabilizer at a concentration of 15 μg/ml were then used for in vitro and in vivo evaluation of PDI-labelled MSCs. The confocal imaging and flow cytometry analysis showed that the PDI nanoparticles remained inside the MSCs after uptake and did not appear to be exocytosed. After injecting the PDI-labelled MSCs subcutaneously in mice, fluorescent imaging showed the presence of PDI-labelled cells in the mouse while the bioluminescence images indicated the MSCs were still alive and proliferated. In vivo MSOT imaging clearly showed the injected PDI-labelled MSCs in the mouse for 1 day, 7 days, and 11 days. The subsequent histology study showed that the MSCs could differentiate into bone and cartilage cells, demonstrating minimal or no impact on MSC differentiation from the PDI nanoparticles.

3.5 References

[1] Ntziachristos, V. Going deeper than microscopy: the optical imaging frontier in biology. *Nat. Methods* **2010**, 7, 603-614.

[2] Mallidi, S.; Luke, G.P.; Emelianov, S. Photoacoustic imaging in cancer detection, diagnosis, and treatment guidance. *Trends Biotechnol,* **2011**, 29, 213 – 221.

[3] Emeliano, S.Y.; Li, P.-C.; O'Donnell, M. Photoacoustics for molecular imaging and therapy. *Phys. Today* **2009**, 62, 34-39.

[4] Wang, L.V.; Hu, S. Photoacoustic tomography: in vivo imaging from organelles to organs. *Science* **2012**, 335, 1458-1462.

[5] Yang, X.; Stein, E.W.; Ashkenazi, S.; Wang, L.V. Nanoparticles for photoacoustic imaging. *WIREs Nanomed. Nanobiotechnol,* **2009**, 1, 360 – 368.

[6] Zhang, Y.; Yu, J.; Kahkoska, A.R.; Gu, Z. Photoacoustic drug delivery. *Sensors* **2017**, 17, 1400.

[7] Wu, D.; Huang, L.; Jiang, M.S.; Jiang, H. Contrast agents for photoacoustic and thermoacoustic imaging: a review. *Int. J. Mol. Sci.,* **2014**, 15, 23616-23639.

[8] Huang, P.; Lin, J.; Li, W.; Rong, P.; Wang, Z.; Wang, S.; Wang, X.; Sun, X.; Aronova, M.; Niu, G.; Leapman, R.D.; Ni, Z.; Chen, X. Biodegradable gold nanovesicles with an ultrastrong plasmonic coupling effect for photoacoustic imaging and photothermal therapy. *Angew. Chem. Int. Ed.* **2013**, 125, 14208-14214.

[9] Li, W.; Chen, X. Gold nanoparticles for photoacoustic imaging. *Nanomed*, **2015**, 10, 299-320.

[10] Mallidi, S.; Larson, T.; Tam, J.; Joshi, P.P.; Karpiouk, A.; Sokolov, K.; Emelianov, S. Multiwavelength photoacoustic imaging and plasmon resonance coupling of gold nanoparticles for selective detection of cancer. *Nano Lett.* **2009**, 9, 2825-2831.

[11] Zhang, Y.S.; Cai, X.; Yao, J.; Xing, W.; Wang, L.V.; Xia, Y. Non-invasive and in situ characterization of the degradation of biomaterial scaffolds by volumetric photoacoustic microscopy. *Angew. Chem. Int. Ed.* **2014**, 53, 184-188.

[12] Cui, D.; Xie, C.; Pu, K. Development of semiconducting polymer nanoparticles for photoacoustic imaging. *Macromol. Rapid Commun.* **2017**, 38, 1700125.

[13] Bhosale, S.V.; Jani, C.H.; Langford, S.J. Chemistry of napththalene diimides. *Chem. Soc. Rev.* **2008**, 37, 331-342.

[14] Avlasevich, Y.; Li, C.; Müllen, K. Synthesis and applications of core-enlarged perylene dyes. *J. Mater. Chem*. **2010**, 20, 3814-3826.

[15] Chen, L.; Li, C.; Müllen, K. Beyond perylene diimides: synthesis, assembly and function of higher rylene chromophores. *J. Mater. Chem. C,* **2014**, 2, 1938-1956.

[16] Würthner, F.; Saha-Möller, C.R.; Fimmel, B.; Oqi, S.; Leowanawat, P.; Schmidt, D. Perylene bisimide dye assemblies as archetype functional supramolecular materials. *Chem. Rev.* **2016**, 116, 962-1052.

[17] Chen, S.; Slattum, P.; Wang, C.; Zang, L. Self-assembly perylene imide molecules into 1D nanostructures. *Chem. Rev.* **2015**, 115, 11967-11998.

[18] Sukul, P.K.; Asthana, D.; Mukhopadhyay, P.; Summa, D.; Muccioli, L.; Zannoni, C.; Beljonne, D.; Rowan, A.E.; Malik, S. Assemblies of perylene diimide derivatives with melamine into luminescent hydrogels. *Chem. Commun.* **2011**, 47, 11858-11860.

[19] Datar, A.; Balakrishnan, K.; Zang, L. One-dimensional self-assembly of a water soluble perylene diimide molecule by pH triggered hydrogelation. *Chem. Commun.,* **2013**, 49, 6894-6896.

[20] Draper, E.R.; Walsh, J.J.; McDonald, T.O.; Zwijnenburg, M.A.; Cameron, P.J.; Cowan, A.J.; Adams, D.J. Air-stable photoconductive films formed from perylene bisimide gelators. *J. Mater. Chem. C*, **2014**, 2, 5570-5575.

[21] Liu, X.; Ahmed, A.; Wang, Z.; Zhang, H. Nanofibrous microspheres via emulsion gelation and carbonization. *Chem. Commun.* **2015**, 51, 16864-16867.

[22] Liu, X.; Roberts, A.; Ahmed, A.; Wang, Z.; Zhang, H. Carbon nanofibers by pyrolysis of self-assembled perylene diimide derivative gels as supercapacitor electrode materials, *J. Mater. Chem. A,* **2015**, 3, 15513-15522.

[23] Sugiyasu, K.; Fujiata, N.; Shinkai, S. Visible-light-harvesting organogel composed of cholesterol-based perylene derivatives. *Angew. Chem. Int. Ed.* **2004**, 43, 1229-1233.

[24] Sukul, P.K.; Datta, A.; Malik, S. Light harvesting and amplification of emission of donor perylene–acceptor perylene aggregates in aqueous medium. *Chem. Eur. J.* **2014**, 20, 3019-3022.

[25] Zhang, Y.; Jeon, M.; Rich, L.J.; Hong, H.; Geng, J.; Zhang, Y.; Shi, S.; Barnhart, T.E.; Alexandridis, P.; Huizinga, J.D.; Seshadri, M.; Cai. W.; Kim, C.; Lovell, J.F. Non-invasive multimodal functional imaging of the intestine with frozen micellar naphthalocyanines. *Nature Nanotechnol,* **2014**, 9, 631-638.

[26] Lee, C.; Kim, J.; Zhang, Y.; Jeon, M.; Liu, C.; Song, L.; Lovell, J.F.; Kim, C. Dual-color photoacoustic lymph node imaging using nanoformulated naphthalocyanines. *Biomaterials*, **2015**, 73, 142-148.

[27] Fan, Q.; Cheng, K.; Yang, Z.; Zhang, R.; Yang, M.; Hu, X.; Ma, X.; Bu, L.; Lu, X.; Xiong, X.; Huang, W.; Zhao, H.; Cheng, Z. Perylene-Diimide-Based Nanoparticles as Highly Efficient Photoacoustic Agents for Deep Brain Tumor Imaging in Living Mice. *Adv. Mater.,* **2015**, 27, 843-847.

[28] Taylor, A.; Herrmann, A.; Moss, D.; Sée, V.; Davies, K.; Williams, S.R.; Murray, P. Assessing the Efficacy of Nano- and Micro-Sized Magnetic Particles as Contrast Agents for MRI Cell Tracking. *PLOS One*, **2014,** 9, e100259,

[29] Juffroy, O.; Noël, D.; Delanoye, A.; Viltart, O.; Wolowczuk, I.; Verwaerde, C. Subcutaneous graft of D1 mouse mesenchymal stem cells leads to the formation of a bone-like structure. *Differentiation*, **2009**, 78, 223-231.

Chapter 4 Synthesis of PDI-functionalised thermo-setting chitosan hydrogel and evaluation of its potential for imaging with MSOT

4.1 Introduction

Hydrogels have been extensively used as scaffolds for drug delivery and tissue engineering, especially the second generation, stimuli-responsive hydrogels, which have taken the main stage [1]. These stimuli include temperature, pH, oxidation states, and ionic strength. Some types of hydrogels are injectable or 'in situ' forming hydrogels where the gelation is usually initiated by a particular stimulus [2]. Injectable hydrogels can offer advantages including easy encapsulation of drugs/cells, minimally invasive implanting, complete filling of the injection site [3]. Injectable hydrogels have been used in various biomedical applications particularly including cartilage, bone tissue engineering, dental and craniofacial regeneration, and other regenerative medicine applications [2-7]. There are two important issues to be considered if the injected hydrogels are used for biomedical applications. The first is biocompatible gelation conditions which may include the use of non-toxic reagents and by-products, mild temperature, and physiological pH. This can be particularly important for biopharmaceuticals and cells. The second issue is the biodegradability of the hydrogel scaffolds. In an ideal situation, the hydrogels should degrade over time and be naturally excreted from the body.

Natural polymers and polysaccharides have thus been extensively used to generate hydrogels, although synthetic polymer hydrogels are also intensively investigated as it is possible to control their molecular structure and functional group

composition [2, 3, 7, 8]. Some widely used natural polymers include chitosan, collagen, gelatin, alginate, hyaluronic acid, and fibrinogen [6]. Cell encapsulation technology is important for regenerative medicine as it provides a way to deliver cells to specific sites in vivo [7, 9], and the encapsulating gel can be tailored for each specific application. In terms of using stimuli to trigger gelation, pH and temperature are mostly used. However, when pH is used, ensuring it is maintained within a physiological range can be difficult, and a pH outside the normal physiological range is detrimental to the survival of the cells. Furthermore, because the host tissue is mostly pH neutral (pH 7), a lower or higher pH would have to be used in the solution before injecting. As such, a thermally-induced (by body temperature) injectable hydrogel is preferred, in which case, the cells would be conveniently suspended in the solution at room temperature (around 20°C), with gelation occurring following implantation in vivo (body temperature, 37°C).

Different types of temperature-sensitive hydrogels have been fabricated and used [1,2,10]. The common systems include poly(N-isopropylacrylamide) (PNIPAm) and their copolymers and amphiphilic tri-block copolymers. The PNIPAm utilizes a phenomenon of low critical solution temperature (LCST) below which a solution is present and above which a gel is formed. The LCST can be tuned to close to body temperature when suitable PNIPAm copolymers are synthesized and used [1,10]. The triblock copolymers include the widely known Pluronics (e.g., F127, PEG-PPG-PEG) or Poloxamers and biodegradable block copolymers with the hydrophobic blocks replaced by the biodegradable poly (ε-caprolactone) (PCL) or poly (lactide-co-glycolide) (PLG) etc. The gelation mechanism is attributed to the aggregation of the self-assembled micelles from these amphiphilic block copolymers [10].

Chitosan-based thermal gelation systems have also been proposed [11]. The credibility of using chitosan hydrogels for biomedical applications has been discussed in Chapter 1. In order to form in situ hydrogels, polyol salts are always required to mix with chitosan in the solution state. For example, glycerol phosphate disodium salt was added in aqueous chitosan solution facilitated by HCl solution. The pH value of the final solution was adjusted to 7.15 before adding cells and heating [11]. In another case, chitosan was dissolved in 0.1 M HCl solution followed by the addition of aqueous β-glycol phosphate disodium salt solution in an ice cold bath [12]. Ringe and co-authors prepared a solution of chitosan- β-glycol phosphate-hydroxyethyl cellulose which exhibited a sol-gel transition at 37°C [13]. Injectable chitosan-based hydrogels were also prepared by crosslinking chitosan with the biocompatible cross-linker, genipin, facilitated by the ionic bonds between chitosan and sodium salts [14]. Different types of sodium salts, including tri-sodium phosphate, sodium sulfate, sodium sulfite or sodium bicarbonate were added to the chitosan-genipin solutions and the gels were formed at room temperature [14].

Cell encapsulation by hydrogels have tremendously advanced regenerative medicine therapies [15], as have been described in Chapter 1 of this thesis. Mesenchymal stem/stromal cells (MSCs) have been widely used in cell encapsulation for enhanced therapy and tissue engineering. Alginate is the commonly used polymer for MSC encapsulation. For example, MSCs were encapsulated in alginate microsphere to enhance the neuro-inflammatory response [16], in injectable oxidized alginate microbeads for bone tissue engineering [17], in 3D alginate and hyaluronic acid hydrogels for sustained release of nerve growth factor and nerve regeneration [18], and in alignate-polyethylene glycol microspheres to decrease liver fibrosis [19]. Some other newly developed hydrogels have also been used to encapsulate MSCs, for example,

injectable crosslinked oligo(poly(ethylene glycol) fumarate and gelatin microparticles [20], injectable thermosensitive poly(N-vinylcaprolactam) hydrogels [21], cell-degradable peptide-functionalized poly(ethylene glycol) hydrogels [22], and poly(ethylene glycol) hydrogels with tethered functional groups [23].

Chitosan hydrogels are used often for cell encapsulation but only limited reports on MSC encapsulation [13, 15, 24]. The thermosensitive injectable chitosan gels for MSC encapsulation is particularly attractive, as demonstrated in β-glycol phosphate-chitosan gel [13]. In this project, our motivation for developing injectable chitosan gels was to encapsulate MSCs for future implantation under the mouse kidney capsule, a previous study having shown that this increased MSC viability and improved therapeutic efficacy following renal ischaemia reperfusion injury [25]. A key aim of this chapter was to functionalise the gels with perylene diimide derivative (PDI) nanoparticles so that they could be monitored in vivo using multispectral optoacoustic tomography (MSOT).

Objectives

1. Optimise a protocol for fabricating chitosan-GP hydrogel
2. Investigate optical properties of the chitosan-GP-PDI hydrogels (MSOT)
3. Monitor release of PDI nanoparticles from chitosan-GP-PDI hydrogel
4. Investigate effect of chitosan-GP-PDI hydrogel on mouse MSC population growth

4.2 Experimental Details

4.2.1 Chemicals and Reagents

β-glycerol phosphate disodium salt hydrate (GP, 99 %), sodium triphosphate pentabasic (NaTPP), chitosan (medium molecular weight), poly(vinyl alcohol) (PVA,

Mw 10K, 80% hydrolysed), hydroxyethyl cellulose (HEC), and acetic acid were purchased from Sigma Aldrich. Chitosan (purified powder, MW 15000) was purchased from Polyscience, distributed by Park Scientific. Distilled water was used for all the water solutions. All chemicals were used without further treatment.

Biological reagents: phosphate buffer solution (PBS), high glucose DMEM (Dulbecco's Modified Eagle's Medium) base medium, non-essential amino acid, L-glutamine, and trypsin- EDTA (Ethylenediaminetetraacetic acid) were obtained from Sigma-Aldrich. The mouse MSC D1 line (CRL-12424) was obtained from ATCC and transduced with lentiviral particles encoding a green fluorescent protein (ZsGreen) and firefly luciferase (Luc) [26].

4.2.2 Synthesis of thermo-setting chitosan-GP hydrogels

Several synthetic recipes for chitosan-GP hydrogels were tried and described below:

(i) 200 mg chitosan (medium MW, Sigma) was dissolved in 9 ml aqueous HCl solution (0.1 M or 0.08 M) while stirring. 600 mg GP was dissolved in 1 ml distilled water. These solutions were cooled down and stored at 4°C. For the preparation of chitosan-GP hydrogel, 1 ml GP solution was added dropwise into 9 ml chitosan solution while stirring at 600 rpm on ice for 10 min and then transferred into a warm oil bath in the temperature range 37°C -60°C for 30 min.

(ii) 150 mg chitosan (Polyscience) was dissolved in 9 ml 0.08 M HCl while stirring. 324 mg GP was dissolved in 1 ml distilled water. 1 ml GP solution was added into 9 ml chitosan solution dropwise while stirring at 600 rpm on ice for 10 minutes, then transferred into a warm oil bath at 37°C for 30 minutes.

(iii) 200 mg chitosan (Polyscience) was dissolved in 10 ml 0.08 M HCL while stirring and 1 g GP was dissolved in 1 ml distilled water. Perylene diimide (PDI) nanoparticle suspension was prepared by the emulsion freeze-drying method with PVA as surfactant (Please see experimental details in Chapter 1. Chitosan-GP-PDI mixture solutions were prepared by mixing 2 ml chitosan solution and 200 µl PDI suspension and then adding a different amount of GP solution by dropping slowly while stirring at 600 rpm: 200 µl, 300 µl, 400 µl, 500 µl and 600 µl. These five different solutions were kept stirring for another 10 minutes. All above procedures were carried out in an ice bath. The solutions were then transferred into an oil bath at 37°C for 30 min.

(iv) The same as (iii) except that 0.07 M HCL was used instead of 0.08 M HCl.

4.2.3 MSOT imaging

MSOT was utilized to image chitosan hydrogels containing PDI nanoparticles. The Chitosan-GP hydrogel solution was prepared with method shown in (iii) above with GP concentration of 5% and PDI concentration of 0.0125 mg/ml. The solution was kept in ice bath to prevent gelation. Then 150 µl solution was injected into one channel in a phantom (4% agar phantom, prepared with the same method detailed in chapter 2) followed by incubation at 37°C for 30 min. The phantom was then moved back to ice bath followed by injection another 150 µl solution into the other channel while kept in ice bath. The phantom was then imaged in MSOT instrument for 10 min. 31 wavelengths from range 680 - 900 nm were chosen for the imaging.

4.2.4 Encapsulating mouse MSCs in chitosan-GP-HEC thermo-setting gel

In order to investigate the potential of using the chitosan hydrogel for the encapsulation of MSCs, the following procedure was developed. Mouse MSCs

expressing ZsGreen and firefly luciferase were used in this experiment. The cell culture conditions are described in chapter 2.

The cell suspension was prepared by suspending 1 x 10^7/ml mouse MSCs in 0.5 ml HEC solution. The HEC solution was prepared by dissolving HEC 200 mg in 10 ml DMEM at a concentration of 20 mg/ml. Firstly, 1.6 ml 2% chitosan solution in 0.07 M HCL (autoclaved for sterilization) and 200 µl PDI suspension (0.2 mg/ml, filtered with 0.22 µm syringe filter) were mixed on ice with stirring under a Lamnar hood. 200 µl β-GP solution (0.3 g/ml, also sterilized by filtration) was added dropwise while stirring on ice for 10 min, followed by the addition of 0.5 ml cell suspension in HEC. The final mixture was transferred into a 12 well plate (0.5 ml/well) and incubated for 30 min at 37°C to induce gelation. The gels were washed gently with MSC medium twice and then 2 ml fresh medium was added and then incubation proceeded for a total of 2 months. The medium was changed every 3 days. Control experiments were prepared at the same time using the same procedures except that the PDI suspension was replaced with PBS.

4.2.5 Cell-IQ real-time imaging

This technique was employed to evaluate the MSCs encapsulated in chitosan hydrogels. To do this, the 12-well plate with MSCs in chitosan gels was placed in the Cell-IQ instrument (ChipMan Technologies) for live imaging for 3 days. Cells were imaged using phase contrast and fluorescence microscopy (488 nm laser for ZsGreen and 560 nm laser for PDI) with a 10x objective. Images were taken once an hour.

4.2.6 Monitoring the release of PDI from the chitosan-GP hydrogel

After the encapsulation of PDI nanoparticles within chitosan-GP hydrogels, it was important to know whether all the PDI nanoparticles remained within the hydrogels. This is a critical issue when monitoring the change of hydrogel scaffolds for tissue engineering via imaging PDI nanoparticles MSOT. This issue was investigated by evaluating the release of PDI nanoparticles from the hydrogel.

The chitosan-GP hydrogel with encapsulated PDI nanoparticles was prepared with the above procedures (no cells added). The hydrogel was formed from 1.25 ml solution in a 10 ml glass vial. The gel was washed with PBS twice and then 2 ml PBS was added to the top of the hydrogel at room temperature. UV-Vis analysis (UV plate reader) was performed to monitor the release of PDI nanoparticles over 27 days. At the defined time, 150 µl x3 PBS solution was taken and measured in a 96-well plate by UV-vis at the wavelength of 698 nm. After the analysis, the PBS was replaced back on the hydrogel.

4.3 Results and discussion.

4.3.1 Optimisation of chitosan-GP-PDI hydrogel fabrication

Based on a previous method [11], chitosan (medium molecular weight) purchased from Sigma was first used to produce the thermo-setting hydrogels. When the chitosan solution was heated in an oil bath, the gels only formed at 60°C under the investigated conditions, which would not be suitable for in situ gelation at body temperature.

Therefore, another grade of chitosan (Mw 15000 from Polysciences) was used for the rest of study. The synthesis was first repeated with a slight modification from ref 12, but gelation still did not occur at 37°C (method (ii) in section 4.2.2). This was improved by increasing the concentration of chitosan and decreasing the concentration

of HCl (200 mg in 10 ml 0.08M HCl solution), and varying the amount of added GP solution. This system was investigated with the inclusion of PDI nanoparticles. **Figure 4-1** shows the chitosan solution and the gels formed. It is clear that the gels can only be formed when the amount of GP solution ≥ 400 µl, equivalent to 16.6 mg/ml GP in the whole gel.

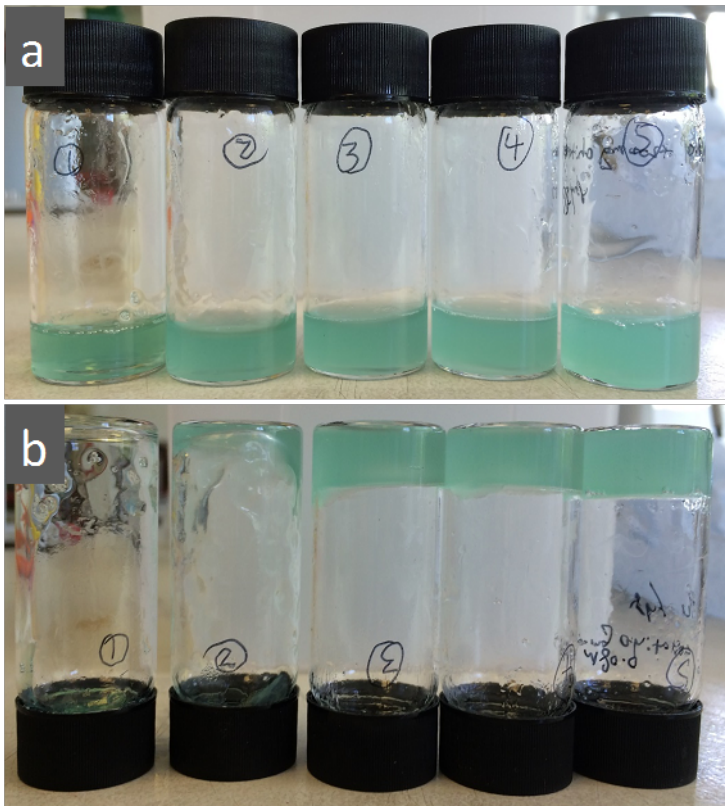

Figure 4-1. Photos show (a) chitosan solution with green PDI nanoparticle and (b) the hydrogel formed after incubation at 37 °C for 30 min. The numbers on the glass bottles indicate the amount of GP solution (1 g/ml) added, i.e., (1) 200 µl, (2) 300 µl, (3) 400 µl, (4) 500 µl, and (5) 600 µl.

It has been reported that cell growth may be reduced by the presence of GP when the concentration is higher than 5%, presumably due to the high osmolality [27]. For this reason, lower concentrations of GP were tested, using a lower concentration of HCl solution (0.07 mM) to dissolve the chitosan (method (iv) in section 4.2.2). It was

found that the gels could be formed with all volumes of added GP solution, from 200 µl to 600 µl, with a GP concentration of 8.8 mg/ml or 8.8 %.

Based on this finding and considering a previous study [13], the concentration of GP was reduced to 0.03 g/ml (3%) with the presence of HEC in the chitosan solution, with gelation being successfully achieved. This methods was then used for subsequent experiments.

4.3.2 Optical properties of the chitosan-GP-PDI hydrogels (MSOT)

The purpose of incorporating PDI nanoparticles in chitosan hydrogel was to monitor the stability of the gels following implantation in vivo using NIR fluorescence or photoacoustic imaging techniques. The chitosan-GP-PDI hydrogel in a phantom was imaged with MSOT and **Figure 4-2** shows the 3D view. It is obvious that both solution and gel states generate a strong signal, although MSOT intensity decreased slightly after gelation (see **Figure 4-3)**. The signals in the 3D images are uneven because the injected chitosan-GP-PDI hydrogel solution is highly viscous and therefore not evenly dispersed in the channels.

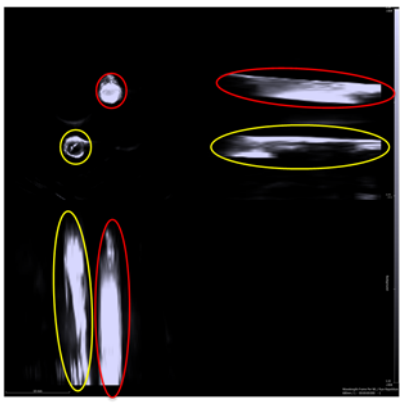

Figure 4-2. MSOT image shows 3 D view of chitosan-GP-PDI hydrogel in a phantom with solution state and gel state (after gelation). Red circles indicate gels and yellow

circles indicate solutions. There are three different cross section images: top left/xy, /top right/xz and bottom left/xy.

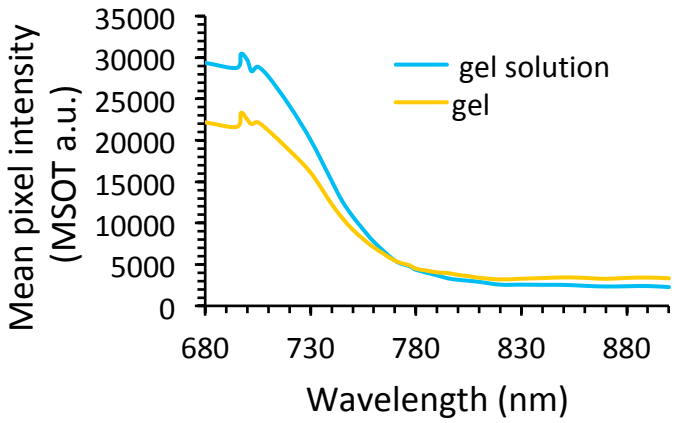

Figure 4-3. Optical property of chitosan-GP-PDI hydrogel with MSOT

4.3.3 Monitoring release of PDI nanoparticles from the chitosan-GP-PDI hydrogel

In order to investigate whether PDI nanoparticles are retained within the chitosan-GP-PDI hydrogel or released over time, the gel was put into PBS solution and monitored over 27 days. When the fresh PBS solution was placed onto the top of the hydrogel, the colourless PBS solution turned light green with time, suggesting the PDI particles were being released from the gel. This release was monitored by UV-vis analysis of the PBS solution, as shown in **Figure 4-4**.

The release of PDI nanoparticles was negligible in the first 5 days but then a relatively slow rate of particle loss was observed between days 5 and 12, which increased from 12 to 19 (Figure 4-4). This may be attributed to the degradation of the chitosan gel in the presence of PBS as tiny pieces of gel were observed floating in the PBS solution. One would expect the release profile to flatten even without further release. A peculiar phenomenon was that the absorbance began to decrease after day

20. The hydrogel was still intact by visual observation, but the appearance of gel fragments in the PBS solution suggested that some degradation must have taken place, and it is possible that these fragments might have affected the absorbance reading. Another contributing factor might have been that every time the UV-Vis was checked, some particles were left behind in the reading plate, leading to a small amount of particle loss with each measurement. The exact reason is unknown at this stage.

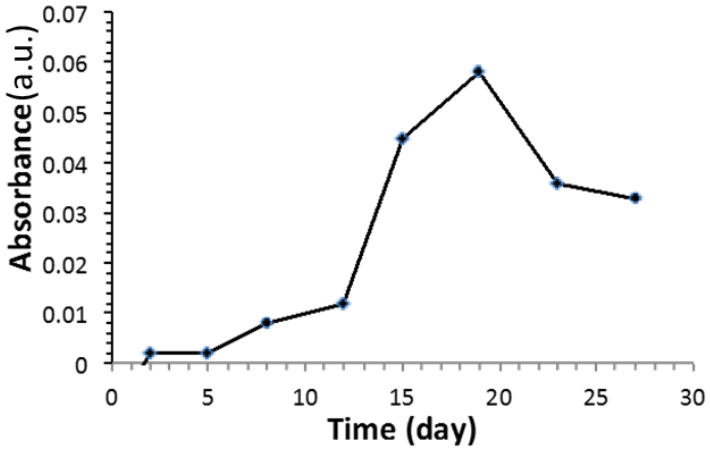

Figure 4-4. The release profile of PDI nanoparticles from chitosan-GP hydrogel, measured by UV-vis at 698 nm.

4.3.4 Effect of chitosan-GP-PDI hydrogel on mouse MSC population growths

Mouse MSCs were encapsulated to evaluate whether the mouse MSC population could expand within the PDI-functionalised hydrogel, and if the cells behaved differently in the PDI-functionalised gel compared with a gel that lacked the PDI particles. After incubating for 24 hours, the hydrogel with mouse MSCs was placed inside the Cell IQ for real-time imaging for 3 days. **Figure 4-5** shows that in both gels, there appeared to be a slight decrease in cell number from day 1 to day 3, as shown by a decrease in the number of ZsGreen-expressing cells. The data from 3 fields

of view from each sample was analysed with Image J. The result shows that the integrated ZsGreen density decreased 37.46% for chitosan hydrogel without PDI nanoparticles and 31.93% for PDI containing chitosan hydrogel (**figure4-6**). This suggested that the cells were not proliferating within the hydrogels, irrespective of the presence of PDI nanoparticles. From all the images over 3 days, the cells appeared spherical and tended to stay in the same place, which suggested they were not migrating within the hydrogel over the 3 day period.

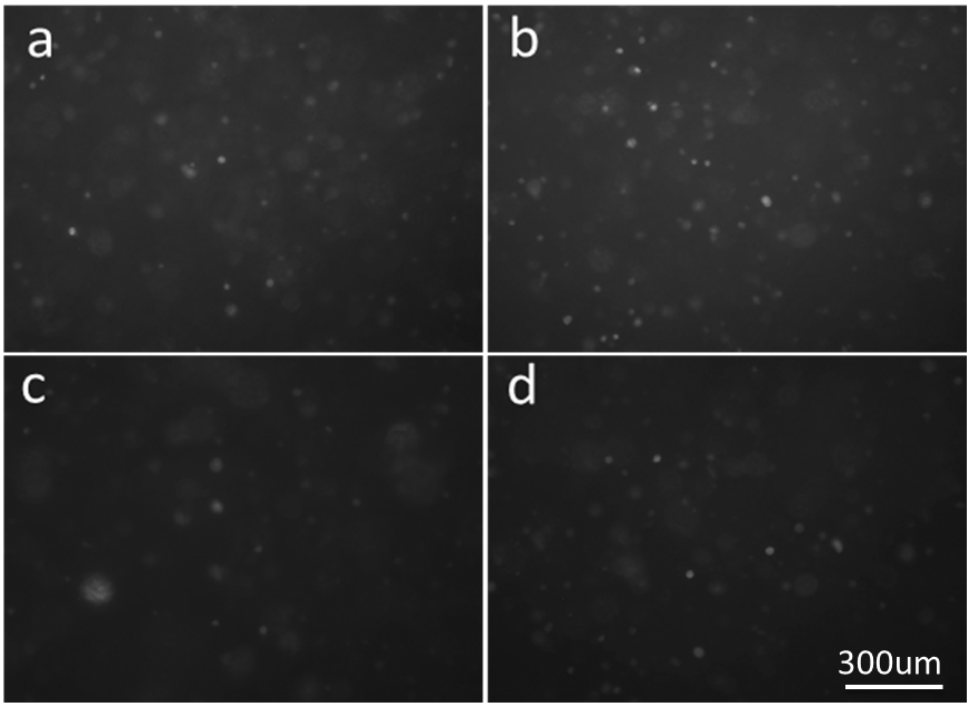

Figure 4-5. The representive ZsGreen images of incubated mouse MSCs after 24 h culture in thermo-setting chitosan-GP-hydrogel, as imaged by Cell IQ, without PDI nanoparticles (a for day 1, c for day 3) and with PDI nanoparticles (b for day 1, d for day 3).

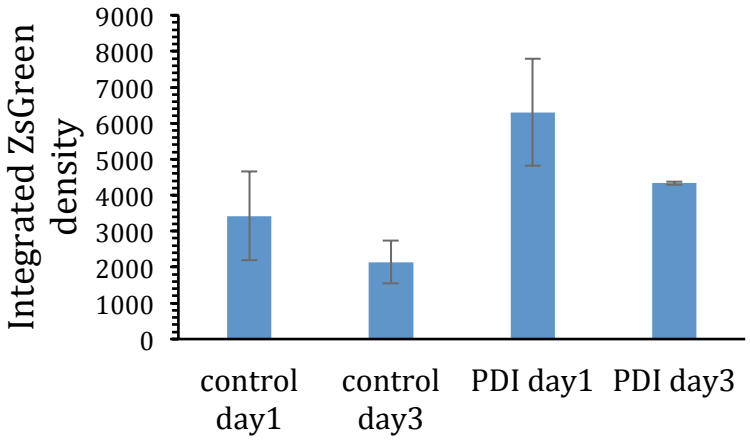

Figure 4-6. The integrated ZsGreen density changes over 3 days imaging time. The controls are for chitosan hydrogel without PDI nanoparticles. The error bars represent SD of 3 technical replicates.

The MSCs in chitosan-GP hydrogels were imaged with Cell-IQ for PDI fluorescence as well as imaging for ZsGreen over the 3 days. The images after incubating for 24 h are shown in **Figure 4-7**. Without PDI nanoparticles in chitosan hydrogel, no fluorescent image was obtained (**Figure 4-7c**). With the inclusion of PDI nanoparticles in the gel, both cells and hydrogels could be clearly observed, with some cells showing even stronger red fluorescence intensity than the gel. However, not all bright red spots corresponded with ZsGreen fluorescence. The most likely explanation for the presence of red spots that did not display green fluorescence is that some of the cells that became labelled with PDI nanoparticles from the gel might have died sometime later, leaving cell remnants containing PDI nanoparticles. There was no noticeable loss of PDI signal strength, suggesting minimal loss of PDI nanoparticles over the 3 days.

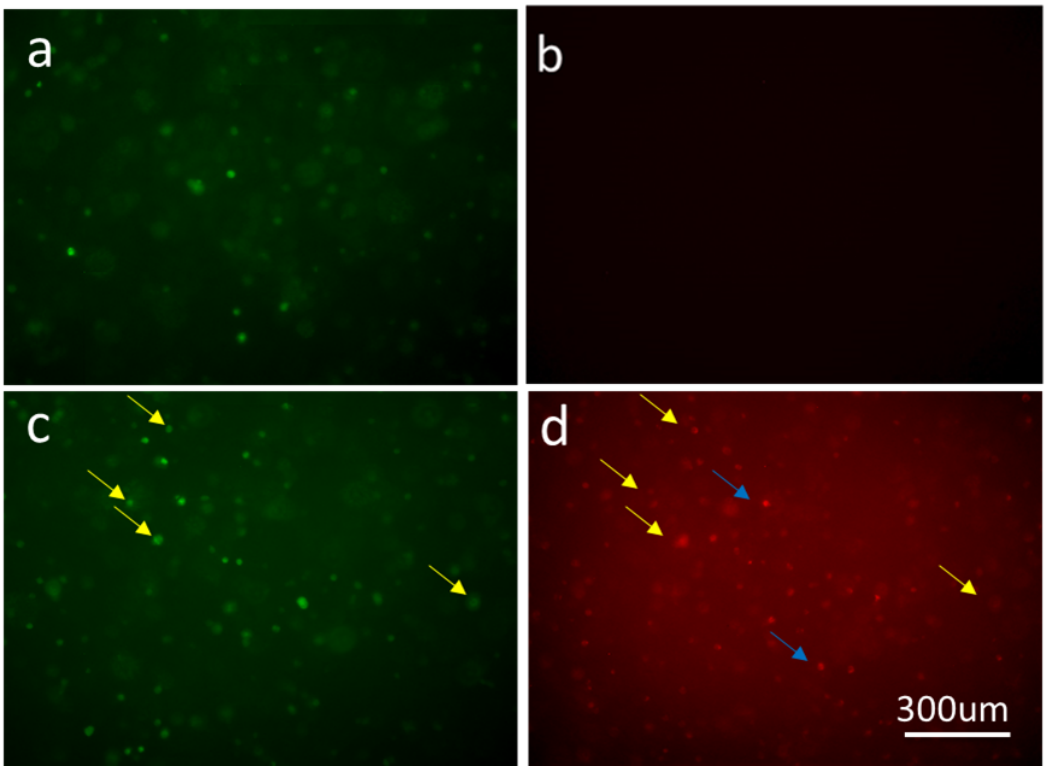

Figure 4-7. The images of incubated mouse MSCs after 24 h culture in thermo-setting chitosan-GP-hydrogel, as imaged by Cell IQ, without PDI nanoparticles (a for ZsGreen, b for PDI) and with PDI nanoparticles (c for ZsGreen, d for PDI). Yellow arrows indicate ZsGreen-expressing cells that appear to have uptaken PDI nanoparticles. Blue arrows indicate bright spots of PDI fluorescence that are not positive for ZsGreen.

The incubation was continued for a total of 2 months to investigate if cells could remain viable over the long-term and if the hydrogel maintained its integrity. For the chitosan hydrogel without PDI, the red colour comes from the phenol in the culture medium. For chitosan hydrogel with PDI, the gel systems look slightly green, due to the dispersed PDI nanoparticles. In all the wells, colonies of MSCs were observed on the gel surface, indicating that these cells must have undergone proliferation (**Figure 4-8**).

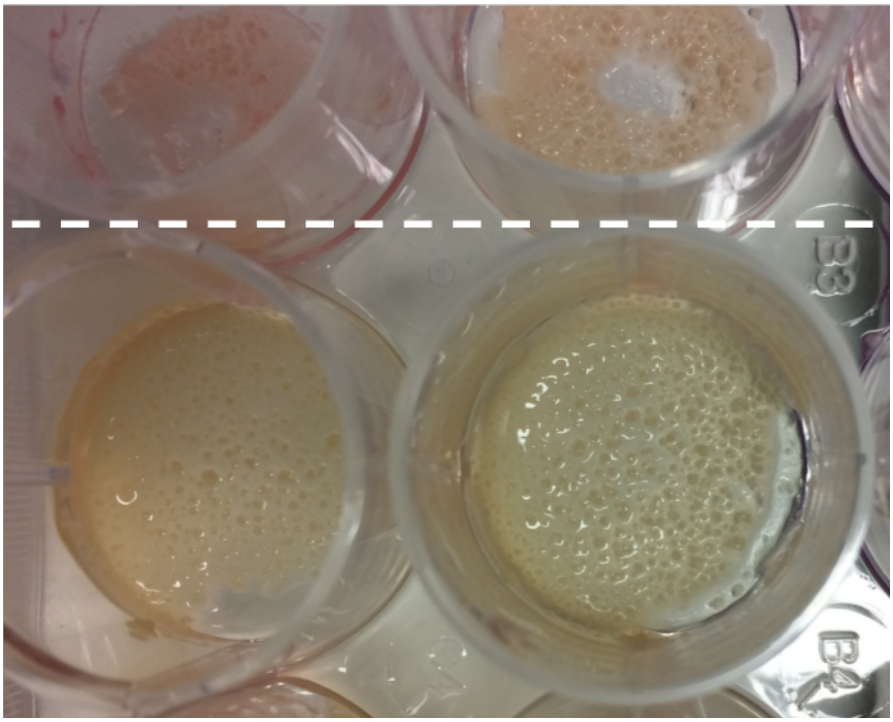

Figure 4-8. The photo of mouse MSCs in chitosan hydrogel after incubating for 2 months. Top row: chitosan hydrogel without PDI nanoparticles; bottom row: chitosan hydrogel with PDI nanoparticles.

Taken together, these results suggest that while MSCs embedded in the gel do not proliferate, those on the surface of the gel are able to do so, as shown by the presence of cell colonies (**Figure 4-8**).

4.4 Conclusions

Thermo-setting chitosan hydrogels have been prepared by carefully controlling the concentrations of chitosan, solution pH, and amount of GP added. The solution was prepared in an ice bath and a stable hydrogel could be formed when incubating the solution at 37 $^{\circ}$C for 30 min. Efforts have been made to reduce the amount of GP used because a higher concentration of GP in the gel could negatively affect cell viability.

With the addition of hydroxyethyl cellulose, the concentration of GP could be as low as 0.3 mg/ml with a stable chitosan hydrogel formed at 37 °C.

NIR-active PDI nanoparticles and mouse MSCs were readily encapsulated within the chitosan hydrogel. The loss of PDI nanoparticles from the hydrogel was recorded, and was slow in the first 5 days and then increased. This could have a negative impact on monitoring the stability and change of the chitosan hydrogel. For the encapsulation of mouse MSCs together with PDI nanoparticles in chitosan hydrogel, the mouse MSCs were found to grow in the hydrogel with or without PDI nanoparticles for 2 months. The fluorescence signals from PDI nanoparticles could be used to image the cells, indicating the uptake of PDI nanoparticles by the mouse MSCs, for up to two weeks. This would render the PDI-functionalised hydrogels unsuitable for in vivo monitoring. Future work should focus on developing functionalised hydrogels where the NIR particles do not transfer to the cells.

4.5 References

[1] Buwalda, S.J.; Boere, K.W.M.; Dijkstra, P.J.; Feijen, J.; Vermonden, T.; Hennink, W.E. Hydrogels in a historical perspective: From simple networks to smart materials. *J. Control. Release* **2014**, 190, 254-273.

[2] Li, Y.; Rodrigues, J.; Tomás, H. Injectable and biodegradable hydrogels: gelation, biodegradation and biomedical applications. *Chem. Soc. Rev*. **2012**, 41, 2193-2221.

[3] Ko, D.Y.; Shinde, U.P.; Yeon, B.; Jeong, B. Recent progress of in situ formed gels for biomedical applications. *Prog. Polym. Sci*. **2013**, 38, 672-701.

[4] Li, M.; Zeng, X.; Ma, C.; Yi, H.; Ali, Z.; Mou, X.; Li, S.; Deng, Y.; He, N. Injectable hydrogels for cartilage and bone tissue engineering. *Bone Res*. **2017**, 5, 17014.

[5] Kondiah, P.J.; Choonara, Y.E.; Kondiah, P.P.D.; Marimuthu, T.; Kumar, P.; du Toit, L.C.; Pillay, V. A review of injectable polymeric hydrogel systems for application in bone tissue engineering. *Molecules* **2016**, 21, 1580.

[6] Chang, B.; Ahuja, N.; Ma, C.; Liu, X. Injectable scaffolds: Preparation and application in dental and craniofacial regeneration. *Mater. Sci. Eng. R*, **2017**, 111, 1-26.

[7] Yang, J.-A.; Yeom, J.; Hwang, B.W.; Hoffman, A.S.; Hahn, S.K. In situ-forming injectable hydrogels for regenerative medicine. *Prog. Polym. Sci*. **2014**, 39, 1973-1986.

[8] Thambi, T.; Phan, V.H.G.; Lee, D.S. Stimuli-sensitive injectable hydrogels based on polysaccharides and their biomedical applications. *Macromol. Rapid Commun*. **2016**, 37, 1881-1896.

[9] Orive, G.; Santos, E.; Pedraz, J.L.; Hernández, R.M. Application of cell encapsulation for controlled delivery of biological therapeutics. *Adv. Drug Del. Rev*. **2014**, 67-68, 3-14.

[10] Liow, S.S.; Karim, A.A.; Loh, X.J. Biodegradable htermogelling polymers for biomedical applications. *MRS Bulletin* **2016**, 41, 557-566.

[11] Chenite, A.; Chaput, C.; Wang, D.; Combes, C.; Buschmann, M.D.; Hoemann, C.D.; Leroux, J.C.; Atkinson, B.L.; Binette, F.; Selmani, A. Novel injectable neutral solutions of chitosan form biodegradable gels in situ. *Biomaterials* **2000**, 21, 2155-2161.

[12] Ahmadi, R.; de Bruijn, J.D. Biocompatibility and gelation of chitosan-glycerol phosphate hydrogel. *J. Biomed. Mater. Res*, **2008**, 86A, 824-832.

[13] Naderi-Meshkin, H.; andreas, K.; Matin, M.M.; Sittinger, M.; Bidkhori, H.R.; Ahmadiankia, N.; Bahrami, A.R.; Ringe, J. Chitosan-based injectable hydrogel as a promising in situ forming scaffold for cartilage tissue engineering. *Cell Biol. Int*. **2014**, 38, 72-84.

[14] Songkroh, T.; Xie, H.; Yu, W.; Liu, X.; Sun, G.; Xu, X.; Ma, X. Injectable *in situ* forming chitosan-based hydrogels for curcumin delivery. *Macromol. Res*. **2015**, 23, 53-59.

[15] Yang, J.; Zhang, Y.S.; Yue, K.; Khademhosseini, A. Cell-laden hydrogels for osteochondral and cartilage tissue engineering. *Acta Biomater*., **2017**, 57, 1-25.

[16] Stucky, E.C.; Schloss, R.S.; Yarmush, M.L.; Shreiber, D.I. Alginate micro-encapsulation of mesenchymal stromal cells enhances modulation of the neuro-inflammatory response. *Cytotherapy*, **2015**, 17, 1353-1364.

[17] Moshaverinia, A.; Chen, C.; Akiyama, K.; Xu, X.; Chee, W.W.L.; Schricker, S.R.; Shi, S. Encapsulated dental-derived mesenchymal stem cells in an injectable and biodegradable scaffold for applications in bone tissue engineering. *J. Biomed. Mater. Res. A*, **2013**, 101A, 3285-3295.

[18] Ansari, S.; Diniz, I.M.; Chen, C.; Sarrion, P.; Tamayol, A.; Wu, B.M.; Moshaverinia, A. Human periodontal ligament- and gingiva-derived mesenchymal stem cells promote nerve regeneration when encapsulated in alginate/hyaluronic acid 3d scaffold. *Adv. Healthcare Mater.*, **2017**, 6, 1700670.

[19] Meier, R.P.H.; Mahou, R.; Morel, P.; Meyer, J.; Montanari, E.; Muller, Y.D.; Christofilopoulos, P.; Wandrey, C.; Gonelle-Gispert, C.; Bühler, L.H.; Microencapsulated human mesenchymal stem cells decrease liver fibrosis in mice. *J. Hepatology*, **2015**, 62, 634-642.

[20] Guo, X.; Park, H.; Liu, G.; Liu, W.; Cao, Y.; Tabata, Y.; Kasper, F.K.; Mikos, A.G. In vitro generation of an osteochondral construct using injectable hydrogel composites encapsulating rabbit marrow mesenchymal stem cells. *Biomaterials*, **2009**, 30, 2741-2752.

[21] Sala, R.L.; Kwon, M.Y.; Kim, M.; Gullbrand, S.E.; Henning, E.A.; Mauck, R.L.; Camargo, E.R.; Burdick, J.A. Thermosensitive poly(N-vinylcaprolactam) injectable hydrogels for cartilage tissue engineering. *Tissue Eng. A*, **2017**, 23, 935-945.

[22] Anderson, S.B.; Lin, C.-C.; Kuntzler, D.V.; Anseth, K.S. The performance of human mesenchymal stem cells encapsulated in cell-degradable polymer-peptide hydrogels. *Biomaterials*, **2011**, 32, 3564-3574.

[23] Benoit, D.S.W.; Schwartz, M.P.; Durney, A.R.; Anseth, K.S. Small functional groups for controlled differentiation of hydrogel-encapsulated human mesenchymal stem cells. *Nat. Mater.*, **2008**, 7, 816-823.

[24] Nelson, V.J.; Dinnunhan, M.F.K.; Turner, P.R.; Faed, J.M.; Cabral, J.D. A chitosan/dextran-based hydrogel as a delivery vehicle of human bone-marrow derived mesenchymal stem cells. *Biomed. Mater.,* **2017**, 12, 035012.

[25] Guowei Feng, Jimin Zhang, Yang Li, Yan Nie, Dashuai Zhu, Ran Wang, Jianfeng Liu, Jie Gao, Na Liu, Ningning He, Wei Du, Hongyan Tao, Yongzhe Che, Yong Xu, Deling Kong, Qiang Zhao and Zongjin Li. IGF-1 C domain–modified hydrogel enhances cell therapy for AKI. *JASN* **2016**, Feb 11, 1-13.

[26] Taylor, A.; Herrmann, A.; Moss, D.; Sée, V.; Davies, K.; Williams, S.R.; Murray, P. Assessing the efficacy of nano- and micro-sized magnetic particles as contrast agents for MRI cell tracking. *PLOS One* **2014,** 9, e100259.

[27] Supper, S.; Anton, N.; Seidel, N.; Riemenschnitter, M.; Curdy, C.; Vandamme, T. Thermosensitive chitosan/glycerophosphate-based hydrogel and its derivatives in pharmaceutical and biomedical applications. *Expert Opin. Drug Deliv*. **2014**, 11, 249 – 267.

Chapter 5. Conclusions and future work

5.1 General conclusions from my PhD work

This is a project that has been carried out in the Department of Chemistry and the Institute of Translational Medicine at the University of Liverpool. The overall target has been to design and fabricate (i) nanoprobes for tracking cells with fluorescence and multispectral optoacoustic tomography (MSOT), and (ii) cell-encapsulating hydrogels functionalised with NIR nanoprobes so that the hydrogels can be monitored in vivo with MSOT. MSOT is a novel type of photoacoustic scanner that can detect multiple photoabsorbers simultaneously, and could therefore allow both the cells and their encapsulating hydrogels to be monitored at the same time in a single animal, as long as the absorbance spectra of the nanomaterials was 40 – 50 nm apart [1]. To this end we synthesized a perylene diimide derivative (PDI) compound and PDI nanoparticles as nanoprobes for cell tracking and hydrogel functionalization. PDI was used because it has strong absorbance in the near infra-red (NIR) region of the spectrum, as well as high photo-stability and low cytotoxicity. Also, PDI is highly tunable, which means that it could be possible to synthesize nanoparticles with different absorbance maxima that could then be distinguished from each other using MSOT.

5.1.1 Synthesis of PDI nanoparticles

In **Chapter 2**, a perylene diimide derivative (PDI) compound was synthesized. The PDI organic solutions showed NIR absorbance, with the absorbance maxima varying according to which solvents were used. However, these first PDI nanoparticles were hydrophobic and could not be dissolved in water. Subsequently, aqueous PDI

nanoparticle suspensions were formed by solvent evaporation (nanoprecipitation) and emulsion freeze-drying methods. For both methods, poly (vinyl alcohol) (PVA) and a biocompatible surfactant Tocopherol polyethylene glycol succinate (TPEG) were effective in stabilizing PDI nanoparticles in water. In addition, a novel block copolymer $DEAMA_{50}DEGDMA_2OEGMA_{80}$ was used with the solvent evaporation method to prepare a stable PDI nanoparticle suspension. An NIR absorbance between 650-700 nm was recorded for the aqueous PDI nanoparticle suspensions in all cases.

5.1.2 Cell tracking with PDI nanoparticles

In **Chapter 3**, the focus was on evaluating the potential of PDI nanoparticles as cell labelling probes for MSOT. First, the cytotoxicity of the PDI nanoparticle suspension on MSCs was assessed. TPEG-stabilized nanoparticles were found to be toxic, whereas PVA-stabilized PDI nanoparticles were not. However, the uptake of these PDI nanoparticles was too low to be detected by UV-vis and MSOT. The low uptake of PVA-stabilized PDI nanoparticles by MSCs was addressed by the use of a novel block copolymer $DEAMA_{50}DEGDMA_2OEGMA_{80}$ in the solvent evaporation method. Strong signals by UV-Vis and flow cytometry were recorded for the MSC cell suspensions labelled with the block copolymer-stabilized PDI nanoparticles. A suitable concentration, with PDI and $DEAMA_{50}DEGDMA_2OEGMA_{80}$ (1:1 w/w), of 15 μg/ml, was found to generate strong signals and no toxicity. Based on these results, the PDI nanoparticles with the block copolymer as stabilizer at the concentration of 15 μg/ml were always used to label the MSCs.

PDI-labelled MSCs were imaged following subcutaneous implantation into mice with various imaging modalities over 11 days. In order to determine if the PDI nanoparticles had any effect on viability of the cells in vivo, MSCs expressing

luciferase were used in the in vivo experiment. By comparing PDI-labelled luciferase$^+$ MSCs with unlabelled luciferase$^+$ MSCs, it could be seen that there was no obvious difference in the bioluminescence signal. This suggested that there were no noticeable effect of the PDI nanoparticles on cell viability and proliferation. Furthermore, histology studies of the MSC masses stained with alizarin red and alcian blue indicated that the labelling with PDI nanoparticles did not affect the ability of MSCs to differentiate into bone or cartilage cells in vivo.

NIR fluorescence imaging could locate the PDI-labelled MSCs, but signal-to-noise was poor, so that it was difficult to distinguish the weakest signals from background. On the other hand, the PDI-labelled MSCs could be easily visualised with MSOT over 11 days (the study end point). This clearly demonstrates the high photo-stability of PDI nanoparticles. Compared with fluorescence imaging, apart from the increased sensitivity, MSOT is better able to pinpoint the location of the cells as it generates a high resolution tomographic image. For preclinical work, it may be ideal to combine bioluminescence imaging with MSOT using the genetic reporter, luciferase, and PDI nanoparticles, respectively, in order to have whole body and tissue-focussed imaging that allows viability and biodistribution to be monitored simultaneously.

Based on the results, PDI nanoparticles could have great potential as NIR imaging probes for regenerative medicine therapies (RMTs). The low toxicity, high photo-stability, and negligible leaking of PDI nanoparticles from the cells, are likely to be very useful for this kind of application. However, it must be considered that the cells were injected as a bolus subcutaneously, which facilitates imaging because the signal intensity per voxel is high. It is likely that imaging PDI-labelled cells following systemic injection would be more challenging because the signal would be much more dilute.

Lipophilic dyes such as DiR and DiO are commonly used for NIR fluorescence imaging in vivo. However, they may not have strong absorbance in the NIR region (emission NIR wavelength for NIR fluorescence imaging) and thus may not be suitable for MSOT. Secondly, these dyes have been found to transfer to neighbouring cells, leading to microenvironment contamination, as discussed in Chapter 1 [2]. Quantum dots, Au nanoparticles, and particularly Au nanorods have been reported widely as NIR probes for fluorescence imaging and MSOT. However, there are potential toxicity issues relating to quantum dots and Au nanorods when they are used in vivo. For instance, quantum dots contain heavy metals, such as cadmium, which are known to be toxic, and as Au is a very stable metal, it is not degraded in vivo, and could potentially persist in organs such as the liver and spleen, leading to toxicity in those organs [3,4]. Furthermore, quantum dots have a broad absorbance spectrum which is not favourable for MSOT [5].

We have shown that the PDI nanoparticles can be very useful for cell tracking pre-clinically, and they could also have some potential for clinical applications. For clinical application, the safety and the fate of PDI nanoparticles (their accumulation and excretion from the body) are crucial issues. While PDIs can be tailor-synthesized with desirable NIR absorbance wavelengths (which is very useful for imaging), the size and surface functionality of the PDI nanoparticles may also be finely tuned to promote excretion from the body after their diagnostic/therapeutic function is completed. This has been considered for further work.

5.1.3 Cell encapsulation with chitosan hydrogel functionalised with PDI nanoparticles

Chapter 4 describes the encapsulation of MSCs in PDI functionalised chitosan hydrogel in order to enable in vivo monitoring of hydrogel with MSOT. The aim was to develop a biocompatible hydrogel that would be fluid at room temperature to facilitate cell incorporation, but would gelate at body temperature. The gel could then be functionalised with PDI nanoparticles. This has been achieved with the preparation of an injectable thermosetting chitosan hydrogel. The key was to control the concentration of glycol phosphate disodium salt solution added into the aqueous chitosan solution. The resulting solution remained as fluid at room temperature but underwent gelation when switched to 37ºC. Aqueous PDI nanoparticles were blended into the chitosan solution, followed by temperature-triggered gelation at 37ºC. Similarly, PDI nanoparticles and the MSCs could be both encapsulated in chitosan hydrogel.

MSOT imaging of the encapsulating chitosan hydrogel functionalised with PDI nanoparticles has been performed in a view to monitoring the status/integrity of the hydrogel. Two problems were encountered with this part of the project. The first problem was that the cells were found to engulf the PDI nanoparticles. This could potentially be addressed in future by using larger PDI nanoparticles or modifying the surface of the PDI nanoparticles so that they would be less likely to be uptaken by the cells and/or would be more firmly attached to the hydrogel (*e.g.*, by crosslinking). The second problem was the loss of NIR nanoparticles from the hydrogels over the longer term. The results suggested that this was likely due to hydrogel degradation. The level of analysis undertaken (due to time constraints) did not allow us to ascertain whether the degree of hydrogel degradation showed a good correlation with the degree of particle loss. This situation may also be improved by using larger NIR particles or

modifying the surface of the NIR nanoparticle so that they can better attached to the hydrogel.

5.2 Perspective for future work

5.2.1 NIR organic nanoparticles

Promising results have been obtained with the use of PDI nanoparticles for MSOT imaging. Although they are very exciting, the observation and data are mostly qualitative, e.g., coefficient for NIR absorbance, the relationship between the absorbance and concentration in different medium. From the point of materials chemistry, there are many things that can be investigated in future. These include (1) Synthesis of perylene diimide derivatives with different functional groups at bay and peri positions to tune absorbance wavelength and solubility; (2) Varying the ratio of block copolymer to PDI to maximise absorbance intensity with high nanoparticle stability and low amount of block copolymer; (3) Using other block copolymers that have been developed in the group to stabilize PDI nanoparticles so that an even better stabilizer can be identified that can be used at lower concentrations. This can improve signal strength per mass and hence reduce potential side effects of the probe material. For MSOT imaging with the PDI nanoparticles, future work may include (i) Labelling other types of cells with PDI nanoparticles; (ii) Further improving the uptake of PDI nanoparticles in the cells (although we don't know yet the maximum uptake) so that even a small number of cells or under greater depth can be tracked; (iii) Investigate if and how the PDI nanoparticles would be excreted out of the body.

5.2.2 Hydrogels with NIR properties

The erosion and degradation of hydrogels have been monitored in vivo by non-invasive fluorescence [6]. Due to its superior properties (e.g., high imaging depth and imaging resolution), the use of MSOT to monitor the change of hydrogels in vivo has been highly anticipated. However, research in this area is rare. This can be mainly attributed to the lack of NIR-active hydrogels with strong absorbance. There has been previous attempts to trap large dye particles in porous PLGA scaffold [7], but these are not hydrogels and there is always the potential risk of dye particles leaching out. Indeed, my own research on encapsulating PDI nanoparticles in chitosan gel has been hampered by the leaking problem although over a relatively long time scale (Chapter 4). This may be addressed by forming PDI hydrogels with NIR absorbance in future work.

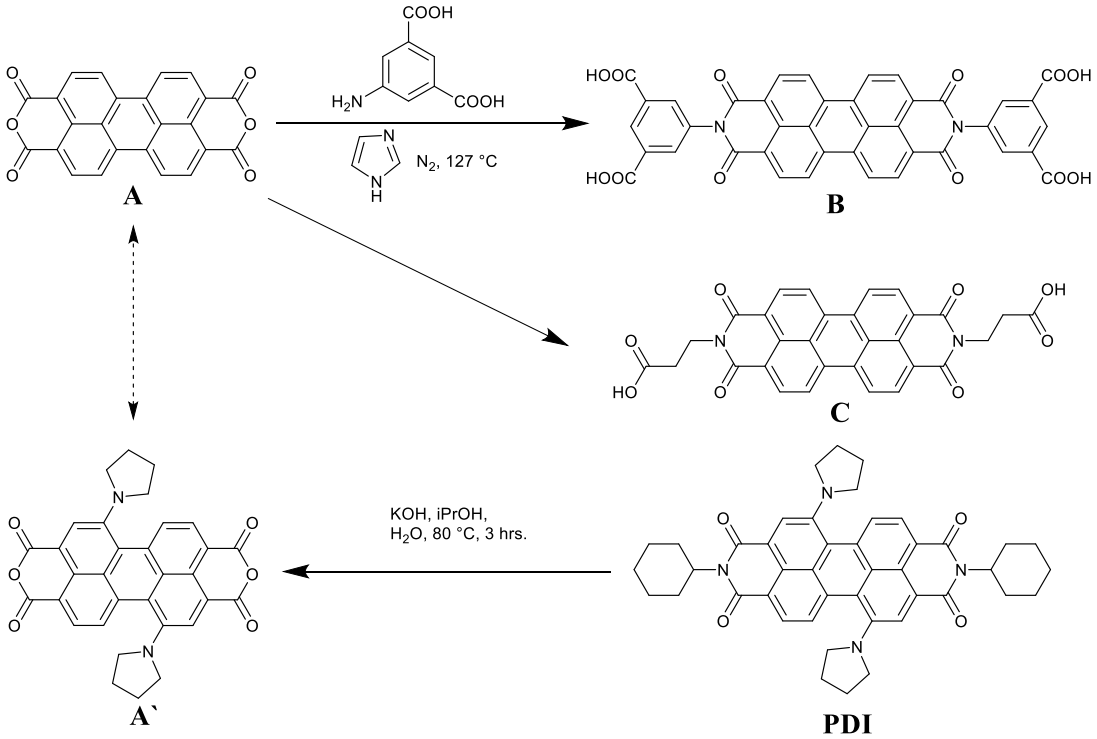

Scheme 5-1. Proposed routes for the synthesis of perylene diimide derivatives.

The Zhang group reported previously the formation of perylene diimide derivative (Compound B) hydrogel, following a synthetic route from Compound A to Compound B, as shown in Scheme 5-1 [8]. The hydrogels were formed by a pH-triggered gelation process. During my project, Compound C was synthesised via the reaction of 3-aminopropanoic acid with Compound A (Scheme 5-1). Similarly, hydrogels could be formed (Figure 5-1A). After freeze-drying the hydrogel, nanofibrous structures could be observed by SEM imaging (Figure 5-1B). This demonstrates the potential of synthesizing different compounds that can then be used to form hydrogels, preferably with desirable functional groups.

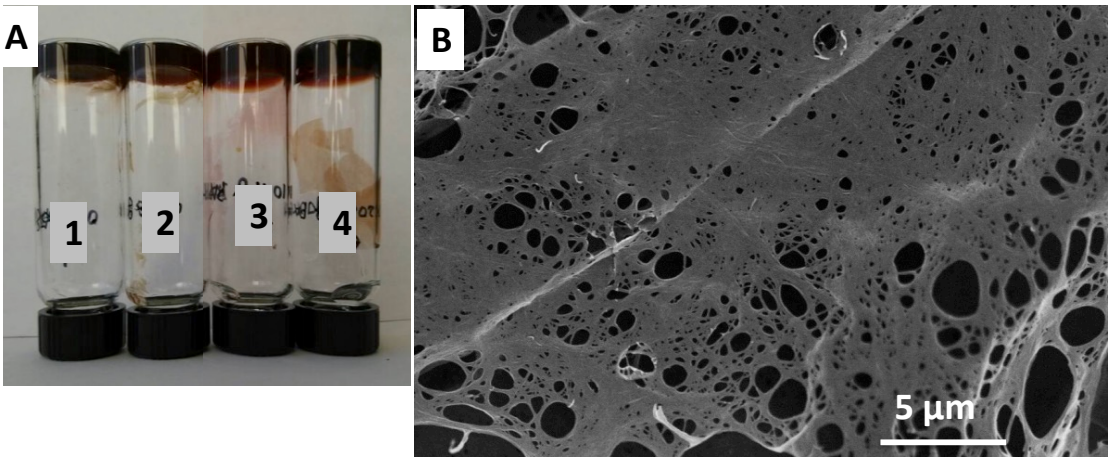

Figure 5-1. (A) The photo shows the hydrogels formed with Compound C in Scheme 5-1 and (B) the dry structure of the hydrogel 1.

It should be pointed out that compounds B and C do not have absorbance in the NIR region due to the lack of functional groups at the bay positions. However, it may be possible to use the PDI synthesized in Chapter 2 to produce the anhydride analogue (Compound A in Scheme 5-1). This anhydride compound may be used to produce hydrogels with NIR absorbance, like the synthesis of the compounds B and C (Scheme 5-1).

The gelation of perylene diimide derivatives can be initiated by the addition of acid or via the hydrolysis of glucono-σ-lactone (GdL) [3]. It may be also formed by blending with aqueous acidic polymer solution. In this regard, the hydrogel has been formed by blending the solution of Compound B in Scheme 1 with chitosan solution. The control of concentration and pH was critical for the formation of uniform hydrogels.

A big challenge is to encapsulate cells into these hydrogels. Because the hydrogels are triggered by low pH, the cells may not survive the low pH environment. Ideas may be borrowed from the chitosan thermosetting hydrogels, by adding some salts, or controlling the rate of hydrolysis so that the pH values do not go down too low.

5.3 References

[1] Taruttis, A.; Morscher, S.; Burton, N. C.; Razansky, D.; NtziachristosFast, V. Multispectral Optoacoustic Tomography (MSOT) for Dynamic Imaging of Pharmacokinetics and Biodistribution in Multiple Organs. *PLoS ONE,* **2012**, 7, e30491.

[2] Lassailly, F.; Griessinger, E.; Bonnet, D. "Microenvironmental contaminations" induced by fluorescent lipophilic dyes used for noninvasive in vitro and in vivo cell tracking. *Blood* **2010**, 115, 5347 – 5354.

[3] Tong, L.; Wei, Q.; Wei, A.; Cheng, J. Gold nanorods as contrast agents for biological imaging: optical properties, surface conjugation, and photothermal effects. *Photochem. Photobiol.* **2009**, 85, 21-32.

[4] Shashkov, E.V.; Everts, M.; Galanzha, E. I.; Zharov, V. P. Quantum dots as multimodal photoacoustic and photothermal contrast agents. *Nano Lett.* **2008**, 8, 3953–3958.

[5] Montalti, M.; Cantelli, A.; Battistelli, G. Nanodiamonds and silicon quantum dots: ultrastable and biocompatibile luminescent nanoprobes for long-term bioimaging. *Chem. Soc. Rev.* **2015**, 44, 4853-4921.

[6] Artzi, N.; Oliva, N.; Puron, C.; Shitreet, S.; Artzi, S.; bon Ramos, A.; Groothuis, A.; Sahagian, G.; Edelman, E.R. In vivo and in vitro tracking of erosion in biodegradable materials using non-invasive fluorescent imaging. *Nat. Mater.* **2011**, 10, 704 – 709.

[7] Zhang, Y.S.; Cai, X.; Yao, J.; Xing, W.; Wang, L.V.; Xia, Y. Non-invasive and in situ characterization of the degradation of biomaterial scaffolds by volumetric photoacoustic microscopy. *Angew. Chem. Int. Ed.* **2014**, 53, 184-188.

[8] Liu, X.; Roberts, A.; Ahmed, A.; Wang, Z.; Zhang, H. Carbon nanofibers by pyrolysis of self-assembled perylene diimide derivative gels as supercapacitor electrode materials. *J. Mater. Chem. A* **2015**, 3, 15513-15522.

Appendix

A-0: List of items:

A-1: List of figures

A-2 List of tables

A-3: List of schemes

A-4: The manuscript on chitosan hydrogel

Chitosan hydrogels crosslinked with benzene tricarboxylic acid and some applications

Yonghong Yang,[†,‡] Patricia Murray,[‡] Haifei Zhang[*,†]

[†] Department of Chemistry, University of Liverpool, Liverpool, L69 7ZD, UK

[‡] Department of Cellular and Molecular Physiology, Institute of Translational Medicine, University of Liverpool, Liverpool, L69 3GE, UK

ABSTRACT: Chitosan hydrogels crosslinked by 1,3,5-benzene tricarboxylic acid (BTC) in the form of beads can be readily prepared at room temperature by adding aqueous chitosan solution dropwise into BTC-ethanol solution. L929 cells could survive for at least 24 h during culturing with the chitosan hydrogel although the cells did not attach to the hydrogel. Both hydrophobic and hydrophilic compounds, as demonstrated with model dyes, could be easily encapsulated within the chitosan gel beads, and the sustainable release of hydrophilic dyes could be achieved. Due to the use of BTC as crosslinker, the chitosan gel beads were used as scaffolds to prepare chitosan-based composite beads by reaction with copper acetate. The composite beads showed the presence of crystalline phase which, however, is not consistent with the powder x-ray diffraction pattern of the targeted metal-organic framework HKUST-1. This may be attributed to the lack of free BTC molecules in the hydrogel and hence it is difficult to form the linkage between Cu^{2+} and BTC as in HKUST-1.

INTRODUCTION

Hydrogels have been extensively used as scaffolds for tissue engineering and as carriers for drug delivery.[1,2] Hydrogels can be formed from both synthetic and natural polymers.[1] The basic requirements include biocompatibility, biodegradability, mild processing conditions, and the ease for further modification. Chitosan, the only cationic natural polymer, has been extensively used as scaffolds for tissue engineering,[3,4] cell culture,[5] and drug delivery.[6,7] Chitosan is the deacetylation product of chitin, which is a natural polysaccharide, poly(β-(1→4)-N-acetyl-D-glucosamine), and is the second most abundant polymer after cellulose.[8] The common sources of chitin are crab and shrimp shells. There are two forms of chitin, α-chitin and β-chitin, with α-chitin being the most common. It is difficult to dissolve chitin in conventional solvents, which limits its applications. Chitin can be deacetylated under heating in concentrated NaOH to produce chitosan.[9]

Chitosan is usually present as a copolymer, defined by the degree of deacetylation. When the degree of deacetylation is greater than 50%, it is called 'chitosan' and can be dissolved in acidic water. The structure of chitosan (considering it is 100 % deacetylated) is very similar to cellulose, with $–NH_2$ group replacing one of the –OH groups on cellulose. The presence of the $–NH_2$ groups on chitosan is significant as it can be protonated to be soluble in water (providing positive charges) and facilitates chemical modifications.[8] One of the most common methods to modify chitosan is by carboxylation at the –O or –N position.[8] Carboxymethyl chitosan is soluble in neutral water and has found unique applications in drug delivery and tissue engineering.[10] There are also other chemical modifications,[8] including, amino acid-modified chitosan for biomedical applications.[11] Chitosan can also be blended with

other polymers to produce hybrid hydrogels; for example, chitosan-alginate hydrogel for tumour treatment,[12] collagen-chitosan for endothelial differentiation and angiogenesis.[13]

Chitosan hydrogels are formed by chemical crosslinking, physical crosslinking, or electrostatic interaction.[14] Due to the positive charge of chitosan in solution, multivalent cations or negatively charged polymers (e.g., certain proteins, nucleic acids) can be used to form hydrogels via ionic interaction. Another way to produce physically crosslinked hydrogels is by adding base into a chitosan solution. The increase of pH leads to deprotonation of chitosan, reduced solubility, and self-assembled gels by H bonding, hydrophobic interaction, and Van der Waals forces. This can be simply achieved by adding NaOH or Na_2CO_3. However, these hydrogels are heterogeneous due to the dramatic change of local pH. Chitosan hydrogels for cell culture are usually produced by crosslinking chitosan with calcium phosphate,[5] triphosphate,[15] and β-glycerol phosphate.[16-18] Chitosan is often chemically crosslinked with glutaraldehyde.[8,19] However, due to its toxicity, glutaraldehyde can be replaced with biocompatible crosslinkers such as heparin[20] and genipin.[21] Chitosan hydrogels may be prepared as bulky gels (by simple gelation of chitosan solution), injectable gels,[16-18] microparticles,[22] nanoparticles,[9,22,23] or nanofibers.[24]

Chitosan is usually dissolved in water with the aid of monocarboxylic acid such as acetic acid or formic acid. Dicarboxylic acids such as oxalic acid, succinic acid, malic acid, and adipic acid have been used to dissolve chitosan and also act as crosslinkers. The chitosan solutions with dicarboxylic acid were either freeze dried[25] or air dried.[26] The resulting dry materials could take up water to form hydrogels with improved mechanical strength.[25] However, to form hydrogels without the drying step, a mixture of N-hydroxysuccinimide (NHS) and 1-ethyl-3-(3-

dimethylaminopropyl)carbodiimide (EDC) was required to facilitate the gelation process.[27,28]

Here, we describe a new method to prepare chitosan hydrogels using 1,3,5-benzyl tricarboxylic acid (BTC) as a crosslinker by dropping aqueous chitosan solution into BTC-ethanol solution. The chitosan gel beads or films can be readily formed at room temperature. To the best of our knowledge, this is the first study to use BTC as a crosslinker to produce chitosan gel, although there has been a report to form supramolecular hydrogels from BTC and hydroxyl pyridines, via the interaction between the –COOH group and –N containing group.[29] The chitosan-BTC hydrogels were evaluated for their cytotoxicity and their potential for encapsulation of hydrophilic and hydrophobic compounds and sustainable release. BTC is a common ligand to synthesize one of the most widely investigated metal-organic framework (MOF) HKUST-1 under mild conditions[30-32] and MOFs are extensively used for a range of applications including biomedical applications such as drug delivery.[33] We have therefore also attempted to synthesize chitosan/HKUST-1 composite beads using the chitosan-BTC hydrogel beads as scaffolds.

RESULTS AND DISCUSSION

Morphological characterization of chitosan hydrogel. Typically the chitosan (medium molecular weight) solution was prepared with 0.6 v/v% acetic acid in water. BTC was dissolved in ethanol and used as the crosslinking agent. The low density of the ethanol solution allows the drops of aqueous solution to sink through. When dropping chitosan solution using a syringe, the droplets gelled rapidly in the BTC solution before hitting the bottom. The gelation process produced the gel beads with sufficient mechanical stability so that no deformation of the beads occurred at the

bottom of the glass beaker. The gel beads were kept in the BTC solution for 1 h at room temperature, to allow for full gelation. The formation of the chitosan gel beads was significantly influenced by the concentrations of both chitosan and BTC. It was noted that a BTC concentration of > 2 mM and chitosan concentration of > 5 mM were required to form the gel beads in a glass vial.

The chitosan gel beads formed were mechanically quite strong and could be handled easily. This was supported by observation of a dense porous structure of the dry bead. The chitosan gel beads were both air dried (Figure 1a-b) and freeze dried (Figure 1 c-d). Freeze-drying is a process that can be used to produce highly porous materials with minimal shrinkage with or without ice crystals as templates.[34] Surface wrinkles were observed in both cases. The higher magnifications of the surface morphology by scanning electron microscopy (SEM) showed no macroporous structures, although some macropores observed on the freeze-dried sample (Figure 1d).

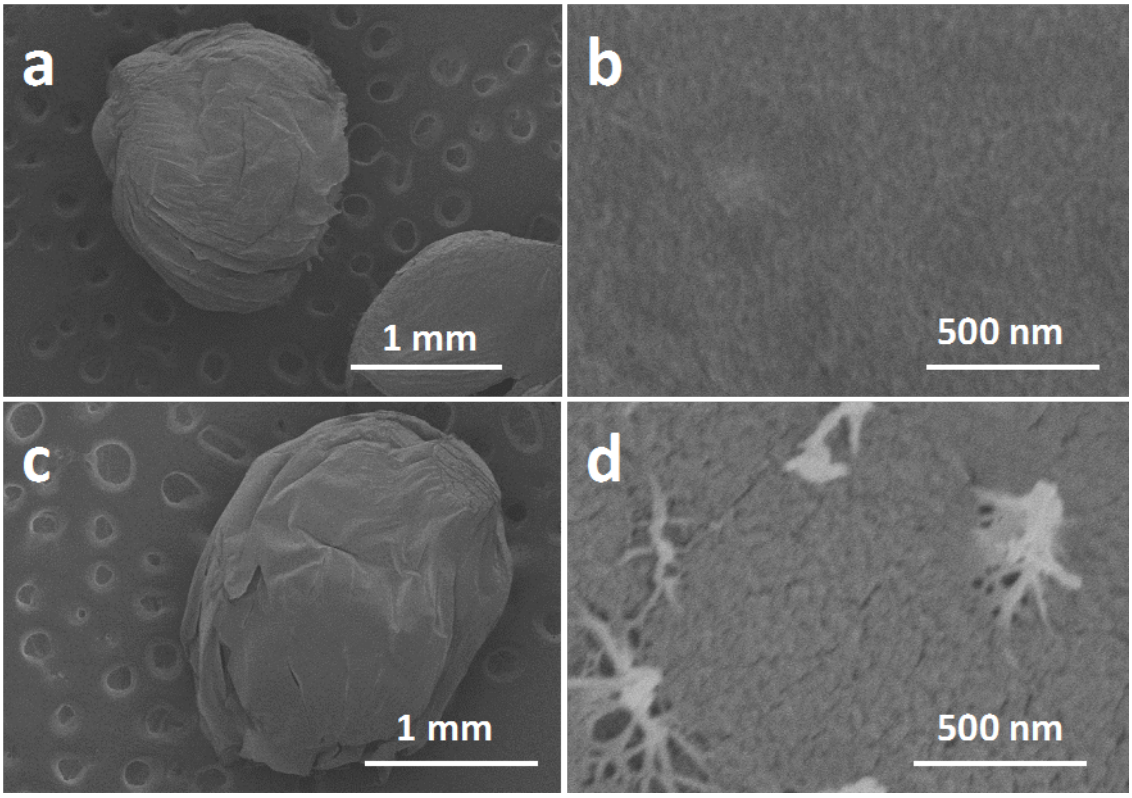

Figure 1. SEM images of dry BTC-chitosan beads prepared by adding 1 wt% chitosan solution into 50 mM BTC-ethanol solution. (a) the air-dried beads and (b) the bead surface at a higher magnification; (c) the freeze-dried bead and (b) its surface structure at higher magnification.

Chitosan beads were also prepared using the conventional crosslinkers sodium triphosphate (NaTPP) and NaOH. In the preparation, aqueous chitosan solution was added dropwise in the aqueous solution containing NaTPP or NaOH. Under similar preparation conditions, the gel beads formed from NaOH and NaTPP were much weaker. Due to the poor mechanical stability, the chitosan gel beads formed from NaOH solution were further chemically crosslinked using the biocompatible crosslinker genipin. Figure 2 shows the photograph and the microscopic image of three types of chitosan beads. As can be seen, the NaTPP-chitosan bead is transparent. The genipin-crosslinked chitosan bead is very stable and shows a dark greenish colour. The BTC-chitosan bead is transparent in ethanol. However, it turns translucent after washing with water.

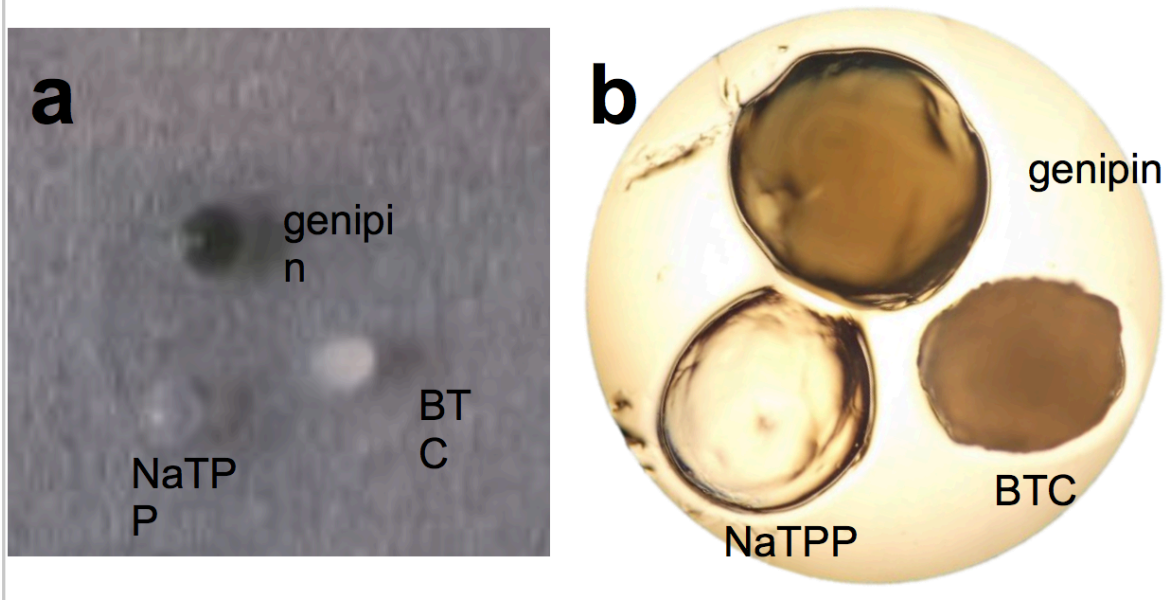

Figure 2. The photograph (a) and the optical microscopic image (b) of chitosan beads (~ 2 mm) prepared using BTC, NaTPP, NaOH/genipin as crosslinkers.

The porous structure of the BTC-chitosan bead was very different from the chitosan beads prepared by the conventional NaTPP and genipin crosslinking methods, where the interconnected macroporous structures could be both observed (Figure 3).

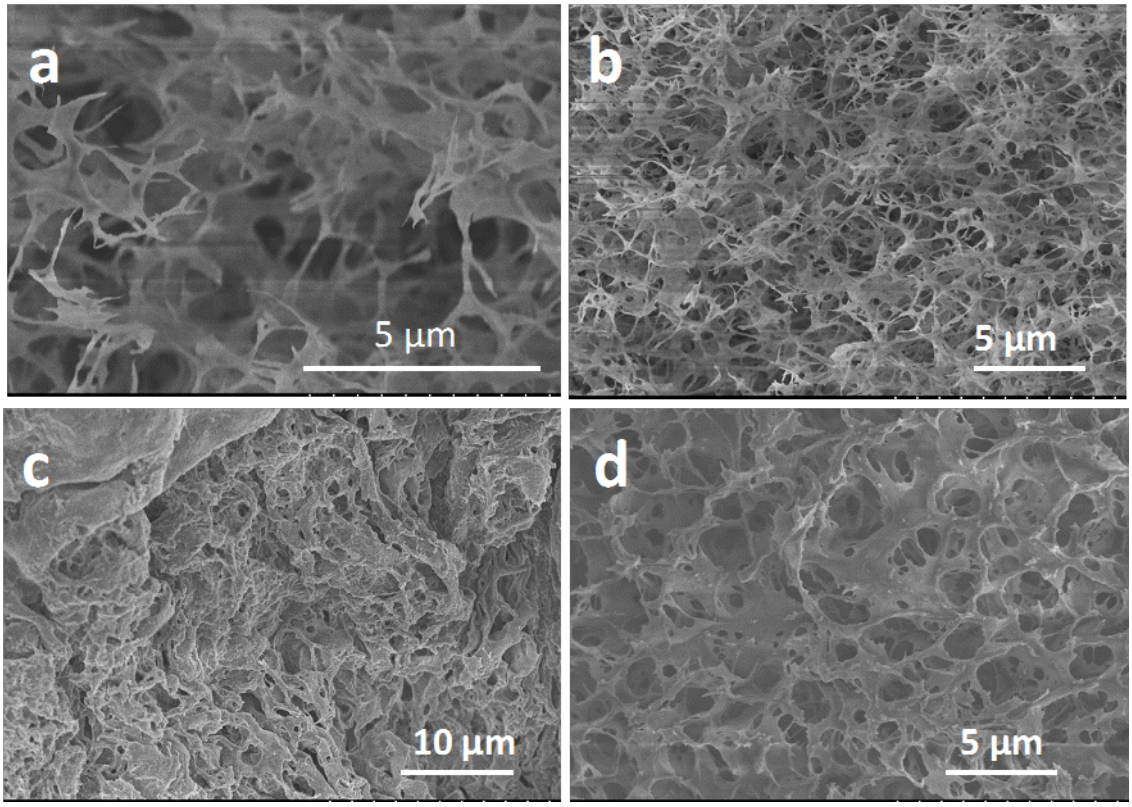

Figure 3. The interconnected macroporous structures of the freeze-dried chitosan gel beads prepared using NaOH/genipin and NaTPP. (a-b) Chitosan beads were firstly formed in dilute NaOH solution and then crosslinked by genipin; (c-d) Chitosan beads were formed directly by dropping chitosan solution into the aqueous NaTPP solution.

Ice-templating and freeze-drying can be used to produce layered porous materials, interconnected porous structures, or nanofibrous structures.[34-36] The freeze-dried BTC-chitosan bead was crushed to reveal the internal structure. Some layered structures were observed, a result of ice templating (Figure 4). No macropores were observed within the layer. This may restrict its use as a 3D scaffold for cell growth. However, this issue may be addressed or improved by preparing chitosan hydrogels with dilute solutions. For example, although the chitosan beads discussed above were formed by dropping 1 wt% chitosan solution in 50 mM BTC-ethanol solution, the decreased concentration of BTC solutions was still able to form chitosan beads. It was

found that chitosan beads could be formed in the concentration range of 20 mM – 0.5 mM. With the lower concentrations, the beads became bigger and softer. When the BTC concentration was lower than 0.5 mM, gel pieces instead of gel beads were formed. Thus, a lower concentration of BTC and/or chitosan may be able to produce chitosan beads with higher porosity.

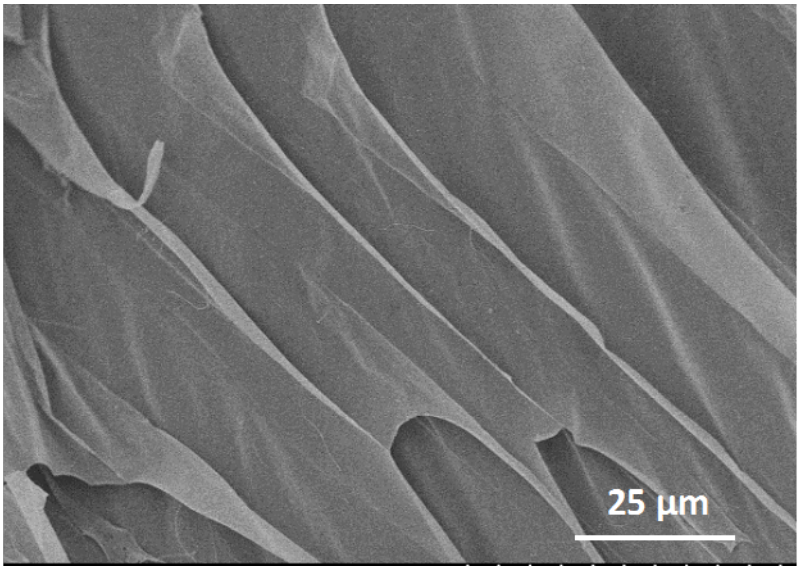

Figure 4. The internal structure of a freeze-dried chitosan gel bead with BTC as revealed by imaging the cross-sectioned bead.

The BTC gelation method is simple and convenient because the gelation occurs at room temperature. Compounds containing two carboxylic groups (*e.g.,* glutamic acid and succinic acid) were used to crosslink chitosan or enhance chitosan gel properties. However, either heating the solution (e.g., to 70 ^{o}C)[27] or an additional room temperature crosslinking mechanism is required.[28] Due to the simplicity of our method, chitosan gel beads, dots, films, or 3D gels could be readily prepared. For example, chitosan gel film could be prepared by evenly spreading on a coverslip and then soaked into BTC solution. Hydrogel dots on coverslip were prepared by placing chitosan

solution droplets on the coverslip instead of evenly spreading the chitosan solution and then immersing into the BTC solution.

Cytotoxicity evaluation of chitosan hydrogel. Chitosan-based hydrogels have been widely used to support cell growth. The chitosan hydrogel dots on the coverslip were evaluated by culturing L929 cells on them. As shown in Figure 5, L929 cells grew well on the glass substrate but did not attach to the gel bead with BTC crosslinking.

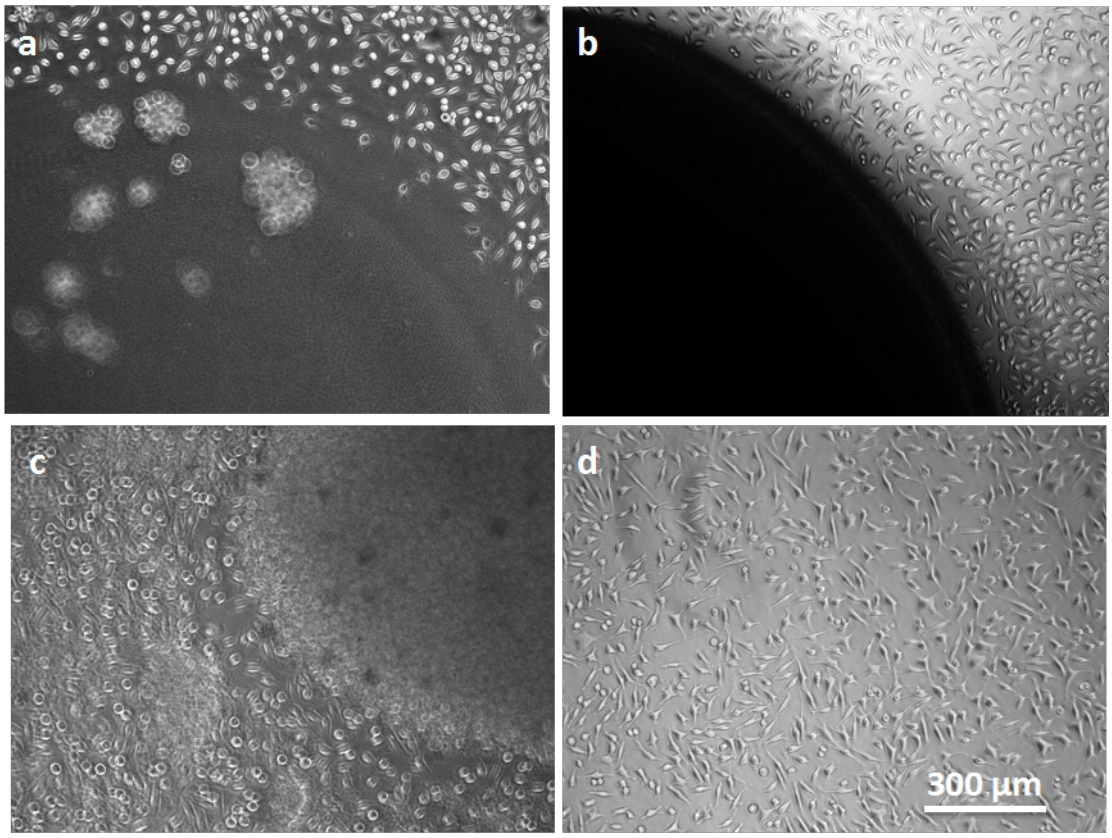

Figure 5. Culturing L929 cells on various substrates. (a) A BTC-crosslinked chitosan bead on glass. The cells grew well on the glass away from the chitosan bead; (b) The chitosan bead formed by genipin crosslinking; (c) The chitosan gel bead formed by NaTPP crosslinking. (d) The control with glass substrate. The scale bar is the same for all images.

For the chitosan dots crosslinked with genipin, the material was too thick to be viewed clearly, but there were cell aggregates on the NaTPP-crosslinked chitosan; the cells on this substrate appeared rounded, and were not elongated like the cells on the glass substrate. Cells cultured on BTC-crosslinked chitosan dots did not survive beyond 24 h. It is speculated that the poor biocompatibility and scaffolding property may be attributed to the presence of trace amounts of ethanol and the BTC in the hydrogel. Developing procedures to completely remove ethanol and BTC may be able to improve the gel's biocompatibility.

Encapsulation of hydrophilic/hydrophobic dyes and sustainable release of hydrophilic dye. To achieve encapsulation, hydrophilic compounds may be dissolved in aqueous chitosan solution and encapsulated *in situ* within the formed chitosan hydrogel. For hydrophobic compounds (e.g., poorly water-soluble drug compounds), the low solubility in water can be a significant issue.[37] Although powders of hydrophobic compounds may be directly encapsulated within chitosan gels, that does not improve water solubility as a result of encapsulation. It is however possible to prepare hydrophobic drug nanoparticles to enhance water solubility [37] and encapsulate them thereafter. It should be pointed out that many of these hydrophobic drug compounds are soluble in polar organic solvents such as ethanol. However, these compounds can be encapsulated into the BTC-chitosan hydrogel, by firstly dissolving them in the ethanol solution with BTC. When dropping chitosan solution into the BTC-ethanol solution to form gel beads, the target compounds may be encapsulated into the gel beads.

Figure 6. Photo of the chitosan-BTC gel beads with encapsulated Oil Red O in 1 wt% acetic acid solution.

This concept was demonstrated by encapsulating two model dyes, the polar Rhodamine 6G (soluble in both water and ethanol) and the hydrophobic Oil Red O (OR, very low solubility in water but good solubility in ethanol) in the BTC-chitosan beads. In both cases, the formed chitosan gel beads were red, indicating that OR and Rhodamine 6G were successfully encapsulated into the beads. Figure 6 shows the OR-encapsulated chitosan beads suspended in 1 wt% acetic acid aqueous solution, demonstrating the encapsulation of the hydrophobic dye and the stability in acidic water. Due to the presence of ethanol in the gel bead and the fact that ethanol is a solvent for OR, the hydrophobic red dye could be released during washing using water. The presence of ethanol in the gel bead may not be ideal for drug release. Because of the difference in vapor pressure for water and ethanol, it is possible to remove ethanol from the gel bead by evaporation or vacuum drying. There will be loss of water during the processing, but the beads can be re-hydrated and used as carriers for release.

The release of the hydrophilic dye, Rhodamine 6G, into aqueous medium from chitosan gel beads was successfully performed. The beads were prepared by adding 2 mL chitosan 1 wt% solution containing 1mg/1mL Rhodamine 6G dropwise into 20 mL 50mM BTC ethanol solution, aged for 10 minutes. After this, the chitosan beads

encapsulated with Rhodamine 6G were taken out from the BTC solution and then immersed in 20 mL freshly prepared phosphate buffer solution (PBS). This was to minimize the release of Rhodamine 6G into ethanol while still maintaining sufficient gelation. As shown in Figure 7a, a near-linear release profile is obtained in the first 20 minutes. There is no burst release as observed previously with the freeze-dried chitosan.[38] The release then slowed down and the releasing profile flattened at about 60 minutes with the absorbance recorded as 0.774. This sustained release profile may be potentially very useful for drug delivery.[39] At this stage, the beads were still red and the red intensity of the release medium was quite similar. The beads were left in the solution for a total of 24 hours, with the absorbance reading 0.819. It is thus clear that there was minimal release in the last 23 hours. This suggests that the release of Rhodamine 6G has reached equilibrium in the first 60 minutes. In order to further release the encapsulated Rhodamine 6G, the still-red chitosan beads were taken out and placed in another 20 mL of freshly prepared PBS solution (Figure 7b). Further release can be clearly seen until about 40 minutes and then slowed down and reached equilibrium at around 60 minutes. The release may be continuous if there is a mechanism that consumes the released compound.

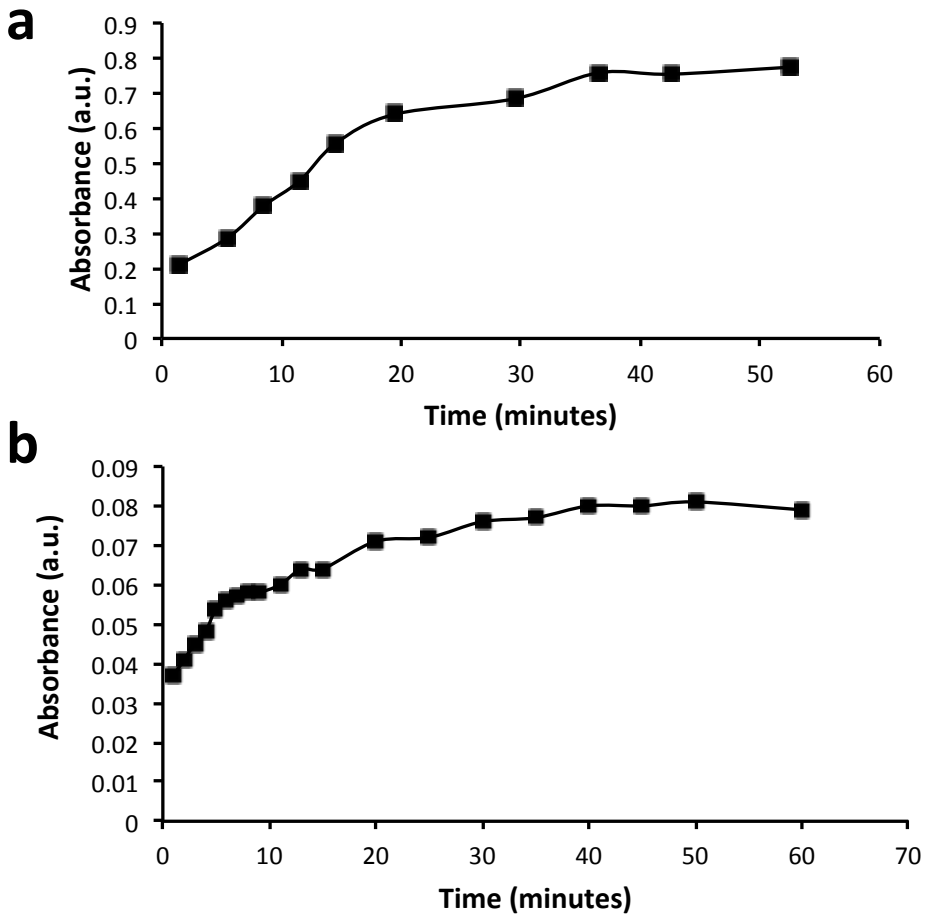

Figure 7. The release of Rhodamine 6G in the PBS at room temperature. (a) As-prepared chitosan bead with encapsulated Rhodamine 6G; (b) The beads from (a) were replaced in fresh PBS.

Chitosan-based composite beads. The reactions of metal ions and organic ligands can produce crystalline microporous MOFs[33] or metal-organic gels (MOGs, usually amorphous porous materials).[40] One of the earliest and most widely investigated MOFs is HKUST-1, which is formed from copper salts (usually copper acetate) and BTC. Although MOFs are commonly synthesized under solvothermal conditions, HKUST-1 can be prepared under mild conditions. For example, BTC and copper acetate powders were mixed and then packed into a column, which was soaked with a suitable amount of solvent. A HKUST-1 monolith was formed after heating in

an oven at 80 ^{o}C.[30] In another study, the DMSO (dimethyl sulfoxide) solution of BTC and copper acetate was freeze-dried and a subsequent thermal treatment in the presence of ethanol vapor was carried out to ensure the formation of highly crystalline and hierarchically porous HKUST-1 monolith.[31] Ameloot et al pumped aqueous solution of copper acetate as droplets into the continuous flow of 1-octanol containing BTC. The reaction at the interface of oil and water phases at room temperature resulted in the production of HKUST-1 hollow capsules.[32] Based on these studies, it was proposed to use the BTC-chitosan gel beads as scaffolds to prepare chitosan-HKUST-1 beads, via the reaction with copper ions in a solution.

The BTC-chitosan gels were soaked in both aqueous and ethanolic solutions of copper acetate with the same concentrations (3.6 g copper acetate in 50 mL distilled water or ethanol). After the reaction, blue beads were obtained in both cases, indicating the incorporation of Cu ions into the gel bead. When the beads were cut into halves, the blue colour was found to be distributed across the whole bead (Figure 8a). The only difference was that a relatively hard blue shell was formed when beads were placed in the aqueous copper acetate solution, while blue translucent jelly beads were formed in the ethanolic solution. The rapid evaporation of ethanol during imaging led to shrinking and roughening of the surface (Figure 8b).

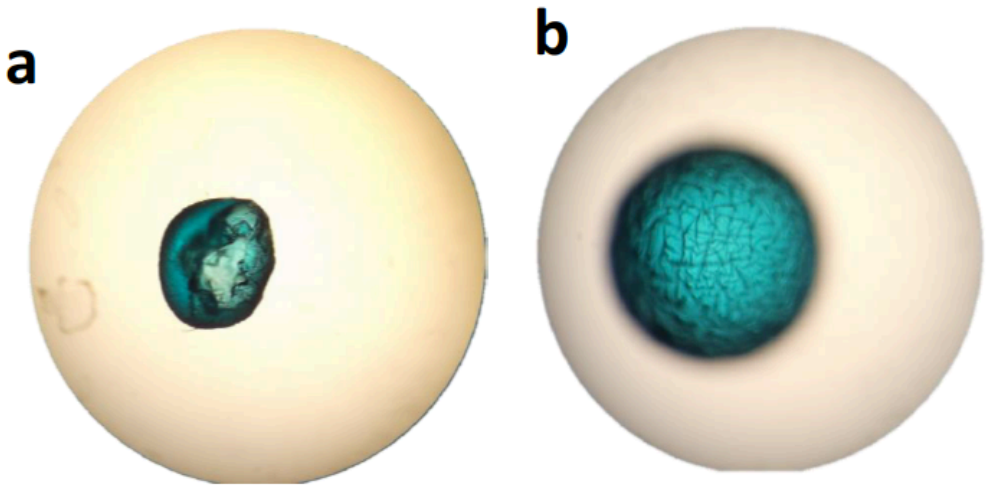

Figure 8. Optical microscopic images show the blue bead produced by immersing the BTC-chitosan gel bead in the ethanol solution of copper acetate. (a) The bead was cut in half and immediately imaged. (b) The rough surface of the bead is the result of rapid evaporation of ethanol during imaging. The beads are around 2 mm in diameter.

When chitosan gel beads were dried in air or under vacuum at room temperature or elevated temperature, the beads shrank considerably and it was very difficult to rehydrate them in water. However, there was no such problem when air drying the blue composite beads. Figure 9a & b show the beads after drying. This was attributed to the reaction of Cu ions with BTC that enhanced the mechanical stability of the beads. Although the surface looked rough by optical microscopic imaging, the completely dry beads exhibited a rather smooth surface at high magnifications. The surface of the beads was very dense and it was difficult to see any pores by SEM imaging even at a relatively high magnification of 60K. The bead was crushed to reveal the internal structure, showing a more porous layer structure with a rough surface (Figure 9c and d).

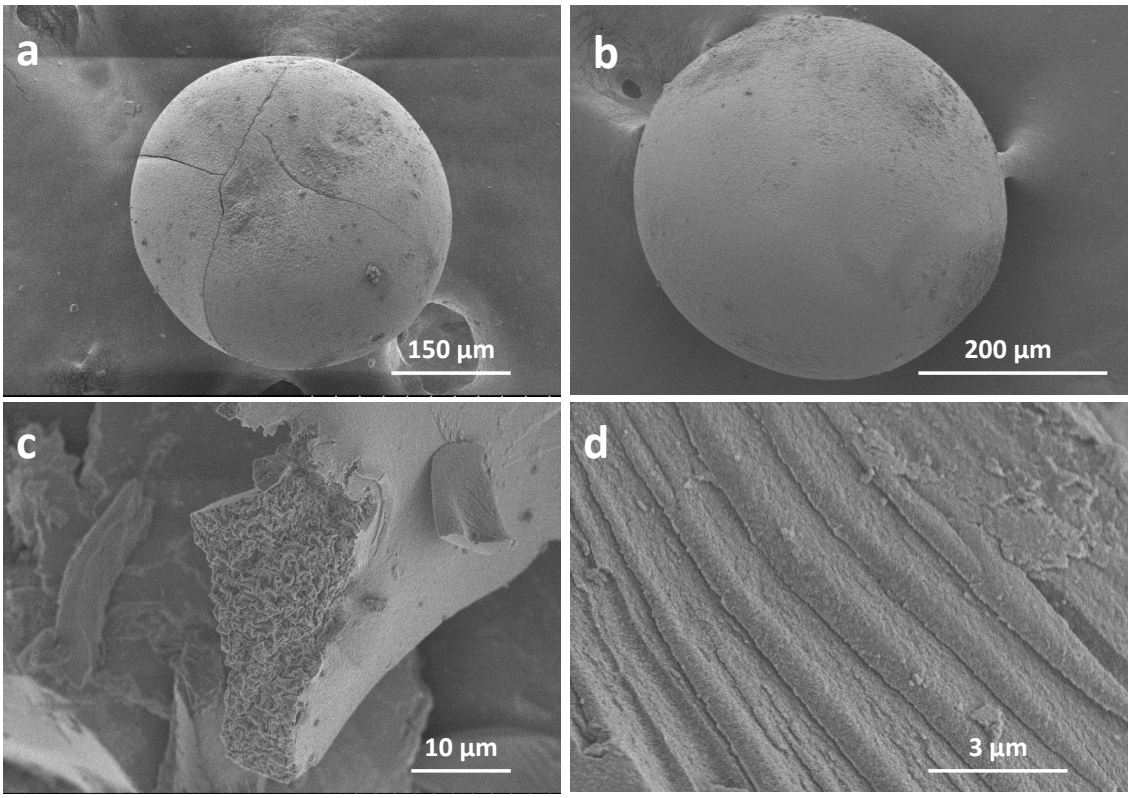

Figure 9. SEM characterization of air-dried BTC-chitosan gel beads after reaction with copper acetate. (a) Bead produced from aqueous copper acetate solution; (b) Bead produced from ethanol copper acetate solution. (c & d) The internal structure of the bead shown in (b) after being crushed.

The crushed bead powders were further examined using powder x-ray diffraction (PXRD) analysis. Similar PXRD patterns were obtained for the beads produced from aqueous and ethanol solution of copper acetate. Figure 10 shows the PXRD pattern for the dry bead prepared from the reaction with ethanol copper acetate solution. A number of sharp peaks can be observed, indicating a crystalline material or a material with high crystalline content. However, this pattern is not consistent with the pattern obtained for standard HKUST-1, indicating that HKUST-1 is not formed.[30-31] We have not identified what the crystalline material is at this stage although it is likely to be copper oxides, copper hydroxides, or another type of MOF structure. The

structure cannot be identified via single crystal x-ray diffraction because the beads are still a type of composite materials and it is not possible to grow a single crystal for analysis. The structure may be determined by comparing with the patterns of crystalline materials in the database. It is possible that a mixture of crystalline materials has been formed.

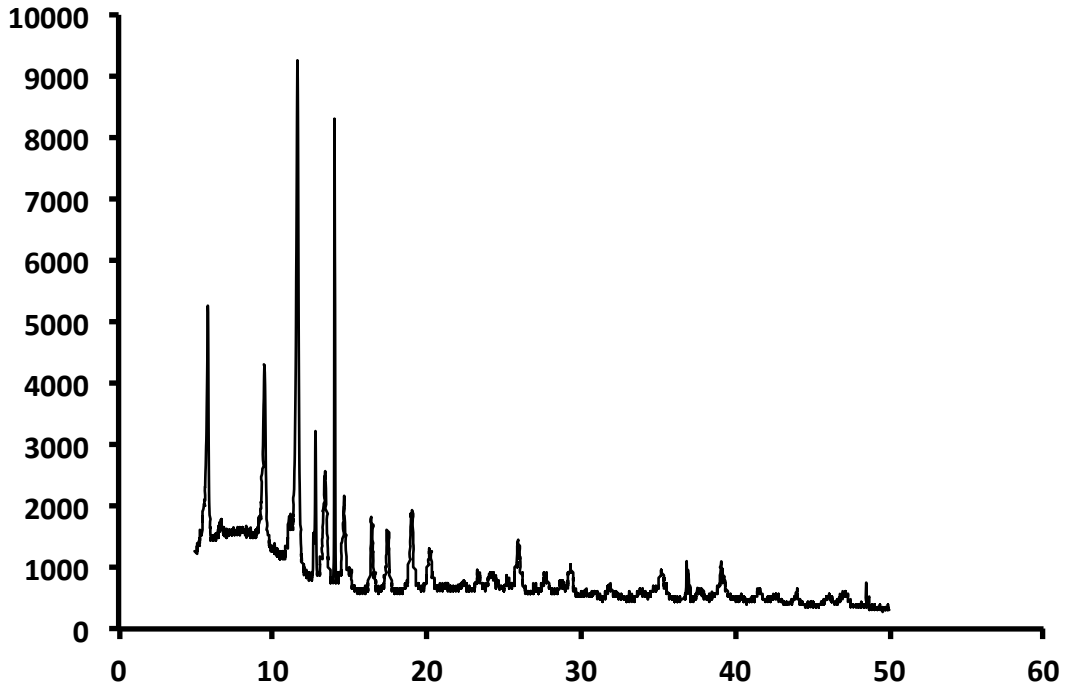

Figure 10. The power x-ray diffraction (PXRD) pattern shows the presence of crystalline phase in the composite beads after reaction in the ethanolic copper acetate solution.

The dry beads were also characterized by N_2 sorption in order to obtain surface area and porosity. This characterization is particularly important if the materials have high surface areas or contain micropores and/or mesopores. Figure 11 shows the isothermal curves and the pore size distribution of the dry bead prepared by the reaction in copper acetate ethanol solution. The adsorption curve and the desorption curve do not coincide with each other. The desorption of N_2 is clearly delayed,

indicating a possible strong interaction of N_2 molecules with the material. This material exhibited a BET surface area of 12.80 m^2/g (possible multiple layer of adsorbed N_2 molecules) and a Langmuir surface area of 18.23 m^2/g (monolayer adsorption of N_2 molecules). The maximum uptake of N_2 was 0.41 mmol/g.

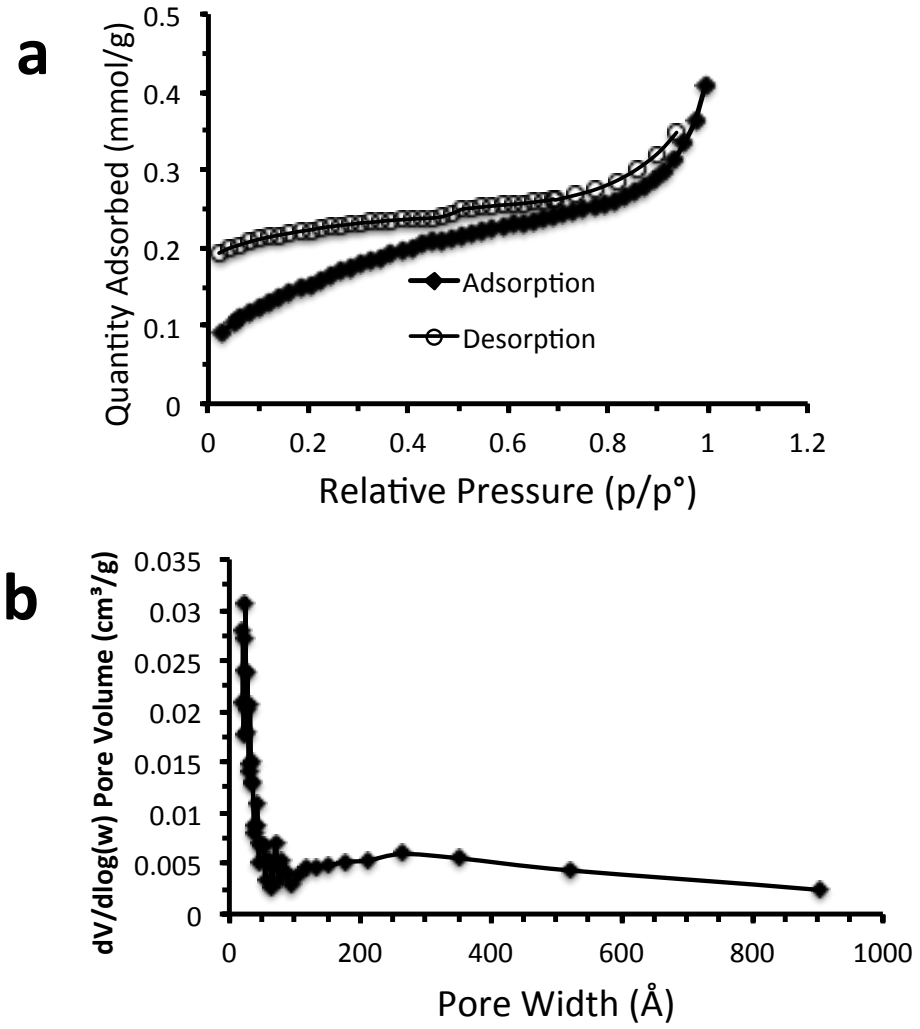

Figure 11. The characterization data of the dry BTC-chitosan gel beads reacted in ethanol copper acetate solution by N_2 sorption at 77 K. (a) The isothermal plot; (b) The pore size distribution obtained by the BJH method from the adsorption data.

Based on Figure 11b, a high proportion of the pores are in the range of < 5 nm. Polymer gels usually show very low surface area and a lack of micropores and mesopores. Thus, the data here indicate that some new structures may be formed in the composite beads. Although the total surface area is not high, there is a possibility that the newly-formed structure has high surface area but the micropores/mesopores may be blocked. In this case, a probe molecule with smaller size, *e.g.,* H_2, may be useful for better examining the porosity.

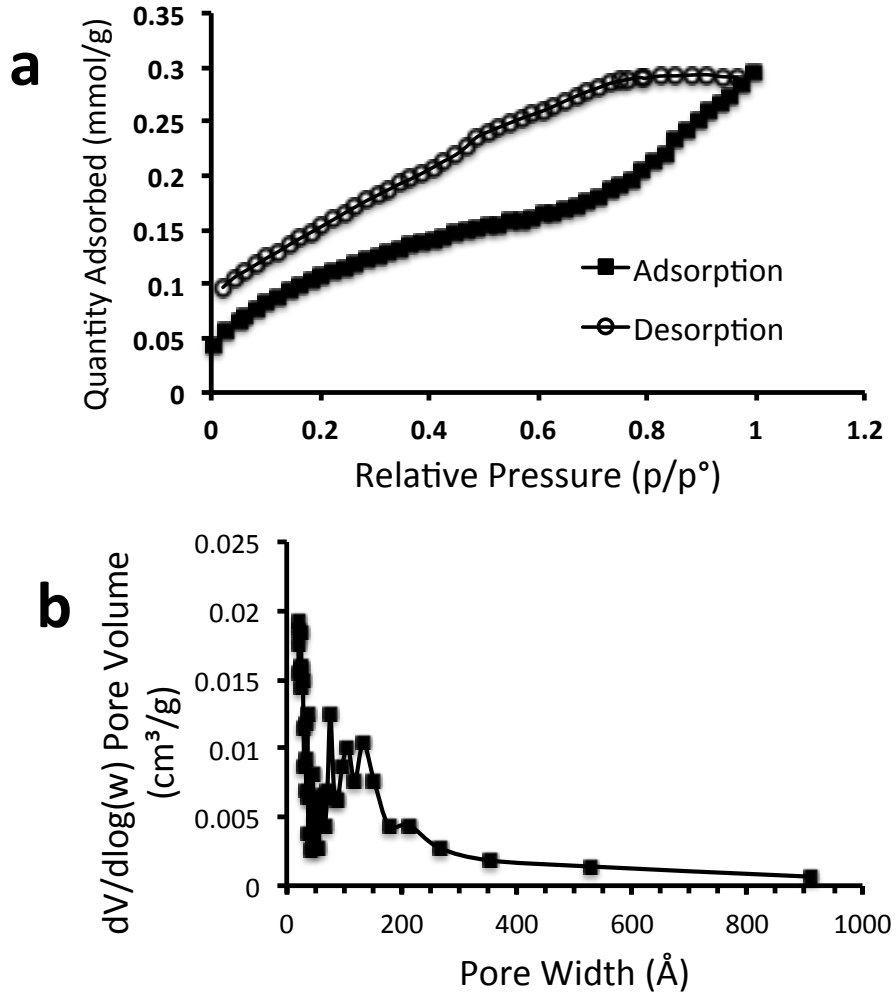

Figure 12. The characterization data of the dry BTC-chitosan gel beads reacted in aqueous copper acetate solution by N_2 sorption at 77 K. (a) The isothermal plot; (b) The pore size distribution obtained by the BJH method from the adsorption data.

Figure 12 shows the isothermal curves and the pore size distribution for the composite bead made from the reaction with aqueous copper acetate solution. There is also a discrepancy between the adsorption and desorption branches, similarly indicating a strong interaction between N_2 molecules and the material. The N_2 uptake was a bit lower, at 0.293 mmol/g. This is reflected by lower BET surface area of 9.15 m^2/g and Langmuir surface area of 13.48 m^2/g. As shown in Figure 12b, the pore size distribution is quite different from that of the beads made from ethanolic copper acetate solution. In addition to the pores < 5 nm, there is a peak across 5-20 nm. It should be pointed out the pore size is associated with the possible intrinsic metal-organic structure and the aggregation/assembly of the nanoparticles as seen in Figure 9d.

CONCLUSION

A new method of preparing chitosan hydrogel using 1,3,5-benzene tricarboxylic acid (BTC) has been reported. The hydrogels can be readily formed at room temperature simply by dropping aqueous chitosan solution into the ethanol-BTC solution. The gel beads are formed instantly but are usually kept in the ethanol-BTC solution for an additional 10 minutes to complete the gelation. Chitosan hydrogel dots or films can be similarly formed by spreading or dotting the chitosan solution on a glass slide which is then immersed in the ethanol-BTC solution.

Some of the useful properties of this method and the chitosan hydrogels have been shown. The chitosan hydrogel is not cytotoxic at least for 24 hours, as demonstrated by culturing with L929 cells. However, the cells did not attach to the hydrogel and tended to aggregate. This has been attributed to the presence of BTC and ethanol in the chitosan hydrogels. It is proposed that a thorough washing procedure may be able to address this issue. However, this new preparation method has found to

be effective for encapsulating hydrophilic or hydrophobic compounds into the chitosan gel, as evidenced by the encapsulation of hydrophobic dye Oil Red O and hydrophilic dye Rhodamine 6G. The sustainable release of Rhodamine 6G has also been shown. Furthermore, the chitosan hydrogel beads have been used as scaffolds to prepare the chitosan-based composite beads via the reactions with copper acetate. Strong blue beads with surface areas in the region of 10 m^2/g and micropores/mesopores have been prepared.

EXPERIMENTAL SECTION

Chemicals and Reagents. Sodium triphosphate pentabasic (NaTPP), NaOH, chitosan (medium molecular weight), acetic acid, Rhodamine 6G, Oil Red O, glutaraldehyde solution, 1,3,5-benzyl tricarboxylic acid (BTC) were purchased from Sigma Aldrich. Genipin was purchased from Alpha Laboratories Ltd. Distilled water was used for all the water solutions. All chemicals were used without further treatment.

The biological reagents: phosphate buffer solution (PBS), high glucose DMEM (Dulbecco's Modified Eagle's Medium) base medium, non-essential aminio acid, L-glutamine, trypsin- EDTA (Ethylenediaminetetraacetic acid) and methylene blue were obtained from Sigma-Aldrich. The L929 cell line (mouse fibroblast cells) was obtained commercially from ATCC.

Preparation of chitosan hydrogels. Aqueous chitosan solution (1 wt%) was prepared by dissolving 2 g chitosan in 200 mL water containing 0.6 v/v% acetic acid by stirring overnight. 50 mM BTC ethanol solution was prepared by dissolving 2.10 g BTC powder in 200 mL ethanol. 10 % TPP aqueous solution was prepared by dissolving 10 g NaTPP in 100 mL deionized water. 0.1 N sodium hydroxide (NaOH) aqueous solution was prepared by dissolving 0.2 g NaOH in 50 mL deionized water.

0.5 wt% genipin solution was prepared by dissolving 0.1 g genipin in 20 ml 50 v/v% ethanol water solution.

Chitosan hydrogel formed in BTC ethanol solution: A syringe with 26 gauge needle was used to inject chitosan solution into BTC ethanol solution drop by drop. Gel beads were instantly formed as chitosan drops were sinking into BTC solution. The gel beads were kept the bottom of the solution for 1 hour before filtration. For chitosan gel film on coverslip, 50 uL 1 wt% chitosan was pipetted on a 13 mm coverslip and evenly spread and then soaked into BTC solution. Gel dots on coverslip were prepared by placing chitosan solution droplets on coverslip instead of evenly spreading chitosan solution. Chitosan hydrogels were always allowed to age for at least 1 hour in the BTC-ethanol solution before collection by filtration.

The same procedure was followed to chitosan hydrogels with 10 wt% aqueous NaTPP solution.

Chitosan hydrogel further crosslinked by genipin: The chitosan gel beads prepared from 0.1 N NaOH solution and the chitosan gel on coverslip formed by soaking in 0.1 N NaOH solution were transferred and soaked in 0.5% genipin solution at room temperature for 1 h.

Cell culture with chitosan hydrogel. Chitosan hydrogel dots on coverslips were used for cell culture experiments. Glass coverslip were used as controls. After gelation, the gel dots were washed with ethanol three times before washing with deionized water three times, and then soaked in full culture medium (10% FBS in high glucose DMEM with supplements: L- glutamine, non-essential amino acid) overnight before seeding cells. The coverslips were carefully put into the 24 well culture plate and the seeding density was 5000 cells per coverslip. Images were taken after culturing for 48 hours using Leica DM 2500 microscope.

Encapsulation and release of hydrophilic/hydrophobic compounds (Rhodamine 6G and Oil Red O). Oil Red O is a hydrophobic dye. It was dissolved in the ethanol solution of BTC (50 mM) with a concentration of around 0.05 w/v%. This results in a clear red solution. The aqueous chitosan solution (1 wt%) was injected into the red BTC solution dropwise. The red gel beads remained in the ethanol solution for 1 hour to complete the gelation process.

Rhodamine 6G is soluble in both water and ethanol. In this study, Rhodamine 6G was dissolved in 1 wt% aqueous chitosan solution with a concentration of 0.1 wt %. The similar preparation procedure was applied to produce the gel beads. Initially, the beads were red. With time, Rhodamine 6G was released into the surrounding ethanol solution.

Preparation of chitosan-based composite beads with copper acetate. Chitosan gel beads prepared with the above procedure were washed with pure ethanol 3 times. The washed gel beads were then immersed in copper acetate solution in water (3.6 g copper acetate dissolved in 50 mL water) for 24 hours. The same experiment was also performed in copper acetate-ethanol solution with the same w/v % concentration for 24 hours. This was because both water and ethanol have been used as solvents to prepare the metal-organic framework HKUST-1 from BTC and copper acetate. After the reaction, the colourless transparent chitosan gel beads turned blue. The blue beads were washed with ethanol, air dried or freeze-dried, crushed as necessary for further characterization.

Characterizations. The morphology of the materials was observed by a Hitachi-S4800 scanning electron microscope (SEM). A small piece of the material was adhered to a stud using double-sided carbon tape. The non-conductive samples were coated with gold using a sputter-coater (EMITECH K550X) for 2 minutes at 25 mA

before SEM imaging. Powder X-ray diffraction (PXRD) patterns were collected on a Panalytical X' Pert Pro Multi-Purpose Diffractometer in high-throughput transmission geometry. Cu anode was operated at 40 kV and 40 mA. Samples were pressed into the well of aluminium plate. XRD patterns were measured over 5-50°2θ with a scan time of 60 min. Brunauer-Emmette-Teller (BET) specific surface areas and Barrette-Joynere-Halenda (BJH) pore size distributions were obtained by N_2 sorption at 77 K using a Micromeritics ASAP 2420 volumetric adsorption analyser. The samples were degassed for 48 h at 120 °C before N_2 sorption analysis. An Olympus CX41 microscope with Plan magnifying lenses was used for imaging hydrogel beads. CellSens entry imaging software by Olympus was used for size measurements. The Leica DM 2500 microscope was used to observe the cell growth.

AUTHOR INFORMATION

Corresponding Author

*Email: zhanghf@liverpool.ac.uk

ORCID

Haifei Zhang: 0000-0001-5142-5824

Author Contributions

Y.Y. carried out the experimental work. Y.Y., T.M., and H.Z. have written up the manuscript.

Notes

The authors declare no competing financial interest.

ACKNOWLEDGEMENT

Y.Y. acknowledges the PhD studentship from the EPSRC.

REFERENCES

(1) Thiele, J.; Ma, Y.; Bruekers, S.M.C.; Ma, S.; Huck, W.T.S. Designer hydrogels for cell cultures: a materials selection guide. *Adv. Mater.* **2014**, *26*, 125-148.

(2) Lee, S.C.; Kwon, I.K.; Park, K. Hydrogels for delivery of bioactive agents: A historical perspective. *Adv. Drug Del. Rev.* **2013**, *65*, 17-20.

(3) Martins, A.M.; Alves, C.M.; Kasper, F.K.; Mikos, A.G.; Reis, R.L. Responsive and in situ-forming chitosan scaffolds for bone tissue engineering applications: an overview of the last decade. *J. Mater. Chem.* **2010**, *20*, 1638-1645.

(4) Custódio, C.A.; Cerqueira, M.T.; Marques, A.P.; Reis, R.L.; Mano, J.F. Cell selective chitosan microparticles as injectable cell carriers for tissue regeneration. *Biomaterials* **2015**, *43*, 23-31.

(5) Moreau, J.L.; Xu, H.H.K. Mesenchymal stem cell proliferation and differentiation on an injectable calcium phosphate – chitosan composite scaffold. *Biomaterials* **2009**, *30*, 2675-2682.

(6) Bernkop-Schnürch, A.; Dünnhaupt, S. Chitosan-based drug delivery systems. *Eur. J. Pharm. Biopharm.* **2012**, *81*, 463-469.

(7) Naahidi, S.; Jafari, M.; Edalat, F.; Raymond, K.; Khademhosseini, A.; Chen, P. Biocompatibility of engineering nanoparticles for drug delivery. *J. Control. Release* **2013**, *166*, 182-194.

(8) Rinaudo, M. Chitin and chitosan: properties and applications. *Prog. Polym. Sci.* **2006**, *31*, 603-632.

(9) Shukla, S.; Mishra, A.K.; Arotiba, O.A.; Mamba, B.B. Chitosan-based nanomaterials: a state-of-the-art review. *Int. J. Biol. Macromol.* **2013**, *59*, 46-58.

(10) Upadhyaya, L.; Singh, J.; Agarwal, V.; Tewari, R.P. The implications of recent advances in carboxymethyl chitosan based targeted drug delivery and tissue engineering applications. *J Control. Release.* **2014**, *186*, 54-87.

(11) Casettari, L.; Vllasaliu, D.; Lam, J.K.W.; Soliman, M.; Illum, L. Biomedical applications of amino acid-modified chitosans: A review. *Biomaterials* **2012**, *33*, 7565-7583.

(12) Kievit, F.M.; Florczyk, S.J.; Leung, M.C.; Veiseh, O.; Park, J.O.; Disis, M.L.; Zhang, M. Chitosan-alginate 3D scaffolds as a mimic of the glioma tumor microenvironment. *Biomaterials* **2010**, *31*, 5903-5910.

(13) Deng, C.; Zhang, P.; Vulesevic, B.; Kuraitis, D.; Li, F.; Yang, A.F.; Griffith, M.; Ruel, M.; Suuronen, E.J. A collagen–chitosan hydrogel for endothelial differentiation and angiogenesis. *Tissue Eng. A* **2010**, *16*, 3099-3109.

(14) Bhattarai, N.; Gunn, J.; Zhang, M. Chitosan-based hydrogels for controlled, localized drug delivery. *Adv. Drug Del. Rev.* **2010**, *62*, 83-99.

(15) Jonassen, H.; Kjøniksen, A.-L.; Hiorth, M. Effects of ionic strength on the size and compactness of chitosan nanoparticles. *Colloid Polym. Sci.* **2012**, *290*, 919-929.

(16) Chenite, A.; Chaput, C.; Wang, D.; Combes, C.; Buschmann, M.D.; Hoemann, C.D.; Leroux, J.C.; Atkinson, B.L.; Binette, F.; Selmani, A. Novel injectable neutral solutions of chitosan form biodegradable gels in situ. *Biomaterials* **2000**, *21*, 2155-2161.

(17) Ahmadi, R.; de Bruijn, J.D. Biocompatibility and gelation of chitosan-glycerol phosphate hydrogel. *J. Biomed. Mater. Res.* **2008**, *86A*, 824-832.

(18) Naderi-Meshkin, H.; andreas, K.; Matin, M.M.; Sittinger, M.; Bidkhori, H.R.; Ahmadiankia, N.; Bahrami, A.R.; Ringe, J. Chitosan-based injectable hydrogel as a

promising in situ forming scaffold for cartilage tissue engineering. *Cell Biol. Int.* **2014**, *38*, 72-84.

(19) Ji, C.; Khademhosseini, A.; Dehghani, F. Enhancing cell penetration and proliferation in chitosan hydrogels for tissue engineering applications. *Biomaterials* **2011**, *32*, 9719-9729.

(20) Skop, N.B.; Calderon, F.; Levison, S.W.; Gandhi, C.D.; Cho, C.H. Heparin crosslinked chitosan microspheres for the delivery of neural stem cells and growth factors for central nervous system repair. *Acta Biomater.* **2013**, *9*, 6834-6843.

(21) Bi, L.; Cao, Z.; Hu, Y.; Song, Y.; Yu, L.; Yang, B.; Mu, J.; Huang, Z.; Han, Y. Effects of different cross-linking conditions on the properties of genipin-cross-linked chitosan/collagen scaffolds for cartilage tissue engineering. *J. Mater. Sci. Mater. Med.* **2011**, *22*, 51-62.

(22) Agnihotri, S.A.; Mallikarjuna, N.N.; Aminabhavi, T.M. Recent advances on chitosan-based micro- and nanoparticles in drug delivery. *J. Control. Release* **2004**, *100*, 5-28.

(23) Grenha, A. Chitosan nanoparticles: a survey of preparation methods. *J. Drug Targeting* **2012**, *20*, 291-300.

(24) Jayakumar, R.; Prabaharan, M. Nair, S. V.; Tamura, H. Novel chitin and chitosan nanofibers in biomedical applications. *Biotechnol. Adv.* **2010**, *28*, 142-150.

(25) Chen, P.; Kuo, T.; Liu, F.; Hwang, Y.; Ho, M.; Wang, D.; Lai, J.; Hsieh, H. Use of dicarboxylic acids to improve and diversity the material properties of porous chitosan membranes. *J. Agric. Food Chem.* **2008**, *56*, 9015-9021.

(26) Ghosh, A.; Ali, M.A. Studies on physicochemical characteristics of chitosan derivatives with dicarboxylic acids. *J. Mater. Sci.* **2012**, *47*, 1196-1204.

(27) Valderruten, N.E.; Valverde, J.D.; Zuluaga, F.; Ruiz-Durantez, E. Synthesis and characterization of chitosan hydrogels cross-linked with dicarboxylic acids. *React. Funct. Polym.* **2014**, *84*, 21-28.

(28) Tsao, C.T.; Chang, C.H.; Li, Y. D.; Wu, M.F.; Lin, C.P.; Han, J.L.; Chen, S.H.; Hsieh, K.H. Development of chitosan/dicarboxylic acid hydrogels as wound dressing materials. *J. Bioactive Compatible Polym.* **2011**, *26*, 519-536.

(29) Tang, L.M.; Wang, Y.J. Highly stable supramolecular hydrogels formed from 1,3,5-benzenetricarboxylic acid and hydroxyl pyridines. *Chin. Chem. Lett.* **2009**, *20*, 1259-1262.

(30) Ahmed, A.; Forster, M.; Clowes, R.; Myers, P.; Zhang, H. Hierarchicaly porous metal-organic framework monoliths. *Chem. Commun.* **2014**, *50*, 14314 – 14316.

(31) Ahmed, A.; Hasell, T.; Clowes, R.; Myers, P.; Cooper, A.I.; Zhang, H. Aligned macroporous monoliths with intrinsic microporosity via a frozen-solvent-templating approach. *Chem. Commun.* **2015**, *51*, 1717-1720.

(32) Ameloot, R.; Vermoortele, F.; Vanhove, W.; Roeffaers, M.B.J.; Sels, B.F.; De Vos, D.E. Interfacial synthesis of hollow metal–organic framework capsules demonstrating selective permeability. *Nat. Chem*. **2011**, *3*, 382 - 387.

(33) Horcajada, P.; Gref, R.; Baati, T.; PAllan, P.K.; Maurin, G.; Couvreur, P.; Ferey, G.; Morris, R.E.; Serre, C. Metal–organic frameworks in biomedicine. *Chem. Rev.* **2012**, *112*, 1232 – 1268.

(34) Qian, L.; Zhang, H. Controlled freezing and freeze drying: a versatile route for porous and micro-/nano-structured materials. *J. Chem. Technol. Biotechnol.* **2011**, *86*, 172-184.

(35) Qian, L.; Ahmed, A.; Foster, A.; Rannard, S.P.; Cooper, A.I.; Zhang, H. Systematic tuning of pore morphologies and pore volumes in macroporous materials by freezing. *J. Mater. Chem.* **2009**, *19*, 5212-5219.

(36) Qian, L.; Willneff, E.; Zhang, H. A novel route to polymeric sub-micron fibers and their use for inorganic structures. *Chem. Commum.* **2009**, 3946-3948.

(37) Wais, U., Jackson, A.W., He, T., Zhang, H. Nanoformulation and encapsulation approaches for poorly water-soluble drug nanoparticles. *Nanoscale* **2016**, *8*, 1746 – 1769.

(38) Qian, L.; Zhang, H. Green synthesis of chitosan-based nanofibers and their applications. *Green Chem*. **2010**, *12*, 1207-1214.

(39) Ahmed, A.; Hearn, J.; Abdelmagid, W.; Zhang, H. Dual-tuned drug release by nanofibrous scaffolds of chitosan and mesoporous silica microspheres. *J. Mater. Chem.* **2012**, *22*, 25027-25035.

(40) Nune, S.K.; Thallapally, P.K.; McGrail, B.P. Metal organic gels (MOGs): a new class of sorbents for CO_2 separation applications. *J. Mater. Chem.* **2010**, *20*, 7623-7625.